

# ***Integration of EBS Models with Generic Disposal System Models***

**Fuel Cycle Research & Development**

**(FCRD-UFD-2012-000277)**

*Prepared for  
U.S. Department of Energy  
Used Fuel Disposition Campaign*

*David C. Sassani, Carlos F. Jové Colón, Philippe Weck  
(Sandia National Laboratories)*

*James L. Jerden Jr., Kurt E. Frey, Terry Cruse, William L.  
Ebert (Argonne National Laboratory)*

*Edgar C. Buck, Richard S. Wittman, Frances N.  
Skomurski, Kirk J. Cantrell, Bruce K. McNamara, Chuck  
Z. Soderquist  
(Pacific Northwest National Laboratory)*

*September 07, 2012*

**SAND2012-7762 P**



#### **DISCLAIMER**

This information was prepared as an account of work sponsored by an agency of the U.S. Government. Neither the U.S. Government nor any agency thereof, nor any of their employees, makes any warranty, expressed or implied, or assumes any legal liability or responsibility for the accuracy, completeness, or usefulness, of any information, apparatus, product, or process disclosed, or represents that its use would not infringe privately owned rights. References herein to any specific commercial product, process, or service by trade name, trade mark, manufacturer, or otherwise, does not necessarily constitute or imply its endorsement, recommendation, or favoring by the U.S. Government or any agency thereof. The views and opinions of authors expressed herein do not necessarily state or reflect those of the U.S. Government or any agency thereof.

Prepared by:

Sandia National Laboratories

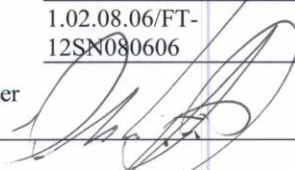
Albuquerque, New Mexico 87185

Sandia National Laboratories is a multi-program laboratory managed and operated by Sandia Corporation, a wholly owned subsidiary of Lockheed Martin Corporation, for the U.S. Department of Energy's National Nuclear Security Administration under contract DE-AC04-94AL85000.



**FCT Quality Assurance Program Document**

**Appendix E  
 FCT Document Cover Sheet**

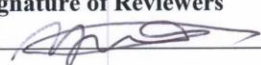
Name/Title of Deliverable/Milestone	Integration of EBS Models with Generic Disposal System Models		
Work Package Title and Number	Engineered Barrier Systems (EBS) Evaluation - SNL (FT-12SN080606)		
Work Package WBS Number	1.02.08.06/FT-12SN080606	Milestone Number	M2FT-12SN0806062
Responsible Work Package Manager	 Carlos F. Jové Colón (Name/Signature)		09/07/2012 (Date Submitted)
Quality Rigor Level for Deliverable/Milestone	<input checked="" type="checkbox"/> QRL-3	<input type="checkbox"/> QRL-2	<input type="checkbox"/> QRL-1 <input type="checkbox"/> Nuclear Data <input type="checkbox"/> N/A*

This deliverable was prepared in accordance with Sandia National Laboratories  
 (Participant/National Laboratory Name)

QA program which meets the requirements of  
 DOE Order 414.1     NQA-1-2000     Other: DOE QA Order

**This Deliverable was subjected to:**

<input checked="" type="checkbox"/> Technical Review	<input type="checkbox"/> Peer Review
<b>Technical Review (TR)</b>	<b>Peer Review (PR)</b>
<b>Review Documentation Provided</b>	<b>Review Documentation Provided</b>
<input type="checkbox"/> Signed TR Report, or TR Report No.: _____	<input type="checkbox"/> Signed PR Report, or PR Report No.: _____
<input type="checkbox"/> Signed TR Concurrence Sheet (attached), or	<input type="checkbox"/> Signed PR Concurrence Sheet (attached), or
<input checked="" type="checkbox"/> Signature of TR Reviewer(s) below	<input type="checkbox"/> Signature of PR Reviewers below

<b>Name and Signature of Reviewers</b>	
Yifeng Wang 	09/06/2012
_____	_____
_____	_____
(Name/Signature)	(Date)

\*Note: In some cases there may be a milestone where an item is being fabricated, maintenance is being performed on a facility, or a document is being issued through a formal document control process where it specifically calls out a formal review of the document. In these cases, documentation (e.g., inspection report, maintenance request, work planning package documentation, or the documented review of the issued document through the document control process) of the completion of the activity along with the Document Cover Sheet is sufficient to demonstrate achieving the milestone. QRL for such milestones may also be marked N/A in the work package provided the work package clearly specifies the requirement to use the Document Cover Sheet and provide supporting documentation.

## ACKNOWLEDGEMENTS

The authors acknowledge our gratitude to Yifeng Wang (SNL), Palmer Vaughn (SNL), Robert Finch (SNL), Geoff Freeze (SNL), Peter Swift (SNL), Kevin McMahon (SNL), William Spezialetti (DOE NE-53), Prasad Nair (DOE NE-53), Mark Tynan (DOE NE-53), Joseph Price (DOE NE-53) and Tim Gunther (DOE NE-53) for their helpful discussions on topics covered in this report. We thank Alexander Thompson and Chris Wolverton (Northwestern University) for providing us with the optimized structure of uranium dioxide with distortion of the oxygen sublattice.

## SUMMARY

The Used Fuel Disposition (UFD) Campaign supports the Fuel Cycle Technology (FCT) Program established by the United States Department of Energy Office of Nuclear Energy (DOE-NE). The mission of the UFD Campaign is to identify alternatives and conduct scientific research and technology development to enable storage, transportation and disposal of used nuclear fuel (UNF) and wastes generated by existing and future nuclear fuel cycles. This report summarizes research activities on engineered barrier system (EBS) model integration with the generic disposal system model (GDSM), and used fuel degradation and radionuclide mobilization (RM) in support of the EBS evaluation and tool development within the UFD campaign.

The engineered barrier system (EBS) work package entails the evaluation, tool development, and integration with generic disposal system models including the study of used nuclear fuel degradation. The latter ultimately determines radionuclide releases beyond the confines of the nuclear fuel and waste container. Integration of EBS models with generic disposal system models is an effort that evolves in parallel with performance and safety assessments (PA and SA), and repository barrier processes (and sub-processes) model development. The analysis of generic disposal concepts requires the accurate understanding of processes leading to radionuclide releases from the EBS, specifically at the barrier interface between fuel assemblies and containment structures. Multilayered EBS concepts and related materials evaluated by the UFD seek to provide the necessary level of confidence to ensure safe and robust long-term waste isolation. However, it is sensible to anticipate that waste containment failure would affect some canisters, therefore exposing fuel to interactions with subsurface fluids and eventually leading to radionuclide release. Given the importance of such processes to long-term repository performance, the main objectives of this effort are:

- Implementation of a predictive model capability for used nuclear fuel degradation based on electrochemical and thermodynamic principles. This model implementation in the form of a computational tool development is based on the Canadian-mixed potential model for  $\text{UO}_2$  fuel dissolution.
- Development of a comprehensive radiolysis model to evaluate the  $\text{U(VI)}\text{-H}_2\text{O-CO}_2$  system. Radiolytic products exert strong effects on  $\text{UO}_2$  dissolution at the solid-aqueous interface. Therefore, the effects of radiolysis on solution redox speciation at this interfacial domain need to be considered along with  $\text{UO}_2$  corrosion models.
- Use of computational methods and approaches based on first principles to study the stable structures of uranium-bearing oxides and its degradation products. Exploitation of these state-of-the-art approaches and their validation with existing structural phase data is an important step towards the evaluation of uranium alteration products where synthetic data is often very difficult to obtain.
- Data analysis and generation of statistical distributions to represent the instant release fraction (IRF) of radionuclides from the nuclear fuel.
- Preliminary development of an integrated framework strategy for passing information between EBS process models and generic disposal system modeling (GDSM) components.

The contributions presented in this report are the result of a concerted effort among three different national laboratories: Argonne National Laboratories (ANL), Sandia National SNL, and PNNL. The main accomplishments of this activity are summarized as follows:

- Computational implementation and validation of the Canadian mixed potential model for  $\text{UO}_2$  fuel corrosion. This model is based on the fundamental electrochemical and thermodynamic properties described by interactions at the fuel – fluid interface. This model captures key processes to fuel degradation such as hydrogen oxidation at the used fuel interface and the catalysis of oxidation/reduction reactions by noble metal particles on the fuel surface (epsilon phases).
- Computational development and implementation of a radiolysis model using a comprehensive set of radiolysis reactions to better account for potential solution compositions to be encountered in repository environments. Such a feature of the current model is not considered by the European radiolysis model and allows for heterogeneous  $\text{CO}_2$  speciation thus accounting for the presence of  $\text{HCO}_3^-$ . Comparisons of modeling results are in good agreement with those reported in other studies.
- A computational first principles study of the structures of the uranyl peroxide hydrates studtite and metastudtite. These two phases are important products of  $\text{UO}_2$  corrosion when exposed to water. The structures obtained from total energy calculations using density functional theory (DFT) are in very good agreement with those characterized by experimental X-ray diffraction methods. Such result is crucial in testing this computational tool to predict the phase stability of  $\text{UO}_2$  corrosion products and quantify their thermodynamic properties. The results of this work have been accepted for publication in the peer-reviewed journal Dalton Transactions.
- Development of distributions for the IRF from the nuclear fuel. The existing data on IRF is largely empirical and strongly dependent on the state of the fuel and cladding, burnup rates, irradiation history (e.g., linear thermal, and extent of interaction with solutions and gases.) Therefore, the IRF of radionuclides is described by initial models using distributions to be sampled by PA models. This is implemented in two sets of distributions: (a) triangular distributions representing minimum, maximum, and mean (apex) values for LWR used fuel with burnup at or below 50 MWd/KgU, and (b) a process model has yet to be developed with functional parametrics.
- Development of an idealized strategy for model integration with generic disposal concepts. Significant efforts have produced process and sub-process models at the EBS scales. However, it is an ongoing task to delineate how these process models will couple to others within the EBS process models and, subsequently, how such coupled models would be incorporated into the generic performance assessment model (GPAM) for generic evaluations of the safety case.

## TABLE OF CONTENTS

Summary .....	v
Acronyms and Abbreviations .....	xiii
1. Engineered Barrier System (EBS) Concepts and Used Fuel Degradation Processes .....	15
1.1 Introduction.....	15
1.1.1 Overview of Engineered Barrier Systems Evaluations .....	16
1.2 Overview of Used Fuel Degradation and Radionuclide Mobilization (RM) Activities.....	23
1.2.1 Introduction and Accomplishments .....	23
1.2.2 Background .....	25
1.2.3 Integration/Interfaces .....	26
1.3 References for Section 1 .....	30
2. The Engineered Barrier System Structure within Generic Performance Assessment Model (GPAM).....	32
2.1 Introduction to Generic Disposal System Modeling and GPAM.....	32
2.1.1 GPAM Concepts and EBS Construct.....	32
2.1.2 GPAM Platform (Freeze et al., 2012 in prep).....	33
2.2 Current Implementation of EBS Models included in GPAM .....	33
2.2.1 Used Fuel Degradation Rate Modeling.....	33
2.3 References for Sec. 2.0 .....	38
3. Used Fuel Degradation and Radionuclide Mobilization Concepts and Models .....	39
3.1 Overview and Concepts .....	40
3.1.1 Background .....	40
3.1.2 Framework of Spent Fuel Degradation and Radionuclide Mobilization Processes .....	42
3.1.3 References for Section 3.1 .....	44
3.2 Fast/Instant Release of Radionuclides .....	45
3.2.1 Used Fuel Structural Considerations.....	45
3.2.2 Models of the Instant Release Fraction Radionuclides .....	48
3.2.3 References for Section 3.2 .....	52
3.3 Radiolytic Processes Modeling .....	54
3.3.1 Radiolysis Process Model Description.....	54
3.3.2 Verification, Validation, and Sensitivity Analyses .....	62
3.3.3 Uncertainty and Conditional Applicability .....	64
3.3.4 Conclusions and Recommendations .....	69
3.3.5 References for Section 3.3 .....	71
3.4 Electrochemical Model for Used Fuel Matrix Degradation Rate .....	73
3.4.1 Introduction and Background.....	73
3.4.2 Used Fuel Degradation Modeling Approach .....	78
3.4.3 Verification of ANL-MPM and Sensitivity Studies of Selected Parameters .....	98
3.4.4 Example Calculation of Used Fuel Matrix Degradation Rate Using the ANL-MPM.....	102
3.4.5 Conceptual Approach for Effects of NMP-Catalyzed Reactions.....	105
3.4.6 Summary and Interface with Generic Performance Assessment Models .....	109

3.4.7	References for Section 3.4 .....	111
3.5	First Principles Modeling of UO <sub>2</sub> and Uranyl Peroxides .....	119
3.5.1	First Principles Evaluation of Surface Properties and Chemistry of Uranium Dioxide.....	119
3.5.2	Structures of uranyl peroxide hydrates: a first-principles study of studtite and metastudtite .....	128
3.5.3	References.....	136
4.	Summary and Conclusions .....	141

## FIGURES

Figure 1.1-1.	EBS coupled process phenomena (center) and interrelations between process models from other domains (modified after Olivella et al. 2011) .....	19
Figure 2.1-1.	Description of the Generic Performance Assessment Model (GPAM) concepts, including interfaces, showing features, and processes throughout the representation (Freeze and Vaughn, 2012).....	33
Figure 2.2-1.	Schematic of Source Term, Degraded Waste Form, and Primary Engineered Barrier Representation (after Clayton et al., 2011; Fig. 3.3-4) .....	35
Figure 3.2-1.	Schematic of a fuel pellet cross section showing the relative locations of radionuclide inventories for the gap, grain boundaries, fuel matrix, and noble metal particles. Also shown are the general locations of accessible grain boundaries and inaccessible grain boundaries. ....	46
Figure 3.2-2.	Schematic of a fuel pellet cross section for high BU used fuel showing the rim region high burnup structure (HBS), transitional region, and core region (after Figure 1 of Serrano-Purroy et al., 2012). ....	47
Figure 3.3-1.	The dose to the surface of used fuel exposed to a mixed water-air environment (10% water) is dominated by long-lived alpha radiation even at relatively short times out of reactor [Adapted from Radulescu et al. 2011]. ....	55
Figure 3.3-2.	Schematic of reaction pathways in the radiolysis model (adapted from Sunder, 1998).....	56
Figure 3.3-3.	Calculated surface environment within 30 mm of a 160 rad/s alpha field in an anoxic environment illustrating the time dependence of dominant species .....	57
Figure 3.3-4.	Radiolysis Model showing generation and diffusion across spatial regions. ....	59
Figure 3.3-5.	Shows the concentration history results for the same conditions (1 hr, 25 rad/s irradiation) as Figure 1 from Pastina and LaVerne (2001). ....	63
Figure 3.3-6.	Radiolysis model result with inputs from Christensen and Sunder (2000). ....	63
Figure 3.3-7.	Radiolysis model result for gamma irradiation with inputs from Ershov and Gordeev (2008). ....	64
Figure 3.3-8.	G-value sensitivity as $\Delta[A]/[A]$ for H <sub>2</sub> O <sub>2</sub> , H <sub>2</sub> O <sub>2</sub> , and •OH. ....	65
Figure 3.3-9.	Rate constant sensitivity as absolute value of $\Delta[H_2O_2]/[H_2O_2]$ . ....	66



Figure 3.3-10. H<sub>2</sub>O<sub>2</sub> concentration as a function of dose for fixed O<sub>2</sub> concentration and range of H<sub>2</sub> concentrations..... 66

Figure 3.3-11. H<sub>2</sub>O<sub>2</sub> concentration as a function of dose rate for cases of *zero* initial O<sub>2</sub> concentration ..... 67

Figure 3.4-1. Optical micrographs of a polished used fuel cross-section showing the distinct microstructural regions that influence degradation and radionuclide release (after Tsai 2003). This sample was cut from an H. B. Robinson PWR Rod with a burnup of 67 GWd/MTU..... 75

Figure 3.4-2. Schematic diagram identifying key surface processes involved in the degradation of used fuel (adapted from Shoesmith, 2007). ..... 78

Figure 3.4-3. Simplified representation of breached canister system used in Shoesmith et al. (2003) MPM for the oxidative degradation of UO<sub>2</sub> fuel due to alpha radiolysis of water. .... 79

Figure 3.4-4. Reaction scheme used in the Shoesmith et al. (2003) (Canadian-MPM) for the oxidative degradation of UO<sub>2</sub> fuel due to alpha radiolysis of water (key half-reactions listed below). ..... 81

Figure 3.4-5. Simplified algorithm for the evolution of the used fuel corrosion potential and interfacial reaction rates with time as calculated by the ANL-MPM: see Table 3.4-3 for concentration input sources. .... 88

Figure 3.4-6. Schematic representation of mixed potential model grid spacing between the used fuel and steel surface boundaries..... 89

Figure 3.4-7. Schematic drawing of the alpha-radiation regions within the ANL-MPM. See Table 3.4-5 and Section 3.4.2.3 for discussion. .... 97

Figure 3.4-8. Moles of H<sub>2</sub>O<sub>2</sub> (normalized to used fuel surface area) produced by alpha-radiolysis (with no U(VI) corrosion layer present) as calculated by the ANL-MPM. .... 98

Figure 3.4-9. Comparison of results from the ANL-MPM, MATLAB scripts (colored lines) with results from the Canadian-MPM (black line) and experimental results from King and Kolar (2002). ..... 100

Figure 3.4-10. Comparison of results from the ANL-MPM, MATLAB scripts (colored lines) with results from the Canadian-MPM (black lines) and experimental results from King and Kolar (2002). ..... 100

Figure 3.4-11. Comparison of results from the ANL-MPM, MATLAB scripts (colored lines) with results from the Canadian-MPM (black line) and experimental results from King and Kolar (2002). ..... 101

Figure 3.4-12. Comparison of results from the ANL-MPM, MATLAB scripts (colored lines) with results from the Canadian-MPM (black line) and experimental results from King and Kolar (2002). ..... 101

Figure 3.4-13. Dissolution rate of uranium dioxide in grams per year per square meter of exposed fuel calculated using the ANL-MPM for one millimolar dissolved carbonate (constant) and initial dissolved oxygen concentration of 1x10<sup>-6</sup> molar. .... 102

Figure 3.4-14. Time dependence of alpha-dose rate in water layer adjacent to used fuel (top) and fuel surface temperature (bottom) used in the example dissolution rate calculation shown in Figure 3.4-13..... 103

Figure 3.4-15. Fractional dissolution of cylindrical uranium dioxide pellet as a function of time calculated using the ANL-MPM and an assumed geometry described equations Eq. 3.4-27 to Eq. 3.4-29. ....	105
Figure 3.4-16. Simplified reaction scheme (not showing all component fluxes) used in the ANL-MPM modified to include catalytic roles of NMP. ....	108
Figure 3.4-17. Schematic representation highlighting the process of interest for the ANL study (top) and the basic experimental approach that will be used (bottom). ....	109
Figure 3.5-1. Crystal structure models of bulk $\text{UO}_2$ ( $Z = 4$ ) with collinear antiferromagnetic (AFM, type-I) arrangement of the uranium moments. ....	122
Figure 3.5-2. Ball-and-stick model of the clean $(2 \times 1)$ $\text{UO}_2(111)$ surface ( $Z = 4$ ) used in the present DFT calculations. ....	123
Figure 3.5-3. Evolution of (a) the lattice parameters and (b) the total energy of bulk $\text{UO}_2$ , with ferromagnetic (FM) and antiferromagnetic (AFM) arrangements of the uranium moments, as functions of the effective Hubbard parameter, $U_{\text{eff}}$ . ....	124
Figure 3.5-4. Variation of (a) the surface energy and (b) the work function of the relaxed $\text{UO}_2(111)$ surface with ferromagnetic (FM) and antiferromagnetic (AFM) arrangements of the uranium moments as functions of the effective Hubbard parameter, $U_{\text{eff}}$ . ....	125
Figure 3.5-5. Ball-and-stick Top view (left) and side view (right) of the $\text{UO}_2(111)$ model surface with half-monolayer coverage ( $\theta = 0.5$ ML) of (a) molecular water, (b) dissociated water, (c) atomic oxygen and (d) a full monolayer coverage ( $\theta = 1$ ML) of water and oxygen. ....	127
Figure 3.5-6. Crystal unit cell of studtite $(\text{UO}_2)_2\text{O}_2(\text{H}_2\text{O})_4$ (space group $C2/c$ , $Z = 4$ ) relaxed with DFT at the GGA/PW91 level of theory. (a) View of the packing of chains showing the uranium coordination polyhedra. Views along the directions: (b) [100], (c) [001] and (d) [010]. ....	131
Figure 3.5-7. Crystal unit cell of metastudtite $(\text{UO}_2)_2\text{O}_2(\text{H}_2\text{O})_2$ (space group $Pnma$ , $Z = 4$ ) relaxed with DFT at the GGA/PW91 level of theory. (a) View of the packing of chains showing the uranium coordination polyhedra. Views along the directions: (b) [010], (c) [100] and (d) [001]. ....	132
Figure 3.5-8. X-ray diffraction pattern of metastudtite. The experimental powder diffraction pattern for $\text{Cu K}_{\alpha 1}$ radiation (Debets, 1963) is represented by blue lines. The diffraction pattern simulated from the orthorhombic structure (space group $Pnma$ , $Z = 4$ ) reported in the present study is shown in red. A full-width at half-maximum (FWHM) parameter of $0.2 \ 2\theta$ was used in the simulation. ....	133
Figure 3.5-9. Ball-and-stick representation of the $(\text{UO}_2)\text{O}(\text{H}_2\text{O})$ complex composing metastudtite. ....	134

## TABLES

Table 1.1-1. Summary of the priority ranking for the EBS for buffer/backfill, seal/liner, waste materials, and waste package with associated FEPs (Nutt et al., 2011). .....	22
Table 1.1-2 (Cont.) Summary of the priority ranking for the EBS for buffer/backfill, seal/liner, waste materials, and waste package with associated FEPs (Nutt et al., 2011). .....	23
Table 1.2-1. Groupings of Potential Waste Form Types (UFD FEPs—Freeze et al., 2010) .....	26
Table 1.2-2. Waste form FEPs (from Table A-1 in Freeze et al., 2010).....	29
Table 3.2-1. Model values and measured values of the Instant Release Fractions (% of radioelement inventory) for spent fuel pellets of various burnups, for a variety of environment conditions, and from various regions of the fuel pellet samples. ....	51
Table 3.3-1. Gamma and Alpha particle $G$ -values adapted from Poinssot <i>et al.</i> , 2005).....	59
Table 3.3-2. Diffusion Constants (Christensen and Sunder, 1996) $D_i$ .....	60
Table 3.3-3. Water Reaction Rate Constants (Poinssot et al. 2005) ( $M^n s^{-1}$ ).....	61
Table 3.3-4. Carbonate Reaction rate constants (Poinssot et al. 2005) ( $M^n s^{-1}$ ). ....	61
Table 3.4-1, Part of the ANL-MPM parameter database: interfacial reactions for $UO_2$ matrix dissolution. See Fig. 3.4-4 for coupling between reactions. ....	83
Table 3.4-2. Part of the ANL-MPM parameter database: homogeneous reactions. See Fig. 3.4-4 for coupling between reactions.....	84
Table 3.4-3. Part of the ANL-MPM parameter database: components (species) included in mass balance equations (see examples Eq. 3.4-21 – Eq. 3.4-25). The concentration column ( $C_i$ ) identifies links to other UFD process models that are being or will be developed as part of the FY-2013 research and development activities (IPC: in-package-chemistry model).....	85
Table 3.4-4. Part of the ANL-MPM parameter database: physical parameters used in electrochemical and mass balance equations (Eq. 3.4-1 – Eq. 3.4-25).....	86
Table 3.4-5. Part of the ANL-MPM parameter database: parameters and variables used in the radiolysis sub-model (see Fig. 3.4-7 and Section 3.4.2.4. for discussion).....	87
Table 3.4-6. Extension of ANL-MPM parameter database to account for oxidation and reduction reactions that may be catalyzed on noble metal particle surfaces. ....	107
Table 3.5-1. Atomic positions and fractional coordinates of the $(UO_2)O(H_2O)$ complex composing metastudtite (space group $Pnma$ , $Z = 4$ ; $a = 8.42$ , $b = 8.78$ , $c = 6.51$ Å). ....	135
Table 3.5-2. Selected interatomic distances (Å), angles ( $^\circ$ ) in the structures of metastudtite and studtite <sup>a</sup> .....	135

## ACRONYMS AND ABBREVIATIONS

ANL	Argonne National Laboratory
ATM	Approved Testing Material
CHLW	Commercial High Level Waste
CP	Collaborative project
DECOVALEX	DEvelopment of COupled Models and their VALidation against Experiments
DHLW	Defense High Level Waste
DOE	Department of Energy (US DOE)
DR	Dissolution rate
EBS	Engineered Barrier System
EC	European Commission
EDS	Energy dispersive system
Eh	Oxidation potential (measured electrode potential)
EXAFS	Extended X-ray absorption fine structure spectroscopy
FACSIMILE	A computer program for modeling the kinetics of chemical systems
FEPs	Features, events, and processes
FCRD	Fuel Cycle Research and Development
FCT	Fuel Cycle Technology
FeO <sub>x</sub>	Iron oxide hydroxide corrosion products
FGR	Fission gas release
FIRST	Fast / Instant Release of Safety Relevant Radionuclides (EC project)
GDS	Generic Disposal System
GDSE	Generic Disposal System Environment
GDSM	Generic Disposal System Modeling
GTCC	Greater than Class C
HBS	High burnup structure
HLW	High Level Waste
HTGR	High temperature gas-cooled reactor
IGD-TP	Implementing Geological Disposal of Radioactive Waste – Technology Platform
IGSC	Integration Group for the Safety Case
IPC	In-package chemistry model
IRF	Instant release fraction
LET	Linear energy transfer
LLNL	Lawrence Livermore National Laboratory
LWR	Light water reactor

MAM	Matrix alteration model
MOX	Mixed oxide fuel (e.g., U and Pu oxides)
MPM	Mixed potential model
NEA	Nuclear Energy Agency
NGNP	Next Generation Nuclear Plant
NMP	Noble Metal Particle
NS	Natural System
ODEPACK	Computer codes for ordinary differential equations
PA	Performance assessment
PNNL	Pacific Northwest National Laboratory
PWR	Pressurized water reactor
R&D	Research and Development
RADFUEL	Radiolytically-aged doped (RAD) synthetic nuclear fuels
RN	Radionuclide
RM	Radionuclide mobilization
ROK	Republic of Korea
S <sub>A</sub>	Surface area (m <sup>2</sup> )
SA	Safety Assessment
SEM	Scanning Electron Microscopy
SNF	Spent Nuclear Fuel
SNL	Sandia National Laboratories
SPFT	Single pass flow-through test
SRA	Strategic Research Agenda
THCM	Thermal-hydrologic-chemical-mechanical (processes)
UF	Used Fuel
UNF	Used Nuclear Fuel
UFD	Used Fuel Disposition
UFDC	Used Fuel Disposition Campaign
UOX	Uranium oxide fuel
XANES	X-ray absorption near-edge spectroscopy
WFC	Waste Form Campaign
WP	Work package

**MINERAL NAMES AND CHEMICAL FORMULAE**

Coffinite	$\text{USiO}_4$
Ferrihydrite	$\text{Fe}_5\text{O}_3(\text{OH})_9$ (more commonly written as $\text{FeOOH}$ )
Goethite	$\alpha\text{-FeOOH}$
Hematite	$\text{Fe}_2\text{O}_3$
Meta-schoepite	$[(\text{UO}_2)_4\text{O}(\text{OH})_6](\text{H}_2\text{O})_5$
Meta-studtite	$\text{UO}_4 \cdot 2\text{H}_2\text{O}$
Schoepite	$[(\text{UO}_2)_8\text{O}_2(\text{OH})_{12}](\text{H}_2\text{O})_{12}$
Studtite	$[(\text{UO}_2)_2\text{O}_2(\text{H}_2\text{O})_2](\text{H}_2\text{O})_2$
Uraninite	$\text{UO}_2$

**UNITS**

$\mu\text{m}$	micrometer
g	grams
Gy	Grays (100 Rads)
Kg	kilograms
Kg	kilograms uranium
M	molarity, mole/liter
Mbq	millibecquerels
mg	milligram
MTU	Metric ton uranium
MWd	megawatt-days

# USED FUEL DISPOSITION (UFD) CAMPAIGN ENGINEERED BARRIER SYSTEMS (EBS) EVALUATIONS: USED FUEL DEGRADATION AND RADIONUCLIDE MOBILIZATION

## 1. Engineered Barrier System (EBS) Concepts and Used Fuel Degradation Processes

### 1.1 Introduction

The generic evaluation of EBS performance in geologic repositories requires an all-inclusive analysis of key processes (and sub-processes) affecting the isolation capacity of engineered barrier domains emplaced within the considered host media. Radionuclide releases from the barrier boundaries of the waste form and waste package assemblage are initiated through interactions with subsurface fluids in deep repository environments. The main processes responsible for radionuclide transport, barrier material degradation, and related advancements in modeling approaches are described in Jove Colon et al. (2011, 2012). These processes include, for example, clay phase transformation and/or chemical degradation, corrosion of metal container structures and nuclear fuel, and alteration of cementitious liners and seals. Jove Colon et al. (2012) outlined the need for a flexible and agile approach to the analysis of generic EBS design concepts and tool development. Flexibility in model and computer code development is needed to capture key features of the process models to provide an adequate and yet highly accurate representation of coupled phenomena in the EBS. The agile attribute involves the ability to adapt and bridge various components of the process model development in a rapid and efficient manner. This strategy also comprises integration of process model components with those needed in the performance assessment (PA) analysis including the generation of input/output parameters and database development.

Jove Colon et al. (2012) described the importance of the analysis of Thermal-Hydrological-Mechanical-Chemical (THMC) processes common to different EBS design concepts for various materials, local environment, and specific interactions as illustrated in Fig. 1.1-1. This figure also depicts other important processes such as used fuel degradation and radionuclide mobilization (RM). Used fuel degradation represents a set of coupled processes defined mainly by interactions between nuclear fuel and fluids in the EBS that ultimately provides the radionuclide source-term. It should be noted that fuel cladding is currently treated as the interface between the used fuel degradation plus RM and EBS. The task of integrating process models to describe cladding evolution/degradation with those of the used fuel degradation is planned to be a growing focus of the used fuel degradation and RM tasks beginning in the latter part of FY2013. Sassani (2011) provided an overview and summary of the modeling and experimental tasks for FY2011 in the used fuel degradation and RM area, and outlined the goals of this work for this FY12. This current work is an integrated collaborative effort among multiple DOE national laboratories: Sandia National Laboratories (SNL), Argonne National Laboratory (ANL), and Pacific Northwest National Laboratory (PNNL) and represents the major content of this report.

This report provides the detailed descriptions of the used fuel degradation and RM process models that have been developed this FY12 and are available for incorporation into the generic

performance assessment model (GPAM) in the next fiscal year. The primary process models are the radiolysis model and the matrix degradation rate model (the mixed potential model). In addition to these two major process models, initial idealized constraints are provided for the fast/instant release fraction for some key radionuclides in the form distribution functions. As part of the effort to incorporate new detailed understanding of the surface chemistry of altering used fuel, additional detailed first principle models for  $\text{UO}_2$  and some of its key alteration products are presented. Along with these detailed presentations of the used fuel degradation and RM models, high-level summaries are given for the other EBS process models that are under development. As these EBS models become fully implemented and ready for incorporation into the GPAM, the details of their implementations will be added to this document. Future revisions of this living document should provide an integrated comprehensive source for the EBS process models implementations. It is expected that this report will be updated on an annual basis.

### 1.1.1 Overview of Engineered Barrier Systems Evaluations

The detailed coverage of ongoing development of EBS models and constraints for the engineered barriers themselves can be found in Jové Colón et al. (2011; 2012). A discussion was provided on the type and key features of various EBS design concepts in The Used Fuel Disposition campaign (UFDC) report “Disposal Systems Evaluations and Tool Development - Engineered Barrier System (EBS) Evaluation” (Jové Colón et al., 2011) consistent with R&D needs and priorities described in the UFDC R&D Roadmap report (Nutt et al., 2011). The above-mentioned UFDC report outlined the need for flexibility in the study of generic EBS design concepts to analyze the complexities of coupled phenomena in the EBS through the use of sophisticated computational tools and methods. Therefore, the study of EBS processes has been focused on the development and application of such tools to assess EBS performance (Jové Colón et al., 2012). The global analysis of the EBS on the basis of its components and their coupled interactions and responses to the local environment are important aspects in the characterization of performance to long-term isolation of the nuclear waste. This gives rise to the idea of “design optimization” as a result of the evaluation of generic EBS concepts from the evaluation of THMC coupled processes and knowledge obtained from experimental activities.

Jové Colón et al. (2011) described some of the conceptual variants of multi-layered barrier configurations as foreseen in EBS studies for backfilled disposal environments. These configurations can have various levels of complexity depending on the type of barrier materials, waste package, nuclear fuel types, and heat loads. Given that barrier materials can be engineered to achieve desired properties such as enhanced thermal conductivity or chemisorption, the concept of “design optimization” requires then the necessary knowledge and tools to analyze the functionality and performance of such EBS design concepts (Jové Colón et al., 2012). The work described in Jové Colón et al., (2012) mainly focus on processes relevant to barrier components and materials that do not include interactions with used nuclear fuel. The importance of modeling tool development and applications of methods to analyze EBS processes affecting barrier performance is summarized as follows (Jové Colón et al., 2012):

- Modeling of THM processes within bentonite and interactions between the EBS and clay host rock. The development of an encompassing TM model such as the extended Barcelona Basic Model (BBM) allows for a more accurate geomechanical representation of expansive clay behavior and swelling strain in response to repository conditions.



- Modeling of reactive diffusion in clay. Implementation of Poisson-Nernst-Planck formulation to capture the effects of clay compaction on the transport of charge aqueous species. This theoretical evaluation allows for better representation of the governing mode of diffusive transport in clay. This work is conducted in parallel with diffusion and sorption experiments in clay. Further, molecular dynamics (MD) studies are also conducted to characterize the influence of temperature on the self-diffusion coefficients of  $\text{Na}^+$  and  $\text{H}_2\text{O}$ . This is important given that the clay buffer/backfill will be exposed to elevated temperatures that could exert strong effects on diffusive transport.
- Experimental investigations of clay phase stability and interactions with other barrier materials at high temperatures and pressures. This study is crucial to the understanding of the transformation of bentonite clay barrier material and interactions with aqueous solutions at high temperatures (up to  $300^\circ\text{C}$ ) and 150 bars pressure. These interactions can result in silica deposition thus affecting the bulk chemical and mechanical properties of the buffer material. Also, these studies will elucidate the extent of sacrificial barrier or the barrier region experiencing the most significant changes in response to thermal effects.
- Thermodynamic database and model development for clay and cementitious phases. This work encompassed the implementation of methods to predict clay thermodynamic properties for various compositions and hydration states. It also described the application of Gibbs energy minimization (GEM) approach to model non-ideal processes such as clay hydration and cement leaching.
- Molecular Dynamics (MD) study of clay hydration at ambient and elevated temperatures. This work provides the foundation to use atomistic calculations and advanced computational methods in the characterization of clay swelling as a function of interlayer cation hydration as a function of clay composition.
- 3D Coupled thermal-mechanical (TM) and thermo-hydrological (TH) modeling in salt using high performance computational tools and methods. This work provides the fundamental platform in the comprehensive study of 3D THM coupled processes characteristic of salt consolidation.
- Thermal analysis case of a mixed buffer multi-layered EBS using the disposal system evaluation framework (DSEF). This analysis provided peak temperature-time profiles for a layered mixed buffer (bentonite clay / graphite) EBS configuration and a 12-assembly UOX fuel with different burnup rates and storage times. This tool, albeit high level, provides for a very useful mean of evaluating the thermal transport in generic EBS design concepts integrated with a database of material thermal properties, characteristic decay heat data for nuclear fuel types, and storage times.

All these activities are either part or captured within key process models at barrier domains and the flow of information between near- and far-field process models is depicted in Fig. 1.1-1. Fig. 1.1-2 shows the breakdown of the two primary modeling approaches for the used fuel degradation and RM processes in the EBS. These two modeling approaches are:

- Process models for UO<sub>2</sub> fuel matrix degradation:
  - Mixed Potential Model (MPM)
  - Radiolysis Model
- Sampled distributions for the instant release fraction (IRF):
  - One set of triangular distributions applicable to represent instantaneous radionuclide releases for used fuel with burnup up to about 50 MWd/KgU that have no functional dependence on burnup
  - One set of linear distributions applicable to represent instantaneous radionuclide releases for used fuel with burnup up to 75 MWd/KgU that are a function of burnup.

The integration of EBS process models in relation to radionuclide mobilization (as illustrated in these two figures) can be envisioned as the passing of information between models that affect transport to/from the barrier domains and waste package. The key pieces of information are the IRF for a given set of radionuclides and those “leached” from the fuel through UO<sub>2</sub> fuel matrix degradation.

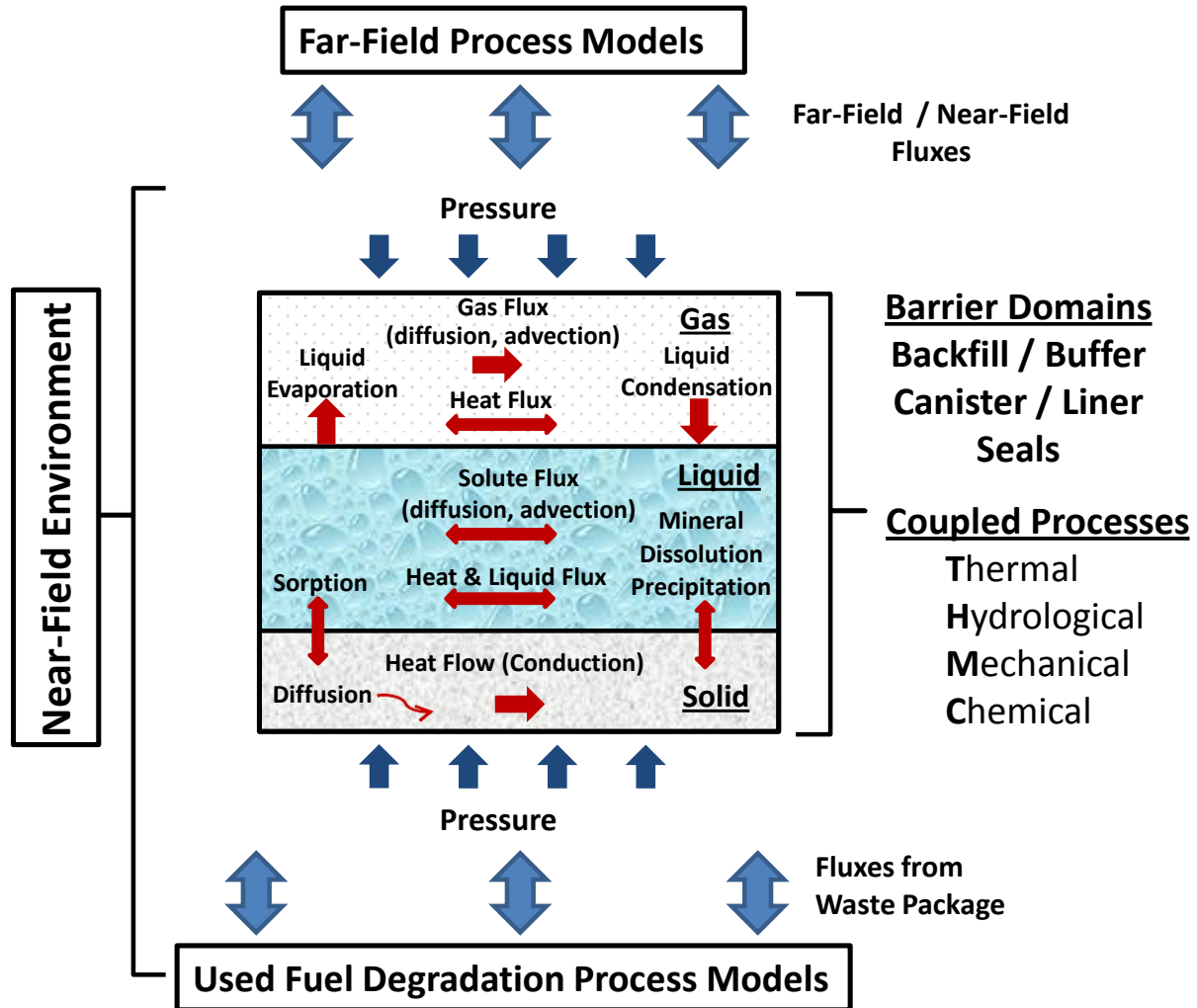


Figure 1.1-1. EBS coupled process phenomena (center) and interrelations between process models from other domains (modified after Olivella et al. 2011)

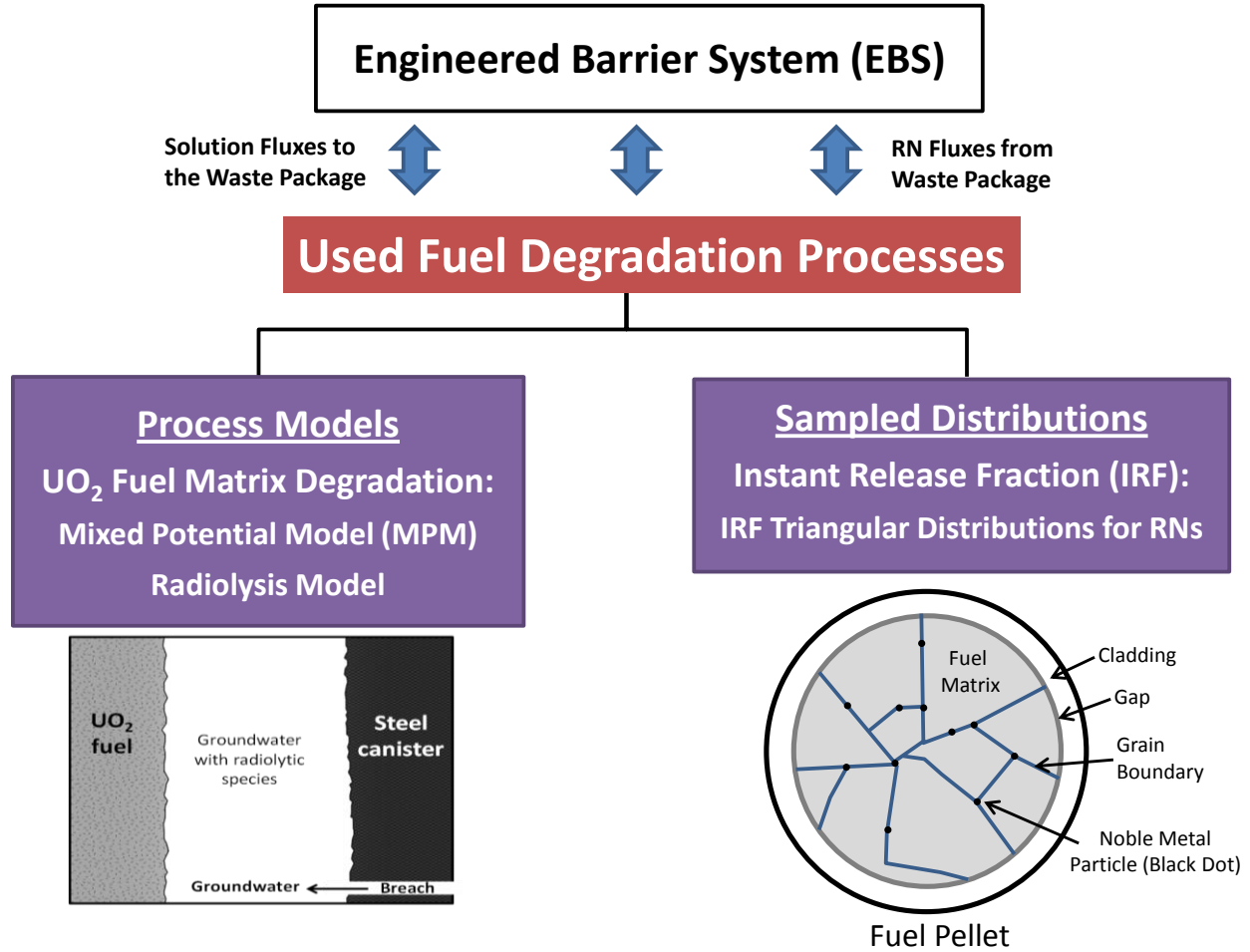


Figure 1.1-2. Schematic description of the approach developed in this report for used fuel degradation processes and radionuclide mobilization (RM) and its relation to EBS processes in the near-field environment.

The passing of information between the used fuel degradation and RM process models and those pertaining to the EBS domain is important to the definition of the source term in the quantification of radionuclide releases and related mass fluxes within the near-field environment. The primary parameters to be handed off from the source-term to the EBS domain pertains to the source concentrations of the radionuclides mobilized from the used fuel (and other waste forms as their degradation and release models become available from the Waste Form Campaign). The primary parameters that the EBS would provide to the used fuel degradation and RM models would be the physical-chemical conditions of the near-field environment such as bulk chemistry of the solutions for each particular disposal environment, as well as any pertinent gas compositions. Additional parameters potentially passed between these two portions of the near field would include any bulk chemical changes originating from reaction of the used fuel (or other waste forms), temperature and pressure conditions, and mechanical changes to EBS configurations.

EBS processes, waste degradation, and their role on radionuclide inventories and mobilization are ranked high in importance as reported in the UFDC Disposal R&D Roadmap. SNF degradation (including cladding or any other outer protective barrier) is important to the safety analysis in determining the level of “credit” assigned to the fuel-cladding assemblage in performance/safety evaluation. Table 1.1-1 summarizes the priority ranking for the EBS for buffer/backfill and seal/liner materials after Nutt et al. (2011). (Note that the highest ranked EBS priorities relate to the radionuclides that are coming from the used fuel degradation source-term, and the used fuel degradation processes are discussed below separately.)

The Strategic Research Agenda (SRA) report (SRA, 2011; [www.igdt.eu](http://www.igdt.eu)) for Implementing Geological Disposal of Radioactive Waste Technology Platform (IGD-TP; European Commission - EC) framework programme identifies rapid release fraction from SNF with a high level of importance within their “Key Topic 2: Waste forms and their behaviour”. The main reasons are the need for improved data and knowledge on the dissolution behavior to satisfy licensing requirements. Such a high prioritization ranking for IRF (or rapid release fraction in SRA report) of UOX used fuel for increased confidence in process knowledge, methods, and tools is consistent with that for waste form (SNF) degradation in the UFDC Disposal R&D Roadmap report (Nutt et al. 2011).

A number of international collaborations provide additional support and collaborative data sharing for testing of EBS models development. These include DECOVALEX 2015; the Republic of Korea (ROK) – US Joint Fuel Cycle Study: Task 2 – Engineered and Natural Barrier Systems databases; and The Nuclear Energy Agency (NEA) Integration Group for the Safety Case (IGSC) Salt Club (see Jové Colón et al., 2012 for detailed descriptions). Additionally, the US DOE NE UFD campaign is participating as an Associated Group (represented by David Sassani – SNL) in the EC international collaborative project on Fast/Instant Release of Safety Relevant Radionuclides from Spent Nuclear Fuel (*FIRST – nuclides*) as discussed further below.

Table 1.1-1. Summary of the priority ranking for the EBS for buffer/backfill, seal/liner, waste materials, and waste package with associated FEPs (Nutt et al., 2011).

<b>BUFFER / BACKFILL (media type) →</b>	<b>Clay</b>	<b>Salt</b>	<b>Crystalline</b>	<b>Mixed Materials</b>
2.1.04.01: BUFFER/BACKFILL	High	Medium	Medium	Medium
2.1.07.02, .03, .04, 09: MECHANICAL PROCESSES	Medium	Medium	Medium	Medium
2.1.08.03, .07, .08: HYDROLOGIC PROCESSES	Medium	Medium	Medium	Medium
2.1.09.01, .03, .07, .09, .13: CHEMICAL PROCESSES - CHEMISTRY	Medium	Medium	Medium	Medium
- Radionuclide speciation/solubility	High	High	High	High
2.1.09.51, .52, .53, .54, .55, .56, .57, .58, .59, .61: CHEMICAL PROCESSES – TRANSPORT	Medium	Medium	Medium	Medium
- Colloid facilitated transport	Low	Low	Low	Low
2.1.11.04: THERMAL PROCESSES	Medium	Medium	Medium	Medium
2.1.12.01, .02, .03: GAS SOURCES AND EFFECTS	Medium	Medium	Medium	Low
<b>SEAL / LINER MATERIAL →</b>	<b>Cement</b>	<b>Asphalt</b>	<b>Metal</b>	<b>Polymer</b>
2.1.05.01: SEALS	Medium	Medium	Medium	Medium
2.1.07.02, .08, .09: MECHANICAL PROCESSES	Medium	Medium	Medium	Medium
2.1.08.04, .05, .07, .08, .09: HYDROLOGIC PROCESSES	Low	Low	Low	Low
- Flow through seals	Medium	Medium	Medium	Medium
2.1.09.01, .04, .07, .09, .13: CHEMICAL PROCESSES – CHEMISTRY	Medium	Medium	Medium	Medium
- Radionuclide speciation/solubility	High	High	High	High
- Advection, diffusion, and sorption	Medium	Medium	Medium	Medium
2.1.11.04: THERMAL PROCESSES	Medium	Medium	Medium	Medium
<b>WASTE MATERIALS → SNF, Glass, Ceramic, Metal</b>				
2.1.01.01, .03, .04: INVENTORY		Low		
2.1.02.01, .06, .03, .05: WASTE FORM		High		

Table 1.1-1 (Cont.) Summary of the priority ranking for the EBS for buffer/backfill, seal/liner, waste materials, and waste package with associated FEPs (Nutt et al., 2011).

<b>WASTE PACKAGE MATERIALS → Steel, Copper, Other Alloys, Novel<sup>1</sup> Materials</b>	<b>Steel</b>
2.1.03.01, .02, .03, .04, .05, .08: WASTE CONTAINER	High
2.1.07.03, .05, .06, .09: MECHANICAL PROCESSES	Medium
2.1.09.01, .02, .09, .13: CHEMICAL PROCESSES - CHEMISTRY	Medium
Radionuclide speciation/solubility	High
2.1.09.51, .52, .53, .54, .55, .56, .57, .58, .59: CHEMICAL PROCESSES - TRANSPORT	Low
Advection, diffusion, and sorption	Medium
2.1.11.01, .02, .04: THERMAL PROCESSES	Medium

Note: FEP number lists delimited by commas show only the change in the fourth field of the FEP

## 1.2 Overview of Used Fuel Degradation and Radionuclide Mobilization (RM) Activities

### 1.2.1 Introduction and Accomplishments

These activities within the generic EBS Evaluations investigate the long-term behavior of used fuel as a waste form. In fiscal year (FY) 2011 efforts focused on developing a comprehensive understanding of the current technical bases for disposing of used fuel in a range of disposal environments and on identifying the opportunities for long-term research and development to enhance our fundamental understanding of these processes to augment the technical bases for disposal. A smaller level of effort has been to integrate the work of the Waste Form campaign (WFC) on performance of other wastes. That integration effort focuses on maintaining a current and consistent understanding of the other potential waste forms that could arise from future nuclear fuel cycles and developing approaches to understand the performance of those potential waste forms. As work in this area progresses, the focus will shift towards implementing and/or enhancing models for each waste form (e.g., the WFC is developing a comprehensive model of degradation of high level waste glass that will be provided to FCT UFDC when completed) to create comprehensive coverage within the generic performance assessment models for all disposal options and waste forms.

In FY2012, the used fuel degradation and RM activities have focused on process model implementation (for both radiolysis and degradation rate of used fuel matrix grains), constraints on the instant release fractions of radionuclides from breached used fuel, preparation for incorporation of models into the GPAM (including fast release fraction constraints), development of first principle models of UO<sub>2</sub> alteration, executing experimental programs for (a)

<sup>1</sup> A novel engineered barrier system material refers either to a new material designed for improved performance within a geologic disposal system or an existing material that has not been extensively studied and used in the design of a geologic disposal system that could lead to improved performance.

generating synthetic fuels for studying radiolytic processes at future fuel conditions and (b) analyzing used fuel degradation process and the role of the epsilon phases using electrochemical cells. Within this fiscal year, these activities generated (or are generating):

- This level 2 milestone report
- The following level 3 and level 4 milestones
  - ANL testing plan—milestone: M4FT-12AN0806011 - Experimental Plan for ANL Electrochemical Corrosion Studies, January 6, 2012.
  - PNNL testing plan—milestone: M4FT-12PN0806052 - Waste Form Degradation and Radionuclide Mobilization Testing Plan, December 2, 2012.
  - ANL modeling report—milestone: M3FT-12AN0806013 - Waste Form Degradation Model Status Report: Electrochemical Model for Used Fuel Matrix Degradation Rate, August 9, 2012.
  - PNNL modeling report—milestone: M3FT-12PN080651- Radiolysis Process Modeling Results for Scenarios, July 2012.
  - ANL status report of experiments—milestone: M3FT-12AN0806015 - Report results of electrochemical experiments, September 21, 2012.
  - PNNL status report of experiments—milestone: M4FT-12PN0806053 - Experimental Results for SimFuels, August 24, 2012.
- The following journal publications (submitted or in preparation) covering
  - PNNL radiolysis model publication (Wittman et al., in preparation)
  - First principle models of  $\text{UO}_2$  bulk and surface properties (Weck et al., in preparation)
  - First principle models of Studtite and metastudtite structures (Weck et al., 2012)
- Model implementations for
  - PNNL Radiolysis Model process model
  - ANL Mixed Potential Model for used fuel matrix degradation rates process model
  - constraints on Fast Release Fraction radionuclides for use in GPAM
  - first principle models and analyses of
    - $\text{UO}_2$  bulk and surface chemistry
    - structures of peroxide corrosion products of  $\text{UO}_2$

In addition, these activities initiated/furthered international collaboration efforts within

- The European Commission (EC) Collaborative Project (CP) on the *Fast / Instant Release of Safety Relevant Radionuclides (FIRST – nuclides) from Spent Nuclear Fuel*
  - D. Sassani represented SNL (and the DOE NE FCT UFD) as an Associate Group
  - *3 year project focused on high-burn-up fuels*
  - *10 organizations; 45 participants*
  - *KIT-INE and AMPHOS21 - Coordinating organizations*
    - Karlsruhe Institute of Technology - Institute for Nuclear Waste Disposal (KIT-INE) in Karlsruhe, Germany



- AMPHOS21 Consulting, Barcelona, Spain
- Associated Groups get information access without specific required contributions - signed non-disclosure agreement – information sharing collaboration
  - Participated in the *FIRST – nuclides* kickoff meeting in February, 2012
    - Presented *Brief Overview of the US DOE Used Fuel Disposition Campaign and activities in the Used Fuel Degradation and Radionuclide Mobilization*
- In conjunction with the kickoff meeting
  - Toured facilities and presented detailed seminar on the US DOE Used Fuel Disposition Campaign and activities in the Used Fuel Degradation and Radionuclide Mobilization area under the EBS WP
    - AMPHOS21 in Barcelona, Spain
    - Karlsruhe Institute of Technology - Institute for Nuclear Waste Disposal (KIT-INE) in Karlsruhe, Germany
- the ROK – US Joint Fuel Cycle Study, Fuel Cycle Alternatives Working Group
  - D. Sassani, technical lead for Task 3 - *Spent Fuel Degradation and Durability over Geologic Time*
    - Participated in Working Group Meetings June 5-7 to define information sharing and priorities between our two groups

### 1.2.2 Background

DOE plans to examine a broad range of fuel cycle strategy options to provide decision-makers with information that will allow them to make informed decisions on how to best manage used fuel. These options include “optimized once through” and “modified open” fuel cycles which will involve direct disposal of the used fuel when it is classified as “spent fuel”. The broad scope of these used fuel degradation and RM activities is therefore defined in part by the range of nuclear fuel types and also by the various disposal environments that need to be considered. The primary focus for the FY2011 activities (Sassani, 2011) was on evaluating current models for used fuel degradation processes applicable to various environments, defining the model to be initially implemented for used fuel degradation, delineating further information needs and testing methodologies, and identifying approaches that can be applied to other potential waste forms (e.g., those being developed in the WFC). Within FY2012 process models were implemented such that they are ready for implementation into GPAM, initial constraints on the fast release fraction of radionuclides from used fuel were developed, first principle models for UO<sub>2</sub> surface reactions and product formation were constructed, and detail plans for the experimental programs were developed and initiated. This report provides detailed coverage of the modeling work and the strategy for incorporation into the GPAM, as well as an overview of the other EBS modeling areas that will be incorporated into GPAM in the future.

The used fuels for which disposal options are to be considered include the current US inventory of used fuels as well as the used fuels that may be generated in the future from the currently-operating reactors and from reactors that may be built and generate spent fuel under the once through and modified open fuel cycle options. The DOE-NE Fuel Cycle Research and Development (FCRD) Program is identifying specific reactor/fuel types and performing science-

based R&D to provide information that will inform future decisions. Identification of commercial used fuel types to be considered in the Used Fuel Disposition (UFD) campaign will therefore be based in part on the reactors/fuels options being evaluated in the FCRD program (Nutt et al., 2011).

Commercial used fuel includes the current inventory of used oxide fuel from commercial light water reactors (LWRs), and the projected future inventory from the LWR fleet (including Gen III+ advanced LWRs being developed through the DOE-NE Nuclear Power 2010 Program). In addition, it may include fuels from the Next Generation Nuclear Plant (NGNP) gas-cooled reactor program (DOE 2010), and from future advanced reactors (GEN IV including the Very High Temperature Gas Reactor – VHTR) that may be introduced into the commercial reactor fleet in support of the fuel cycle options mentioned above. Hence, the used fuel options to be considered in this activity include LWR oxide fuels (uranium oxide -UOX and mixed uranium and plutonium - MOX), gas-cooled reactor fuels (e.g. tri-isotropic –TRISO - coated fuel particles), and advanced reactor fuels. This report addresses UOX and MOX fuels only.

The UFD features, events, and processes (FEPs) activity (Freeze et al. 2010) designated a set of 6 potential waste form type as broad groupings (Table 1.2-1) to define the expected range (based on current knowledge) of similarly behaving waste forms that would be potentially disposed. Within the FY11 work on FEPS, the focus was decreased to only the first four of these groups (Freeze et al., 2011). This used fuel degradation and RM activity focuses on group number 1 in this and the next fiscal year, with shifting focus to some of the others as information and models are developed within the WFC.

Table 1.2-1. Groupings of Potential Waste Form Types (UFD FEPs—Freeze et al., 2010)

Group Number	Waste Form Type	Description
1	Used Nuclear Fuel (UNF)	e.g., Commercial, DOE-Owned, HTGR
2	High-Level Waste (HLW) Glass	Current (e.g., borosilicate) and future (e.g., no minor actinides)
3	High-Level Waste (HLW) Glass Ceramic / Ceramic	Current (glass bonded sodalite) and future (e.g., from electrochemical processing)
4	High-Level Waste (HLW) Metal Alloy	From electrochemical or aqueous reprocessing, cermets
5	Lower Than HLW (LTHLW)	Class A, B, and C, and GTCC
6	Other	Molten salt, electro-chemical refining waste, etc.

Note: HTGR = High-temperature gas-cooled reactor; GTCC = Greater than Class C.

The types of potential disposal environments to be considered have been categorized also under the UFD FEPs activity (Freeze et al. 2010) and include mined repositories in saturated media (granite/crystalline rock, shale/clay, and salt), mined repositories in unsaturated media (granite/crystalline rock or tuff), and deep boreholes (granite/crystalline rock). Groundwater Eh conditions in these potential disposal settings span a broad range from reducing to oxidizing conditions (Jové Colón et al. 2010).

### 1.2.3 Integration/Interfaces

The UFDC has several interfaces, both internal to the Fuel Cycle Technology (FCT) program and external. The interfaces within the FCT program are (from Nutt et al., 2011):

- *FCT Separations/Waste Form Campaign: This campaign is responsible for conducting R&D related to waste forms that would be generated from separations/ recycling processes (FCT 2010). A wide variety of waste forms are under investigation within that campaign. A research and development roadmap for these investigations has been developed and is being implemented (Peters et al. 2008). The UFDC is responsible for conducting R&D to enable the direct disposal of used nuclear fuel as a waste form in a geologic environment, should that decision be chosen, and the disposal of any waste forms that would be developed under a future advanced nuclear fuel cycle.*
- *FCT Advanced Fuels Campaign: This campaign is responsible for conducting R&D on advanced fuels that could be used in future nuclear reactors (FCT 2010). Since the UFDC is responsible for SNF as a waste form, knowledge and understanding of the properties and characteristics of the fuels following irradiation is needed. The FCT Advanced Fuels Campaign will conduct the R&D to determine these properties and characteristics.*
- *FCT System Analysis Campaign: This campaign is responsible for developing the system-analysis tools to evaluate future advanced fuel cycles (FCT 2010). The UFDC R&D will help inform the development of these tools in the area of waste management. In addition, the System Analysis campaign evaluates the merits of different fuel cycle approaches (trade studies and alternative analysis). The UFDC R&D will both inform and support these analyses.*
- *FCT System Engineering: The FCT program is applying system engineering principals and techniques to prioritize activities (FCT 2010). UFDC R&D will support the development of quantitative and qualitative metrics related to waste management that will be used to rank different fuel cycle alternatives.*

The UFDC recognizes that a considerable amount of work has been completed in other countries regarding the geologic media being considered by the UFDC and for a variety of engineered materials within these media. The UFDC will leverage this information and conduct future R&D through international collaborations as discussed in the Used Fuel Disposition Campaign International Activities Implementation Plan (Nutt et al., 2011). The UFDC will also collaborate with industry, as appropriate, to obtain their expertise in areas regarding geosciences and the geologic disposal of radioactive waste. In addition, the UFDC will also collaborate with research and development organizations conducting R&D on geologic systems (i.e., geothermal energy and carbon sequestration).

UFDC geologic disposal R&D is also tightly integrated with the storage/transportation part of the UFDC program. The properties and characteristics of the materials that would be disposed of after long term storage and transportation are input conditions to disposal-related R&D. The development of the FEPs for UFD (Freeze et al. 2010) resulted in a number of FEPs directly applicable to the waste form (Table 1.2-2). Note that each of these waste form FEPs listed in Table 1.2-2 have had status updates in FY11 (Freeze et al., 2011), which amounts to additional

information added to the FEP evaluations. The focus of the work in this report is primarily on FEP 2.1.02.01, whereas integration with WFC would address FEP 2.1.02.02. There are also FEPs related to waste form that are cross-referenced under the “Associated Processes” column of Table 1.2-2 (e.g., see Complexation in EBS in 2.1.09.54). Additionally, there are other FEPs in various areas that relate in an less direct but still relevant way to waste form such as many of those in “Inventory” 2.1.01.00, and a number in “Chemical Processes – Chemistry” 2.1.09.00. In the future, the focus of activities in this Used Fuel Degradation and Radionuclide Mobilization activity will shift to implementation and integration of models for additional waste forms, as well as to addressing the additional FEPs comprehensively. One area that will begin to be addressed in the next fiscal year is that of integration and coupling of models for cladding degradation with the models for degradation of used fuel.

Table 1.2-2. Waste form FEPs (from Table A-1 in Freeze et al., 2010).

UFD FEP Number	Description	Associated Processes	Related YMP FEPs
2.1.02.00	1.02. WASTE FORM		
2.1.02.01	SNF (Commercial, DOE) Degradation - Alteration / Phase Separation - Dissolution / Leaching - Radionuclide Release	Degradation is dependent on: - Composition - Geometry / Structure - Enrichment / Burn-up - Surface Area - Gap and Grain Fraction - Damaged Area - THC Conditions  [see also Mechanical Impact in 2.1.07.06 and Thermal-Mechanical Effects in 2.1.11.06]	2.1.02.02.0A 2.1.02.01.0A 2.1.02.28.0A 2.1.02.07.0A
2.1.02.02	HLW (Glass, Ceramic, Metal) Degradation - Alteration / Phase Separation - Dissolution / Leaching - Cracking - Radionuclide Release	Degradation is dependent on: - Composition - Geometry / Structure - Surface Area - Damaged / Cracked Area - Mechanical Impact - THC Conditions  [see also Mechanical Impact in 2.1.07.07 and Thermal-Mechanical Effects in 2.1.11.06]	2.1.02.03.0A 2.1.02.05.0A
2.1.02.03	Degradation of Organic/Cellulosic Materials in Waste	[see also Complexation in EBS in 2.1.09.54]	2.1.02.10.0A
2.1.02.04	HLW (Glass, Ceramic, Metal) Recrystallization		2.1.02.06.0A
2.1.02.05	Pyrophoricity or Flammable Gas from SNF or HLW	[see also Gas Explosions in EBS in 2.1.12.04]	2.1.02.08.0A 2.1.02.29.0A
2.1.02.06	SNF Cladding Degradation and Failure	- Initial damage - General Corrosion - Microbially Influenced Corrosion - Localized Corrosion - Enhanced Corrosion (silica, fluoride) - Stress Corrosion Cracking - Hydride Cracking - Unzipping - Creep - Internal Pressure - Mechanical Impact	2.1.02.11.0A 2.1.02.12.0A 2.1.02.13.0A 2.1.02.14.0A 2.1.02.15.0A 2.1.02.16.0A 2.1.02.17.0A 2.1.02.18.0A 2.1.02.27.0A 2.1.02.21.0A 2.1.02.22.0A 2.1.02.23.0A 2.1.02.25.0A 2.1.02.25.0B 2.1.02.19.0A 2.1.02.26.0A 2.1.02.20.0A 2.1.02.24.0A 2.1.09.03.0A

### 1.3 References for Section 1

- DOE 2010, Next Generation Nuclear Plant, A Report to Congress prepared by DOE, Office of Nuclear Energy, April 2010. Geneste, P., Raynal, M., Atabek, R., Dardaine, M., and Oliver, J., 1990, Characterization of a French Clay Barrier and Outline of the Experimental Program: *Engineering Geology*, v. 28, no. 3-4, p. 443-454.
- Fuel Cycle Technology Program, DOE-NE (FCT), 2010. Research Objective 3 Implementation Plan, Developing Sustainable Fuel Cycle Options, FCRD-TIO-2011-000025.
- Freeze, G., P. Mariner, J. Houseworth, J. Cunnane, and F. Caporuscio, 2010, Used Fuel Disposition Campaign Features, Events, and Processes (FEPs): FY10 Progress Report.
- Freeze, G., Mariner, P., Blink, J. A., Caporuscio, F. A., Houseworth, J. E., and Cunnane, J. C., 2011, Disposal System Features, Events, and Processes (FEPs): FY11 Progress Report, FCRD-UFD-2011-000254 (M31UF033802), U.S. Department of Energy, Office of Nuclear Energy, Used Fuel Disposition Campaign, Washington, D.C., SAND2011-6059.
- Jové Colón, C. F., F. A. Caporuscio, S. S. Levy, H. Xu, J.A. Blink, W. G. Halsey, T. Buscheck, M. Sutton, M. A. Serrano de Caro, T. J. Wolery, Hui-Hai Liu, J. Birkholzer, C. I. Steefel, J. Rutqvist, Chin-Fu Tsang, E. Sonnenthal, 2010, Disposal System Evaluation and Tool Development – Engineered Barrier System (EBS) Evaluation, 204 pp.
- Jové Colón, C. F., Caporuscio, F. A., Levy, S. S., Blink, J. A., Greenberg, H. R., Halsey, W. G., Fratoni, M., Sutton, M., Wolery, T. J., Rutqvist, J., Liu, H. H., Birkholzer, J., Steefel, C. I., and Galindez, J., 2011, Disposal Systems Evaluations and Tool Development - Engineered Barrier System (EBS) Evaluation, 192 pp.
- Jové Colón, C. F., Greathouse, J. A., Teich-McGoldrick, S., Cygan, R. T., Hadgu, T., Bean, J. E., Martinez, M. J., Hopkins, P. L., Argüello, J. G., Hansen, F. D., Caporuscio, F. A., Cheshire, M., Levy, S. S., McCarney, M. K., Greenberg, H. R., Wolery, T. J., Sutton, M., Rutqvist, J., Steefel, C. I., Birkholzer, J., Liu, H. H., Davis, J. A., Tinnacher, R., Bourg, I., Holmboe, M., and Galindez, J., 2012, Evaluation of Generic EBS Design Concepts and Process Models: Implications to EBS Design Optimization, 250 pp.
- Nutt, M., Voegelé, M., Jové Colón, C., Wang, Y., Howard, R., Blink, J., Liu, H.-H., Hardin, E., and Jenni, K., 2011, Used Fuel Disposition Campaign Disposal Research and Development Roadmap (Fuel Cycle Research and Development), Prepared for U.S. Department of Energy Used Fuel Disposition Campaign FCR&D-USED-2011-000065
- Olivella, S., Castagna, S., Alonso, E. E., and Lloret, A., 2011, Porosity Variations in Saline Media Induced by Temperature Gradients: Experimental Evidences and Modelling: *Transport in Porous Media*, v. 90, no. 3, p. 763-777.
- Peters, M.T., Ewing, R.C., and Steefel, C.I. 2008. GNEP Waste From Campaign Science & Technology and Modeling and Simulation Program: Roadmap with Rationale & Recommendations, GNEP-M50-3040-303 and GNEP-M50-3030-101.
- Sassani, D. C., 2011, Used Fuel Degradation and Radionuclide Mobilization FY11 Summary Report, FCRD-USED-2011-000403, 41 pp.

SRA, 2011, Implementing Geological Disposal of Radioactive Waste Technology Platform Strategic Research Agenda 2011 (IGD-TP), European Community (EC) Euratom framework programme, 63 pp. (ISBN 978-91-979786-0-6) ([www.igntp.eu](http://www.igntp.eu))

Weck, P. F., Kim, E., Jové Colón, C. F., and Sassani, D. C., 2012, Structures of uranyl peroxide hydrates: a first-principles study of studtite and metastudtite, Dalton Transactions, DOI: 10.1039/c2dt31242e.

## 2. The Engineered Barrier System Structure within Generic Performance Assessment Model (GPAM)

As discussed in Clayton et al. (2011), the generic disposal system modeling (GDSM) of different disposal environments and waste form options has the following three-year goal (fiscal year (FY) 2014):

*Have in place the necessary system architecture and computational environment to support the evaluation of postclosure risk. Maintain the flexibility in the system model architecture to meet the evolving needs of the DOE-NE/UFD mission. Provide risk information throughout the potential future phases of the mission including the following:*

1. *Viability*
2. *Screening*
3. *Selection*
4. *Characterization / Engineering Design*
5. *Licensing*

That GDSM FY2011 status report provides description of the GDSM work on four main generic disposal system environment (GDSE) options that cover mined repositories in three geologic media (salt, clay, and granite) and the deep borehole disposal concept in crystalline rock. In addition, Clayton et al. (2011) provides the development of the generic performance assessment model (GPAM) architecture to facilitate integrating individual GDSE models into a single consistent approach that is flexible enough to evaluate a range of environments, potential waste forms, and to incorporate evolving understanding and implementation of fundamental processes. For each GDSE analyzed, the rock type is identified at a broad level. (For example, the salt disposal environment includes both bedded and domal salt formations; the clay disposal environment includes a broad range of fine-grained sedimentary rocks ranging from shales to soft clays; and the granite environment includes various related crystalline rocks. The options for the waste stream being considered are used fuel and high-level radioactive waste (HLW). Types of HLW include DOE high-level radioactive waste (DHLW) and commercial high-level radioactive waste (CHLW) generated from hypothetical reprocessing of commercial UNF. The work in the used fuel degradation and radionuclide mobilization activities presented in detail below would be used to augment or supplant the current idealized treatment of used fuel degradation that is currently in the GDSM as described below.

### 2.1 Introduction to Generic Disposal System Modeling and GPAM

#### 2.1.1 GPAM Concepts and EBS Construct

The GPAM provides a common conceptual and computational framework for the simulation of the coupled thermal-hydrologic-chemical-mechanical-biological-radiological (THCMBR) processes that govern the behavior nuclear waste disposal systems (Fig. 2.1-1; Freeze and Vaughn, 2012). Within the common GPAM framework, a range of disposal system alternatives (combinations of inventory, EBS design, and geologic setting) can be evaluated using appropriate model fidelity that can range from simplified reduced-dimension representations running on a desktop to complex coupled relationships running in a high-performance computing environment. The EBS is shown with a number of major barriers of various types depending on



disposal environment, as well as with various waste forms, including used fuel that is the primary topic of this report. Most of the current models implemented in the GPAM for EBS are more simplified than fully coupled, but the plan is to augment or replace those with more comprehensively coupled process models as the work progresses. The models for used fuel degradation processes presented in detail in Section 3 are the first round of those augmentations.

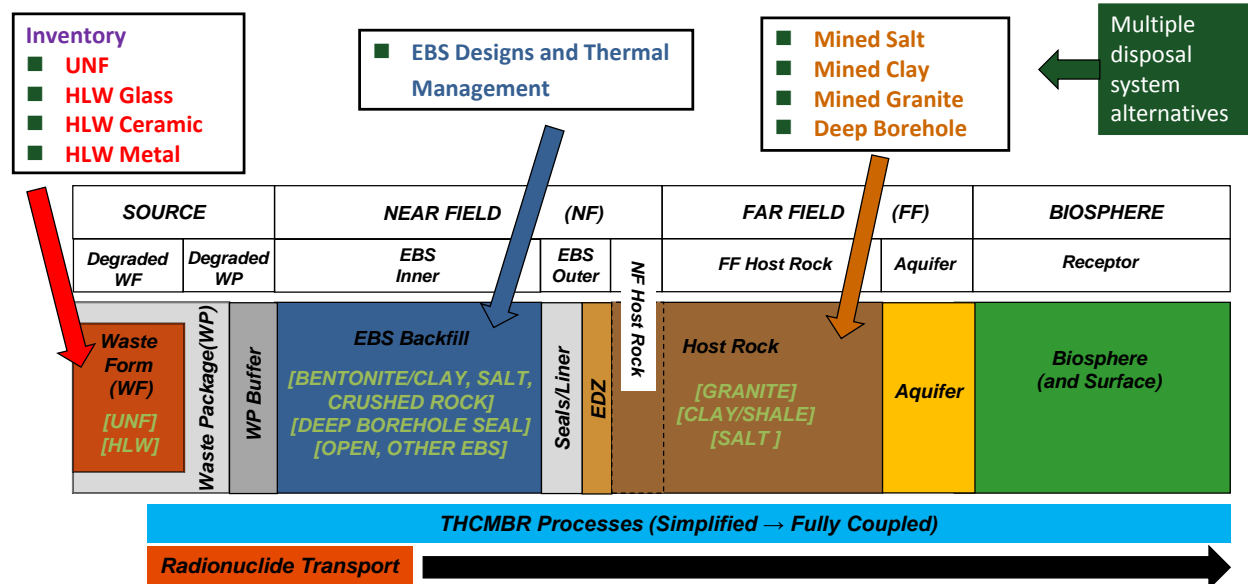


Figure 2.1-1. Description of the Generic Performance Assessment Model (GPAM) concepts, including interfaces, showing features, and processes throughout the representation (modified after Freeze and Vaughn, 2012).

### 2.1.2 GPAM Platform (Freeze and Vaughn, 2012)

The GPAM initial implementation platform was GoldSim (Clayton et al., 2011) but this was being used while additional architectures were being evaluated for ultimate employment of a flexible and powerful GPAM. Although the transition to another platform was planned for some time in FY2013, it was decided in mid-FY2012 to cease updating the GoldSim implementation of GPAM and focus on transition to another platform (Freeze and Vaughn, 2012). Here, we focus on the open source Albany code platform. As such, implementation of any of the EBS used fuel degradation and RM models into GPAM is not expected to start until sometime in FY2013.

## 2.2 Current Implementation of EBS Models included in GPAM

For this initial version of this milestone report, this section covers the implementation of only the used fuel degradation rate within the GPAM because this report provides currently more detailed model implementations only for used fuel degradation and RM processes. In future versions of this report, the additional EBS models with detailed implementations herein will also have their GPAM implementations included.

### 2.2.1 Used Fuel Degradation Rate Modeling

For the source-term modeling in the four GDSE in the current GPAM, the model implementations are generally simplified. For example, Clayton et al (2011) describe the source-term component of the Salt GDSM as follows

*Waste form degradation is assumed to release radionuclides into a large uniformly mixed container representative of the source-term water volume. The source-term water volume is obtained by multiplying the source-term bulk volume by its porosity. The dissolved concentrations of radionuclides in the source term mixing cell are then calculated based on the mass of radionuclides released from the waste form, the source-term water volume, and the radionuclide solubility. In the salt GDS source-term model, the source-term mixing cell is conceptualized to include the bulk volume of all of the near-field components (waste form, waste package, crushed salt backfill, near-field salt rock, etc.). This is a reasonable assumption for the current GDS analysis, considering that waste package performance is not taken into account for the analysis and that the entire waste inventory becomes available for reactions in the near field from time zero. As the model matures and information becomes available, more realistic representations of the processes will replace this initial simplified approach.*

Within that source-term model of the salt GDSE, two components relate directly to the degradation of used fuel—(a) waste form degradation, and (b) solubility of key radio-elements for the GPAM analyses. This used fuel degradation and RM work is focused currently on models that would provide augmented process models for part (a), specifically for used fuel as a waste form. The current representation of the waste form degradation within the GDSE is shown in Fig. 2.2-1 (from Clayton et al., 2011), which displays the schematic of the source-term, degraded waste form, and primary engineered barriers components of the clay GDSM. At the far left of the figure, within the gray boxes, the “No gap/grain boundary fraction” and the “Fractional Degradation Rate” are two examples of simplified aspects that would be updated based on the models in this report.

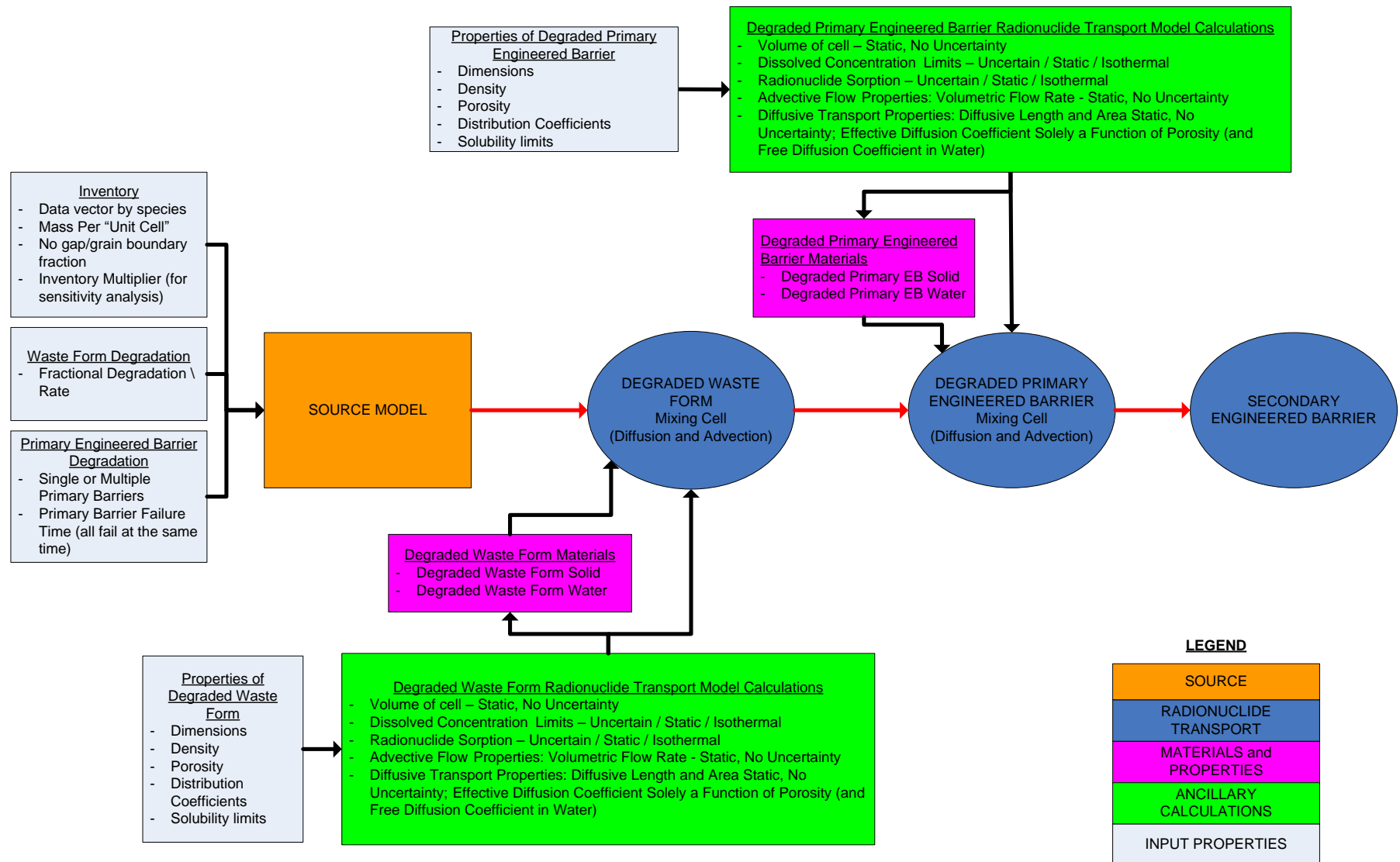


Figure 2.2-1. Schematic of Source Term, Degraded Waste Form, and Primary Engineered Barrier Representation (Clayton et al., 2011; Fig. 3.3-4)

### 2.2.1.1 Current GDSE Representation

Within the various GDSE, very similar implementations of the waste form degradation have been included. The models presented within this report are primarily applicable to the granitic generic disposal system environment and, because of the host rocks being similar, also applies fairly directly to the deep borehole GDSE. The current implementation for used fuel degradation the deep borehole GDSM is described in somewhat more detail by Clayton et al. (2011; Section 3.4.1.1.2) as

*Waste form degradation for the deep borehole GDSM is treated the same as for the salt GDSM (Section 3.1.2.5) and the granite GDSM (Section 3.2.2.2.2). For commercial UNF, the waste form is the UNF matrix, which is predominantly  $UO_2$ . For the DHLW and CHLW, the waste form is borosilicate glass. For both waste form types, the waste form degradation in the deep borehole GDS near field is modeled with an annual fractional degradation rate (i.e., fraction of remaining waste mass degraded per year), with a distribution that captures potential range of degradation rates for deep borehole GDS conditions. The deep borehole GDS is expected to be located in a chemically reducing zone with varying degrees of redox conditions of groundwater in contact with the waste form. The chemically reducing conditions for the deep borehole GDS are assumed to be the same conditions as for the salt GDS and the granite GDS. Therefore the same probabilistic degradation rate models for the UNF matrix and for the borosilicate glass were used (Section 3.1.2.5).*

This fractional degradation approach offers a very direct methodology to plug more advanced models of used fuel degradation into the GPAM to facilitate enhancing the processes being directly captured.

### 2.2.1.2 Overview of Used Fuel Degradation Modeling Connections within GPAM

The primary connection into the GPAM for the used fuel degradation and RM models is that of fractional degradation rate (FDR) that is currently sampled from a distribution as indicated above. This primary coupling allows for development of more process-based models that are able to supplant the FDR distribution by supplying that parameter as a result of the process model (see Section 3 for the process models that provide this). This is the initial connection that is needed for implementation of the used fuel degradation rate model described in Section 3. In addition, a second radionuclide release sampling similar to this FDR distribution may be simply added to the GPAM to describe the fast/instant release fraction radionuclides that are mobilized in a single instant at the point of cladding breach. This would only need to be sampled at the start of used fuel degradation for any fuel rod represented. Distributions for these are supplied as initial constraints for key radionuclides in Section 3 as well.

It is planned to develop some conditional and process based correlations with the structural and phase compositional information for used fuels in this work next year. A coarse connection to chemical environment (defined in the GPAM and needed as input to the used fuel degradation and RM models) exists in the current GDSM models. At present this is sufficient as the used fuel degradation and RM models below are developed for granitic reducing environments and explicit coupling to chemistry variation is expected to be developed next fiscal year with a primary target of extending the applicability into brine environments appropriate to salt systems. This is also the

case for thermal and pressure dependencies that will begin to be explicitly incorporated into the used fuel degradation and RM models in FY2013. It is expected that as these enhanced models are incorporated into the GPAM, providing expanded environment coverage will become more efficient.

Our general strategy for integration process models with each other and within the GPAM is to identify the major modeling feeds among the models and from the models to GPAM (as described above for this implementation). For coupling into GPAM, our approach begins with the direct, though idealized, interface connections that exist, with further couplings added as the process models themselves become more highly coupled. An example of this would be initially defining various specific used fuel degradation and RM matrix degradation rate models for specific generic disposal chemical environments (e.g., granitic groundwater and salt system brine), and simply allowing the GPAM to select the appropriate one depending on which environment was being analyzed. This unidirectional coupling would progress to the GPAM passing water compositional parameters (potentially from other internal chemistry models) to the used fuel degradation and RM matrix degradation rate model so that it could analyze and provide the fractional degradation rate for those specific water compositions. This would be a bidirectional coupling example. Further coupling of the process model with full suite of coupled thermo-hydro-chemical processes would allow a fully coupled feedback where not only the fractional degradation rate was being provided to the GPAM, but the entire change to the water composition based on the used fuel degradation would be passed back to the GPAM as well. Such a staged strategy facilitates incorporation of process-level detail as it is developed and permits an evolving level of complexity to be incorporated in a deliberate manner.

### 2.3 References for Sec. 2.0

Clayton D., Freeze, G., Hadgu, T., Hardin, E., Lee, J., Prouty, J., Rogers, R., Nutt, W. M., Birkholzer, J., Liu, H.H., Zheng, L., and Chu, S., 2011, *Generic Disposal System Modeling—Fiscal Year 2011 Progress Report*, FCRD-USED-2011-000184, pp. 443.

Freeze, G. and Vaughn, P., 2012, Performance Assessment Framework Requirements for Advanced Disposal System Modeling, FCRD-UFD-2012-000227 (M3FT-12SN0808062), U.S. Department of Energy, Office of Nuclear Energy, Used Fuel Disposition Campaign, Washington, D.C.

### 3. Used Fuel Degradation and Radionuclide Mobilization Concepts and Models

Once the cladding around used fuel is breached in a failed waste package (see FEP 2.1.02.06), the used fuel will be exposed to ingress of water and/or humid air. The radionuclide mobilization from such exposed used fuel can depend on the type of cladding breach and on the progression of the used fuel rod degradation following the initial cladding breach. Several hypothetical scenarios for the evolution of the state of a fuel rod following breach of its cladding are plausible. In one case, the corrosion of the fuel and precipitation of alteration products in a breached fuel rod could quickly lead to axial splitting, or “unzipping,” of the cladding. Another case is that the precipitating alteration phases will seal the gap and fracture openings and, as a result, limit the rate of further fuel degradation and radionuclide release. A further possibility is that cladding corrosion from the fuel-side will cause extensive cladding degradation and exposure of the fuel pellet fragments (Cunnane et al., 2003). Because the specific effects of cladding failure are planned to be evaluated and integrated into the models of used fuel degradation in the future, this report assumes as an idealized case that the breached cladding does not influence the fuel matrix degradation or radionuclide mobilization.

Currently, generic disposal system models (GDSM) for various repository settings are including constraints on radionuclide release from spent fuel based on sampling distributions of general ranges of fractional degradation rates of used fuel taken from the literature (see Section 2 above). In addition the GDSM are constraining radionuclide mobilization away from the used fuel using published solubility-limited radionuclide concentrations for those radioelements expected to be reprecipitated locally as driven by the system conditions near their point of release from the used fuel (e.g., within the EBS).

The degradation rate sampling and sampled solubility limited concentrations used in these general representations are to be supplanted with specific used fuel degradation and radionuclide release models that account more directly for the effects of the major chemical variables on the used fuel degradation rates and radionuclide releases in the various repository settings. Ultimately the goal is to implement fully-coupled models of these chemical and transport processes within the GPAM. This report provides the initial implementations of the primary models for integration into GPAM as the next step for improved resolution of used fuel degradation processes within the generic performance assessment. These models are:

- the fast/instant release fraction of radionuclides
- the ANL Mixed Potential Model for used fuel matrix degradation rate
- the PNNL Radiolysis Model for the production of oxidative radiolytic species

In addition, first principle models are presented below for bulk  $\text{UO}_2$  chemical properties and surface chemistry, as well as for the structures of studtite and metastudtite (peroxide alteration phases that can form from used fuel in a radiolytic environment). These first principle models will enable detailed evaluation of surface redox chemistry of  $\text{UO}_2$  and its alteration products from reactions with species such as oxygen, water, and hydrogen peroxide. Such capabilities provide a useful methodology for evaluating/validating continuum scale models of degradation of used fuel, as well as allowing enhanced investigation of the mechanisms controlling such degradation processes.

## 3.1 Overview and Concepts

### 3.1.1 Background

Commercial LWR fuel rods consist of stacks of ceramic oxide pellets encased in sealed zircaloy (zirconium alloy) tubing. The state (microstructure, physicochemical condition, and distribution of fission products and actinide elements) of freshly irradiated spent uranium oxide (UOX) and mixed (plutonium and uranium) oxide (MOX) nuclear fuels has been extensively investigated in postirradiation examinations conducted throughout the world (e.g., see review by Dehaut 2001, Section 5.2). Features of irradiated fuel that may influence its degradation and radionuclide mobilization are the chemical composition of the fuel matrix (the region within the UOX or MOX grains), the oxygen potential in the fuel (which controls the oxidation states of the radionuclides), the macro- and micro-scale structure of the fuel (gap dimensions, fuel pellet fracturing, fuel connected porosity, and grain boundary structure), and the distribution of the fission product inventory within these fuel features. The oxygen potential refers to the chemical potential of oxygen of the fuel as represented by the fuel's oxygen stoichiometry, or degree of non-stoichiometry, which is set initially by the gas composition used at synthesis—see below). Many of these features are affected by the degree of irradiation (i.e., burnup) of the fuel. The following is a summary of the features relevant to radionuclide mobilization in potential repository host rock settings primarily condensed from the review by Dehaut (2001, p. 49).

After irradiation, the macroscale structure of spent fuel rods is changed from the as-fabricated condition. For example, the gap between the fuel pellets and the cladding decreases with increasing burnup (Dehaut 2001, p. 196) and the fuel pellets are extensively cracked with the cracks running radially and axially through the irradiated fuel pellets. This cracking results from the differential expansion and the associated tensile stresses caused by the radial temperature gradients in the fuel rod, mostly when it is subjected to initial power increase in the reactor. Although the fuel pellet fragments formed initially may subsequently undergo further fragmentation, much of the cracking occurs early in the irradiation history (Dehaut 2001 p. 87). The radial and transverse cracking of the fuel pellets result in the creation of 15 to 20 fragments per pellet with the number of cracks somewhat dependent on the fuel burnup (Dehaut 2001, pp. 106 and 176).

Although the as-fabricated fuel pellets have a few percent porosity, this porosity is mostly due to pore formers added during the pellet fabrication and is in the form of isolated pores (usually referred to as “closed porosity”) (Pelletier 2001, Section 5.4.3.1.1) as opposed to connected cracks. The release of fission gasses in spent fuel irradiated at high power (or to high burnup) generates lens-shaped bubbles within the pellet. Such bubbles are commonly associated with metallic fission product inclusions that decorate the bubbles and grain boundaries. The bubbles can become interconnected on the grain boundary surfaces and form gas tunnels that conduct the fission gas to the gap region of the fuel rod. The fission gas release leaves some residual grain boundary decohesion and connected or “open” porosity at grain boundaries in the fuel pellets.

At burnups higher than approximately 45 MWd/kgU, a “rim region” (150 to 250 $\mu$ m thick) is formed at the outer surface of the pellets. This rim region is characterized by a very fine-grained fuel microstructure, up to 10 to 15 percent porosity, and local burnup up to three times higher than the pellet average burnup. Further details of the microstructural features and effects of



fission gas release on irradiated spent fuel are summarized elsewhere (Dehaut 2001, Sections 5.2.5.2 and 5.2.5.3; Barner 1985, pp. 4.14 and 4.15).

The chemical states and distributions of fission product elements in irradiated used fuels have been studied using thermodynamic equilibrium calculations and experimental measurements (Dehaut 2001, Section 5.2.6.3). The oxygen potential refers to the chemical potential of oxygen, initially imposed at  $\text{UO}_2$  synthesis conditions (high temperature) using various gas compositions (Lindemer and Besmann, 1985). Values are calculated from the ratio of the partial pressure of oxygen ( $p\text{O}_2$ ) used at the synthesis temperature and the standard state oxygen partial pressure ( $p^\circ\text{O}_2$ ) (i.e., oxygen potential =  $RT\ln[p\text{O}_2/p^\circ\text{O}_2]$  where R represents the gas constant and the absolute temperature (T) in Kelvin). The oxygen potential in fuel at synthesis is generally less than about -400 kJ/mol (Dehaut 2001, Section 5.2.6.5). Under these very low oxygen potential conditions the uranium and plutonium in the used fuel matrix is present mostly in the tetravalent (or IV) oxidation state. Likewise, the other radionuclides in the fuel matrix are in low, or even zero (metallic) valence states (Kleykamp 1985). The fact that the fuel matrix elements and radionuclides are present in the fuel in lower valence (and less soluble) states is important because used fuel degradation and RM are very slow processes unless both the fuel matrix and the associated radionuclides are oxidized under disposal conditions.

Most fission product elements are retained within the lattice structure of the fuel matrix (a fluorite-type lattice structure). For example, Np is expected to be present as a solid solution of  $\text{NpO}_2$  in the  $\text{UO}_2$  fluorite-type crystal structure with which it is compatible (Dehaut 2001, Section 5.2.6.5). Recent X-ray absorption near-edge spectroscopy (XANES) data indicate that the oxidation state of Np in the used fuel matrix is Np(IV). Supporting this, structural measurements using extended X-ray absorption fine structure spectra (EXAFS) data indicate that the Np(IV) is present in a  $\text{UO}_2$  – like phase, which is consistent with it being in solid solution in the fuel's  $\text{UO}_2$  fluorite-type crystal lattice structure (Kropf et al. 2004).

The more noble transition metal fission products (e.g., Pd, Ru, and Rh) are in metallic form and accumulate, in part, as discrete noble metal particles that are exsolved from the fuel matrix (Kleykamp 1985). (Note, these metallic phases are referred to herein as noble metal particles, noble metal alloy particles, or more specifically as five-metal alloy particles and, most specifically, as the epsilon phase.) This formation of a discrete metallic phase occurs because some of the fission product elements are not fully soluble in the matrix phases ( $\text{UO}_2$ ,  $\text{PuO}_2$ ) and so a portion of these elements migrates out of the fuel matrix under normal reactor operating conditions (Pelletier 2001, Section 5.4). After irradiation, these fission products are found primarily in the form of metallic alloy particles distributed within the fuel grains and at grain boundaries. The extent of migration of these fission products out of the fuel matrix, and the subsequent migration and accumulation at the grain boundaries and in gap regions of the fuel, depend on the diffusion coefficients of the individual fission product elements in the spent fuel matrix and the available mechanisms for migration and accumulation at the grain boundaries and in the gap region of the fuel rods (as discussed below, such redistribution plays a role in the radionuclide release processes). This amassing of noble metals in alloy particles is more evident in the higher-powered regions of the fuel (Barner 1985, p. 4.17; Guenther et al. 1988, Section 4.6).

As mentioned above, the factors controlling the diffusion and release of fission gases from used fuel grains are described by Pelletier (2001, Sections 5.4.5 and 5.4.6). The factors and processes

that are involved in migration from the grain boundaries to the gap regions are also discussed by Dehaut (2001, Section 5.2.9). Like the fission gasses, some of the cesium and iodine fission products diffuse out of the fuel grains and accumulate at the grain boundaries and in the gap region between the fuel pellets and the cladding (Dehaut 2001, Section 5.2.9.6). The extents to which the cesium and iodine migrate (as well as the metallic fission products) depend on the fuel burnup, operating temperatures, and temperature gradients, as determined by the fuel's linear power history in the reactor (Guenther et al. 1988, Sections 4.3 and 4.5.2).

### 3.1.2 Framework of Spent Fuel Degradation and Radionuclide Mobilization Processes

In addition to the part of the radionuclide inventory that is present as solid solution in the fuel matrix, both the discrete phases (i.e., the five-metal alloy particles) and the inaccessible portions of grain boundaries that are surrounded by fuel grains are not available for dissolution until the fuel matrix is dissolved or otherwise altered. This part of the inventory is referred to here as the "matrix inventory". Additionally in this document the noble metal particles (i.e. the five-metal alloy phases) are considered to be a further unique part of the inventory because they corrode very differently from the rest of the fuel matrix.

Other than the portion of the fuel controlled by fuel matrix degradation, there is a fraction of the inventory of fission gases and of more volatile radioelements (e.g., cesium, iodine, and technetium) that is released almost instantaneously upon cladding breach (i.e., the fast release fraction). Most of this fast release fraction is the fission products that have migrated out of the matrix during in-reactor operations and accumulated as gaseous and minor condensed phases along the fuel gap (i.e., the interface between the pellets and the cladding), the rod plenum regions, and in the readily accessible pellet fracture (grain boundary) surfaces. Within this document, these locations are collectively referred to as the "gap region" that contains the fast release fraction of fission products whose releases are independent of the fuel degradation rate.

On the basis of the above discussion, the radionuclide inventory in used fuel can be subdivided in this manner:

- The fast/rapid release fraction (called instant release fraction herein) inventory (which includes fission gases) comprised of fission products located in
  - The rod plenum regions (fission gases like Kr and Xe)
  - The fuel gap (between the pellet and the cladding – see Fig. 1.1-2)
  - The *accessible* grain boundaries/pellet fractures
- The matrix degradation inventory that includes the matrix itself and fission products located in
  - The *inaccessible* grain boundaries/pellet fractures
  - The solid solutions within the matrix
  - The noble metal particles (which undergo their own degradation rate once exposed by matrix degradation)

These inventories, the major rate limiting processes (e.g., matrix degradation, noble metal particle degradation), and radionuclide mobilization processes for each of these fractions are summarized below.

The major elemental components comprising the matrix of the UOX and MOX used fuels are U and Pu. Minor elemental constituents (e.g. Pd and other noble metal fission products) may also

influence the corrosion of the fuel matrix, for example by catalyzing cathodic reactions. When the fuel matrix is corroding, the inherent corrosion potential of the primary mass of the oxide grains (UOX and MOX) controls and buffers the electrochemical conditions at and near the corroding surface. Many of the radioelements in used fuel (e.g. U, Pu, Np, Tc, I) are multivalent elements. The valence of the ions produced in the corrosion process depends on the corrosion conditions (e.g., potential and pH) at the surface of the corroding used fuel matrix. Because oxidation and dissolution of U and Pu produces high valence cations (oxidation states higher than 4), they undergo extensive hydrolysis and precipitation following their dissolution forming rind layers. Other multivalent radionuclides may only be present in their lower oxidation states during the fuel matrix corrosion process if the corrosion potential of the fuel matrix in its disposal environment is sufficiently low. Consequently, the radionuclides mobilized in lower valence (and less soluble) states may be retained in the rind layer unless they are subsequently oxidized to a higher oxidation state and dissolved into the bulk solution.

As discussed above, the conceptual model for radionuclide release processes from the used fuel matrix is based on hydrolysis of the cations produced in the corrosion process via the dissolution, oxidative dissolution, and/or precipitation/co-precipitation of these cations (to form a rind layer). Any incongruent release observed for the elemental components of the fuel matrix is due to the combined effects of the chemical reactions (i.e., hydrolysis, dissolution, oxidative dissolution, and precipitation) that occur in the precipitated rind layer and the mass transport processes out of that layer. Because the precipitated rind layer is expected to be porous, the local chemical environment in this layer, as well as mass transport processes through it, are expected to be coupled to the external bulk water chemistry and hydrodynamic conditions in a disposal system. These processes and those governing the instant release fraction of radionuclides are key to constraining the source term within performance assessment of geologic disposal environments. The Strategic Research Agenda (SRA) report (SRA, 2011) for the Implementing Geological Disposal of Radioactive Waste Technology Platform (IGD-TP) program lists the waste form one of their priorities in their “Key Topic 2: Waste Forms and their Behaviour”, and identifies the rapid release fraction from SNF with a high level of importance within.

### 3.1.3 References for Section 3.1

- Barner, J.O. 1985. *Characterization of LWR Spent Fuel MCC-Approved Testing Material—ATM-101*. PNL-5109, Rev. 1. Richland, Washington: Pacific Northwest Laboratory.
- BSC, 2004, CSNF Waste Form Degradation: Summary Abstraction, ANL-EBS-MD-000015 REV02.
- Cunnane, J., Fortner, J.A., Finch, R., 2003, The behavior of light water reactor fuel after the cladding is breached under unsaturated test conditions, MRS Symposium Proceedings 757, p. 385 – 392.
- Dehaut, P., 2001, State of the Art of the Oxidation of Spent Nuclear Fuel., Section 7.2 of *Synthesis on the Long Term Behavior of the Spent Nuclear Fuel*. Poinssot, C., ed. CEA-R-5958(E). Volume II. Paris, France: Commissariat à l'Énergie Atomique.
- Guenther, R.J., Blahnik, D.E., Campbell, T.K.; Jenquin, U.P., Mendel, J.E., Thornhill, C.K. 1988. *Characterization of Spent Fuel Approved Testing Material—ATM-106*. PNL-5109-106. Richland, Washington: Pacific Northwest Laboratory. (1988)
- Kleykamp, H., 1985, The chemical state of the fission products in oxide fuels, *Journal of Nuclear Materials*, 131, p. 221-246.
- Kropf, A.J., Fortner, J. A., Finch, R.J., Cunnane, J.C., Karanfil, C., 2004, A Bent Silicon Crystal in the Laue Geometry to Resolve Actinide X-Ray Fluorescence for X-Ray Absorption Spectroscopy, *Physica Scripta*, T115, p. 998.
- Lindemer, T. B., and Besmann, T. M., 1985, Chemical Thermodynamic Representation of  $\langle \text{UO}_{2\pm x} \rangle$ , *Journal of Nuclear Materials*, 130, p. 473-488.
- Pelletier, M., 2001, State of the Art on the Potential Migration of Species, Section 5.4 of “*Synthesis on the Long Term Behavior of the Spent Nuclear Fuel*”, Poinssot, C., ed. CEA-R-5958(E). Volume I. [Paris], France: Commissariat à l'Énergie Atomique.
- SRA, 2011, *Implementing Geological Disposal of Radioactive Waste Technology Platform Strategic Research Agenda 2011 (IGD-TP)*, European Community (EC) Euratom framework programme, 63 pp. (ISBN 978-91-979786-0-6) ([www.igdtp.eu](http://www.igdtp.eu)).

## 3.2 Fast/Instant Release of Radionuclides

Irradiation of fuel at high power (or to high burnup) releases fission gasses in used fuel and generates lens-shaped bubbles within the fuel pellet. Such bubbles are commonly associated with metallic fission product inclusions that decorate the bubbles and grain boundaries. In addition to the diffusive migration to form such phases, the bubbles can become interconnected on the grain boundary surfaces and may then form gas tunnels that conduct the fission gas to the gap region of the fuel rod. Like the fission gasses, some of the volatile (e.g., cesium and iodine, among others) fission products diffuse out of the fuel grains and accumulate at the grain boundaries and in the gap region between the fuel pellets and the cladding (Dehaut 2001, Section 5.2.9.6). The extents to which the cesium and iodine migrate (as well as other volatile fission products) depend on the radioelements diffusion coefficients, the fuel burnup, operating temperatures, and temperature gradients, as determined by the fuel's linear power history in the reactor (Guenther et al. 1988, Sections 4.3 and 4.5.2). In this manner, the physical distributions of these volatile radioelements within the used fuel may reflect those of the fission gases (to an extent depending on similarity of diffusion rates, etc.).

Radionuclides in the gap inventory are available for dissolution immediately upon ingress of groundwater into failed fuel rods and its contact with those radionuclides in the gap region (see Fig. 3.2-1). Because the radionuclides involved are soluble and because their dissolution is apparently rapid and does not saturate the available groundwater, the dissolution and mobilization of gap radionuclides is assumed to be limited only by the fraction of their inventories available in the gap region. This gap inventory and a portion of the grain boundary radionuclide inventory (the accessible grain boundary inventory) comprise a rapid (or instantaneous) release fraction (IRF) of radionuclides from used fuel that is mobilized at the time that the cladding is breached.

Experimentally determined values for various used fuels provide constraints on the amount of the IRF. The IRF appears to have a non-trivial dependence on the history of the used fuel rod including original fabrication conditions, burnup, linear power rating, and centerline temperature, among other factors. In general, studies have evaluated the correlations between IRF of radionuclides and the amounts of FGR for fuels of various burnups (e.g., Johnson et al., 2005; 2012). Given the number of variables affecting the specific amount of IRF for any particular used fuel rod, general constraints suitable for use in performance assessments of the safety of generic disposal environments are provided below with limited dependence on these variables. As such, these constraints can be used for assessing the performance of a generic repository environment in a bounding manner that allows investigation of some of the major uncertainties in the system.

### 3.2.1 Used Fuel Structural Considerations

Within the grain-boundary region of the fuel pellet, radionuclides may be readily releasable (accessible grain boundary inventory), or may be inaccessible (the inaccessible grain boundary inventory – see Fig. 3.2-1). This latter portion would remain unreleased until degradation of the fuel pellet matrix occurs to the point where these grain boundaries are now exposed to fluids. Mobilization of the inaccessible grain-boundary inventory requires prior degradation of the matrix grains to make accessible these initially inaccessible grain boundaries in the used fuel. Degradation of the grain boundaries may occur due to the effects of helium production from  $\alpha$ -

particle decay on the mechanical stability of the grain boundaries (Ferry et al. 2006) or from preferential corrosion at/along the grain boundaries. Although this is straightforward in concept, delineation of the accessible grain boundaries from the inaccessible ones is not a simplistic task and methods of measuring the grain boundary inventories (e.g., grinding of samples) tend to capture the total (e.g., BSC 2004; Roudil et al., 2007).

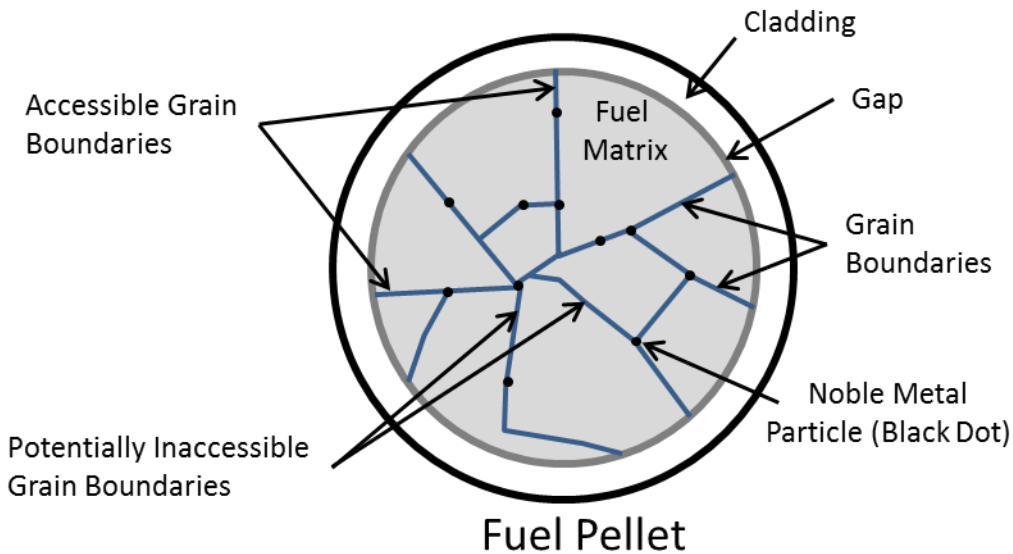


Figure 3.2-1. Schematic of a fuel pellet cross section showing the relative locations of radionuclide inventories for the gap, grain boundaries, fuel matrix, and noble metal particles. Also shown are the general locations of accessible grain boundaries and inaccessible grain boundaries.

Because the initial fraction of inaccessible grain boundary and the progression of the grain boundary corrosion within geologic disposal systems are not well understood, it has been common for the entire grain boundary inventory to be conservatively assumed to be released instantaneously (i.e., as part of the IRF) upon water ingress into the breached fuel rods (e.g., BSC 2004; Johnson et al., 2005). Additional empirical data obtained from long-term fuel corrosion testing indicates that the oxidative dissolution process of the fuel matrix is a general corrosion process and does not exhibit substantial preferential corrosion along the grain boundaries (BSC 2004; Une and Kashibe 1996). This suggests that the inaccessible grain boundary inventory would be mobilized at a rate similar to radionuclides within the fuel matrix, and could therefore be released in proportion to the matrix degradation. Further data for distribution of inaccessible grain boundary radionuclide inventory and advanced understanding of grain boundary degradation in used fuel would facilitate this approach, particularly for high-burnup used fuels with their added structural changes as burnup increases.

### 3.2.1.1 Additional Structural Considerations for High Burnup Used Fuel

For the purposes of this report, a transition point to high burnup fuels is defined as occurring at 45 MWd/kgU such that any used fuel that has a burnup >45 MWd/kgU is referred to as high burnup. This is in part based on the observation that the amount of fission gas release (FGR; e.g.,

Kr and Xe) for LWR used fuel depends more strongly on the magnitude of BU for fuels above 45 MWd/kgU (e.g., see Johnson et al., 2012; Fig. 1). Besides having more fission product content, such high burnup used fuels exhibit distinct structural changes at the pellet rim that are driven by locally increased  $^{239}\text{Pu}$  content, which causes elevated local burnup (factor of 2 to 3) that results in a finer-grained, higher closed-porosity (containing fission gases) layer (Johnson et al., 2005; Serrano-Purroy et al., 2012). This rim layer of high-burnup structure (HBS; see Fig. 3.2-2) is noticeable in used fuels starting around a burnup of 40 MWd/kgU (Johnson et al., 2005), grows progressively thicker with burnup and other parameters of the irradiation history (de Pablo et al., 2009), and develops a transition region towards a core lacking any HBS (Serrano-Purroy et al., 2012).

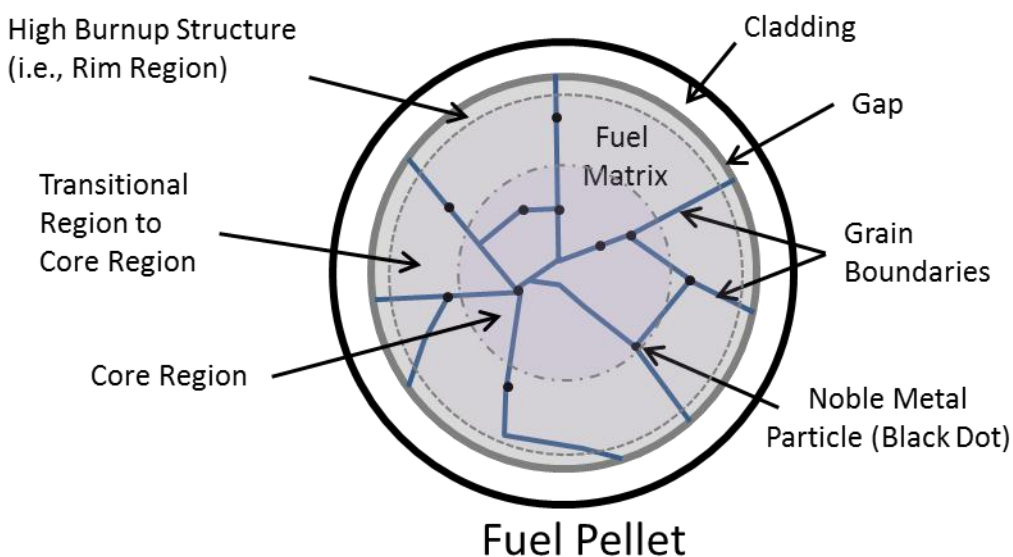


Figure 3.2-2. . Schematic of a fuel pellet cross section for high BU used fuel showing the rim region high burnup structure (HBS), transitional region, and core region (after Fig. 1 of Serrano-Purroy et al., 2012).

Discussions of whether this HBS represents a larger source of IRF because of its fine-grained nature and enrichment in fission products has led to some studies that evaluate separately the IRF from the rim region versus the core regions (de Pablo et al., 2008; 2009; Serrano-Purroy et al., 2012 – see Table 3.2-1 below). Some of these studies (de Pablo et al., 2009; Serrano-Purroy et al., 2012) conclude that core samples always release faster than rim samples, and can show higher IRF than rim samples for some radioelements, especially for comparison of grain boundary release. However, evaluation of measured values is challenging because of aspects of sample preparation, including the manner in which cladding is removed from the fuel pellet (Johnson et al., 2012), who indicated that the amount of damage to the sample affects directly the observed IRF values, but leaving cladding attached may prevent observation of appropriate IRF values also. The Johnson et al. (2012) study of the HBS rim IRF indicates that this region may be protective rather than facilitating to the IRF for radioelements in that material. Such information provides a path for additional exploration to develop more comprehensive data sets that

differentiate among these processes and allow a more detailed model to be developed that captures these salient features of the used fuel.

Though sample treatment is concluded to have a direct effect on measured IRF (Johnson et al., 2012), less information is available for the effect of water composition. In their study of IRF, de Pablo et al. (2009) conclude no effect of water composition in their results, although examination of the values in Table 3.2-1 suggests that in some cases there may be some enhancement in the bicarbonate water over the bentonitic granitic water (more pronounced for the samples from de Pablo et al., 2008). However, examination of the results of Serrano-Purroy et al. (2012) indicates little to no difference in the results in these two solution compositions. The uncertainty in the measurements is assessed in Serrano-Purroy et al. (2012) where it can be seen to range from about 20 to 80% relative uncertainty depending on the radioelement and portion of the inventory being constrained (i.e., gap versus grain boundary). As such the variation observed in some of the measurements for different water compositions appears to be within the measurement uncertainties and is therefore a challenge to delineate with the present data.

An effort to address the sparse data for IRF on high burnup fuels has been started by the European Commission (EC) Collaborative Project (CP) on the *Fast / Instant Release of Safety Relevant Radionuclides (FIRST – nuclides) from Spent Nuclear Fuel*. This three (3) year project is focused on experiments to determine IRF from high burnup used fuel and model development of those IRF for use in assessing the safety of disposal sites. This CP plans to evaluate FGR, grain boundary processes, and the IRF dependency on used fuel manufacture condition, evolution of BU and irradiation history, linear power and fuel temperature history and storage duration. As discussed above, D. Sassani is the SNL representative (and the DOE NE FCT UFD proxy representative) participating in the *FIRST – Nuclides* CP as an Associate Group. As data are generated from this CP, they will be used to further address the dependencies of major variables affecting the IRF and would potentially provide the bases for quantitative correlations of the IRF with some of these major parametric dependencies.

Although used fuel burnup and measured FGR have been the primary parameters evaluated for their effects on the IRF of used fuel, other variables can have just as large an effect and provide a source of conceptual uncertainty to models that are parameterized solely on BU or FGR. Some of the major variables to consider are linear power history, center line temperature, and thermal gradient within a used fuel rod (de Pablo et al., 2009; Johnson et al., 2012). Original Fuel density may also play a role, especially in FGR as pointed out by Johnson et al. (2012) that ATM-106 fuel rods fabricated in 1970's have a substantially lower density ( $\sim 10.05$  to  $10.3$  g/cm<sup>3</sup>) compared with more modern fuels ( $\sim 10.5$  g/cm<sup>3</sup>) that may explain higher FGR (11 and 18% for BU of 46 and 50 MWd/KgU) due to higher connected porosity in the original pellets. Such factors complicate direct correlation of IRF with a single parameter such as BU or FGR.

### 3.2.2 Models of the Instant Release Fraction Radionuclides

Models that have been developed for mobilization of the gap and grain-boundary inventories assume conservatively that they are instantaneously released when groundwater contacts the used fuel (BSC 2004; Johnson et al. 2005) through the breached cladding for even a pinhole failure. The model values developed in BSC (2004) are principally aligned with the values of FGR from the spent fuels (and cover a range from 0.59 to 18% FGR), but the constraints are provided as distributions (Table 3.2-1) spanning the entire range of FGR evaluated because of



the inherent complexity of parametric correlation for these data sets. It is recommended that these BSC (2004) distributions be used to analyze IRF in performance assessment with consideration of the uncertainty for fuels of burnup at or below about 50 MWd/KgU (e.g., some used fuel like ATM-106) in a conservative manner, although temporal evolution of potential IRF radionuclides is not included. As discussed in BSC (2004; Section 7.1.1) comparison to additional literature data indicates that the BSC (2004) distributions for Sr and Tc release may not be conservative (similar conclusions could be drawn from comparison with other model values and data in Table 3.2-1). However, BSC (2004) also notes that both Tc and Sr are radioelements that can be largely affected by matrix dissolution within testing data. Application of the BSC (2004) distributions for fuels above 50 MWd/KgU is not as demonstrably conservative (though may still be for some radioelements - i.e., I and perhaps Cs) as compared to the model values developed by Johnson et al. (2005) that are specifically dependent on BU.

An extensive evaluation of IRFs for UO<sub>2</sub> (and MOX) fuels has been conducted based on correlation of leaching data with fission gas release (e.g., Xe) and has been used to extrapolate IRF data for estimates of instant release fractions for higher burnups (Johnson et al. 2005). Based on such correlations of the IRF with the fission gas release, “best estimate” and “pessimistic estimate” IRF values have been developed for fuels as a function of the fuel burnup (Johnson et al. 2005) and are listed in Table 3.2-1. These estimates are considered to be reliable for low to moderate burnup UO<sub>2</sub> fuels, and less reliable for the higher burnup fuels for which experimental leaching data are sparse. However, additional studies of high burnup fuels, some explicitly analyzing the HBS rim regions and used fuel cores separately (see values in Table 3.2-1), suggest that these model values may be conservative estimates of the IRF (especially in regard to Tc).

Because of the potential need to evaluate more closely the variability of used fuel burnup in the source-term of performance assessment, it is recommended that the values in Table 3.2-1 from Johnson et al. (2005) be used to define linear distributions with the best estimate values (labeled BE) used as the minimum value and the pessimistic estimate values (labeled PE) used as the maximum value for each value of burnup listed. This will allow the GPAM model to capture at a first order a major variation for used fuel with burnup as high as 75 MWd/KgU. Linear interpolation between the specific burnup values would be reasonable to construct similar linear distributions for intermediate burnup values, but no extrapolation beyond the maximum burnup given should be performed. Note that there are also first order pessimistic estimates for IRF of C and Cl radioelements (Johnson et al., 2005) from used fuel that provide conservative order-of-magnitude constraints for their instant release amounts without any dependence on burnup (most of this easily released C is from the fuel hardware) and these could be applied within the GPAM.

Johnson et al. (2005) utilize direct consideration of both FGR and BU for constructing their model values. In addition, Johnson et al. (2012) point out that high FGR in some fuels (specifically 11% and 18% in ATM-106 with burnups of 46 and 50 MWd/KgU, respectively) is not due to higher burnup, rather it is likely due to original lower density of the manufactured fuel providing higher open porosity. This would mean that simply using estimates dependent solely on FGR could lead to overestimates of the IRF in such cases. Mobilization models for the IRF estimate the fraction of the inventory of key radionuclides in the IRF and could be parameterized to include changes to this fraction that may occur over time as a result of additional migration of radionuclides within the used fuel structure (Johnson et al. 2005; Poinssot et al. 2005).

Development of such further detailed parametric correlations and potential evolution of reservoirs for instant release will be evaluated in future analyses of the available data. As data are collected within the EC *FIRST – nuclides* CP, additional understanding of the interdependence of the primary parameters controlling IRF in higher burnup fuels will be incorporated into constraints for GPAM source-terms. Future development of model dependencies could be tied to the better constrained FGR information (Johnson et al., 2012), or could be correlated simultaneously with multiple major variables if the data were abundant enough to support such. Future work in this area will evaluate coupling of cladding models to the used fuel degradation and could develop various correlations to be used depending on particular cladding failure scenarios (e.g., pinhole versus crushed) and physical damage to used fuel.

Table 3.2-1. Model values and measured values of the Instant Release Fractions (% of radioelement inventory) for spent fuel pellets of various burnups, for a variety of environment conditions, and from various regions of the fuel pellet samples.

Model or Data Set		YMP Distributions (triangular) <sup>1</sup>			Johnson 2005 Model <sup>2</sup>					de Pablo Values <sup>3</sup>								Serrano-Purroy Values <sup>4</sup>				Roudil Values <sup>5</sup>
Fuel(BU)		LWR(range)			PWR(37)	PWR(41)	PWR(48)	PWR(60)	PWR(75)	PWR(48)				PWR(60)				PWR(60)				PWR(60)
Conditions <sup>6</sup>		min	max	mode	BE(PE)	BE(PE)	BE(PE)	BE(PE)	BE(PE)	BIC	BIC	BGW	BGW	BIC	BIC	BGW	BGW	BIC (+gb)	BIC (+gb)	BGW (+gb)	BGW (+gb)	Gap and gb
Radio-element	Radial Location	all	all	all	all	all	all	all	all	core	rim	core	rim	core	rim	core	rim	core	rim	core	rim	all
C (%)		--	--	--	10	10	10	10	10	--	--	--	--	--	--	--	--	--	--	--	--	--
Cl (%)		--	--	--	5	5	5	5	5	--	--	--	--	--	--	--	--	--	--	--	--	--
Sr (%)		0.03	0.23	0.1	1(1)	1(2)	3(4)	7(11)	11(17)	5.3	0.5	2.8	0.3	4.3	2.7	3.6	1.9	1.96 (2.86)	1.52 (2.02)	1.98 (3.68)	1.89 (2.49)	0.21
I (%)		2.11	27.33	11.26	3(3)	3(3)	4(6)	10(16)	18(26)	--	--	--	--	--	--	--	--	--	--	--	--	--
Cs (%)		0.4	11.73	3.7	2(2)	2(2)	4(6)	10(16)	18(26)	4.6	4.8	4.9	4.5	10.9	4.5	6.3	6	2.45 (3.85)	3.59 (4.89)	2.15 (3.65)	4.26 (5.56)	1.4
Tc (%)		0.01	0.18	0.05	1(1)	1(2)	3(4)	7(11)	11(17)	0.02	0.01	<0.01	0.01	0.2	0.2	0.4	0.2	0.31 (0.42)	0.1 (0.21)	0.4 (0.42)	0.03 (0.18)	--

NOTES: BU – mean burnup (MWday/KgU); BE - best estimate; PE - pessimistic estimate; BIC – synthetic bicarbonate water; BGW – bentonitic granitic water; gb – grain boundaries;

1 – BSC (2004); from data covering burnups from x to y in dilute oxidizing acidic solutions.

2 – Johnson et al. (2005)

3 – de Pablo et al. (2008; 2009; for PWR(60) and PWR48, respectively).

4 – Serrano-Purroy et al. (2012); values are for gap and accessible grain boundaries or for gap and total grain boundaries (+gb).

5 – Roudil et al. (2007); air atmosphere, dilute carbonated water and dilute sodium bicarbonate solution.

6 – Provides solution composition conditions for “Values” and model applicability for model parameters.

### 3.2.3 References for Section 3.2

- BSC, 2004, CSNF Waste Form Degradation: Summary Abstraction, ANL-EBS-MD-000015 REV02.
- Buck, E.C., Wittman, R.S., Hayes, J.W., Kiser, S.M., 2011, Repository Science/ Waste Form Degradation: Progress Report, PNNL draft report, level 4 UFD milestone, July 2011.
- De Pablo, J., Casas, I., Gimenez, J., Clarens, F., Gonzalez-Robles, E., Serrano-Purroy, D., Glatz, J.-P., Wegen, D. H., Christiansen, B., Martinez-Esparza, A., 2008, Contribution to leaching studies of high-burnup spent nuclear fuel, *Proceedings of the 12<sup>th</sup> International High-Level Radioactive Waste Management (IHLRWM) Conference, Steps toward reality for safe disposal*, Las Vegas, NV.
- De Pablo, J., Serrano-Purroy, D., Gonzalez-Robles, E., Clarens, F., Martinez-Esparza, A., Wegen, D. H., Casas, I., Christiansen, B., Glatz, J.-P., Gimenez, J., 2009, Effect of HBS Structure in Fast Release Fraction of 48 GWd/tU PWR Fuel, *Mater. Res. Soc. Symp. Proc.*, 1193, 613 doi:10.1557/PROC-1193-613.
- Dehaut, P., (2001) Physical and Chemical State<sup>“”</sup> of the Nuclear Spent Fuel after Irradiation, Subsection 5.2 of Intrinsic Evolution of Spent Nuclear Fuel in a Closed System (2<sup>nd</sup> Subprogram) in *Synthesis on the Long Term Behavior of the Spent Nuclear Fuel*. Poinssot, C., ed. CEA-R-5958(E). Volume II. Paris, France: Commissariat à l'Énergie Atomique.
- Ferry, C., Poinssot, C., Cappelaere, C., Desgranges, L., Jégou, C., Miserque, F., Piron, J.P., Roudil, D., Gras, J-M., 2006, Specific Outcomes of the Research on the Spent Fuel Long-Term Evolution in Interim Dry Storage and Deep Geological Disposal, *Journal of Nuclear Materials*, 352, p. 246-253.
- Guenther, R.J., Blahnik, D.E., Campbell, T.K., Jenquin, U.P., Mendel, J.E., Thornhill, C.K., 1988. Characterization of Spent Fuel Approved Testing Material—ATM-106, PNL-5109-106. Richland, Washington: Pacific Northwest Laboratory.
- Johnson, L., Ferry, C., Poinssot, C., Lovera, P., 2005, Spent fuel radionuclide source term model for assessing spent fuel performance in geological disposal. Part I: Assessment of the Instant Release Fraction, *Journal of Nuclear Materials*, 346, p. 66-77.
- Johnson, L., Gunther-Leopold, I., Kobler Waldis, J., Linder, H. P., Low, J., Cui, D., Ekeroth, E. Spahiu, K., Evins, L. Z., 2012, Rapid aqueous release of fission products from high burn-up LWR fuel: Experimental results and correlations with fission gas release, *Journal of Nuclear Materials*, 420, p. 54-62.
- Poinssot, C., Ferry, C., Lovera, P., Jégou, C., Gras, J-M., 2005, Spent fuel radionuclide source term model for assessing spent fuel performance in geological disposal. Part II: Matrix alteration model and global performance, *Journal of Nuclear Materials*, 346, p. 66-77.
- Roudil, D., Jégou, C., Broudic, V. Muzeau, B., Peugeot, S., Deschanel, X., 2007, Gap and grain boundaries inventories from pressurized water reactor spent fuels, *Journal of Nuclear Materials*, 362, p. 411-415.
- Serrano-Purroy, D., Clarens, F., Gonzalez-Robles, E., Glatz, J.-P., Wegen, D. H., De Pablo, J., Casas, I., Gimenez, J., Martinez-Esparza, A., 2012, Instant release fraction and matrix

release of high burn-up  $\text{UO}_2$  spent nuclear fuel: Effect of high burn-up structure and leaching solution composition, *Journal of Nuclear Materials*, 427, p. 249-258.

Une, K., Kashibe, S., 1996, Corrosion behavior of irradiated oxide fuel pellets in high temperature water, *Journal of Nuclear Materials*, 232, p. 240-247.

### 3.3 Radiolytic Processes Modeling

The work in this section is being conducted at PNNL and more details can be found in the Used Fuel Disposition M3 Milestone, Radiolysis Products Modeling Results for Scenarios, (M3FT-12PN080651).

Assessing the performance of Spent (or Used) Nuclear Fuel (UNF) in geological repository requires quantification of time-dependent phenomena that may influence its behavior on a time-scale up to millions of years. A high-level waste repository environment will be a dynamic redox system because of the time-dependent generation of radiolytic oxidants and reductants and the corrosion of Fe-bearing canister materials (Stroes-Gascoyne et al. 2005; Shoesmith et al. 2003). One major difference between used fuel and natural analogues, including unirradiated  $\text{UO}_2$ , is the intense radiolytic field. The radiation emitted by used fuel can produce radiolysis products in the presence of water vapor or a thin-film of water (including hydroxide ( $\text{OH}\cdot$ ) and hydrogen ( $\text{H}\cdot$ ) radicals, oxygen ion ( $\text{O}_2^-$ ), aqueous electron ( $e_{\text{aq}}$ ), hydrogen peroxide ( $\text{H}_2\text{O}_2$ ), hydrogen gas ( $\text{H}_2$ ), and the secondary radiolysis product, oxygen ( $\text{O}_2$ )) that may increase the waste form degradation rate and change radionuclide behavior.

Hydrogen peroxide ( $\text{H}_2\text{O}_2$ ) is the dominant oxidant for spent nuclear fuel in an  $\text{O}_2$ -depleted water environment. The most sensitive parameters have been identified with respect to predictions of a radiolysis model under typical conditions. As compared with the full model with about 100 reactions, it was found that only 30 to 40 of the reactions are required to determine  $[\text{H}_2\text{O}_2]$  to one part in  $10^{-5}$  and to preserve most of the predictions for major species. This allows a systematic approach for model simplification and offers guidance in designing experiments for validation.

#### 3.3.1 Radiolysis Process Model Description

As the radiation emitted by used fuel produce radiolysis products (including hydroxide ( $\text{OH}\cdot$ ) and hydrogen ( $\text{H}\cdot$ ) radicals, oxygen ion ( $\text{O}_2^-$ ), aqueous electron ( $e_{\text{aq}}$ ), hydrogen peroxide ( $\text{H}_2\text{O}_2$ ), hydrogen gas ( $\text{H}_2$ ), and the secondary radiolysis product, oxygen ( $\text{O}_2$ )) in a thin-film of water on used fuel,  $\text{H}_2$  may escape from the water layer surface creating local conditions at the fuel/water interface (i.e., within the first 300  $\mu\text{m}$ ) that may always be oxidizing in the  $\alpha$ -radiolytic field, even in reducing environments. Experiments with used fuel are thought to be significantly influenced by their high  $\beta,\gamma$ -radiation field, which results in generation of powerful oxidizing radiolytic species (e.g.,  $\text{OH}\cdot$  and  $\text{H}_2\text{O}_2$ ). However, at the fuel/water interface, the  $\beta,\gamma$ -radiation field is not as intense as the alpha field (Radulescu et al. 2011) (see Figure 3.3-1).

Hence, although Shoesmith et al. (2003) has argued that it is highly conservative to use rates of reaction from relatively fresh used fuel for performance assessment calculations; surface radiolytic calculations indicate that the  $\beta,\gamma$ -radiation field is not impacting the surface reactions. Burns et al. (2012) have argued that the oxidizing nature of a repository should be one of the most important selection criteria for the long-term disposal of used fuel. Higher oxidation rates would indeed be predicted by the corrosion models in the presence of atmospheric concentrations of  $\text{O}_2$ ; however, the radiolytic field from the fuel surface will result in localized oxidizing conditions. Reducing geologic environments have been suggested by Burns et al. (2012) for used fuel that are similar to those planned for the Swedish nuclear waste disposal program. The Swedish repository design also incorporates large quantities of cast iron, embedded in bentonite at a depth of about 500 m in granitic bedrock. An  $\text{H}_2$  pressure of 50 bar (725 psi) has been predicted to be generated due to the anoxic corrosion of the iron canisters by

groundwater (Cui et al. 2012). Dissolved hydrogen at low temperature is chemically inert and can significantly contribute to establishing reducing conditions in the near field (Carbol et al., 2009; Ekeroth et al., 2006; Jegou et al., 2005) that may effectively shut down the  $UO_2$  oxidation process.

However, in the case of the localized corrosion of used fuel in conditions where the alpha field is dominant, some fuel corrosion should occur under any conditions if water contacts the fuel surface. Fuel corrosion leading to the transition of  $U^{4+}$  to  $U^{6+}$  will occur from exposure to water vapor regardless of the repository environment; although, the presence of oxygen in the Engineered Barrier System (EBS) environment should lead to higher overall  $UO_2$  oxidation rates (even in the presence of radiolysis). Reducing conditions in the EBS may result in the precipitation of  $U^{4+}/U^{5+}$  phases. After 300 years, the  $\beta/\gamma$ -radiolytic field will be reduced by 3 to 4 orders of magnitude; yet, the dose at the fuel surface from alpha will remain undiminished. This means that data on the alteration behavior of used fuel may be relevant for interpreting the possible future condition of used fuel in a geologic environment.

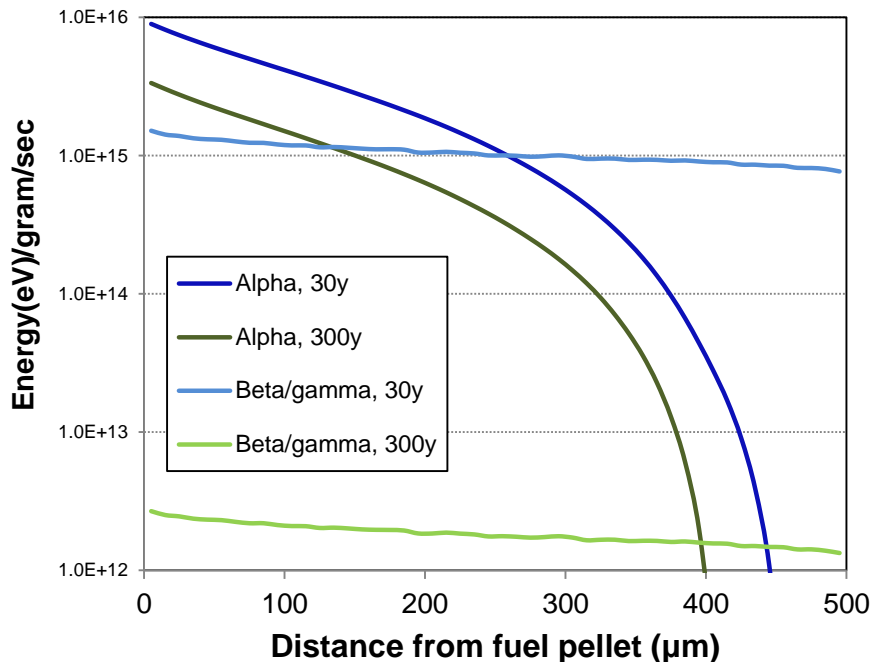


Figure 3.3-1. The dose to the surface of used fuel exposed to a mixed water-air environment (10% water) is dominated by long-lived alpha radiation even at relatively short times out of reactor [Adapted from Radulescu et al. 2011].

### 3.3.1.1 Modeling Concepts and Processes

A model is being developed to estimate radiolysis products for the the uranyl-water-carbonate radiolytic system that can be used to predict the corrosion rate of  $UO_2$ . Initial efforts concentrated on repeating the work of Sunder (1998), Christensen and Sunder (2000), Sunder et al. (1997), and Poinssot et al. (2005) and creating a more inclusive model. We have incorporated the best concepts from the literature to develop a more comprehensive super-set of radiolytic

reactions and conducted analyses to determine the most important processes under a large variety of conditions than has been done previously.

A schematic diagram showing the various processes involved in the interaction of ionizing radiation in water is shown in Figure 3.3-2. In this study, we are concerned mainly with the effectively long time processes that result in the formation of the six radiolytic species. G-values for these species have been established for all forms of ionizing radiation (See Table 3.3-1). There is a significant difference in the G value for  $\text{H}_2\text{O}_2$  in water compared to brine environments and a significant difference in G values between alpha and gamma radiations. Experiments by Cera et al. (2007) have led to the establishment of effective G-values for  $\text{H}_2\text{O}_2$  generation that consider the effect of iron and  $\text{UO}_2$  surfaces; however, such approaches may be inappropriate under different disposal scenarios. King et al. (1999) have developed a mixed potential model for predicting the effects of  $\alpha$ -radiolysis, the precipitation of uranyl secondary minerals (e.g., uranophane, schoepite,.) and redox processes with Fe(0) and Fe(II) on the dissolution of  $\text{UO}_2$ . However, these models do not model the formation of oxidants directly but rather assume constant values.

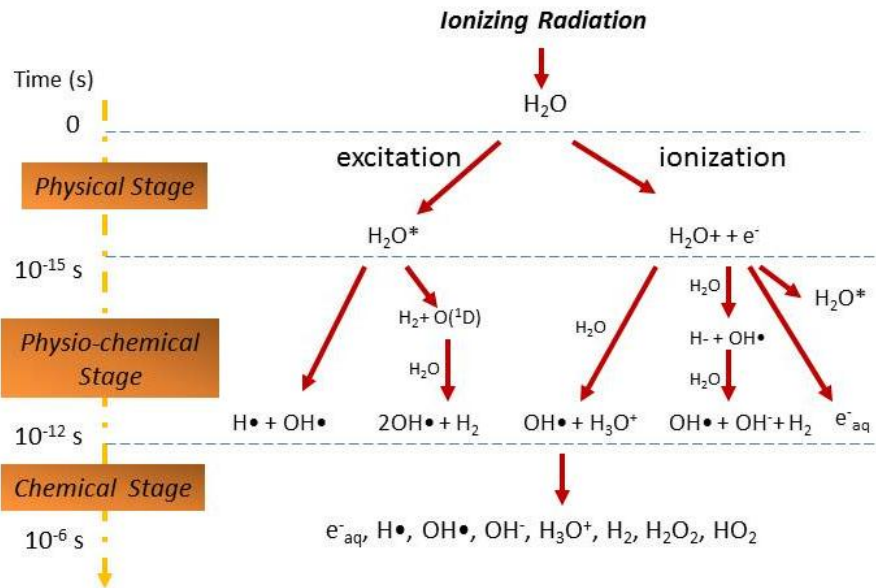


Figure 3.3-2. Schematic of reaction pathways in the radiolysis model (adapted from Sunder, 1998).

Indeed, only  $\text{H}_2\text{O}_2$  generation was considered in the model in the 1999 version of the mixed potential model developed by King et al. (1999) and Sunder (1998); hence, this model could be improved with a more comprehensive radiolysis component. Most radiolysis modeling has concentrated on gamma irradiation rather than alpha irradiation and there are few, if any, examples in the literature of radiolytic species predictions under alpha radiolysis.

As a base model, we considered the reaction kinetics of Christensen and Sunder (2000) applied to the heterogeneous system of  $\text{UO}_2$  dissolution at a solid-aqueous boundary. As expected, radiolysis products, increasing with dose rate, have a strong effect on the predicted oxidative dissolution rate. We find that these predicted rates are sensitive to the specifics of the radiolysis chemistry represented. For instance, even the inclusion of the slow reaction:





can change the  $\text{UO}_2$  dissolution rate by almost a factor of two. Of course, uncertainty in model parameters and reaction mechanisms results in uncertain predictions. We performed a limited analysis to quantify the sensitivity of dissolution rate to model parameters. This will enable identification of where model uncertainty can be reduced to have greatest benefit to predictability. Additionally, these investigations will help identify experiments that can best reduce the driving model uncertainties. In Figure 3.3-3, radiolysis predictions are shown for fuel corrosion in an anoxic environment and within a thin layer of water. The plot is divided into a time dependent portion and the second half shows the concentration of species varying with distance once the system has achieved steady state conditions. The carbonate level was set at 0.1 mM.  $\text{H}_2\text{O}_2$  and  $\text{H}_2$  concentrations build rapidly and reach steady state levels at ~15 minutes. These concentrations persist 1 mm from the surface of the fuel; in contrast, the radicals have very short diffusion lengths (see Table 3.3-2). There is evidence for the formation of persistent oxalate species at extremely low concentrations.

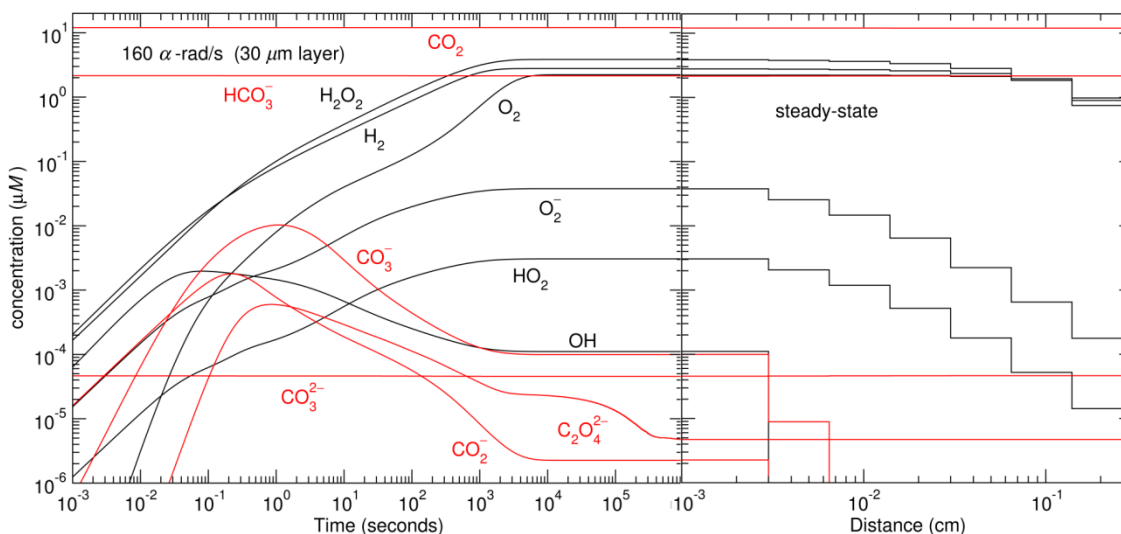


Figure 3.3-3. Calculated surface environment within 30 mm of a 160 rad/s alpha field in an anoxic environment illustrating the time dependence of dominant species

The early versions of the PNNL model were verified by using the reactions reported by Pastina and LaVerne (2001) and those of Poinssot et al. (2005) to reproduce their results, which had been done using FACSIMILE<sup>2</sup> and MAKSIMA-CHEMIST<sup>3</sup> kinetic software products. Using the complete list of equations (see Tables 3.3 3-3 and 3.3-4 for the list of reactions), the match to Pastina and LaVerne (2001) simulation was unsatisfactory; however, when reaction (1) was removed (see above), the agreement was good. This one reaction results in a large change in the radiolytic species predicted. Without validation by experiment, it is difficult to determine which processes need to be considered. Experimental work on radiolysis will be reported elsewhere.

<sup>2</sup> Developed by Richard Ball and Alan Barton, MCPA software Ltd, United Kingdom.

<sup>3</sup> Developed by Atomic Energy of Canada Ltd., Chalk River (Ontario).

The computational work will help identify future experiments that can best reduce the driving model uncertainties. The existing radiolytic model has been expanded to include heterogeneous environments consisting of solid-water layer-gas phase and chloride dominated environments that would be relevant to a generic salt repository.

Trummer and Jonsson (2010) have shown that the computational radiolysis simulations indicate that  $H_2$  affects the  $H_2O_2$  concentration during  $\alpha$ -radiolysis. The magnitude of the effect depends on the dose rate and the  $H_2$  pressure as well as on the concentration of  $HCO_3^-$ . The following reactions reduce the  $H_2O_2$  concentration in the presence of  $H_2$ .



The impact of the radiolytic  $H_2$  effect on the rate of  $\alpha$ -radiation induced dissolution of used fuel is discussed along with other ( $\alpha$ - and  $\gamma$ -) radiation induced processes capable of reducing the concentration of uranium in solution. As most anticipated EBS environments will contain  $HCO_3^-$  in mM concentrations, the radiolytically produced hydroxyl radical will be scavenged according to reaction:



In the presence of  $H_2$ , this reaction and reactions (2 and 3) will compete, and hence, the inhibiting effect of  $H_2$  is expected to decrease with increasing  $HCO_3^-$  concentration. Ekeröth et al. (2006) have shown that the presence of  $H_2$  (40 bar) in the absence of  $HCO_3^-$  reduced the total rate of  $UO_2$  oxidation by a factor of 200. In contrast, in the presence of  $H_2$  and  $HCO_3^-$ , however, the total rate of  $UO_2$  oxidation reduced by a factor of 3.5.

Along with ionization, the interaction of energetic radiation with water molecules can generate very short-lived ( $10^{-15}$  s) electronic excitations that favorably de-excite through intermediate atomic and molecular radicals. The reaction of these radicals with the surrounding aqueous environment occurs on the scale of  $10^{-9}$  s resulting in several dominant species – both stable and unstable. We take the conventional approach in representing the radiolytic generated species at the later time scale with effective  $G$ -values. The  $G$ -values account for the effective fraction of radiative energy that contributes to the formation energy of the dominate radiolytic species. Values for alpha radiolysis used in this work are given in Table 3.3-1. The products of  $G$ -values with the dose rate act as source terms to the kinetics equations for each for the species and is represented in Figure 3.3-2.

While for shorter fuel decay times the gamma dose is considerably higher for the far-field region around the fuel, the near-field dose at the fuel surface is strongly dominated by alpha dose for decay times greater than 30 years when it is approximately 160 rad/s for 50 GWd/MTU spent fuel. Consistent with alpha decay radiation, the dose rate is assumed to be nonzero only in the nearest 30  $\mu m$  to the fuel surface (Figure 3.3-1). Figure 3.3-4 shows the spatial regions modeled from near the fuel surface to the external solution boundary considered to be at 0.3 cm. Concentrations in each region are coupled through diffusive currents and are expressed in Equations 3.3-5 and 3.3-6.

Table 3.3-1. Gamma and Alpha particle *G*-values adapted from Poinssot et al., 2005).

Species	Gamma		Alpha		5 MeV Alpha <sup>4</sup>
	Water	5 M NaCl	Water	5 M NaCl	Water
H <sub>2</sub> O <sub>2</sub>	0.70	0.09	0.98	0.23	1.00
•HO <sub>2</sub>	0	0	0.22	0.05	0.10
H <sub>2</sub>	0.45	0.60	1.30	1.52	1.20
•H	0.55	0.03	0.21	0.26	0.10
e <sub>aq</sub>	2.65	3.89	0.06	0.06	0.15
•OH	2.70	0.09	0.25	0.06	0.35
OH <sup>-</sup>	0	0	0	1.01	0
H <sup>+</sup>	2.65	0.44	0.06	0	0.18
Cl <sup>-</sup>	0	-6.26	0	-1.62	0
Cl <sub>2</sub>	0	2.43	0	0	0
ClOH <sup>-</sup>	0	0.38	0	0.55	0
•HClO	0	1.02	0	1.07	0
H <sub>2</sub> O	-4.10	-1.67	-2.65	-3.25	-2.58

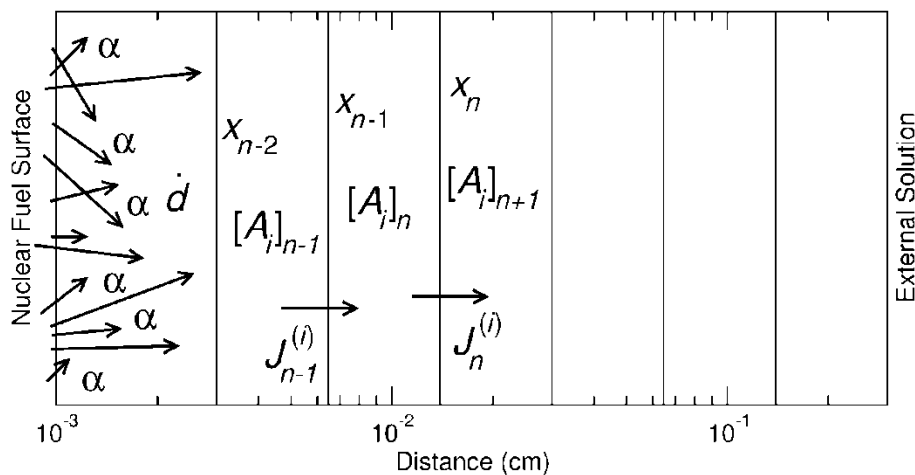


Figure 3.3-4. Radiolysis Model showing generation and diffusion across spatial regions.

The coupled kinetics rate equations for the component concentrations  $[A_i]_n$  are

$$\frac{d[A_i]_n}{dt} + \frac{J_n^{(i)} - J_{n-1}^{(i)}}{x_n - x_{n-1}} = G_i \dot{d}_n + \sum_{r=1}^{N_r} k_{ir} \prod_{j_r=1}^{n_r} [A_{j_r}]_n^{O_{j_r}} \quad (3.3-5)$$

<sup>4</sup> Values used in this model report.

with rate constants  $k_{ir}$ , dose rate  $\dot{d}_n$  and radiolytic generation constants  $G_i$ , where the diffusive currents ( $J^{(i)}$ ) and diffusion constants ( $D_i$ ) appear in the discretized Fick's Law according to

$$J_n^{(i)} = -2D_i \frac{[A_i]_{n+1} - [A_i]_n}{x_{n+1} - x_{n-1}} \tag{3.3-6}$$

for each component  $i$  in region  $n$ . Table 3.3-2 shows the values of diffusion constants used in the model.

Table 3.3-2. Diffusion Constants (Christensen and Sunder, 1996)  $D_i$ .

Species	e <sup>-</sup>	·OH	O <sub>2</sub> <sup>-</sup>	H <sub>2</sub> O <sub>2</sub>	O <sub>2</sub>	H <sub>2</sub>	Others
$D_i$ ( $10^{-5}$ cm <sup>2</sup> s <sup>-1</sup> )	4.9	2.3	1.5	1.9	2.5	6.0	1.5
Sensitivity ( $\Delta[H_2O_2]/[H_2O_2]$ )	$1 \times 10^{-7}$	$5 \times 10^{-5}$	0.0052	-25.5	$-1 \times 10^{-3}$	-0.275	----

Table 3.3 3 and Table 3.3-4 list the base values for all the reaction rate constants where the numbers in parentheses indicate the negative log<sub>10</sub> of the equilibrium constant used with appropriate rate constants to define the reverse reaction rate.

Some reactions such as 74 and 75<sup>5</sup> are present to make comparisons with results from other studies and are intentionally set to zero here for physical consistency. Fig. 3.3-5 shows the time dependence (left side) and steady state spatial dependence (right side) of the highest concentration species for a surface alpha dose of 160 rad/s. In this case the initial O<sub>2</sub> concentration was assumed to be zero to represent an oxygen depleted environment that might reflect repository conditions that are externally reducing.

The concentrations of unstable species are seen to decrease in regions away from the fuel surface where they are generated (right side of Fig. 3.3-2). The bottom row of Table 3.3-2 shows that the concentration of H<sub>2</sub>O<sub>2</sub> would be about 25 times greater without diffusion.

<sup>5</sup> The 'D' in equations 74 and 75 in Table 3.3-3 represents the loss of O<sub>2</sub> and H<sub>2</sub> from the system through diffusion (see Christensen and Sunder, 2000).

Table 3.3-3. Water Reaction Rate Constants (Poinssot et al. 2005) ( $M^n s^{-1}$ ).

	Reaction	$k_r$		Reaction	$k_r$
1	$H^+ + OH^- \rightarrow H_2O$	$1.4 \times 10^{11}$	40	$\cdot H + O_3 \rightarrow \cdot HO_3$	$3.8 \times 10^{10}$
2	$H_2O \rightarrow H^+ + OH^-$	(13.999)	41	$2 \cdot OH \rightarrow H_2O_2$	$3.6 \times 10^9$
3	$H_2O_2 \rightarrow H^+ + \cdot HO_2^-$	(11.65)	42	$\cdot OH + \cdot HO_2 \rightarrow H_2O + O_2$	$6.0 \times 10^9$
4	$H^+ + \cdot HO_2^- \rightarrow H_2O_2$	$5.0 \times 10^{10}$	43	$\cdot OH + O_2^- \rightarrow OH^- + O_2$	$8.2 \times 10^9$
5	$H_2O_2 + OH^- \rightarrow \cdot HO_2^- + H_2O$	$1.3 \times 10^{10}$	44	$\cdot OH + H_2 \rightarrow \cdot H + H_2O$	$4.3 \times 10^7$
6	$\cdot HO_2^- + H_2O \rightarrow H_2O_2 + OH^-$	(11.65)	45	$\cdot OH + H_2O_2 \rightarrow \cdot HO_2 + H_2O$	$2.7 \times 10^7$
7	$e^- + H_2O \rightarrow \cdot H + OH^-$	$1.9 \times 10^1$	46	$\cdot OH + \cdot O^- \rightarrow \cdot HO_2^-$	$2.5 \times 10^{10}$
8	$\cdot H + OH^- \rightarrow e^- + H_2O$	$2.2 \times 10^7$	47	$\cdot OH + \cdot HO_2^- \rightarrow \cdot HO_2 + OH^-$	$7.5 \times 10^9$
9	$\cdot H \rightarrow e^- + H^+$	(9.77)	48	$\cdot OH + O_3^- \rightarrow O_3 + OH^-$	$2.6 \times 10^9$
10	$e^- + H^+ \rightarrow H$	$2.3 \times 10^{10}$	49	$\cdot OH + O_3^- \rightarrow O_2^- + O_2 + H^+$	$6.0 \times 10^9$
11	$\cdot OH + OH^- \rightarrow \cdot O^- + H_2O$	$1.3 \times 10^{10}$	50	$\cdot OH + O_3 \rightarrow \cdot HO_2 + O_2$	$1.1 \times 10^8$
12	$\cdot O^- + H_2O \rightarrow \cdot OH + OH^-$	(11.9)	51	$\cdot HO_2 + O_2^- \rightarrow \cdot HO_2^- + O_2$	$8.0 \times 10^7$
13	$\cdot OH \rightarrow \cdot O^- + H^+$	(11.9)	52	$\cdot HO_2 + \cdot HO_2 \rightarrow H_2O_2 + O_2$	$7.0 \times 10^5$
14	$\cdot O^- + H^+ \rightarrow \cdot OH$	$1.0 \times 10^{11}$	53	$\cdot HO_2 + \cdot O^- \rightarrow O_2 + OH^-$	$6.0 \times 10^9$
15	$\cdot HO_2 \rightarrow O_2^- + H^+$	(4.57)	54	$\cdot HO_2 + H_2O_2 \rightarrow \cdot OH + O_2 + H_2O$	$5.0 \times 10^{-1}$
16	$O_2^- + H^+ \rightarrow \cdot HO_2$	$5.0 \times 10^{10}$	55	$\cdot HO_2 + \cdot HO_2^- \rightarrow \cdot OH + O_2 + OH^-$	$5.0 \times 10^{-1}$
17	$\cdot HO_2 + OH^- \rightarrow O_2^- + H_2O$	$5.0 \times 10^{10}$	56	$\cdot HO_2 + O_3^- \rightarrow 2O_2 + OH^-$	$6.0 \times 10^9$
18	$O_2^- + H_2O \rightarrow \cdot HO_2 + OH^-$	(4.57)	57	$\cdot HO_2 + O_3 \rightarrow \cdot HO_3 + O_2$	$5.0 \times 10^8$
19	$e^- + \cdot OH \rightarrow OH^-$	$3.0 \times 10^{10}$	58	$2O_2^- + 2H_2O \rightarrow H_2O_2 + O_2 + 2OH^-$	$1.0 \times 10^2$
20	$e^- + H_2O_2 \rightarrow \cdot OH + OH^-$	$1.1 \times 10^{10}$	59	$O_2^- + \cdot O^- + H_2O \rightarrow O_2 + 2OH^-$	$6.0 \times 10^8$
21	$e^- + O_2^- + H_2O \rightarrow \cdot HO_2^- + OH^-$	$1.3 \times 10^{10}$	60	$O_2^- + H_2O_2 \rightarrow \cdot OH + O_2 + OH^-$	$1.3 \times 10^{-1}$
22	$e^- + \cdot HO_2 \rightarrow \cdot HO_2^-$	$2.0 \times 10^{10}$	61	$O_2^- + \cdot HO_2^- \rightarrow \cdot O^- + O_2 + OH^-$	$1.3 \times 10^{-1}$
23	$e^- + O_2 \rightarrow O_2^-$	$1.9 \times 10^{10}$	62	$O_2^- + O_3^- + H_2O \rightarrow 2O_2 + 2OH^-$	$1.0 \times 10^4$
24	$2e^- + H_2O + H_2O \rightarrow H_2 + 2OH^-$	$5.5 \times 10^9$	63	$O_2^- + O_3 \rightarrow O_3^- + O_2$	$1.5 \times 10^9$
25	$e^- + \cdot H + H_2O \rightarrow H_2 + OH^-$	$2.5 \times 10^{10}$	64	$\cdot O^- + \cdot O^- + H_2O \rightarrow \cdot HO_2^- + OH^-$	$1.0 \times 10^9$
26	$e^- + \cdot HO_2^- \rightarrow \cdot O^- + OH^-$	$3.5 \times 10^9$	65	$\cdot O^- + O_2 \rightarrow O_3^-$	$3.6 \times 10^9$
27	$e^- + \cdot O^- + H_2O \rightarrow OH^- + OH^-$	$2.2 \times 10^{10}$	66	$\cdot O^- + H_2 \rightarrow \cdot H + OH^-$	$8.0 \times 10^7$
28	$e^- + O_3^- + H_2O \rightarrow O_2 + 2OH^-$	$1.6 \times 10^{10}$	67	$\cdot O^- + H_2O_2 \rightarrow O_2^- + H_2O$	$5.0 \times 10^8$
29	$e^- + O_3 \rightarrow O_3^-$	$3.6 \times 10^{10}$	68	$\cdot O^- + \cdot HO_2^- \rightarrow O_2^- + OH^-$	$4.0 \times 10^8$
30	$\cdot H + H_2O \rightarrow H_2 + \cdot OH$	$1.1 \times 10^1$	69	$\cdot O^- + O_3^- \rightarrow O_2^- + O_2^-$	$7.0 \times 10^8$
31	$\cdot H + \cdot O^- \rightarrow OH^-$	$1.0 \times 10^{10}$	70	$\cdot O^- + O_3 \rightarrow O_2^- + O_2$	$5.0 \times 10^9$
32	$\cdot H + \cdot HO_2^- \rightarrow \cdot OH + OH^-$	$9.0 \times 10^7$	71	$O_3^- \rightarrow O_2 + \cdot O^-$	$3.3 \times 10^3$
33	$\cdot H + O_3^- \rightarrow OH^- + O_2$	$1.0 \times 10^{10}$	72	$O_3^- + H^+ \rightarrow O_2 + \cdot OH$	$9.0 \times 10^{10}$
34	$2 \cdot H \rightarrow H_2$	$7.8 \times 10^9$	73	$\cdot HO_3 \rightarrow O_2 + \cdot OH$	$1.1 \times 10^5$
35	$\cdot H + \cdot OH \rightarrow H_2O$	$7.0 \times 10^9$	74	$O_2 \rightarrow O_2D$	0
36	$\cdot H + H_2O_2 \rightarrow \cdot OH + H_2O$	$9.0 \times 10^7$	75	$H_2 \rightarrow H_2D$	0
37	$\cdot H + O_2 \rightarrow \cdot HO_2$	$2.1 \times 10^{10}$	76	$H_2O_2 \rightarrow H_2O + \cdot O$	$1.0 \times 10^{-3}$
38	$\cdot H + \cdot HO_2 \rightarrow H_2O_2$	$1.8 \times 10^{10}$	77	$\cdot O + \cdot O \rightarrow O_2$	$1.0 \times 10^9$
39	$\cdot H + O_2^- \rightarrow \cdot HO_2^-$	$1.8 \times 10^{10}$			

Table 3.3-4. Carbonate Reaction rate constants (Poinssot et al. 2005) ( $M^n s^{-1}$ ).

	Reaction	$k_r$		Reaction	$k_r$
78	$H^+ + CO_3^{2-} \rightarrow HCO_3^-$	$5.0 \times 10^{10}$	96	$CO_2^- + H_2O_2 \rightarrow CO_2 + OH^- + \cdot OH$	$7.3 \times 10^5$
79	$CO_2 + H_2O \rightarrow H^+ + HCO_3^-$	$7.0 \times 10^1$	97	$CO_2^- + HCO_3^- \rightarrow HCO_2^- + \cdot CO_3^-$	$1.0 \times 10^3$
80	$H^+ + HCO_3^- \rightarrow CO_2 + H_2O$	$1.0 \times 10^{10}$	98	$C_2O_6^{2-} \rightarrow C_2O_4^{2-} + O_2$	$1.0 \times 10^0$
81	$HCO_3^- \rightarrow CO_3^{2-} + H^+$	$2.0 \times 10^0$	99	$C_2O_6^{2-} \rightarrow \cdot HO_2^- + OH^- + 2CO_2 - H_2O$	$2.0 \times 10^2$
82	$CO_2 + e^- \rightarrow CO_2^-$	$7.7 \times 10^9$	100	$\cdot CO_3^- + C_2O_4^{2-} \rightarrow C_2O_4^- + CO_3^{2-}$	$3.0 \times 10^3$
83	$HCO_3^- + \cdot OH \rightarrow \cdot CO_3^- + H_2O$	$8.5 \times 10^6$	101	$C_2O_4^{2-} + e^- \rightarrow C_2O_4^{3-}$	0
84	$CO_3^{2-} + \cdot OH \rightarrow \cdot CO_3^- + OH^-$	$3.9 \times 10^8$	102	$C_2O_4^{3-} + \cdot OH \rightarrow C_2O_4^- + OH^-$	$7.7 \times 10^6$
85	$HCO_3^- + \cdot H \rightarrow H_2 + \cdot CO_3^-$	$4.4 \times 10^4$	103	$C_2O_4^- + C_2O_4^- \rightarrow 2CO_2 + C_2O_4^{2-}$	$4.8 \times 10^8$
86	$CO_3^{2-} + e^- \rightarrow CO_2^- + 2OH^- - H_2O$	$3.9 \times 10^5$	104	$C_2O_4^- + O_2 \rightarrow O_2^- + CO_2 + CO_2$	$5. \times 10^9$
87	$\cdot CO_3^- + \cdot CO_3^- \rightarrow C_2O_6^{2-}$	$1.4 \times 10^7$	105	$C_2O_4^- \rightarrow CO_2 + CO_2^-$	0
88	$\cdot CO_3^- + \cdot CO_3^- \rightarrow CO_2 + CO_4^{2-}$	$7. \times 10^6$	106	$\cdot CO_3^- + HCO_2^- \rightarrow HCO_3^- + CO_2^-$	$1.5 \times 10^5$
89	$\cdot CO_3^- + H_2O_2 \rightarrow CO_3^{2-} + O_2^- + 2H^+$	$9.8 \times 10^5$	107	$HCO_2^- + \cdot OH \rightarrow H_2O + CO_2^-$	$3.2 \times 10^9$
90	$\cdot CO_3^- + \cdot HO_2 \rightarrow CO_3^{2-} + O_2^- + H^+$	$1.0 \times 10^7$	108	$HCO_2^- + \cdot H \rightarrow H_2 + CO_2^-$	$2.1 \times 10^8$
91	$\cdot CO_3^- + O_2^- \rightarrow CO_3^{2-} + O_2$	$4.0 \times 10^8$	109	$HCO_2^- + e^- \rightarrow H_2 + CO_2^- - H^+$	$8.0 \times 10^8$
92	$\cdot CO_3^- + CO_2 \rightarrow CO_3^{2-} + CO_2$	$3.0 \times 10^8$	110	$OH^- + HCO_3^- \rightarrow CO_3^{2-} + H_2O$	$1.0 \times 10^9$
93	$CO_2 + e^- \rightarrow HCO_2^- + OH^- - H_2O$	$1.0 \times 10^9$	111	$CO_3^{2-} + H_2O \rightarrow OH^- + HCO_3^-$	$3.6 \times 10^3$
94	$CO_2 + CO_2^- \rightarrow C_2O_4^{2-}$	$6.5 \times 10^8$	112	$\cdot CO_3^- + \cdot CO_3^- \rightarrow CO_4^{2-} + CO_2$	$7.0 \times 10^6$
95	$CO_2 + O_2 \rightarrow CO_2 + O_2^-$	$2.0 \times 10^9$	113	$H_2O + CO_4^{2-} \rightarrow \cdot HO_2^- + CO_2 + OH^-$	$2.0 \times 10^{-1}$

### 3.3.2 Verification, Validation, and Sensitivity Analyses

Radiolytic models do not have a wide acceptance for heterogeneous systems due to limited availability of kinetic data, the difficulty in handling interfaces, and a lack of experimental validation. It is important to note that there were no examples in the literature of radiolytic modeling simulations with alpha irradiation that would have provided a basis for comparison; hence, the current PNNL model was verified against other radiolysis models by using gamma irradiation simulations. To build confidence in the use of the PNNL computational radiolysis model, it was also necessary to compare consistency between existing kinetic models. Poinssott et al. (2005) compared the results from “CHEMSIMUL” and “MAKSIMA-CHEMIST”. In the worst case, the differences were  $< 1\%$  and these were because of the different integration methods used for resolving the differential equations, numerical precision used in each code, the number of significant figures used in the G-values and kinetics constants. Fig. 3.3-5 shows an examples of results for comparison with Pastina and LaVerne (2001; Fig. 1) where it was possible to duplicate their result with the PNNL code.

During development the radiolysis model has been tested for its internal consistency and for predictions that are verifiable with available models in the literature (Christian and Sunder, 2000, Ershov and Gordeev, 2008). The PNNL model is organized for internal checking of atom and charge balance. Both total atoms and charge were shown to balance within relative solution accuracy of  $\sim 10^{-10}$ . The basic model solver is a routine from ODEPACK (Hindmarsh, 1983; Petzold, 1983) for solving stiff and non-stiff ordinary differential equations. Solution run-times for concentration histories out to  $10^8$  seconds normally run in under one minute on a single processor desktop computer.

The methodology of coding the reaction equations was verified by comparing model results to published results of other models for specific cases. Three cases are reported here and in all instances, the ionizing radiation was gamma as there are no literature model predictions using alpha irradiation.

Figure 3.3-6 shows the concentration history results as a function of time for the conditions reported in Christensen and Sunder (2000; Figs. 9a and 9b). The  $\text{UO}_2$  dissolution rates reported by Christensen and Sunder (2000) were shown to be the same as those from the PNNL model using the same input parameters verifying consistency between the computational approaches.

Figure 3.3-7 shows the model results for the steady-state concentration as a function of the square-root of dose for the conditions reported by Ershov and Gordeev (2008; Fig. 5). In each of the three cases the model results reported here are nearly indistinguishable from the results reported in the figures of each of the three references. Note that there is a predicted square root dose dependence for  $\text{H}_2\text{O}_2$  under gamma irradiation; whereas, we have shown that there is a linear dependence with dose under alpha irradiation. However, there are currently no alpha irradiation studies to validate the PNNL model approach.

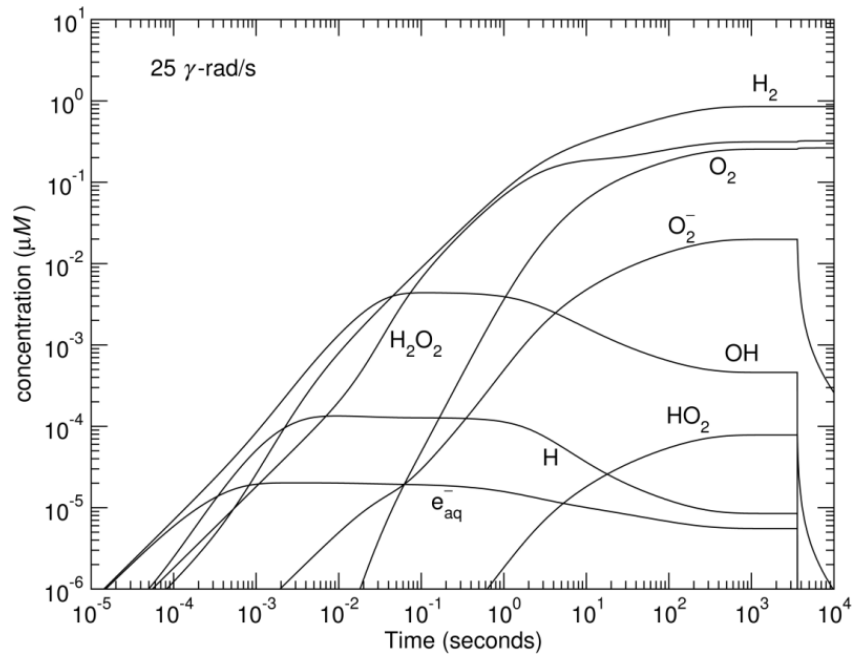


Fig. 3.3-5. Shows the concentration history results for the same conditions (1 hr, 25 rad/s irradiation) as Fig. 1 from Pastina and LaVerne (2001).

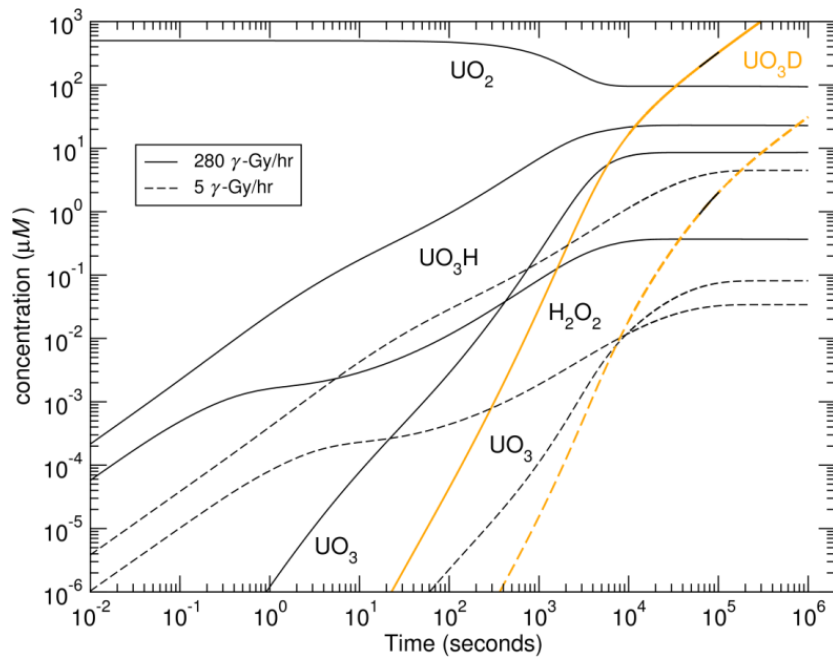


Figure 3.3-6. Radiolysis model result with inputs from Christensen and Sunder (2000).

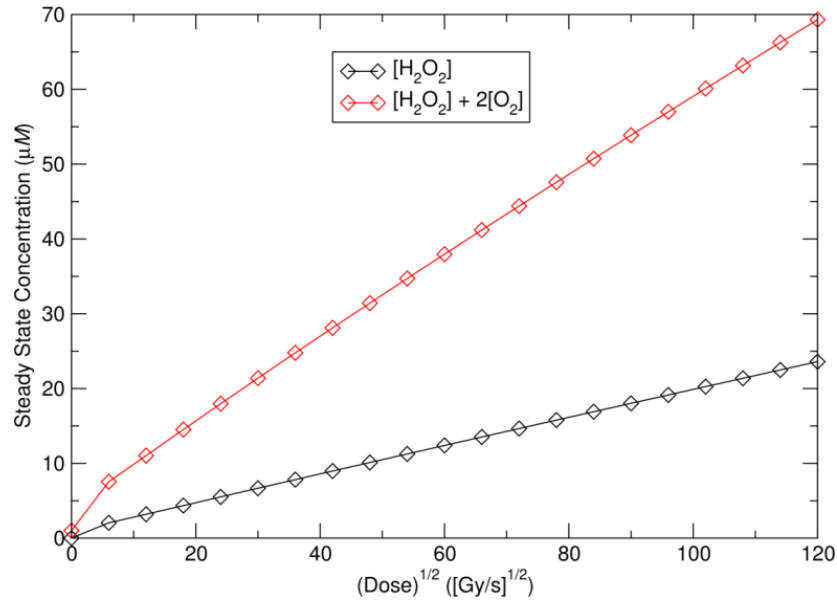


Figure 3.3-7. Radiolysis model result for gamma irradiation with inputs from Ershov and Gordeev (2008).

### 3.3.3 Uncertainty and Conditional Applicability

Identification of the most sensitive parameters for steady state  $\text{H}_2\text{O}_2$  concentration were determined as the relative change  $\Delta[\text{H}_2\text{O}_2]/[\text{H}_2\text{O}_2]$  for each parameter – the relative difference between model result with nonzero and zero value for a parameter. As already mentioned, the bottom row of Table 3.3-2 shows the sensitivity of  $[\text{H}_2\text{O}_2]$  to the diffusion constants. Figure 3.3-8 is the sensitivity result of three oxidizing species for each  $G$ -value. Of course  $[\text{H}_2\text{O}_2]$  is most sensitive to its own  $G$ -value – the  $\text{O}_2$  concentration is also sensitive to the  $\text{H}_2\text{O}_2$   $G$ -value because  $\text{H}_2\text{O}_2$  decomposition is a source for  $\text{O}_2$ . Also, because the  $\bullet\text{OH}$  radical and  $\text{OH}^-$  ion can react with  $\text{H}_2\text{O}_2$ , their  $G$ -values result in a negative change for  $[\text{H}_2\text{O}_2]$ . This is consistent with the small positive change for the  $\bullet\text{OH}$  diffusion constant (Table 3.3-2), that is,  $\text{H}_2\text{O}_2$  is increased slightly because  $\bullet\text{OH}$  diffuses away from the production region.

In order to evaluate the relative importance of all equations shown in



Table 3.3-3 on the steady state concentration of  $H_2O_2$ , each reaction was switched off independently and allowed to run until steady state conditions were reached. The resulting plot is shown in Figure 3.3-9 and shows the absolute value of the relative change in  $[H_2O_2]$  with the top reactions shown as red/black for  $\pm$  values. Removal of all reactions below the horizontal red line, which represents relative changes of less than  $1$  in  $10^5$  for the  $H_2O_2$ , and results in no perceptible changes to concentrations in Figure 3.3-4 other than oxalate  $[(C_2O_4)^{2-}]$ .

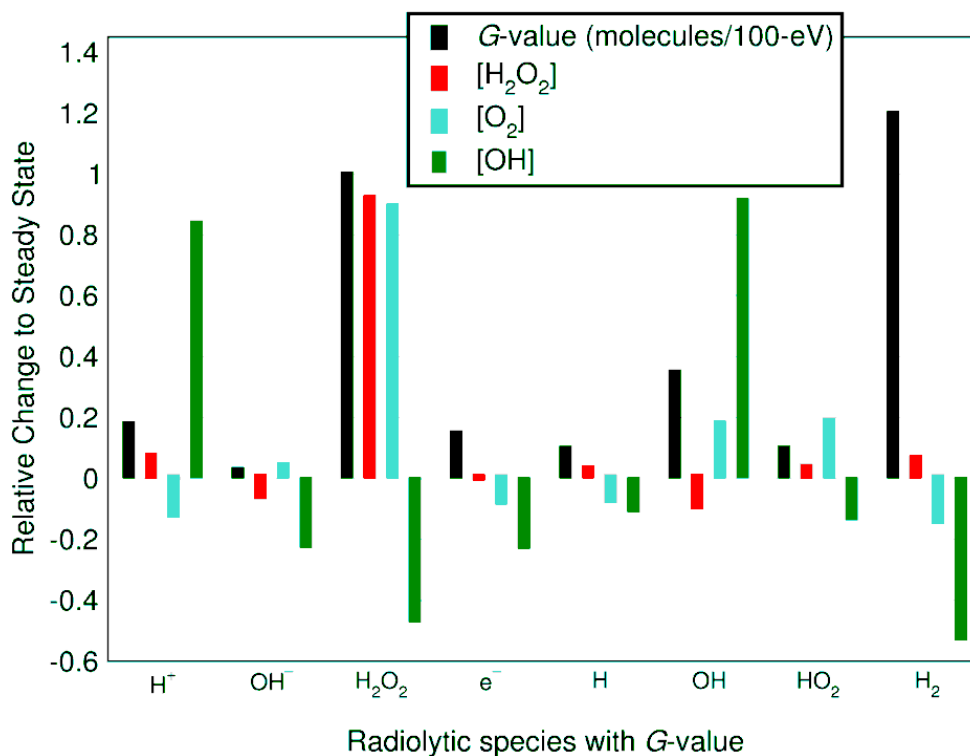


Figure 3.3-8. G-value sensitivity as  $\Delta[A]/[A]$  for  $H_2O_2$ ,  $H_2O_2$ , and  $\bullet OH$ .

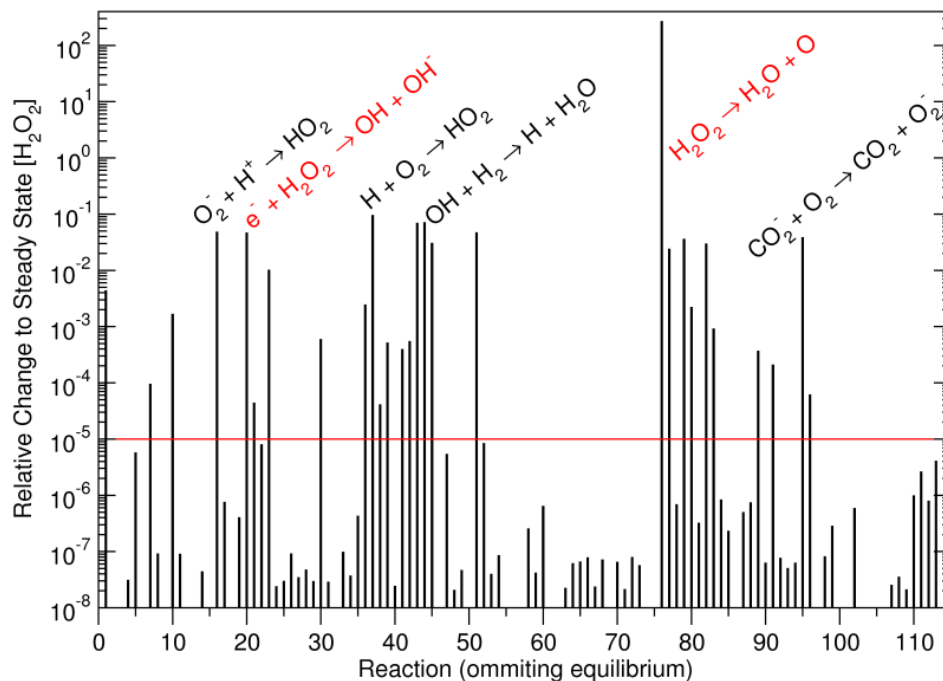


Figure 3.3-9. Rate constant sensitivity as absolute value of  $\Delta[\text{H}_2\text{O}_2]/[\text{H}_2\text{O}_2]$ .

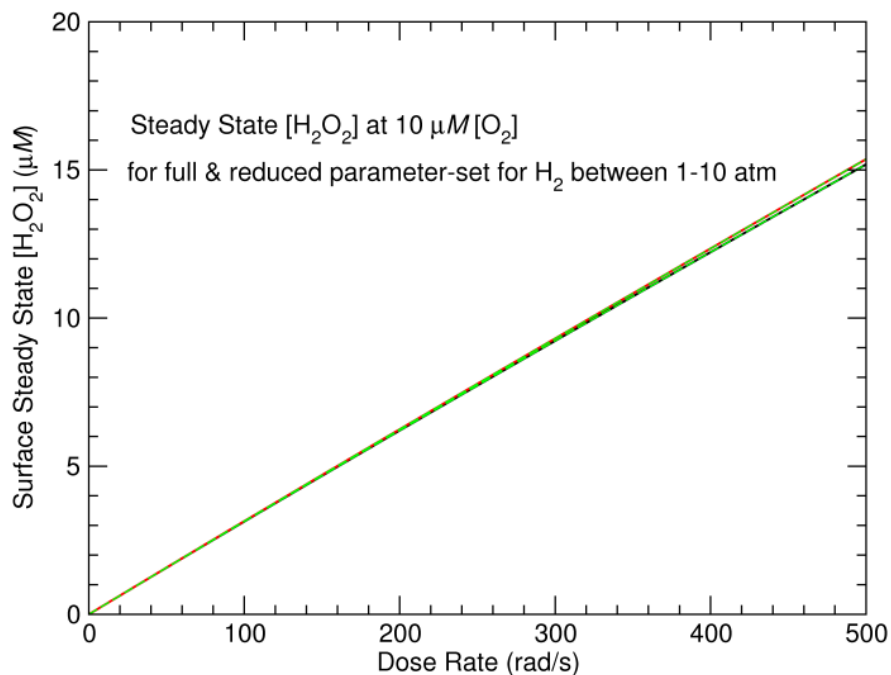


Figure 3.3-10.  $\text{H}_2\text{O}_2$  concentration as a function of dose for fixed  $\text{O}_2$  concentration and range of  $\text{H}_2$  concentrations.

An important result for input into other corrosion models is the total concentration of  $\text{H}_2\text{O}_2$  with dose. In Fig. 3.3-10 the linear relationship between dose and the steady-state  $\text{H}_2\text{O}_2$  oxidant

concentration is shown. This relationship holds for a range of H<sub>2</sub> concentrations. There was only a slight difference beginning to show between the full and reduced parameter set at very high doses.

During the investigation of the steady state concentration of H<sub>2</sub>O<sub>2</sub> under anoxic conditions with changing radiation dose, it was observed that there was a sudden change in the H<sub>2</sub>O<sub>2</sub> concentration at a critical dose value. The actual position of this jump varied depending on the initial conditions. The specific initial conditions require zero O<sub>2</sub> concentration. Figure 3.3-11 (right) is a case with H<sub>2</sub> concentration fixed at 7.8×10<sup>-4</sup> M (0.1 atm) where the jump occur between 141 and 142 rad/s. It was determined that at least two steady-state solutions to the kinetic equations exist for dose rates greater than 142 rad/s. This can be seen in Figure 3.3-11 (left panel), where the dashed (pink) and solid (pink) lines are steady state solutions for the same conditions (water system 0.1 atm H<sub>2</sub>) with the only difference being a non-zero oxygen concentration for the dashed line result. This is an example where the model loses its ability to uniquely predict the [H<sub>2</sub>O<sub>2</sub>]; hence, we consider the condition of exactly zero [O<sub>2</sub>] to be outside the applicability of the current PNNL model.

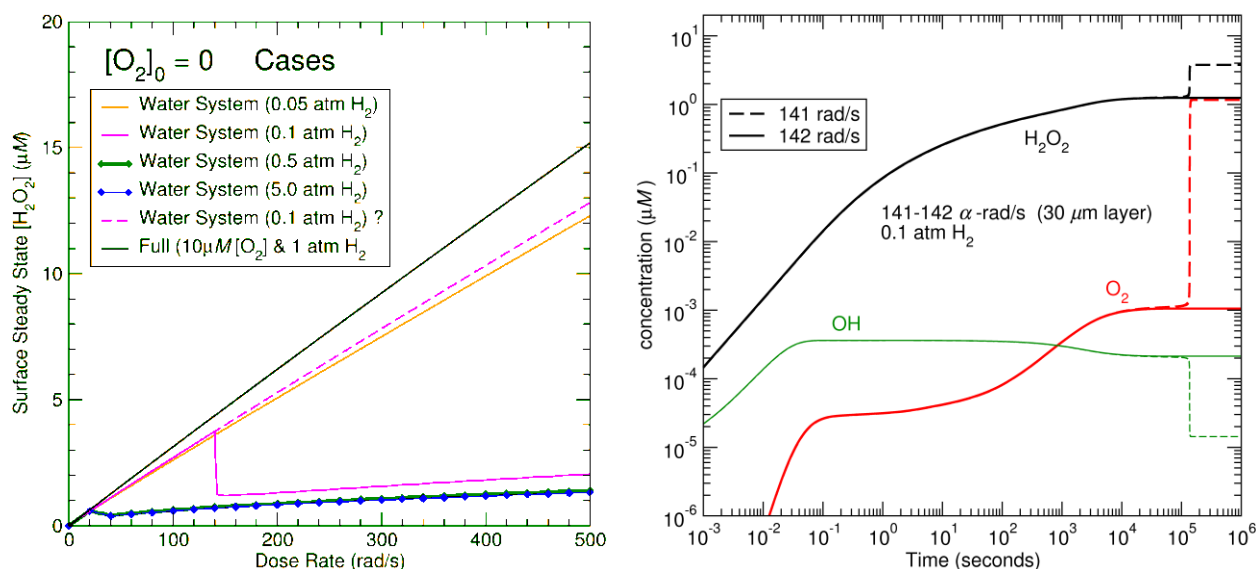


Figure 3.3-11. H<sub>2</sub>O<sub>2</sub> concentration as a function of dose rate for cases of zero initial O<sub>2</sub> concentration

Both the full and reduced set of reactions exhibited these non-unique steady state solutions at critical values of dose rate for initially very low concentrations of [O<sub>2</sub>] and [H<sub>2</sub>]. The reasons for this effect need to be examined in greater depth and should be validated through experiment.

### 3.3.3.1 Hydrogen

An important environmental constraint in the used fuel dissolution model is the potential stabilizing effect of H<sub>2</sub>, mainly from canister corrosion and, to a lesser extent, from radiolysis. Consideration of H<sub>2</sub> formation in the water just from radiolysis may not to be sufficient to describe the experimentally observed H<sub>2</sub> effect (Carbol et al., 2005). Experiments by Pastina and LaVerne (2001) that examined the generation of H<sub>2</sub> and H<sub>2</sub>O<sub>2</sub> under irradiation indicated that

there remain significant uncertainties regarding the basic reactions. The European models all show a strong decrease in reaction rates with increasing  $H_2$  concentration. The reasons for this rate reduction in relation to  $H_2$  pressure is an active area of research. The potential catalytic role of metallic epsilon particles was considered by Ershov and Gordeev (2008) resulting in faster consumption of  $H_2$ .

In addition to radiolysis, hydrogen can be generated by anoxic corrosion of various metal components of the waste and packaging (primarily iron based materials) (Carbol et al. 2005). Anoxic conditions can only be expected under inundated conditions, where brine has somehow accumulated and completely surrounds the waste. Estimates of the rates of hydrogen production under anoxic and fully brine inundated conditions may be made, however these rates are quite uncertain. After initial closure of a panel, oxygen-rich conditions will prevail, and the iron will oxidize (rust) with no hydrogen generation possible until all of the oxygen has been consumed. The oxidation rate is highly dependent on humidity as well, and is expected to decrease in low relative humidity environments. The accumulation of hydrogen may be mitigated by its ease of diffusion through even highly impermeable materials.

### **3.3.3.2 The Role of Bicarbonate and Oxalate Formation**

Carbonate is known to strongly enhance dissolution of oxidized spent fuel. The radiolysis model included the effect of  $HCO_3^-$  on the radiolytic reaction scheme. The heterogeneous model considers fuel oxidation and dissolution separately; whereas, the European models do not include these effects. The observation of oxalate formation at trace levels indicates that the presence of  $CO_2$  could result in the formation of complexing agents that could increase the solubility of some radionuclides.

### **3.3.3.3 Secondary Uranium phases**

The deposition of secondary phases at the  $UO_2$  surface may strongly limit the quantity of water which is accessible at the fuel surface for radiolytic processes. Diffusion of radiolytic species to the non-oxidized fuel is probably strongly limited. The model did not account explicitly for this effect, but it might be possible to include by considering diffusion parallel to the fuel surface and in the presence of lower quantities of water. Experimental data from Carbol et al. (2009) suggests that the corrosion potential is sufficiently low that no formation of U(VI) solid phases will occur. Under these conditions solid state oxidation products such as  $UO_{2+x}$  and  $U_3O_7$  may still form. However, the reaction of  $UO_2$  to form  $U_3O_7$  is not a dissolution/precipitation process but better described as a solid state transformation which would create some kind of boundary layer. This boundary would not impact alpha radiolysis as there would be no significant compositional change during the transformation.

### **3.3.3.4 Brine**

The early radiolysis processes in concentrated NaCl brine are different from those in diluted aqueous solutions. Whereas  $Na^+$  is under radiation chemically inert, the  $Cl^-$  reacts very efficiently with oxidizing radicals. Because of the high  $Cl^-$  concentration such reactions take place already in the tracks and spurs. In this way with less radical recombination in the tracks and spurs- the total yield of species diffusing out of the tracks and spurs increases. Furthermore, there is a change in the species spectrum reaching a homogeneous distribution and becoming available for other reactants. In contrast to dilute solutions, there is a direct radiation effect on the solute in concentrated chloride brine. From the number of electrons attached to the  $Cl^-$  ions

compared to all electrons present in the solvent and the solute a portion of 15% for the direct effect on  $\text{Cl}^-$  can be estimated for 5 M NaCl solution.

### 3.3.4 Conclusions and Recommendations

Based on the work done for the PNNL Radiolysis model, the following conclusions have been drawn:

- The  $\text{H}_2\text{O}_2$  G-value of course has the greatest effect on the steady state  $[\text{H}_2\text{O}_2]$  (with small negative effect from the  $\bullet\text{OH}$  radical).
- Only 45-46 reactions of the water-carbonate system are important (out of  $\approx 120$ ) for determining  $[\text{H}_2\text{O}_2]$ .
- Determining  $[\text{H}_2\text{O}_2]$  to within 0.1% is possible with 22 reactions of the water-carbonate system
- Concentration of  $\text{H}_2$  has very small effect on  $[\text{H}_2\text{O}_2]$  as a function of dose rate (with  $\text{O}_2$  present) and the effect is linear.
- For extremely low  $[\text{O}_2]$  nonlinear effects were observed in both water only and water-carbonate systems (even for the reduced parameter set).

Future investigation will examine direct coupling of the PNNL Radiolysis Model with the ANL Mixed Potential Model to evaluate the explicit sensitivity on  $\text{UO}_2$  stability in various disposal environments.

Assuming that steady state  $\text{H}_2\text{O}_2$  is the dominant oxidant for spent nuclear fuel in an  $\text{O}_2$  depleted water environment, the most sensitive parameters have been identified with respect to predictions of a radiolysis model under typical conditions. As compared with the full model with about 100 reactions it was found that only 30-40 of the reactions (above red line of Figure 3.3-9) are required to determine  $[\text{H}_2\text{O}_2]$  to one part in  $10^{-5}$  and to preserve most of the predictions for major species. This allows a systematic approach for model simplification and offers guidance in designing experiments for validation. For instance, an experiment that accurately measures  $\text{H}_2\text{O}_2$  decomposition could have a significant effect on improving model accuracy. The approach described here will be applied to the prediction of the fuel behavior of the combined models to assess how the corrosion processes may affect the sensitivities to radiolysis model parameters.

In an anoxic water-dominated geologic repository  $\text{H}_2\text{O}_2$  will be the most important oxidizing species that is produced from the radiolysis of water in contact with used nuclear fuel. In a brine system, other oxidants may be more important. Understanding the mechanisms involved in the production of oxidants is important both from a fundamental science perspective and for performance assessment calculations for long-term storage. Recently, Roth and Laverne (2011) have shown larger effects on  $G(\text{H}_2\text{O}_2)$  have been observed in the presence of nanoparticles of various metal oxides, similar to earlier studies on the role of heterogeneous interfaces in radiolytic environments. These types of effects may be more difficult to model and will require experiments to obtain fundamental data for the more advanced models.

Although the PNNL radiolysis model is being used to describe potential radiolytic processes that may occur in the unlikely case of groundwater directly contacting a failed nuclear fuel storage package at some distant time in the future, the model is highly adaptable to other scenarios. Under fuel storage conditions, doses will be dominated by gamma fields rather than alpha fields, the temperature will be considerably higher than for a disposal environment, the physical

environments will be different, as well as the gas composition. However, as long as the appropriate rate constants are available for the relevant processes, this model could be easily applied to fuel storage environments.

### 3.3.5 References for Section 3.3

- Burns, P. C., Ewing, R. C., Navrotsky, A., 2012, Nuclear fuel in a reactor accident, *Science*, 335, p. 1184-1188.
- Carbol, P., Fors, P., Van Winckel, S., Spahiu, K., 2009, Corrosion of irradiated MOX fuel in presence of dissolved H<sub>2</sub>, *Journal of Nuclear Materials*, 392, p. 45-54
- Cera, E., Bruno, J., Duro, L., 2007, Experimental determination and chemical modeling of radiolytic processes at the spent fuel /water interface, Svensk Karnbranslehantering AB Report, TR-06-07, Stockholm, Sweden.
- Christensen, H., Sunder. S., 2000, Current state of knowledge of water radiolysis effects on spent nuclear fuel corrosion, *Nuclear Technology*, 131, p. 102-123.
- Christensen, H., Sunder. S., 1996, An evaluation of water layer thickness effective in oxidation of UO<sub>2</sub> fuel due to radiolysis of water, *Journal of Nuclear Materials*, 298, p. 70-77.
- Cui, D., Rondinella, V. V., Fortner, J. A., Kropf, A. J., Eriksson, L., Wronkiewicz, D. J., Spahiu, K., 2012, Characterization of alloy particles extracted from spent nuclear fuel, *Journal of Nuclear Materials*, 420, p. 328-333.
- Ekeroth, E., Roth, O., Jonsson, M., 2006, The relative impact of radiolysis products in radiation induced oxidative dissolution of UO<sub>2</sub>, *Journal of Nuclear Materials*, 355, p. 38-46
- Ershov, B. G., Gordeev, A.V., 2008, A model for radiolysis of water and aqueous solutions of H<sub>2</sub>, H<sub>2</sub>O<sub>2</sub> and O<sub>2</sub>, *Radiation Physics and Chemistry*, 77, p. 928-935.
- Hughes-Kubatko, K-A., Helean, K. B., Navrotsky, A., Burns, P.C.. 2003, Stability of peroxide-containing uranyl minerals, *Science*, 302, p. 1191-1193.
- Jégou , C., Muzeau, B., Broudic, V., Peugeot, S., Poulesquen, A., Roudil, D., Corbel, C., 2005, Effect of external gamma irradiation on dissolution of the spent UO<sub>2</sub> fuel matrix, *Journal of Nuclear Materials*, 341, p. 62-82.
- Hindmarsh, A. C., 1983, ODEPACK, A Systematized Collection of ODE Solvers, in *Scientific Computing*, R. S. Stepleman et al. (Eds.), North-Holland, Amsterdam, p. 55-64.
- King, F., M. Kolar, Shoesmith, D. W., 1999, Modeling the oxidative dissolution of UO<sub>2</sub>. *Materials Research Society Symposium Proceedings*, 556, p. 463-470.
- Pastina, B., LaVerne, J. A., 2001, Effect of molecular hydrogen on hydrogen peroxide in water radiolysis, *Journal of Physics and Chemistry*, B105, p. 9316-9322.
- Petzold, L. R., 1983, Automatic Selection of methods for solving stiff and nonstiff systems of ordinary Differential Equations, *Journal on Scientific and Statistical Computing*, 4, p. 136-148.
- Poinsot, C., Ferry, C., Kelm, M., Grambow, B., Martinez, A., Johnson, L., Andriambolona, Z., Bruno, J., Cachior, C., Cavedon, J. M., Christensen, H., Corbel, C., Jegou, C., Lemmens, K., Loida, A., Lovera, P., Miserque, F., de Pablo, J., Poulesquen, A., Quinones, J., Rondinella, V., Spahiu, K., Wegen, D. H., 2005, Spent Fuel Stability under Repository Conditions – Final Report of the European Project, European Commission.

- Radulescu, G., 2011, Radiation Transport Evaluations for Repository Science, ORNL/LTR-2011/294, Oak Ridge National Laboratory, August, 2011.
- Roth, O. and Laverne, J. A., 2011, Effect of pH on H<sub>2</sub>O<sub>2</sub> production in the radiolysis of water, *Journal of Physics and Chemistry*, A115, p. 700-708.
- Shoesmith, D. W., Kolar, M., King, F., 2003, A mixed-potential model to predict fuel (uranium dioxide) corrosion within a failed nuclear waste container, *Corrosion*, 59, p. 802-816.
- Stroes-Gascoyne, S., Garisto, F., Betteridge, J.S., 2005, The effects of alpha-radiolysis on UO<sub>2</sub> dissolution determined from batch experiments with <sup>238</sup>Pu-doped UO<sub>2</sub>, *Journal of Nuclear Materials*, 346, p. 5-15.
- Sunder, S., Shoesmith, D.W., Miller, N.H., 1997, Oxidation and dissolution of nuclear fuel (UO<sub>2</sub>) by the products of the alpha radiolysis of water, *Journal of Nuclear Materials*, 244, p. 66-74.
- Sunder, S., 1998, Calculation of radiation dose rates in a water layer in contact with used CANDU UO<sub>2</sub> fuel, *Nuclear Technology*, 122, p. 211-221.
- Trummer, M., Jonsson, M., 2010, Resolving the H<sub>2</sub> effect on radiation induced dissolution of UO<sub>2</sub>-based spent nuclear fuel, *Journal of Nuclear Materials*, 396, p. 163-169.



### 3.4 Electrochemical Model for Used Fuel Matrix Degradation Rate

This work is being performed at ANL as part of the DOE NE Used Fuel Disposition (UFD) Campaign's Engineered Barrier Systems (EBS) Evaluations, work package: FT-12AN080601. The overall objective of this work was to implement a predictive model for the degradation of used uranium oxide fuel that is based on fundamental electrochemical and thermodynamic principles. This objective was achieved by implementing the Canadian-mixed potential model for  $\text{UO}_2$  fuel dissolution (King and Kolar, 1999, King and Kolar, 2003, Shoesmith et.al., 2003) using MATLAB scripts. The initial version of the MATLAB implementation of mixed potential model, referred to as the ANL-MPM, extends the Canadian version to include hydrogen oxidation at the used fuel surface with provisions to include reactions catalyzed by noble metal particles present at the fuel surface. The specific objectives for this project that have been achieved this year (FY-2012) and are discussed in this Section are as follows:

- Implemented, using our own scripts/code, an established and well documented used fuel degradation model (Canadian-mixed potential model) that is based on mixed potential theory.
- Verified our scripting and coding by reproducing published results from the Canadian model.
- Performed sensitivity analyses to determine which model parameters and input variables have the strongest impact on the calculated used fuel degradation rate.
- Completed a critical review of the sources of all model parameters and input variables to determine which values need further investigation through literature review or experimental studies. This review also identified which variables must be provided by other process models.
- Extended the base-case model to quantify the role of dissolved hydrogen in protecting used fuel from oxidative dissolution by lowering the electrochemical potential at the fuel surface.
- Developed a plan to extend the base-case model to account for the catalytic effects of fission product alloy phase (noble metal particles on reactions affecting  $\text{UO}_2$  dissolution, such as the kinetic balance of  $\text{H}_2$  oxidation and  $\text{H}_2\text{O}_2$  reduction).

It is anticipated that this process model will provide the fractional degradation rate of used fuel and radionuclide source terms as direct input to the generic system performance model which is currently being implemented (e.g., Geoff Freeze, 2012, Advanced Implementation of the Generic Performance Assessment Model, presentation at Used Fuel Disposition Working Group Meeting, May 16, 2012, Las Vegas, NV).

#### 3.4.1 Introduction and Background

It is anticipated that this process model will provide the fractional degradation rate of used fuel and radionuclide source terms as direct input to the generic system performance model which is currently being implemented (e.g., Geoff Freeze, 2012, Advanced Implementation of the Generic Performance Assessment Model, presentation at Used Fuel Disposition Working Group Meeting, May 16, 2012, Las Vegas, NV).

The approach is to tailor the Mixed Potential Model (MPM) that was developed as part of the Canadian repository program (Canadian-MPM) for application to US disposal systems and to extend the model to account for key dissolution rate determining processes not included in the original Canadian model. Key processes that are being incorporated into the ANL mixed potential model (ANL-MPM) are the role of hydrogen oxidation at the used fuel interface and the catalysis of oxidation/reduction reactions (hydrogen oxidation, hydrogen peroxide, oxygen reduction) by noble metal particles on the fuel surface (epsilon phases).

Sensitivity studies with the ANL extension of the Canadian model (ANL-MPM) are used to identify key model parameters for which values relevant to US disposal systems must be determined from literature data, measured experimentally, or calculated with submodels, such as the concentrations of radiolytic products. As part of the work at ANL experimental methods have been developed to measure electrochemical and reaction kinetic parameters to support modeling investigations (Jerden et al., 2012).

#### **3.4.1.1 Used Fuel Microstructure and Radionuclide Distribution**

The chemical state and distribution of fission product elements in irradiated used fuels have been studied using thermodynamic equilibrium calculations and experimental measurements (Dehaut 2001). In fuels at synthesis, the oxygen potential is less than approximately  $-400$  kJ/mol (Dehaut 2001). Under these very low oxygen potential conditions the uranium in the used fuel matrix is present mostly in the U(IV) oxidation state. Likewise, the other radionuclides in the fuel matrix are in low or zero valent states (Kleykamp 1985). Noble transition metal fission products in metallic (zero valent) form accumulate in grain boundaries and fractures as they exsolve from the fuel matrix grains during burnup (Kleykamp 1985). The fact that the fuel matrix elements and radionuclides are present in the fuel in lower valence (and less soluble) states is important because degradation and mobilization will be a slow process unless both the fuel matrix and the associated radionuclides become oxidized under the disposal conditions. *The electrochemical model that was implemented as part of the present study (ANL-MPM) accounts for the rate of oxidative dissolution of the used fuel matrix and thus can be used to predict an overall radionuclide release rate.*

Most fission product and neutron capture elements are retained within the fluorite lattice structure of the fuel matrix. However, because some of the fission product elements are not soluble in the  $\text{UO}_2$  matrix, a fraction of the inventory of these elements migrates out of the fuel grains under normal reactor operating conditions (Pelletier 2001). The extent of migration of these fission products out of the fuel grains and the subsequent accumulation at the grain boundaries and in gap regions of the fuel depend on the diffusion coefficients of the individual fission product elements in the used fuel matrix and the available mechanisms for migration. The distribution of radionuclides in a used fuel rod thus strongly depends on the thermal history and burnup conditions of the fuel.

Like the fission gasses, some of the fission product cesium and iodine diffuses out of the fuel grains and is found at the grain boundaries and in the gap region between the fuel pellets and the cladding (Dehaut 2001). After irradiation, part of the fission product molybdenum, ruthenium, technetium, rhodium, and palladium inventory is found in the form of metallic alloy particles located within the fuel grains and at grain boundaries. In this report these fission product alloy phases are referred to as the Noble Metal bearing Particles (NMP). This accumulation of noble metals in alloy particles is more evident in the higher-powered regions of the fuel, such as the

pellet rim regions (Barner 1985; Guenther et al. 1988). The extent to which the metallic fission products as well as cesium and iodine migrate depends on the fuel burnup, operating temperatures, and temperature gradients, as determined by the fuel's linear power history in the reactor (Guenther et al. 1988). Fig. 3.4-1 shows the key microstructural regions of  $UO_2$  used fuel that influence degradation and radionuclide release.

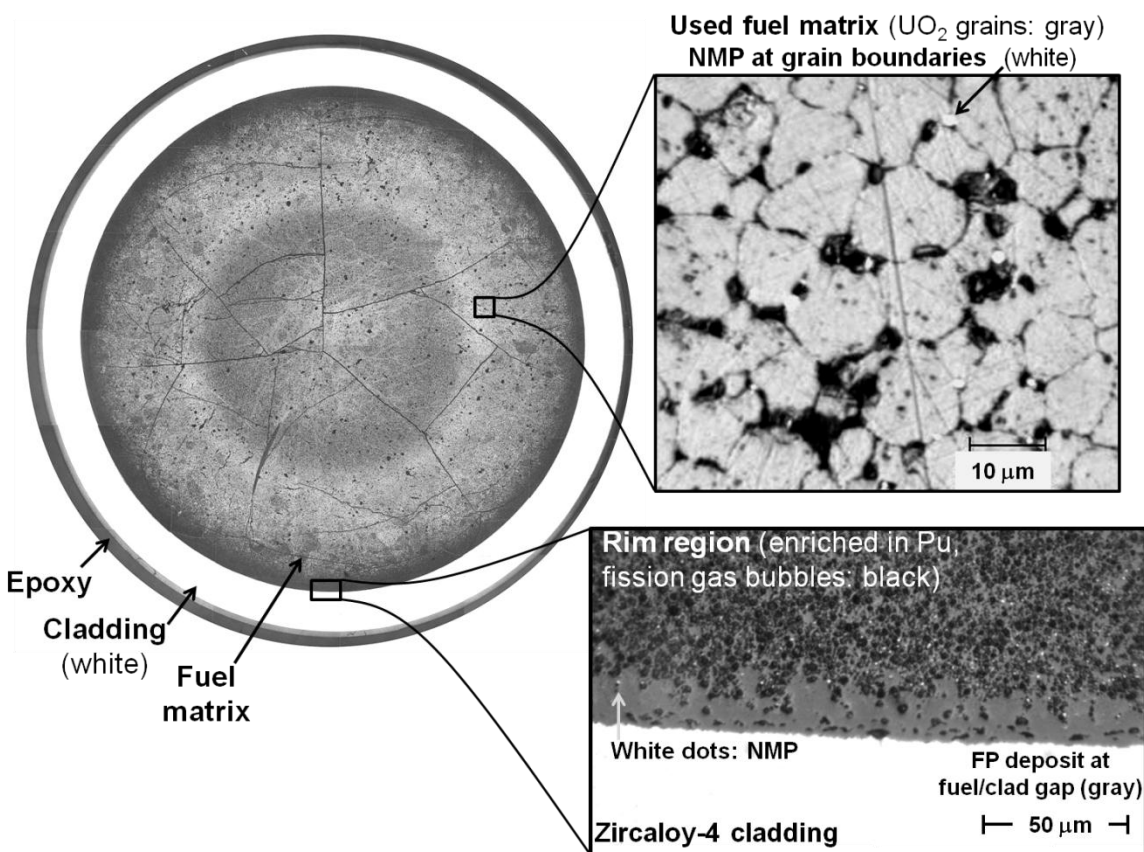


Figure 3.4-1. Optical micrographs of a polished used fuel cross-section showing the distinct microstructural regions that influence degradation and radionuclide release (after Tsai 2003). This sample was cut from an H. B. Robinson PWR Rod with a burnup of 67 GWd/MTU.

### 3.4.1.2 Fuel Matrix Degradation Process

On the basis of the above discussion, the radionuclide inventory can be subdivided into four fractions:

- The gap inventory
- The grain boundary inventory
- The matrix inventory
- The noble metal particle inventory

Radionuclides in the gap inventory are immediately made available for transport once a waste package and fuel rod cladding have been breached (e.g., Shoesmith, 2000). Degradation of the fuel matrix is the first step leading to mobilization of the matrix, grain boundary, and noble metal particle inventory fractions. The principal degradation process when used fuel is contacted by an in-package solution is either oxidative or chemical dissolution. The rate of dissolution of multivalent elements such as uranium and plutonium (of which the used fuel matrix is composed) depends on their oxidation state and hence the electrochemical potential at the dissolving surface. Oxidative dissolution of the fuel leads to rapid degradation and radionuclide release relative to chemical dissolution. This is due to the observation that key radionuclides (e.g., U, Pu, Np, Tc) contained within matrix and grain boundary phases are more soluble higher oxidation states (e.g., Shoesmith, 2000). Chemical dissolution of used fuel can be orders of magnitude slower than oxidative dissolution because the rate is determined by the solubility of  $\text{UO}_2$  and  $\text{PuO}_2$  (which are refractory ceramics) and diffusion of dissolved uranium and plutonium away from the surface (a process slowed by low dissolved concentrations). The dominant degradation mode of used fuel, chemical vs. oxidative dissolution, is determined by the electrochemical potential at the used fuel/solution interface. This potential is determined by the state of the exposed used fuel and the chemistry of the in-package solution. The degradation rate model implemented as part of the present study accounts for both chemical and oxidative dissolution. The key processes involved in chemical and oxidative dissolution of used fuel are summarized in Fig. 3.4-2.

Under sufficiently low electrochemical potential conditions, the fuel matrix will not be oxidized upon solution contact and the fuel dissolution rate and radionuclide solubilities are low. Under more oxidizing electrochemical conditions, the fuel surface can be oxidized to higher oxidation states that are more soluble and dissolve faster. For a given set of physical and chemical conditions one can define an electrochemical threshold, defined by the potential at the used fuel surface, above which oxidative dissolution processes dominate (Fig. 3.4-2).

Because the uranium and plutonium atoms in the uranium oxide (UOX) and mixed oxide (MOX) fuels are initially in the (IV) valence state, the electrochemical steps in the used fuel degradation mechanism involve atoms (ions) in the fuel matrix giving up electrons and dissolving into the solution, with the electrons migrating to locations where they are consumed by oxidizing agents. These oxidizing agents are species that are reduced to “complete the circuit” and maintain electrical neutrality in the system.



The reactants and reaction products have to be transported to and from the locations where the oxidation/reduction reactions can occur and, depending on the local micro-chemical environment at the surface of the corroding metal, the oxidized species and the reduced oxidizing agents may both undergo hydrolysis, participate in complexation and precipitation/co-precipitation reactions, and/or dissolve into the bulk solution. The electrochemical model implemented as part of this work accounts for these processes.

Although the radiolysis of groundwater will produce oxidizing agents near the fuel surface that may drive oxidative dissolution even in relatively reducing repository settings, recent results indicate that hydrogen produced by corrosion of the waste package materials (and radiolysis) may be very effective in scavenging the radiolytic oxidizing agents and thereby inhibiting or preventing the oxidation of the fuel (Shoesmith 2007; Poinssot et al. 2004; Nagra 2005). The limited understanding of this process has limited the credit that is being taken for this effect in current calculations of the performance of spent fuel in geological repositories. Providing a technical basis to support taking credit for this effect is expected to show spent UOX and MOX fuels to be very durable indeed in reducing repository settings (e.g. Poinssot et al. 2004).

Several mechanisms have been proposed to explain the inhibiting effects of hydrogen on the rate of corrosion of UOX and MOX but additional studies are needed to better understand the effect before it can be taken into account in long-term assessments of repository performance (Muzeau et al. 2009). However, the practical effectiveness of dissolved hydrogen in scavenging radiolytic oxidizing agents has been employed by General Electric Company in their patented NobleChem™ process which is based on injection of hydrogen together with noble metals to scavenge radiolytic oxidizing species in Boiling Water Reactors and thereby reduce the corrosion potential and mitigate stress corrosion cracking issues (Hettiarachchi 2005).

Fig. 3.4-2 illustrates the dependence of the  $\text{UO}_2$  fuel degradation mechanism on the electrochemical potential at pH 9.5, which represents the environment in a Canadian disposal system (adapted from Shoesmith 2007). The range identified as **MPM** in Fig. 3.4-2 indicates the range of surface potentials predicted by Shoesmith et al. (2003) to occur due to alpha radiolysis in granitic groundwaters. At potentials more positive than -0.16 V,  $\text{UO}_2$  fuel dissolves rapidly by a two-step oxidative dissolution mechanism the kinetics of which is controlled by the oxidation of U(IV) to U(VI).  $\text{UO}_2$  oxidation does not occur at potentials more negative than -0.16 V, so fuel degradation is controlled by the very slow chemical dissolution of the U(IV)-dominated surface. The electrochemical potential at the surface determines which mechanism is operative, and the potential is affected by the kinetics of oxidation and reduction reactions occurring at the fuel surface.

The competing kinetics of all of the oxidation (anodic) and reduction (cathodic) reactions at the used fuel surface generate a steady state surface potential during the oxidative dissolution process. This potential is defined as the corrosion potential of the system ( $E_{\text{CORR}}$ ). The surface potential at which the mechanism for fuel corrosion changes from (slow) chemical dissolution to (rapid) oxidative dissolution (shown as -160 mV in Fig. 3.4-2) depends on many factors (e.g., pH, T, aqueous speciation). A major goal for our work, therefore, is to develop a used fuel degradation rate model that quantifies the contributions of all processes to determine the corrosion potential at the used fuel surface. This includes processes that have not been taken into account in other electrochemical models for used fuel degradation, such as the role of ( $\text{H}_2$ ) as a reducing agent and the role surface phases catalyzing redox reactions (e.g., the noble metal bearing fission product phase – NMP). This includes calculating source concentrations of reagents due to the corrosion of engineering materials and radiolysis reactions, measuring surface-catalyzed reaction kinetics, estimating mass transport, and quantifying the effects of secondary phase precipitation.

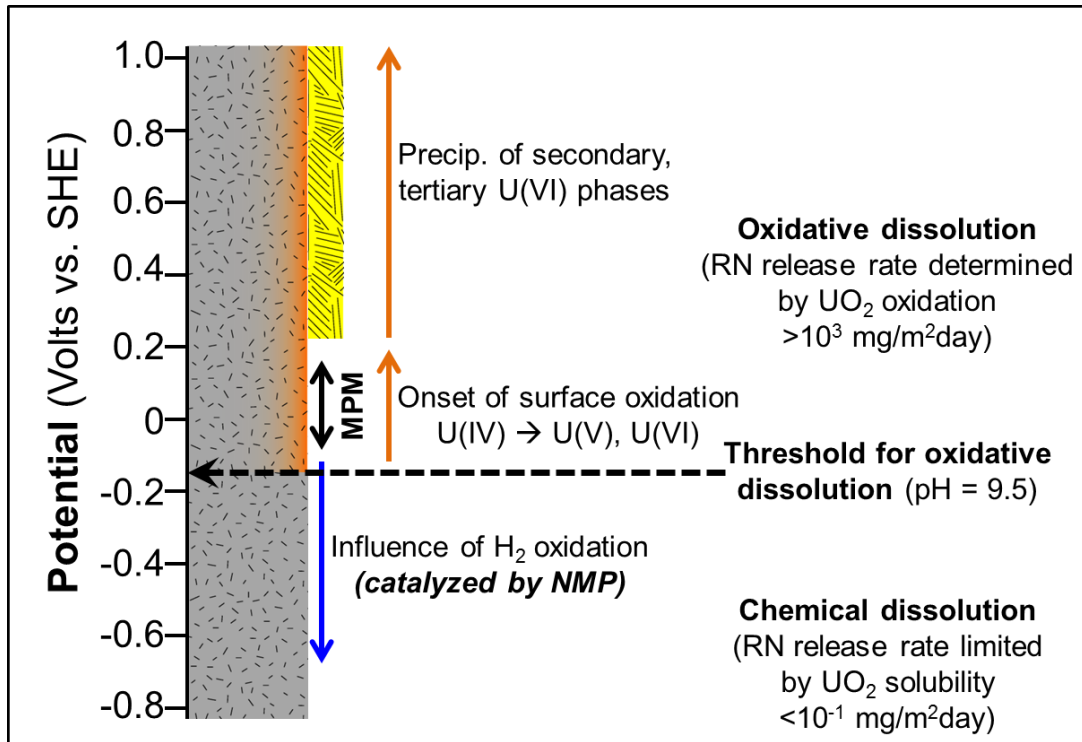


Figure 3.4-2. Schematic diagram identifying key surface processes involved in the degradation of used fuel (adapted from Shoesmith, 2007).

### 3.4.2 Used Fuel Degradation Modeling Approach

To account for the key oxidation/reduction and chemical processes that determine the rate of used fuel degradation a model based on mixed potential theory was implemented (Fig. 3.4-2). Mixed potential theory is based on two fundamental principles: (1) any electrochemical reaction can be divided into two or more partial oxidation and reduction reactions, and (2) there is no net accumulation of electric charge during the electrochemical reaction (Wagner and Traud, 1938). The first statement has been demonstrated experimentally and the second statement is based on the law of conservation of charge (Bockris and Reddy, 1977). Mixed potential theory has been used to quantify and predict the rate of corrosion of electrical conductors or semi-conductors (e.g., UO<sub>2</sub>) by relating the potentials and currents from a number distinct oxidation and reduction reactions occurring simultaneously (e.g., Shoesmith et. al., 2003).

The primary advantage of using mixed potential theory as a basis for used fuel degradation modeling is that it captures the fundamental electrochemistry and thermodynamics of the chemical phenomena of interest. Since it is based on fundamentals, such a model is applicable to a wide range of environmental conditions. By using the appropriate parameter values and input variables, the MPM for fuel degradation can be extended to all of the repository concepts being studied as part of the Used Fuel Disposition Campaign.

The mixed potential model that we chose to base our used fuel degradation model on was developed as part of the Canadian nuclear waste disposal research and development program (King and Kolar, 1999, King and Kolar, 2003, Shoesmith et.al., 2003). Our approach is to first

implement the existing Canadian mixed potential model in our own format using the programming language MATLAB. The language MATLAB was chosen because its modular environment and well-tested equation solvers facilitate the rapid implementation of relatively complex kinetic models. That model is being extended to include additional redox reactions and account for additional phases present in the fuel, most importantly noble metal particles and other oxides.

### 3.4.2.1 Canadian Mixed Potential Model (Canadian-MPM)

The Canadian model was developed to predict the corrosion behavior of used fuel inside a failed steel container under anticipated conditions in a granitic repository setting (Shoesmith et al. 2003). This system identifies the solution chemistry, including important solution species that interact with the fuel surface and concentration ranges, the key redox reactions, complexants, potential secondary phases, etc. The approach to modeling the system involves first calculating the electrochemical potential dependences for oxidative dissolution of the  $\text{UO}_2$  matrix (anode) and the oxidant reduction (cathodic) half reactions, and then coupling the anodic and cathodic half reactions using the charge conservation constraint (Shoesmith et al. 2003). The Canadian-MPM also accounts for important homogeneous reactions and mass transport processes that are coupled to the heterogeneous reactions occurring at the surface of the corroding  $\text{UO}_2$  fuel (Shoesmith et al. 2003). The physical system being modeled in the Canadian scenario is shown schematically in Fig. 3.4-3. The diagram on the left of Fig. 3.4-3 is the initial configuration and the diagram on the right shows the configuration after oxidative corrosion of both the  $\text{UO}_2$  fuel and steel canister surface. The used fuel cladding is not accounted for in this model (a conservative assumption). Corrosion of the fuel and the steel result in the formation of porous corrosion layers that serve as transport barriers which effectively decrease the reactive surface area of the corroding materials. A mathematical description of the model is presented in below.

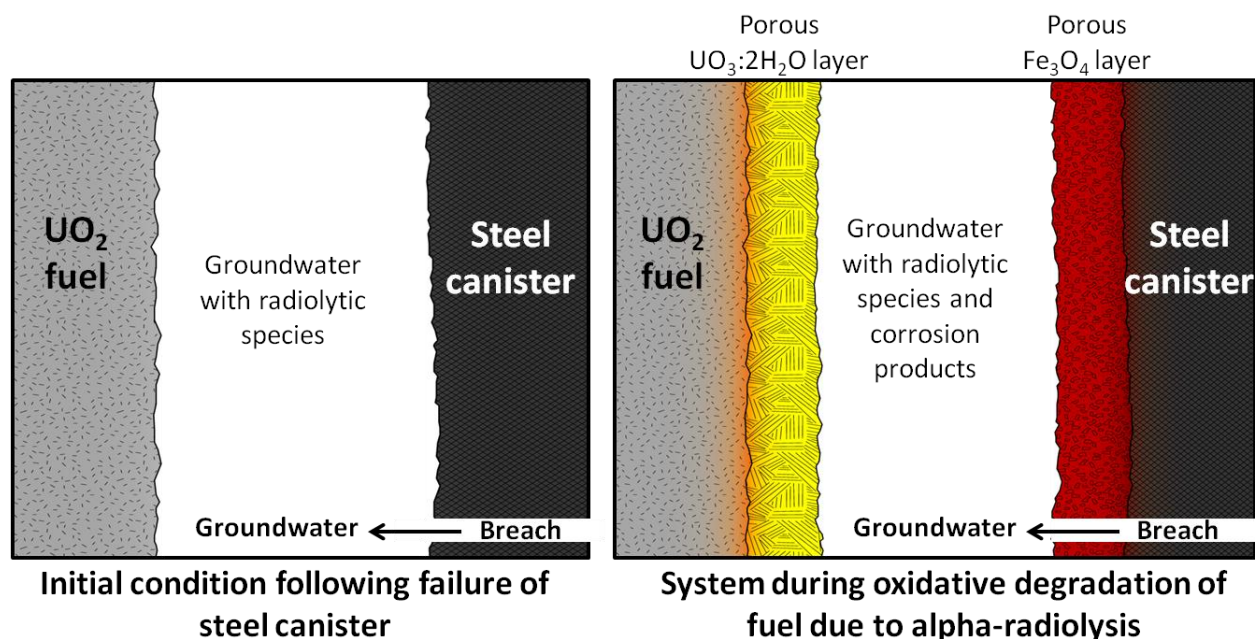


Figure 3.4-3. Simplified representation of breached canister system used in Shoesmith et al. (2003) MPM for the oxidative degradation of  $\text{UO}_2$  fuel due to alpha radiolysis of water.

The Canadian-MPM is a one dimensional reaction-diffusion model that accounts for both heterogeneous (surface) reactions and homogeneous (aqueous bulk) reactions through a series of mass and charge balance equations. The fundamental assumptions on which this model is based are (Shoesmith et.al., 2003):

- 1-D model geometry with non-uniform spatial distribution with emphasis on surface reactions at used fuel and steel (Fe) interfaces.
- Uniform dissolution of fuel surface (no localized effects, e.g., grain boundary etching).
- Mass transport by diffusion only.
- System is saturated with groundwater, the supply of groundwater is not limiting.
- Used fuel cladding is not accounted for.
- $U(VI)O_3 \cdot 2H_2O$  and  $Fe_3O_4$  corrosion layers are treated as equivalent porous media with spatially and temporally constant porosity and tortuosity.
- $U(VI)O_3 \cdot 2H_2O$  corrosion layer is assumed to be electrically insulating with electrochemical reactions restricted to base of pores.
- $U(VI)O_3 \cdot 2H_2O$  corrosion layer attenuates alpha dose rate at the fuel surface.
- $U(VI)O_3 \cdot 2H_2O$  corrosion layer may contain alpha-emitting radionuclides (user input).
- $Fe_3O_4$  is assumed to be the stable corrosion product of carbon steel.
- pH is constant (buffered) throughout system.

The reaction scheme for the Canadian-MPM is shown in Fig. 3.4-4. The processes accounted for in the model include heterogeneous reactions on the fuel and steel surfaces and homogeneous reactions within the groundwater. Although many more reactions occur, these have been identified as the key reactions in the Canadian disposal system modeled by Shoesmith et al. 2003.



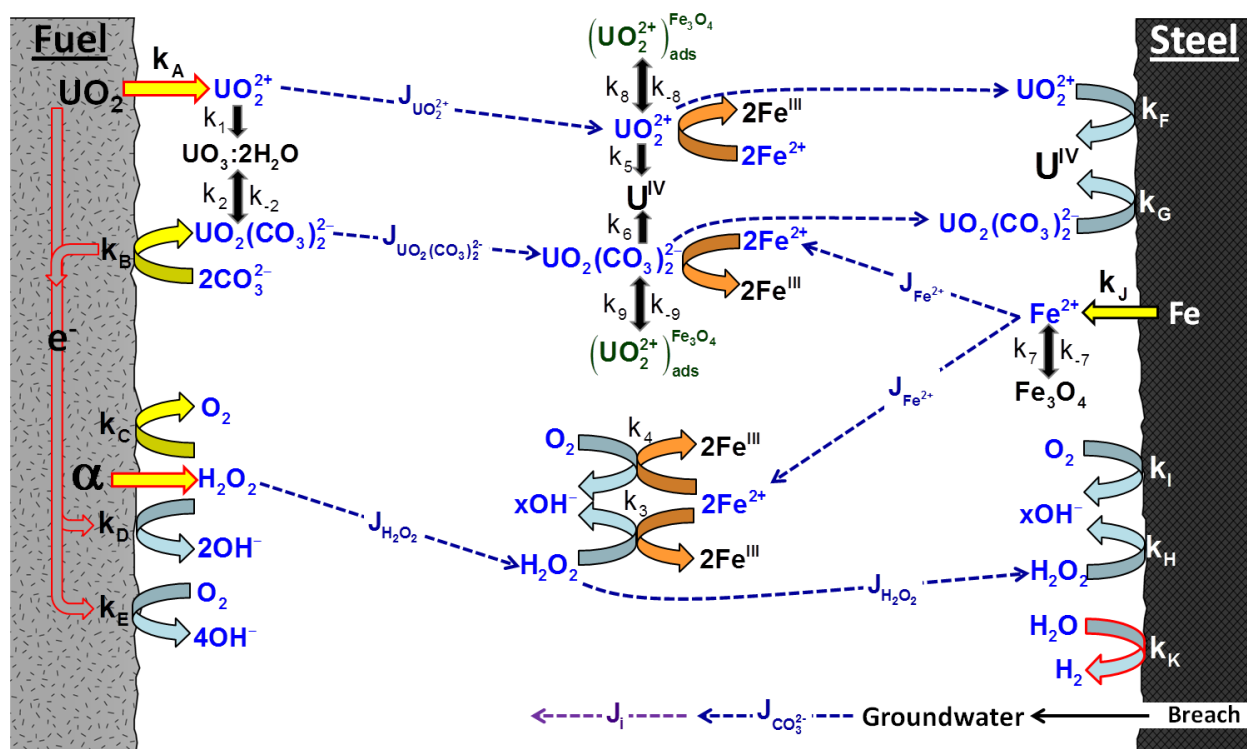


Figure 3.4-4. Reaction scheme used in the Shoesmith et al. (2003) (Canadian-MPM) for the oxidative degradation of UO<sub>2</sub> fuel due to alpha radiolysis of water (key half-reactions listed below). Aqueous species are shown in blue, dotted lines represent diffusive fluxes. The “k” labels represent rate expressions for the individual half-reactions. Reactions labeled with letters are for heterogeneous (surface) processes and those labeled with numbers describe homogeneous processes. Anodic reactions are noted with yellow or orange arrows and the cathodic reactions are shown in blue arrows. “ads” stands for adsorbed.

Groundwaters in a granitic repository scenario, such as the Canadian concept modeled by the MPM, will be basic (pH around 9.5), carbonate bearing, anoxic solutions (Shoesmith et al., 2003). Therefore, over the time scales of interest (hundreds to tens of thousands of years), the dominant oxidant will be hydrogen peroxide produced by water radiolysis. In the Canadian-MPM, the dissolved concentration of O<sub>2</sub> is defined by the modeler and the dissolved concentration of H<sub>2</sub>O<sub>2</sub> is determined by a radiolysis sub-routine included in the MPM (described below).

### 3.4.2.2 ANL Implementation of the Canadian Mixed Potential Model

A working version of the Canadian-MPM was implemented by ANL researchers in MATLAB based on the work of King and Kolar (1999), King and Kolar (2003), and Shoesmith et al. (2003). This model, referred hereafter to as the **ANL-MPM**, serves as our base-case used fuel degradation model which is being extended to take into account other key phenomena affecting the fuel degradation rate. These other phenomena include (but are not limited to):

- The role of H<sub>2</sub> oxidation reactions in protecting the fuel from oxidative dissolution.

- The role of NMP in catalyzing key interfacial redox reactions
- The evolution of reactive surface areas of fuel and NMP during fuel dissolution

As shown in Figs. 3.4-3 and 3.4-4, the Canadian-MPM models the corrosion of both a UO<sub>2</sub> fuel surface and a carbon steel container surface. In the implementation of the ANL-MPM we have focused on corrosion of the UO<sub>2</sub> fuel surface, since the purpose of our model is to predict the degradation rate of the used fuel matrix. The ANL-MPM does have the built-in capability of modeling steel corrosion; however it is envisioned that canister failure and corrosion will be dealt with in a separate process model within the UFD campaign that will be linked with the ANL-MPM. Therefore, the following discussion of the ANL-MPM deals only with the corrosion of the used fuel surface. For more information on how the steel canister surface is modeled in the Canadian-MPM see King and Kolar (1999), King and Kolar (2003), and Shoesmith et.al. (2003).

### **3.4.2.3 Parameter Database for ANL Implementation of the Canadian Mixed Potential Model**

The core of the MPM is the parameter database (Tables 3.4-1 to 3.4-3). Extension of the ANL-implementation of the MPM (ANL-MPM) to other disposal scenarios requires optimizing and revising the parameter database for the new conditions of interest. The source of parameter values and input variables for the ANL-MPM are identified in Tables 3.4-1 to 3.4-3. This database is currently being optimized using values from recent literature as well as an on-going experimental program involving electrochemical tests that are specifically focused on providing parameter values for the ANL-MPM (Jerden et al., 2012). Unless otherwise noted the parameters listed in Tables 3.4-1 to 3.4-5 come directly from King and Kolar (1999), and King and Kolar (2003) (and references therein). Some of the parameter values used in the Canadian-MPM of King and Kolar (1999) are essentially “place holders” that are based on reasonable assumptions. For example, an activation energy of  $6.0 \times 10^4$  J/mole is being used for all heterogeneous redox reactions (Table 3.4-1) until the temperature dependencies of the individual reactions can be fully quantified by experiment or extracted from existing literature. The initial use of this particular activation energy is justified by the observation that many chemical processes of the type being modeled in the ANL-MPM have measured activation energies around  $6.0 \times 10^4$  J/mole. Calculations and experimental measurements will be performed to determine the sensitivity of the fuel dissolution rate to the temperature and if more accurate activation energy values are required.

Table 3.4-1, Part of the ANL-MPM parameter database: interfacial reactions for UO<sub>2</sub> matrix dissolution. See Fig. 3.4-4 for coupling between reactions.

<b>Anodic reactions on fuel surface</b>	Reaction label (Fig 3.4-4)	25°C Rate const: K <sub>i</sub> (cm/s) or (mol/cm <sup>2</sup> s)*	Activation energy for k <sub>i</sub> : ΔHk <sub>i</sub> (J/mol)	Charge Transfer coefficient: α <sub>i</sub>	25°C Stand. Pot: E <sub>i</sub> <sup>0</sup> (V <sub>SCE</sub> )	T dependence of E <sup>0</sup> : ΔE <sub>i</sub> <sup>0</sup> (V <sub>SCE</sub> /K)
UO <sub>2</sub> → UO <sub>2</sub> <sup>2+</sup> + 2e <sup>-</sup>	<b>A</b>	5.0E-12*	6.0E+04 <sup>II</sup>	0.96	0.169	-2.48E-04
UO <sub>2</sub> + 2CO <sub>3</sub> <sup>2-</sup> → UO <sub>2</sub> (CO <sub>3</sub> ) <sub>2</sub> <sup>2-</sup> + 2e <sup>-</sup>	<b>B</b>	1.3E-12*	6.0E+04	0.82	-0.173	2.10E-03
H <sub>2</sub> O <sub>2</sub> → O <sub>2</sub> + 2H <sup>+</sup> + 2e <sup>-</sup>	<b>C</b>	7.4E-06	6.0E+04	0.41	-0.121	-9.93E-04
H <sub>2</sub> → 2H <sup>+</sup> + 2e <sup>-</sup>	<b>L</b>	Experiment <sup>I</sup>	Experimental <sup>I</sup>	Experimental <sup>I</sup>	Literature	Literature
<b>Cathodic reactions on fuel surface</b>						
H <sub>2</sub> O <sub>2</sub> + 2e <sup>-</sup> → 2OH <sup>-</sup>	<b>D</b>	1.2E-10	6.0E+04	0.41	-0.973	-6.98E-04
O <sub>2</sub> + 2H <sub>2</sub> O + 4e <sup>-</sup> → 4OH <sup>-</sup>	<b>E</b>	1.4E-10	6.0E+04	0.50	-0.426	-1.23E-04

**I.** Electrochemical experiments initiated in FY-2012 are focused on providing unknown parameter values for the ANL-MPM as well as confirming literature values that are currently being used (Jerden et al., 2012).

**II.** The activation energy of 6.0x10<sup>4</sup> is being used as a “place-holder” value until these temperature dependencies can be quantified by experiment or identified in existing literature. The use of this particular value is justified by the observation that many chemical processes of the type being modeled in the ANL-MPM have measured activation energies around 6.0x10<sup>4</sup> J/mol.

Table 3.4-2. Part of the ANL-MPM parameter database: homogeneous reactions. See Fig. 3.4-4 for coupling between reactions.

Homogeneous Bulk Reactions	Reaction	25°C Rate const:			Activation energy
	label (Fig.4)	$K_i$ ( $s^{-1}$ )	$K_i$ ( $mol/cm^2s$ )	$K_i$ ( $cm^3/mol s$ )	for $k_i$ : $\Delta H_{ki}$ ( $J/mol$ ) <sup>II</sup>
$UO_2^{2+} + 2H_2O \rightarrow UO_3 \cdot 2H_2O + 2H^+$	<b>1</b>	1.0E-03	----	----	6.0E+04
$UO_2(CO_3)_2^{2-} + 2H_2O \rightarrow UO_3 \cdot H_2O + 2CO_3^{2-} + 2H^+$	<b>2</b>	1.0E-04	----	----	6.0E+04
$UO_3 \cdot H_2O + 2CO_3^{2-} + 2H^+ \rightarrow UO_2(CO_3)_2^{2-} + 2H_2O$	<b>-2</b>	----	6.3E-16	----	6.0E+04
$O_2 + 2H_2O + 4Fe^{2+} \rightarrow 4Fe(III) + 4OH^-$	<b>3</b>	----	----	5.9E+05	6.0E+04
$H_2O_2 + 2Fe^{2+} \rightarrow 2Fe(III) + 2OH^-$	<b>4</b>	----	----	6.9E+04	4.20E+04
$UO_2^{2+} + Fe^{2+} \rightarrow Fe(III) + U(IV)$	<b>5</b>	----	----	1.0E+04	6.0E+04
$UO_2(CO_3)_2^{2-} + Fe^{2+} \rightarrow Fe(III) + U(IV) + 2CO_3^{2-}$	<b>6</b>	----	----	1.0E+03	6.0E+04
$Fe^{2+} + Fe(III) + 4H_2O \rightarrow Fe_3O_4 + 8H^+$	<b>7</b>	1.0E-03	----	----	6.0E+04
$Fe_3O_4 + 8H^+ \rightarrow Fe^{2+} + Fe(III) + 4H_2O$	<b>-7</b>	----	Function	----	6.0E+04
$UO_2^{2+} \rightarrow (UO_2^{2+})_{ads}$	<b>8</b>	----	----	1.0E-3	0
$(UO_2^{2+})_{ads} \rightarrow UO_2^{2+}$	<b>-8</b>	1.0E-06	----	----	----
$UO_2(CO_3)_2^{2-} \rightarrow (UO_2^{2+})_{ads} + CO_3^{2-}$	<b>9</b>	----	----	1.0E-03	0
$(UO_2^{2+})_{ads} + CO_3^{2-} \rightarrow UO_2(CO_3)_2^{2-}$	<b>-9</b>	1.0E-06	----	----	----
$UO_2 + 2H_2O \rightarrow U(OH)_4(aq)$	<b>10</b>	----	1.0E-17	----	6.E+04
$H_2O_2 \rightarrow H_2O + 0.5O_2$	<b>11</b>	Experimental <sup>I</sup>	Experimental <sup>I</sup>	Experimental <sup>I</sup>	Experimental <sup>I</sup>

**I.** Electrochemical experiments initiated in FY-2012 are focused on providing unknown parameter values for the ANL-MPM as well as confirming literature values that are currently being used (Jerden et al., 2012).

**II.** The activation energy of  $6.0 \times 10^4$  is being used as a “place-holder” value until these temperature dependencies can be quantified by experiment or identified in existing literature. The use of this particular value is justified by the observation that many chemical processes of the type being modeled in the ANL-MPM have measured activation energies around  $6.0 \times 10^4$  J/mol.

Table 3.4-3. Part of the ANL-MPM parameter database: components (species) included in mass balance equations (see examples Eq. 3.4-21 – Eq. 3.4-25). The concentration column ( $C_i$ ) identifies links to other UFD process models that are being or will be developed as part of the FY-2013 research and development activities (IPC: in-package-chemistry model).

Species	Species Type	Con: $C_i$ (mole/L)	Saturated con: $C_i^{sat}$ (mole/cm <sup>3</sup> )	T dependence of $C_i^{sat}$ : $\Delta H_{sat}$ (J/mole)	Diffusion coeff. $D_i$ (cm <sup>2</sup> /s)	Activation energy $\Delta H_{Di}$ (J/mole)
UO <sub>2</sub> <sup>2+</sup>	Aqueous	Calculated by ANL-MPM	3.20E-05	6.E+04	5.0E-06	1.5E+4
UO <sub>2</sub> (CO <sub>3</sub> ) <sub>2</sub> <sup>2-</sup>	Aqueous	Calculated by ANL-MPM	5.12[CO <sub>3</sub> ] <sup>1.34</sup>	6.E+04	5.0E-06	1.5E+4
U(IV)	Homogeneous solid	Calculated by ANL-MPM	----	----	----	----
CO <sub>3</sub> <sup>2-</sup>	Aqueous	Environmental input (link to IPC)	----	----	1.7E-05	1.5E+4
O <sub>2</sub>	Aqueous	Environmental input (link to IPC)	----	----	1.7E-05	1.5E+4
H <sub>2</sub> O <sub>2</sub>	Aqueous	EBS Radiolysis Model	----	----	1.7E-05	1.5E+4
Fe <sup>2+</sup>	Aqueous	Environmental input (link to IPC)	1.0E-08	6.E+04	5.0E-06	1.5E+4
H <sub>2</sub>	Aqueous	Environmental input (link to IPC)	----	----	Literature	Literature
U(OH) <sub>4</sub>	Aqueous	Calculated by ANL-MPM	----	----	Literature	Literature
UO <sub>3</sub> ·2H <sub>2</sub> O	Homogeneous solid	Calculated by ANL-MPM	Precip. UO <sub>2</sub> <sup>2+</sup> , UO <sub>2</sub> (CO <sub>3</sub> ) <sub>2</sub> <sup>2-</sup>	----	----	----
Fe <sub>3</sub> O <sub>4</sub>	Homogeneous solid	Calculated by ANL-MPM	Precip. Fe <sup>2+</sup>	----	----	----
Fe(III)	Homogeneous solid	Calculated by ANL-MPM	Precip. Fe <sup>2+</sup>	----	----	----

Table 3.4-4. Part of the ANL-MPM parameter database: physical parameters used in electrochemical and mass balance equations (Eq. 3.4-1 – Eq. 3.4-25).

Parameter	Symbol	Value	Units
Porosity of $\text{UO}_3 \cdot 2\text{H}_2\text{O}$ layer	$\epsilon_1$	0.45	$\text{cm}^3/\text{cm}^3$
Porosity of bulk solution <sup>I</sup>	$\epsilon_2$	1	$\text{cm}^3/\text{cm}^3$
Faraday constant	F	96487	C/mol
Gas constant	R	8.314	J/K mol
Absolute temperature	T	<i>Input profile</i>	K
Dry density of $\text{UO}_3 \cdot 2\text{H}_2\text{O}$ layer	$\rho_1$	4.98	$\text{g}/\text{cm}^3$
Dry density of solution layer <sup>I</sup>	$\rho_2$	1	$\text{g}/\text{cm}^3$
Tortuosity factor of $\text{UO}_3 \cdot 2\text{H}_2\text{O}$ layer	$\tau_1$	0.1	----
Tortuosity factor: bulk solution <sup>I</sup>	$\tau_2$	1	----
Reaction order dependence of dissolution rate of $\text{UO}_3 \cdot 2\text{H}_2\text{O}$ on $[\text{CO}_3]$	p	0	----
Reaction order for the dependence of the rate of anodic dissolution of $\text{UO}_2$ on $[\text{CO}_3]$	m	6.6E-01	----
Function for dissolution of porous corrosion layer: approximated by finite width profile	$\delta$	<i>Function</i>	----

I. The porosity, density, and tortuosity of the bulk solution are specified in the ANL-MPM to facilitate the incorporation of porous media into future version of the model (e.g., a porous mass of in-package corrosion products in place of the bulk aqueous solution phase used in the current model).

Table 3.4-5. Part of the ANL-MPM parameter database: parameters and variables used in the radiolysis sub-model (see Fig. 3.4-7 and Section 3.4.2.4. for discussion).

Parameter	Symbol	Value	Units
G-value for the primary a-radiolysis yield of H <sub>2</sub> O <sub>2</sub>	G <sub>H2O2</sub>	1.02E-10	mol/Gy cm <sup>3</sup>
Time-dependent α-ration dose rate to the solution	R <sub>aq(t)</sub>	Calculated	----
Spatial- and time dependent alpha-radiation dose rate	R <sub>D(x,t)</sub>	Calculated	----
Ratio of dose rate from U(VI) corrosion layer to dose rate from fuel	R <sub>film</sub>	0 - 1	----
Geometrical factor describing a-radiation field (see Note below)	g <sub>f(x)</sub>	Input	----
α-particle penetration depth in water	α <sub>pen</sub>	35	μm
Scaling factor for dose rate	R <sub>scale</sub>	1	----

**Note:**

- g<sub>f(x)</sub> = 1 if 0 < x ≤ α<sub>PEN</sub> and x<sub>A</sub> = 0,
- g<sub>f(x)</sub> = 1+2R<sub>film</sub> if 0 < x ≤ min(x<sub>A</sub>, α<sub>PEN</sub>),
- g<sub>f(x)</sub> = 2R<sub>film</sub> if α<sub>PEN</sub> ≤ x < x<sub>A</sub>,
- g<sub>f(x)</sub> = ε+R<sub>film</sub> (1-ε) if 0 < x<sub>A</sub> ≤ x ≤ α<sub>PEN</sub>,
- g<sub>f(x)</sub> = R<sub>film</sub> (1-ε) if max(x<sub>A</sub>, α<sub>PEN</sub>) < x ≤ x<sub>A</sub>+α<sub>PEN</sub>,
- g<sub>f(x)</sub> = 0 if x > x<sub>A</sub>+α<sub>PEN</sub>,

Based on the work of King and Kolar, 1999, King and Kolar, 2003, Shoesmith et.al., 2003 and the lists of parameter values and variables shown in Table 3.4-1 – 3.4-5, the ANL-MPM was implemented through a series of one-dimensional reaction-diffusion equations that describe the mass transport, precipitation/dissolution, adsorption/desorption, and redox transitions for each of the chemical species identified in Table 3.4-3.

The ANL-MPM is based on a set of ordinary differential equations in which concentrations are the state variables. Given initial concentrations at the used fuel surface, a corrosion potential is calculated such that the total current flow at that surface is zero (this is the fundamental axiom of mixed potential theory). The overall rates for all surface reactions are then calculated at that corrosion potential. The rates of the surface reactions control the flux of chemical species from the surface into solution. Species flux from the fuel surface is used to update the concentrations in the solution at the fuel surface. The cycle of calculations is repeated for the desired length of time.

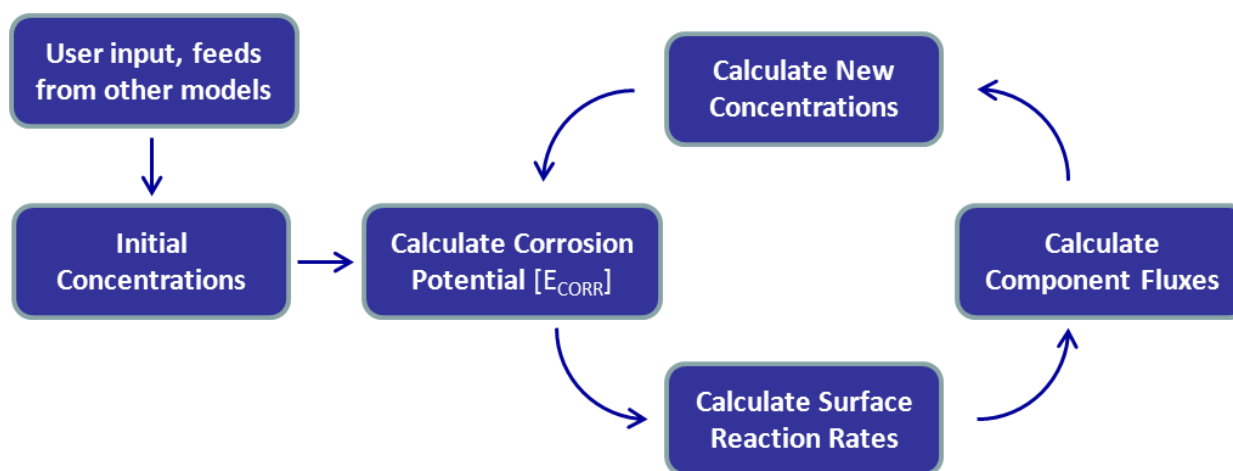


Figure 3.4-5. Simplified algorithm for the evolution of the used fuel corrosion potential and interfacial reaction rates with time as calculated by the ANL-MPM: see Table 3.4-3 for concentration input sources.

Implementation of the ANL-MPM is summarized as follows:

- The time derivatives of the species identified in Table 3.4-1 were calculated explicitly to reduce the model to a system of ordinary differential equations.
- Several well tested, built-in mathematical tools available in MATLAB were used to facilitate rapid model implementation.
- Modeling systems of partial differential equations like the MPM requires discretization in order to calculate approximate derivative values. The spatial dimension, which is the distance between the used fuel and the steel surface (Fig. 3.4-2), was divided into multiple cells (the current model uses 250 cells). The cell spacing is logarithmic with finer spacing at the fuel and steel interfaces (Fig. 3.4-6).



- Placeholder values for physical constants that are not explicitly documented in the Canadian-MPM (e.g., reaction rates and diffusivities) were used to implement the model. The relevant physical constants will be updated based on analyses of literature data and from on-going electrochemical experiments.
- The temperature and radioactive dose profiles are functions of time that are supplied explicitly as an argument to the MPM and are not a result of the calculations.

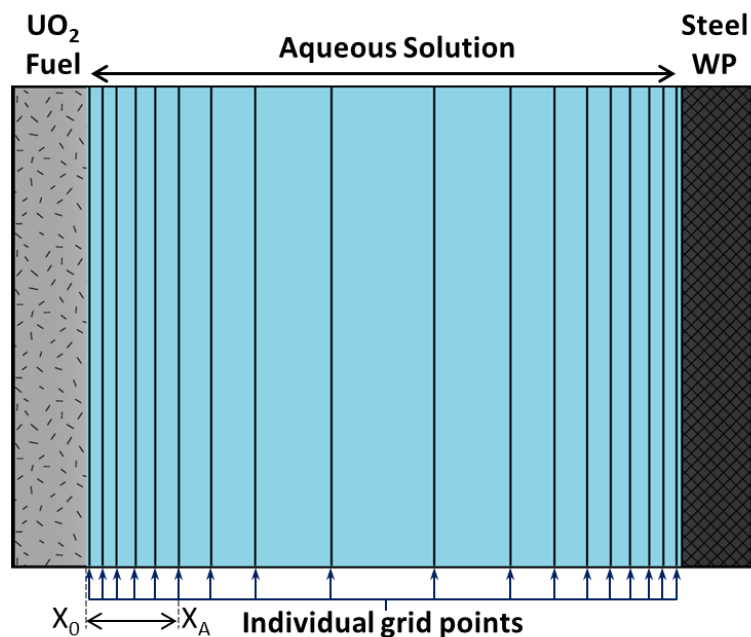


Figure 3.4-6. Schematic representation of mixed potential model grid spacing between the used fuel and steel surface boundaries (not all spacings are shown). Spacing is logarithmic with finer intervals at the two interfaces. The current implementation of the ANL-MPM contains 250 grid points with a minimum grid spacing of 1 micrometers and a maximum spacing of 1000 micrometers.

The steel waste package is shown to define the spacing and mass transport calculations. The reactions for corrosion of the steel have been implemented into the ANL-MPM, but the rates are currently set to zero to match available results for the Canadian MPM.

#### 3.4.2.4 ***Governing Equations and Fundamental Electrochemical Relationships Used in Mixed Potential Model Implementation***

In the MPM, the rate of mass loss from the used fuel (a quantification of degradation) is directly related to the corrosion current density by Faradays Law (Equation 3.4-1). The corrosion current density is defined as the sum of the current densities of the anodic fuel oxidation reactions (Reactions A and B in Table 3.4-1, Equation 3.4-2 below).

$$\frac{ML^{\text{Fuel}}}{\text{time}} = \frac{i_{\text{CORR}}^{\text{Fuel}} MW^{\text{Fuel}}}{nF} \quad (3.4-1)$$

$$i_{\text{CORR}}^{\text{Fuel}} = i_A + i_B \quad (3.4-2)$$

where  $ML^{\text{Fuel}}/\text{time}$  is the total mass loss rate (grams/m<sup>2</sup>days) due to oxidative and chemical dissolution,  $i_{\text{CORR}}^{\text{Fuel}}$  is the corrosion current density (amp/m<sup>2</sup>),  $MW^{\text{Fuel}}$  is the molecular weight (grams/mole),  $n$  is the number of electrons transferred,  $F$  is the Faraday constant (amp days/mole). The corrosion current density is related to the used fuel corrosion potential by the Tafel Equation (Equation 3.4-3).

$$E_{\text{CORR}}^{\text{Fuel}} = E_A^0 + \frac{RT}{\alpha_A F} \ln \left( \frac{i_{\text{CORR}}}{nF\varepsilon(SA)k_A} \right) \quad (3.4-3)$$

where  $E_{\text{CORR}}^{\text{Fuel}}$  is the corrosion potential (Volts),  $E_A^0$  is the standard potential for Reaction A (see Table 3.4-1),  $\alpha_A$  is the electrical charge transfer coefficient (related to Tafel slope for reaction of interest),  $\varepsilon$  is the porosity of the U(VI) corrosion layer covering the used fuel surface (m<sup>3</sup> void/m<sup>3</sup> corrosion phase),  $(SA)$  is the reactive surface area of the fuel (m<sup>2</sup>),  $k_A$  is the rate constant for Reaction A (see Table 3.4-1), and  $R$ ,  $T$ ,  $F$ ,  $n$  are the ideal gas constant, absolute temperature, Faraday's constant and the number of electrons transferred respectively. As implied in Fig. 3.4-5, the used fuel corrosion potential is also a function ( $E_0$ ) of the concentrations of species involved in the oxidative dissolution of uranium (see Table 3.4-1 for reactions).

$$E_{\text{CORR}}^{\text{Fuel}} = E_0([\text{CO}_3^{2-}], [\text{O}_2], [\text{H}_2\text{O}_2], [\text{H}_2]) \quad (3.4-4)$$

The relationships between reaction currents (directly proportional to reaction rates), rate constants, standard potentials and the corrosion potential for individual half-cell reactions at the used fuel surface (Table 3.4-1, Fig. 3.4-4) are derived from the Tafel equations and quantified as follows:

$$i_A = nF\varepsilon k_A \exp \left[ \frac{\alpha_A F}{RT} (E_{\text{CORR}}^{\text{Fuel}} - E_A^0) \right] \quad (3.4-5)$$

$$i_B = nF\epsilon k_B [\text{CO}_3^{2-}]^2 \exp\left[\frac{\alpha_B F}{RT} (E_{\text{CORR}}^{\text{Fuel}} - E_B^0)\right] \quad (3.4-6)$$

$$i_C = nF\epsilon k_C [\text{H}_2\text{O}_2] \exp\left[\frac{\alpha_C F}{RT} (E_{\text{CORR}}^{\text{Fuel}} - E_C^0)\right] \quad (3.4-7)$$

$$-i_D = nF\epsilon k_D [\text{H}_2\text{O}_2] \exp\left[\frac{-\alpha_D F}{RT} (E_{\text{CORR}}^{\text{Fuel}} - E_D^0)\right] \quad (3.4-8)$$

$$-i_E = nF\epsilon k_E [\text{O}_2] \exp\left[\frac{-\alpha_E F}{RT} (E_{\text{CORR}}^{\text{Fuel}} - E_E^0)\right] \quad (3.4-9)$$

$$-i_L = nF\epsilon k_L [\text{H}_2] \exp\left[\frac{-\alpha_L F}{RT} (E_{\text{CORR}}^{\text{Fuel}} - E_L^0)\right] \quad (3.4-10)$$

where  $E_{\text{CORR}}^{\text{Fuel}}$  is the corrosion potential (Volts),  $E_A^0$  is the standard potential for Reaction A (see Table 3.4-1),  $\alpha_A$  is the electrical charge transfer coefficient (related to Tafel slope for reaction of interest),  $\epsilon$  is the porosity of the U(VI) corrosion layer covering the used fuel surface ( $\text{m}^3$  void/ $\text{m}^3$  corrosion phase),  $S$  is the reactive surface area of the fuel ( $\text{m}^2$ ),  $k_A$  is the rate constant for Reaction A (see Table 3.4-1), and  $R$ ,  $T$ ,  $F$ ,  $n$  are the ideal gas constant, absolute temperature, Faraday's constant and the number of electrons transferred respectively.

It follows from Equations Eq. 3.4-1 - Eq. 3.4-3 that the corrosion current densities for each half cell reaction can also be calculated based on the fluxes of key redox species (Table 3.4-3):

$$2i_C + i_E = -nF\tau_f \epsilon D_{\text{O}_2} \frac{\partial C_{\text{O}_2}(0, t)}{\partial x} \quad (3.4-11)$$

$$i_C - i_D = -nF\tau_f \epsilon D_{\text{H}_2\text{O}_2} \frac{\partial C_{\text{H}_2\text{O}_2}(0, t)}{\partial x} \quad (3.4-12)$$

$$i_B = -nF\tau_f \varepsilon D_{\text{UO}_2(\text{CO}_3)_2^-} \frac{\partial C_{\text{UO}_2(\text{CO}_3)_2^-}(0,t)}{\partial x} \quad (3.4-13)$$

$$i_A = -nF\tau_f \varepsilon D_{\text{UO}_2^{2+}} \frac{\partial C_{\text{UO}_2^{2+}}(0,t)}{\partial x} \quad (3.4-14)$$

$$i_L = -nF\tau_f \varepsilon D_{\text{H}_2} \frac{\partial C_{\text{H}_2}(0,t)}{\partial x} \quad (3.4-15)$$

where  $\tau_f$  and  $\varepsilon$  are the tortuosity and porosity of the U(VI) corrosion layer,  $D$  is the diffusion coefficient and  $C$  is the molar concentration,  $x$  is the distance from the used fuel surface (Fig. 6) and  $(0,t)$  refers to the partial derivative of concentration at  $x = 0$  and time =  $t$ .

The fundamental axiom on which kinetic mixed potential theory models (such as the ANL-MPM) is thus quantified by the equation Equation 3.4-16 (see Reactions A - L in Fig. 3.4-4 and Table 3.4-1):

$$i_A + i_B + i_L - i_C - i_D - i_E = 0 \quad (3.4-16)$$

The temperature dependence of the used fuel degradation rate is captured in the ANL-MPM using Arrhenius relationships for rate constants (Equation 3.4-17), saturation concentrations (Eq. 3.4-18) and diffusion coefficients (Eq. 3.4-19). A linear temperature dependency is used for standard electrochemical potentials (Eq. 3.4-20).

$$k_i = k_i(T_r) \exp \left[ \frac{\Delta H_i}{R} \left( \frac{1}{T_r} - \frac{1}{T} \right) \right] \quad (3.4-17)$$

$$C_i^{\text{sat}} = C_i^{\text{sat}}(T_r) \exp \left[ \frac{\Delta H_i^{\text{sat}}}{R} \left( \frac{1}{T_r} - \frac{1}{T} \right) \right] \quad (3.4-18)$$

$$D_i = D_i(T_r) \exp \left[ \frac{\Delta H_{D_i}}{R} \left( \frac{1}{T_r} - \frac{1}{T} \right) \right] \quad (3.4-19)$$

$$E_i^0 = E_i^0(T_r) + \Delta E_i^0(T - T_r) \quad (3.4-20)$$

where  $k$  is a rate constant,  $T_r$  is the reference temperature used in determining the activation energy ( $\Delta H$ ) and temperature dependence of the standard potential for a given half-cell reaction ( $\Delta E^0$ ),  $R$  is the ideal gas constant,  $C^{\text{sat}}$  is the molar concentration at which a given corrosion phase precipitates ( $\text{UO}_3 \cdot 2\text{H}_2\text{O}$  for corrosion of fuel surface), and  $D_i$  is the diffusion coefficient for component  $i$ .

A 1-D reaction-diffusion (mass-balance) equation is written for each species tracked in the MPM (see Table 3.4-3 for list of species). For example, the concentrations of  $\text{UO}_2^{2+}$  and  $\text{H}_2\text{O}_2$  are tracked using the following equations:

$$\begin{aligned} \varepsilon \frac{\partial C_{\text{UO}_2^{2+}}}{\partial t} = \frac{\partial}{\partial x} \left( \tau_f \varepsilon D_{\text{UO}_2^{2+}} \frac{\partial C_{\text{UO}_2^{2+}}}{\partial x} \right) - \varepsilon k_8 C_{\text{UO}_2^{2+}} (C_{\text{U(VI)ads}}^{\text{max}} - C_{\text{U(VI)ads}}) \rho + \\ k_{-8} C_{\text{U(VI)ads}} \rho - \varepsilon k_5 C_{\text{UO}_2^{2+}} C_{\text{Fe}^{2+}} - \varepsilon k_1 \max(0, C_{\text{UO}_2^{2+}} - C_{\text{UO}_2^{2+}}^{\text{sat}}) \end{aligned} \quad (3.4-21)$$

$$\begin{aligned} \varepsilon \frac{\partial C_{\text{UO}_2(\text{CO}_3)_2^{2-}}}{\partial t} = \frac{\partial}{\partial x} \left( \tau_f \varepsilon D_{\text{UO}_2(\text{CO}_3)_2^{2-}} \frac{\partial C_{\text{UO}_2(\text{CO}_3)_2^{2-}}}{\partial x} \right) - \\ \varepsilon k_9 C_{\text{UO}_2(\text{CO}_3)_2^{2-}} (C_{\text{U(VI)ads}}^{\text{max}} - C_{\text{U(VI)ads}}) \rho + k_{-9} C_{\text{U(VI)ads}} \rho - \varepsilon k_6 C_{\text{UO}_2(\text{CO}_3)_2^{2-}} C_{\text{Fe}^{2+}} - \\ \varepsilon k_2 \max(0, C_{\text{UO}_2(\text{CO}_3)_2^{2-}} - C_{\text{UO}_2(\text{CO}_3)_2^{2-}}^{\text{sat}}) + k_{-2} C_{\text{CO}_3^{2-}}^{\text{p}} \delta(x - x_A) \end{aligned} \quad (3.4-22)$$

$$\begin{aligned} \varepsilon \frac{\partial C_{\text{CO}_3^{2-}}}{\partial t} = \frac{\partial}{\partial x} \left( \tau_f \varepsilon D_{\text{CO}_3^{2-}} \frac{\partial C_{\text{CO}_3^{2-}}}{\partial x} \right) + \varepsilon k_9 C_{\text{UO}_2(\text{CO}_3)_2^{2-}} (C_{\text{U(VI)ads}}^{\text{max}} - C_{\text{U(VI)ads}}) \rho - \\ 2k_{-9} C_{\text{U(VI)ads}} \rho + \varepsilon k_5 C_{\text{UO}_2^{2+}} C_{\text{Fe}^{2+}} - 2\varepsilon k_6 C_{\text{UO}_2(\text{CO}_3)_2^{2-}} C_{\text{Fe}^{2+}} + \\ 2\varepsilon k_2 \max(0, C_{\text{UO}_2(\text{CO}_3)_2^{2-}} - C_{\text{UO}_2(\text{CO}_3)_2^{2-}}^{\text{sat}}) - 2k_{-2} C_{\text{CO}_3^{2-}}^{\text{p}} \delta(x - x_A) \end{aligned} \quad (3.4-23)$$

$$\varepsilon \frac{\partial C_{O_2}}{\partial t} = \frac{\partial}{\partial x} \left( \tau_f \varepsilon D_{O_2} \frac{\partial C_{O_2}}{\partial x} \right) - \varepsilon k_3 C_{O_2} C_{Fe^{2+}} - \rho - \varepsilon k_5 C_{UO_2^{2+}} C_{Fe^{2+}} \quad (3.4-24)$$

$$\varepsilon \frac{\partial C_{H_2O_2}}{\partial t} = \frac{\partial}{\partial x} \left( \tau_f \varepsilon D_{H_2O_2} \frac{\partial C_{H_2O_2}}{\partial x} \right) + \varepsilon G_{H_2O_2} R_D - \varepsilon k_4 C_{H_2O_2} C_{Fe^{2+}} \quad (3.4-25)$$

where  $G_{H_2O_2}$  is the primary  $\alpha$ -radiolysis yield of  $H_2O_2$  (mol/Gy  $cm^3$ ),  $R_D$  is the spatial and time-dependent  $\alpha$ -radiation dose rate,  $\varepsilon$  is the porosity of the U(VI) corrosion layer covering the used fuel surface ( $m^3$  void/ $m^3$  corrosion phase),  $\rho$  is the dry density of fuel and steel corrosion layers ( $g/cm^3$ ),  $\tau_f$  is the tortuosity factor for corrosion layers

Similar expressions can be written for other species. One objective of the ANL experimental activity is to identify those species having a significant effect that should be tracked in the model. Most importantly, the mixed potential model of Shoemith et al. (2003) does not account for the experimentally observed catalysis of  $H_2(aq)$  oxidation on the grain boundary noble metal particles in used oxide fuel and does not track reactions involving  $H_2(aq)$ . Extending the Canadian MPM to include the effects of reactions involving  $H_2(aq)$  was the first modification.

The spatial and time dependent alpha dose rate ( $R_D$ ) is a function of the parameters described in Table 3.4-5. The radiolysis model used to calculate the  $H_2O_2$  source term for the ANL-MPM is discussed in detail in Section 3.4.2.5 below. The general equation used to calculate the alpha-dose rate within 10 – 50 micrometers of the used fuel surface and corrosion layer is:

$$R_D(x,t) = R_{scale} R_{aq}(t) g_f(x) \quad (3.4-26)$$

where  $R_{aq}$  is the average dose rate received by an aqueous solution in immediate contact with the used fuel,  $R_{scale}$  is an arbitrary scaling factor useful for sensitivity calculations and  $g_f(x)$  is a geometry factor, which has the following dependence on the distance from the used fuel surface and the presence or absence ( $x_A \neq 0$ ) of the U(VI) corrosion product layer of porosity  $\varepsilon$  and thickness ( $x_A$ ) (for discussion see Section 3.4.2.5. below and Appendix B of King and Kolar, 1999).

### 3.4.2.5 Radiolysis Model Included in the Base-Case Mixed Potential Model Implementation (Canadian-MPM and ANL-MPM)

Alpha-particles are assumed to have a constant energy of 5.3MeV in the Canadian-MPM and a solution penetration distance ( $\alpha_{PEN}$ ) of approximately 35  $\mu m$ . The ANL-MPM allows the model user to set the penetration distance over the range of  $\alpha_{PEN} = 45\mu m$  for  $\sim 6.0$ MeV alpha-particles down to  $\alpha_{PEN} = 10\mu m$  for  $\sim 2.3$  MeV particles (King and Kolar, 1999). The quantity of hydrogen

peroxide produced by alpha-radiolysis per unit of absorbed dose ( $G_{H_2O_2}$ ) in both models is assumed to be  $1.021E^{-10}$  mol/Gy  $cm^3$  (Christensen and Sunder 1998).

Fuel corrosion by oxidative dissolution may result in a layer of corrosion products (secondary phases) on the fuel surface, which will affect the rate of continuing degradation. The spatial dependence of the alpha-dose rate and the effects of the corrosion layer on the effective dose rate are taken into account through the factor  $g_f(x)$  (King and Kolar, 1999). Three cases are considered: (a) no U(VI) corrosion layer, (b) a corrosion layer thickness ( $x_A$ ) less than the penetration distance of alpha-particles in solution, and (c) a corrosion layer thickness greater than the alpha-particle penetration distance (i.e.,  $x_A > \alpha_{PEN}$ ). For the ANL-MPM, the precipitated U(VI) corrosion phase ( $UO_3 \cdot 2H_2O$ ) is modeled as a porous medium containing a series of parallel pores, having a bulk porosity  $\epsilon$  and an effective pore cross-sectional surface area of  $\epsilon(GA)$ , where  $(GA)$  is the geometrical surface area of the used fuel (King and Betteridge 1998). Future versions of ANL-MPM will account for other uranium oxide fuel corrosion products such as mixed oxides ( $UO_{2+x}$ ), uranyl peroxides, uranyl silicates and others depending on groundwater/in-package solution chemistry.

In the case of no U(VI) corrosion layer, the solution adjacent to the fuel is irradiated uniformly to a distance equal to  $\alpha_{PEN}$  (Fig. 3.4-7, top diagram).. The dose rate for this scenario is labeled  $R_{aq}(t)$ . For regions beyond this layer (i.e.,  $x_A > \alpha_{PEN}$ ),  $R_D(x,t) = 0$ . In the case of a corrosion layer of thickness  $x_A \leq \alpha_{PEN}$ , four regions are considered: (1) solution within the cylindrical pores of the U(VI) corrosion layer which is irradiated by the fuel and the U(VI) phase (Region 1, middle diagram of Fig. 3.4-7).

The pore diameter within the  $UO_3 \cdot 2H_2O$  corrosion layer are  $<5$  mm (King and Betteridge, 1998). The solution within the pores is assumed to be uniformly irradiated and the pores are sufficiently widely spaced so that the pore solution is not irradiated by alpha-particles emitted from adjacent pores. The ratio of the dose rates from the U(VI) corrosion layer and the used fuel surface is assumed to be constant and is an input parameter in the ANL-MPM ( $R_{film}$ ). Thus, the effective dose rate within the pores of the corrosion layer is given by  $\epsilon R_{aq}(x,t)(1+2R_{film})$ .

Region 2 (middle diagram, Fig. 3.4-7) is between the surface of the U(VI) corrosion layer and the penetration distance of the alpha-particles, i.e.,  $x_A < x \leq \alpha_{PEN}$ . The solution in this region is irradiated by the exposed used fuel at the base of the pores [effective surface area  $\epsilon(GA)$ ] and by the surface of the U(VI) corrosion layer [effective surface area  $(1-\epsilon)(GA)$ ]. The effective dose rate per unit area in this region, therefore, is  $(R_{aq}(x,t)(1-\epsilon)R_{film})$ .

Region 3 (middle diagram, Fig. 3.4-7) is between the distance  $\alpha_{PEN}$  and  $(x_A + \alpha_{PEN})$ . This region of the solution is irradiated by alpha-particles emitted from the surface of the U(VI) corrosion layer that has a surface area of  $(1-\epsilon)(GA)$ . The effective dose rate per unit area in this region is  $R_{aq}(x,t)(1-\epsilon)R_{film}$ .

When the U(VI) corrosion layer thickness is greater than  $\alpha_{PEN}$ , three irradiation regions are considered (Fig. 3.4-7, bottom diagram). Within a distance of  $\alpha_{PEN}$ , the pore solution is irradiated by both the exposed used fuel surface and by the lower portion of the alpha emitting U(VI) corrosion phase (Region 1, bottom diagram, Fig. 3.4-7). The effective dose rate in this region per unit geometrical area is  $\epsilon R_{aq}(x,t)(1+2R_{film})$ . For regions beyond  $\alpha_{PEN}$  (i.e.,  $\alpha_{PEN} < x <$

$x_A$ ), the pore solution is irradiated only by the pore walls (Region 2, bottom diagram, Fig. 3.4-7). The effective dose rate per unit geometrical surface area is  $2\varepsilon R_{aq}(x,t)R_{film}$ .

The region of bulk solution within  $x_A < x \leq (x_A + \alpha_{PEN})$  is irradiated by the surface of the porous U(VI) corrosion layer of cross-sectional area  $(GA)(1-\varepsilon)$  (Fig. 3.4-7, bottom diagram, Region 3). The effective dose rate in this region per unit geometrical surface area is  $R_{aq}(x,t)(1-\varepsilon)R_{film}$ .

An example of the rate of production of hydrogen peroxide, as predicted by the ANL-MPM, is shown in Fig. 3.4-8. The parameters and input variables for this model run are shown in Tables 3.4-1 – 3.4-5 and at the top of the figure. No U(VI) corrosion layer forms during the simulation shown in Fig. 3.4-8. In this figure the brown line is the total hydrogen peroxide formed, the red dotted line is the amount of free hydrogen peroxide and the purple dotted line is the amount of hydrogen peroxide that has been consumed through oxidative dissolution of the fuel. It should be noted that the hydrogen peroxide concentration shown in Fig. 3.4-8 is conservative because the ANL-MPM does not yet account for the spontaneous thermal decomposition (e.g., oxidation) of  $H_2O_2$  nor does it account for rapid radiolytic reactions that consume  $H_2O_2$ . Results in Fig. 3.4-8 indicate that at within a few seconds of starting the reaction a majority of the  $H_2O_2$  produced is being consumed by the oxidative dissolution of  $UO_2$ .



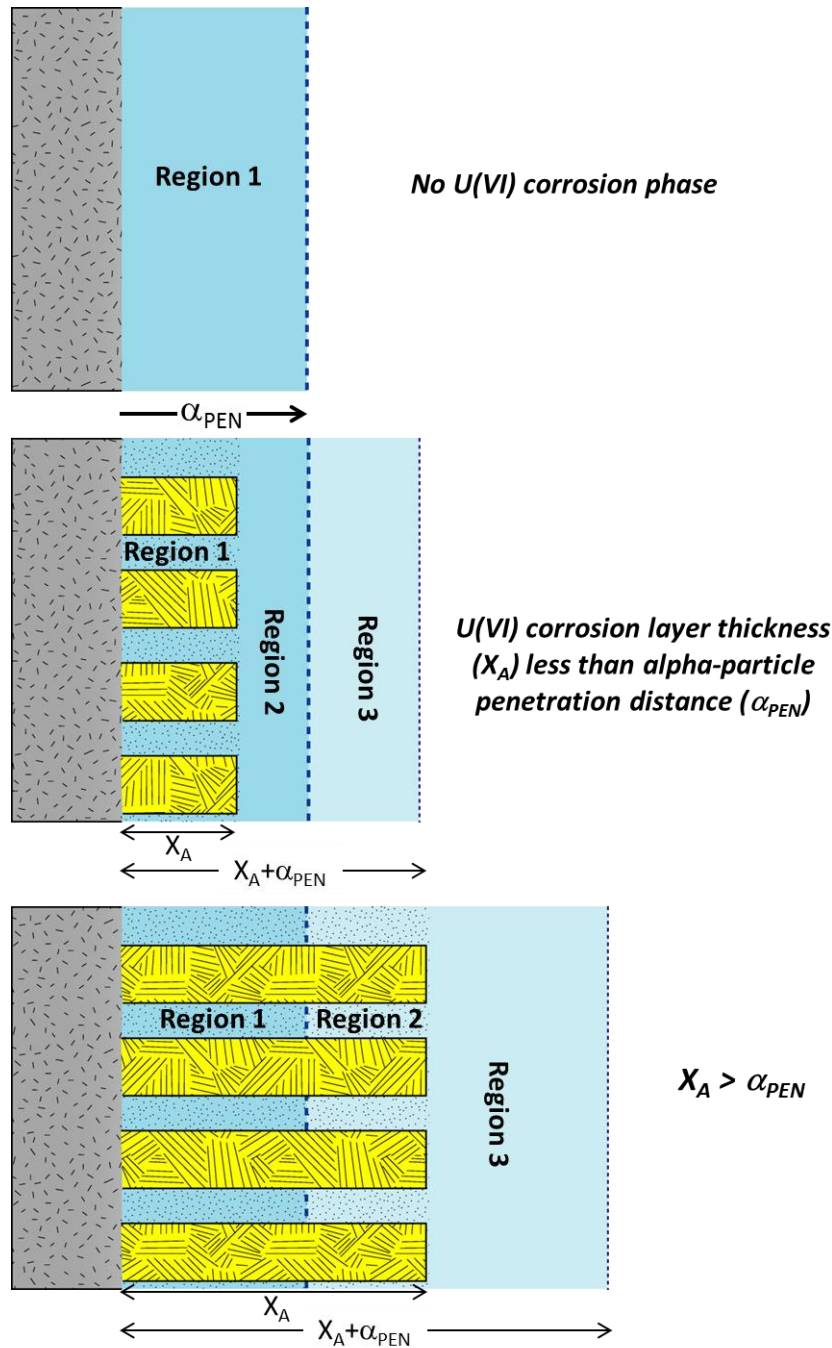


Figure 3.4-7. Schematic drawing of the alpha-radiation regions within the ANL-MPM. See Table 3.4-5 and Section 3.4.2.3 for discussion.

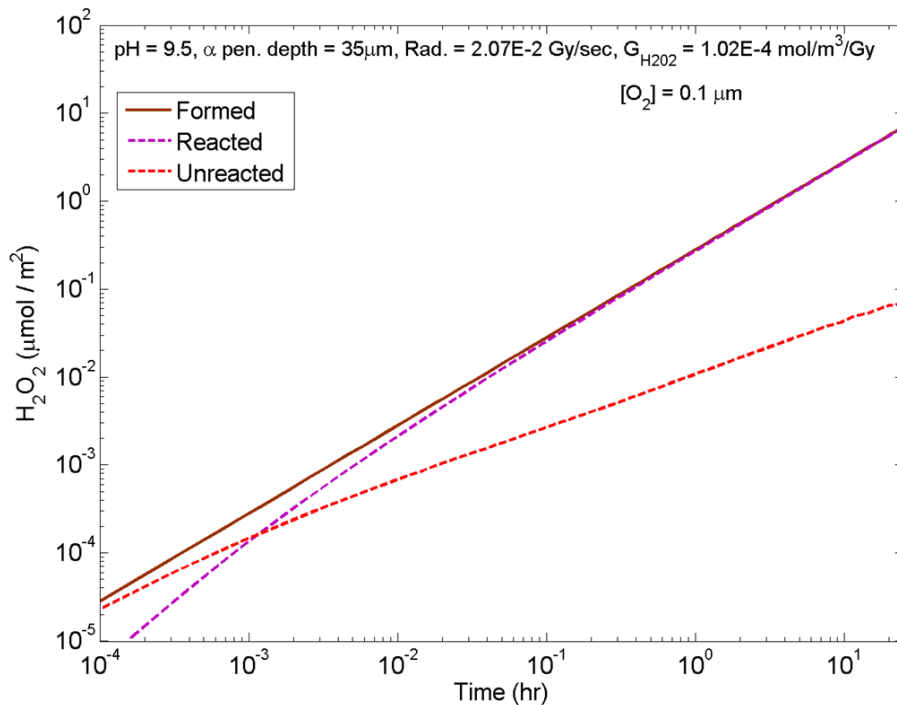


Figure 3.4-8. Moles of  $\text{H}_2\text{O}_2$  (normalized to used fuel surface area) produced by alpha-radiolysis (with no U(VI) corrosion layer present) as calculated by the ANL-MPM: the brown line is the total hydrogen peroxide formed, the red dotted line is the amount of free hydrogen peroxide and the purple dotted line is the amount of hydrogen peroxide that has been consumed through oxidative dissolution of the fuel.

### 3.4.3 Verification of ANL-MPM and Sensitivity Studies of Selected Parameters

To confirm that the scripts written in MATLAB for the ANL-MPM accurately reproduce the Canadian-MPM documented in King and Kolar (1999), King and Kolar (2003), and Shoesmith et al. (2003), the ANL-MPM was run using the same parameters and input variables that were used to produce Figs. 3.4-5, 3.4-7, 3.4-10 and 3.4-12 in the Canadian-MPM verification and validation study of King and Kolar (2002) (see Tables 3.4-1 through 3.4-5 above for parameters and input variables used).

The comparison of model results from the ANL-MPM scripts and those of the Canadian-MPM are shown in Figures 3.4-9 to 3.4-12. Unless otherwise stated the experimental data shown in Figs. 3.4-9 to 3.4-12 are from electrochemical tests performed at a pH  $\sim 9$  and  $\sim 1\text{E-}4$  molar total carbonate (King and Kolar, 2002).

The comparisons show that, within plotting errors, the ANL-MPM reproduces the Canadian-MPM results accurately. Figs. 3.4-9 to 3.4-12 also show examples of some sensitivity studies done with the ANL-MPM that are being done to identify dominant parameters and input variables. Results from the parameter/variable sensitivity studies are being used to prioritize the on-going electrochemical experimental studies (Jerden et al., 2012).

In Fig. 3.4-9, the black curve shows the results of the Canadian MPM and the red dotted curve shows the results from the ANL-MPM. The curves are identical. The blue curve is from the ANL-MPM sensitivity analyses showing how the dissolution rate of  $\text{UO}_2$  is affected by the presence of carbonate and the brown curve shows the effect of increasing temperature. Increasing the carbonate concentration and temperature can both significantly increase the predicted dissolution rate.

In Fig. 3.4-10, the black curves show results of the Canadian-MPM. The top black curve is the dissolution rate calculated using the uranyl and uranyl carbonate species, while the lower black line is calculated using uranyl carbonate only. The dashed blue and red curves show the corresponding results of the ANL-MPM, which are identical. The solid blue line (calculated using ANL-MPM) shows that decreasing the temperature by  $25^\circ\text{C}$  causes a decrease in the used fuel dissolution rate that ranges from a factor 2x at relatively low carbonate concentrations ( $1 \times 10^{-4}$  molar) to a factor of around 1.2x for relatively high carbonate concentrations (1.0 molar).

The black line in Fig. 3.4-11 shows how the corrosion potential of the  $\text{UO}_2$  fuel surface varies with increasing hydrogen peroxide concentration as calculated by the Canadian-MPM. The colored lines were calculated using the ANL-MPM. Again the main point in Fig. 3.4-11 is that for the same conditions, the ANL-MPM accurately reproduces results from the Canadian-MPM (compare black line to red dotted line).

Results from ANL-MPM sensitivity runs shown in Fig. 3.4-11 indicate that the calculated used fuel corrosion potential is sensitive to the hydrogen peroxide concentration for values less than  $1 \times 10^{-3}$  molar. Hydrogen peroxide concentrations greater than  $1 \times 10^{-3}$  molar are not expected in either Canadian or US used fuel disposal systems (King and Kolar, 2002); however, for the sake of comparing the mixed potential model predictions to experimental results, calculations were run for concentration values as high as 0.1 molar (Fig. 3.4-11). The comparison shows that when the hydrogen peroxide concentration is above  $1 \times 10^{-3}$  molar, the corrosion potential of the fuel reaches a maximum value of around 0.32 volts (SHE). The experimental  $E_{\text{CORR}}$  values that exceed the MPM predicted  $E_{\text{CORR}}$  at  $[\text{H}_2\text{O}_2] > 1 \times 10^{-2}$  molar are interpreted to be caused by localized acidification within pores at the fuel surface (King and Kolar, 2002). This type of localized acidification process, which is known to occur under highly oxidizing conditions (Shoosmith, 2000), is not accounted for in the current version of the ANL-MPM but may be readily added in future versions of the model.

Fig. 3.4-12 shows how the ratio of the rates of Reactions C/(A+B) (see Table 3.4-1; rates quantified as reaction current densities) varies with increasing hydrogen peroxide concentration. The increase in the oxidation of  $\text{H}_2\text{O}_2$  (Reaction C) normalized to the overall fuel dissolution rate (Reactions A and B) increases in a nearly linear fashion with the steady state concentration of  $\text{H}_2\text{O}_2$ . This demonstrates that not all of the radiolytic  $\text{H}_2\text{O}_2$  goes to oxidizing the used fuel, rather, some fraction of the  $\text{H}_2\text{O}_2$  produced decomposes to produce  $\text{O}_2$  at the fuel surface ( $\text{H}_2\text{O}_2 \rightarrow \text{O}_2 + 2\text{H}^+ + 2\text{e}^-$ ). When the current density ratio of the hydrogen peroxide oxidation reaction (C) to the uranium oxidation reaction (A+B) exceeds approximately 2 the slope of the curve increases. This increase, which corresponds to the establishment of the  $E_{\text{CORR}}$  plateau shown in Fig. 3.4-10, is due to fact that, at this point, most of the total anodic current density is due to  $\text{H}_2\text{O}_2$  oxidation rather than U(IV) oxidation. The dominance of the  $\text{H}_2\text{O}_2$  oxidation reaction increases with increasing hydrogen peroxide concentration.

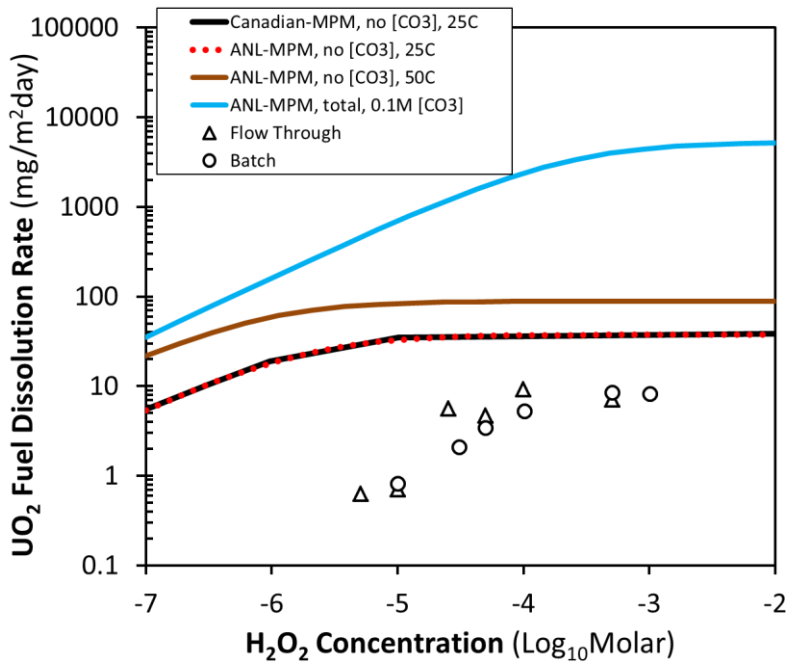


Figure 3.4-9. Comparison of results from the ANL-MPM, MATLAB scripts (colored lines) with results from the Canadian-MPM (black line) and experimental results from King and Kolar (2002).

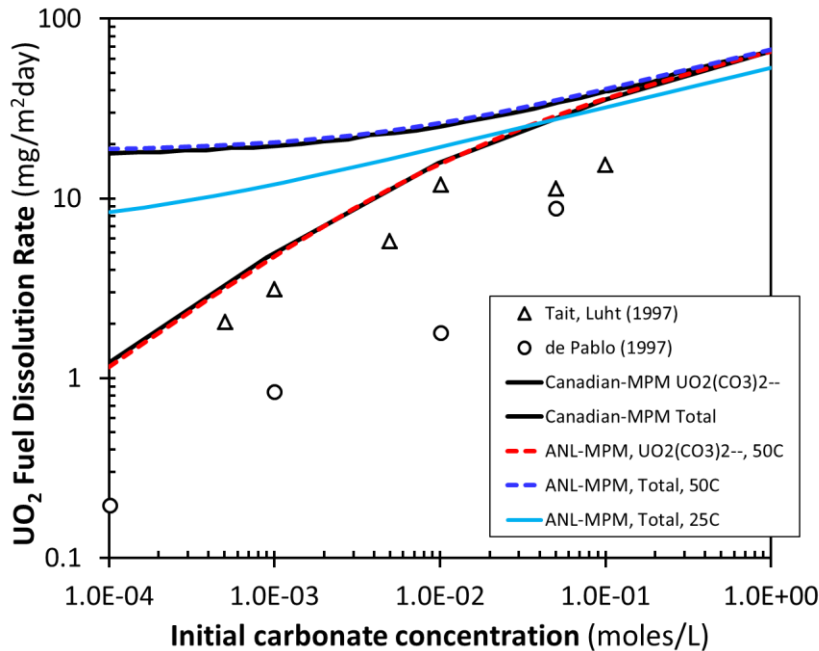


Figure 3.4-10. Comparison of results from the ANL-MPM, MATLAB scripts (colored lines) with results from the Canadian-MPM (black lines) and experimental results from King and Kolar (2002).

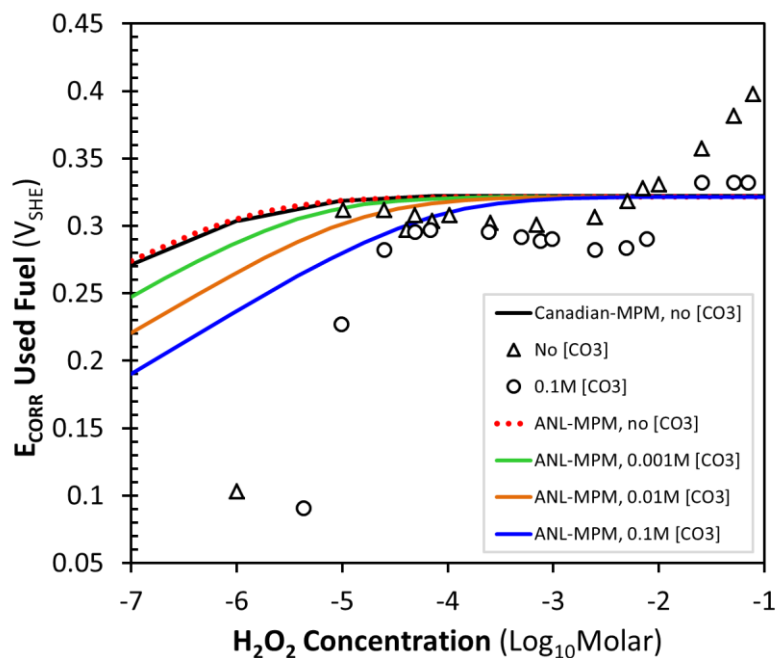


Figure 3.4-11. Comparison of results from the ANL-MPM, MATLAB scripts (colored lines) with results from the Canadian-MPM (black line) and experimental results from King and Kolar (2002).

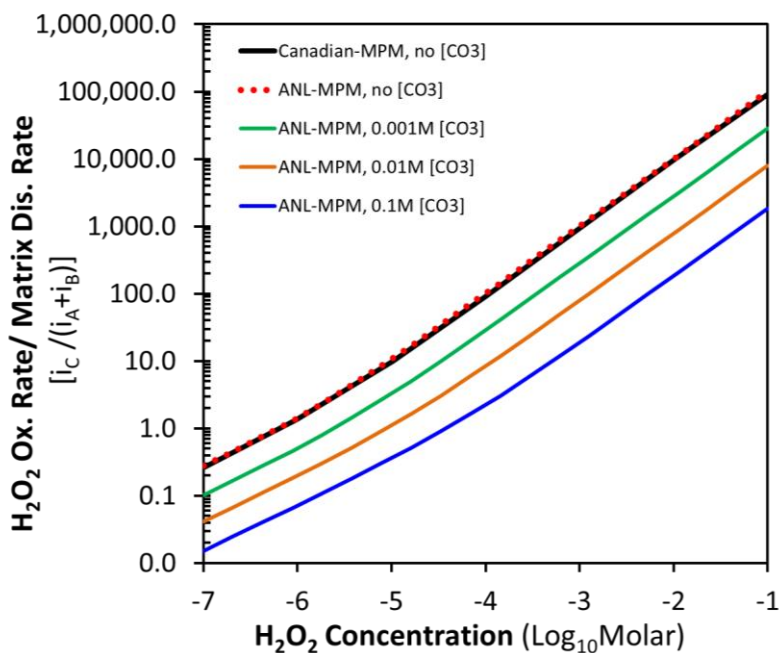


Figure 3.4-12. Comparison of results from the ANL-MPM, MATLAB scripts (colored lines) with results from the Canadian-MPM (black line) and experimental results from King and Kolar (2002).

### 3.4.4 Example Calculation of Used Fuel Matrix Degradation Rate Using the ANL-MPM

The fractional dissolution of the used fuel is calculated based on a dissolution rate provided from the ANL-MPM along with an assumed geometry for the fuel matrix. This approach allows flexibility in that the matrix dissolution rate calculation is independent of the fuel assembly and waste package geometry; therefore, a single matrix degradation rate profile may be applied to a number of candidate disposal scenario geometries at low computational cost.

Fig. 3.4-13 shows an example  $\text{UO}_2$  matrix dissolution rate profile that was calculated using the ANL-MPM for a 5000 year interval following initial exposure of the  $\text{UO}_2$  fuel to a groundwater/in-package solution consisting of an initial dissolved oxygen concentration of  $1 \times 10^{-6}$  molar and a constant dissolved carbonate concentration of  $1 \times 10^{-3}$  molar. The temperature and fuel dose profiles for this example (Fig. 3.4-14) are assumed to be identical to that of the Canadian repository scenario (King and Kolar, 1999). This assumption was made because the ANL-MPM is based on the Canadian-MPM; therefore, reproducing the results from the Canadian studies represents a further verification that the ANL-MPM accurately reproduces the experimentally validated Canadian code of King and Kolar, 1999, 2002; Shoesmith, 2003.

The matrix dissolution rate (oxidative dissolution of  $\text{UO}_2$ ) in our example is dominated by the rate of reduction of hydrogen peroxide at the  $\text{UO}_2$  surface. In this model all of the hydrogen peroxide present is produced through alpha-radiolysis (see Section 3.4.2.5. above for discussion of how  $\text{H}_2\text{O}_2$  production is modeled).

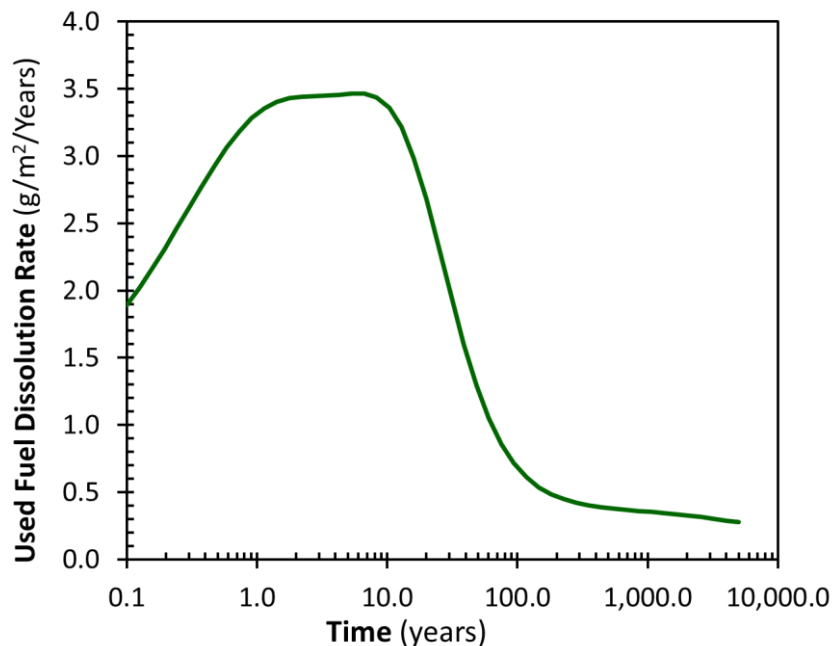


Figure 3.4-13. Dissolution rate of uranium dioxide in grams per year per square meter of exposed fuel calculated using the ANL-MPM for one millimolar dissolved carbonate (constant) and initial dissolved oxygen concentration of  $1 \times 10^{-6}$  molar. The temperature and dose profiles used for this calculation are shown in Fig. 3.4-14.

The peak in the predicted used fuel dissolution rate between 1 and 10 years (Fig. 3.4-13) corresponds to the peak in dose absorbed by the solution within 40 or so micrometers of the used fuel surface and correspondingly to the peak fuel surface temperature (Fig. 3.4-14). This initial duration (0-100 yr; i.e., 2% duration) contributes disproportionately to the total dissolution per area over the 5000 year interval (10% of the dissolution).

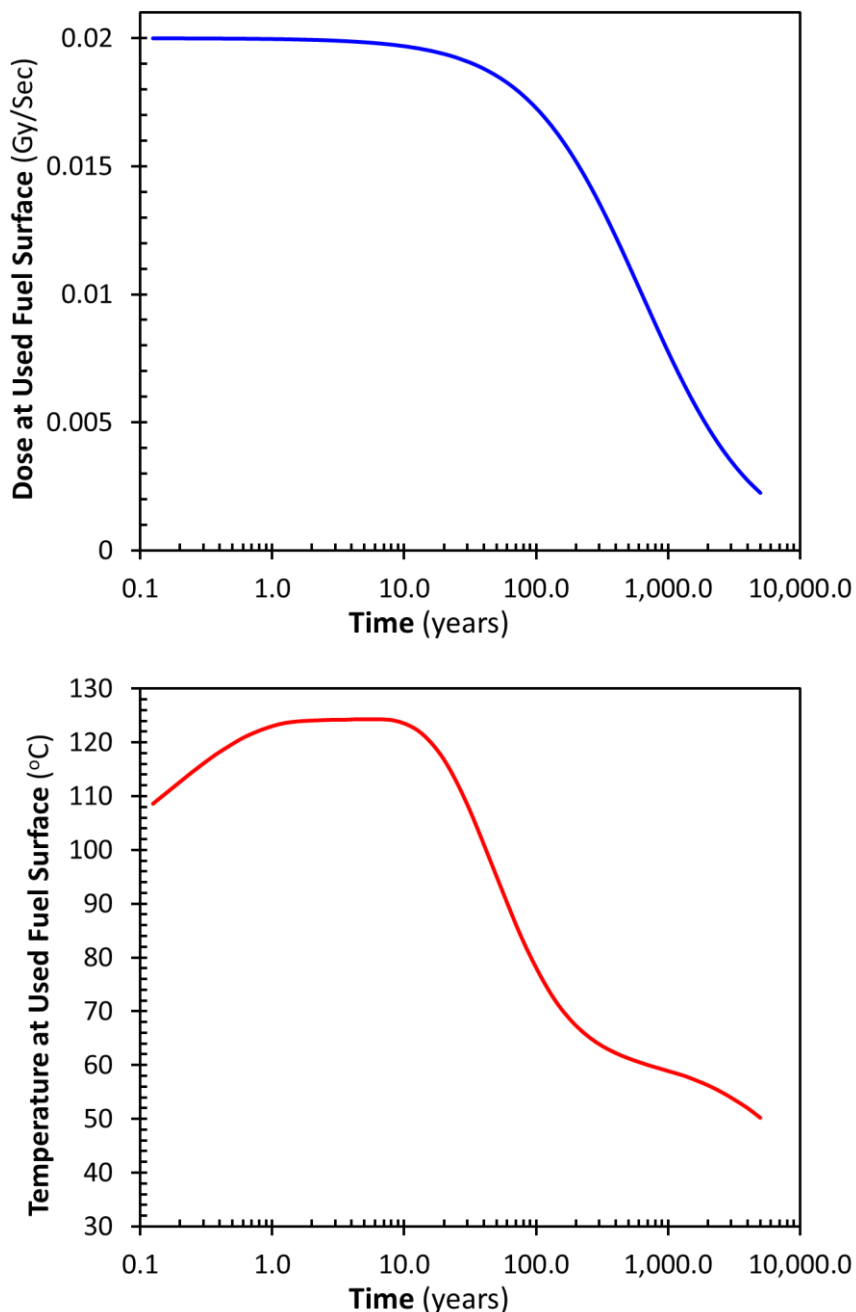


Figure 3.4-14. Time dependence of alpha-dose rate in water layer adjacent to used fuel (top) and fuel surface temperature (bottom) used in the example dissolution rate calculation shown in Fig. 3.4-13. The dose and temperature profiles are from King and Kolar (1999).

An example geometry must be assumed in order to describe how the exposed surface area changes with time. This geometry should not be smaller than the local environment length scale used in the dissolution rate calculation. Fig. 3.4-13 was produced by assuming a local environment length scale of 5 cm; that is, no other external dissolution processes are occurring within 5 cm (corresponds to horizontal length between surfaces in Figs. 3.4-3, 3.4-4 and 3.4-6). An individual spherical grain within the fuel matrix would be an inappropriate choice of geometry because it is unlikely that grain would be isolated to a distance of 5 cm.

For this example, the geometry is assumed to be a cylindrical fuel pellet with a 1 cm initial radius ( $r_0 = 1$  cm) with a height of 1 cm ( $h = 1$  cm). Dissolution occurs only along sides and excludes the top and bottom. This pellet is a plausible model for the contents of a failed fuel pin (i.e., exposed to external environment containing electrolyte). Independence of this geometry from the dissolution rate requires assuming that the spacing between failed fuel pins is sufficient that significant amounts of dissolution products from one pin are not present in the local environment of other failed pins.

Using the dissolution of a cylindrical pellet as an assumed geometry, the change in mass of this pellet due to dissolution along its sides is given in equation Eq. 3.4-27.

$$\frac{dm}{dt} = -2\pi D \sqrt{\frac{m}{\pi\rho}} \quad (\text{Eq. 3.4-27})$$

Density ( $\rho$ ) is assumed to be constant at 11 g/cm<sup>3</sup>; the dissolution rate ( $D$ ) is taken from the data presented in Fig. 3.4-1. This density implies an initial pellet mass of 34.6 g (i.e.,  $m_0 = 11\pi$  g)

Fractional degradation ( $f$ ) can then be expressed as in equation Eq. 3.4-28.

$$\sqrt{1-f} = 1 + \int_0^t -D \sqrt{\frac{\pi h}{\rho m_0}} dt \quad (\text{Eq. 3.4-28})$$

Equation Eq. 3.4-28 can be rewritten using the specific constants selected above.

$$\sqrt{1-f} = 1 + \int_0^t \frac{-D}{11 \cdot 100^2} dt \quad (\text{Eq. 3.4-29})$$

Fractional dissolution as a function of time calculated according to equation Eq. 3.4-29 is shown in Fig. 3.4-15 as the solid line labeled “Variable”. The rate of dissolution is approximately constant after the first hundred years, and is sufficiently slow that the surface area of the pellet does not change significantly. Assuming both a constant surface area and constant dissolution



rate over the 5000 year interval produces the dashed line in Fig. 3.4-15 labeled “Constant”. This example shows that simplifying the calculation using constant values results in a non-conservative fractional dissolution rate. This observation emphasizes the importance of using a fuel matrix degradation model such as the ANL-MPM that accounts for the inter-dependent; time-variable processes (e.g., dose rate and temperature dependence of  $H_2O_2$  production and reaction rates).

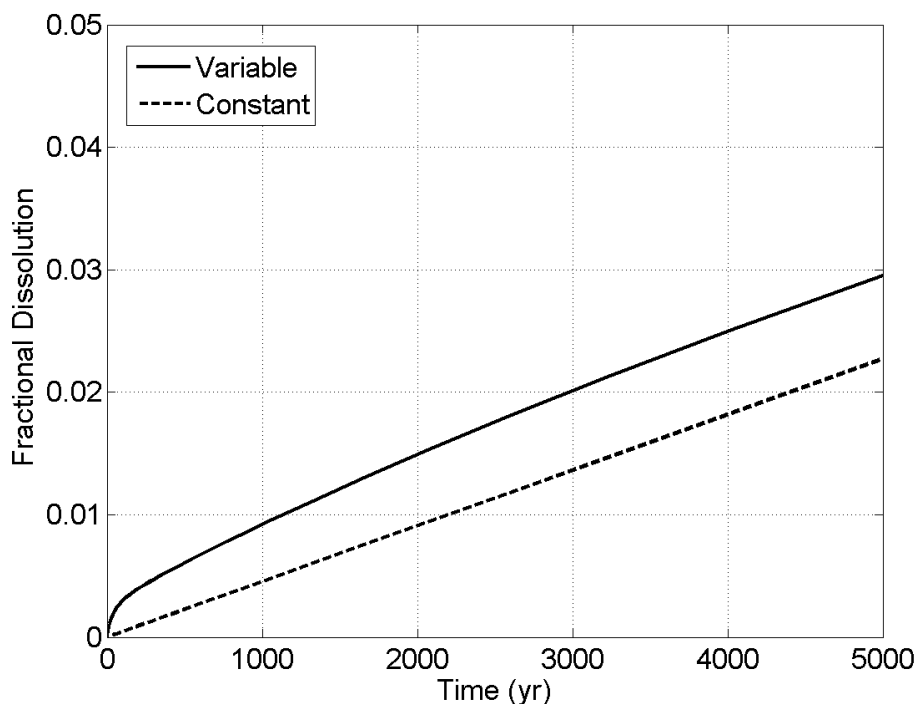


Figure 3.4-15. Fractional dissolution of cylindrical uranium dioxide pellet as a function of time calculated using the ANL-MPM and an assumed geometry described equations Eq. 3.4-27 to Eq. 3.4-29.

### 3.4.5 Conceptual Approach for Effects of NMP-Catalyzed Reactions

The conceptual approach for incorporating the catalytic effects of the NMP into the ANL-MPM is shown schematically Fig. 3.4-16 and the reactions are shown in Table 3.4-6. Fig. 3.4-17 shows a detailed view of the process of interest (top diagram) as well as a schematic of the electrochemical experimental set-up that is being used to provide parameter values for the model (Fig. 3.4-17 bottom diagram). As shown in Fig. 3.4-16 the main new feature of the extended ANL-MPM is the incorporation of the NMP surface as a separate domain at the used fuel/solution interface which is electrically coupled to the used fuel matrix by a user specified resistance. This two domain electrochemical concept is paralleled by our experimental set up (Jerden et al., 2012), which is shown schematically in Fig. 3.4-17 (bottom diagram).

Fig. 3.4-15 represents the possible result of the catalysis of  $H_2$  oxidation at the NMP surfaces, namely, the inhibition of oxidative dissolution of the fuel surface due to rapid reductive destruction of  $H_2O_2$  in Reaction D\* and  $O_2$  in Reaction E\* (not shown) at the fuel surface by

electrons supplied by the catalyzed oxidation of  $H_2$  in Reaction L\* at the NMP surface and the galvanic protection of the fuel from corrosion.

Table 3.4-6. Extension of ANL-MPM parameter database to account for oxidation and reduction reactions that may be catalyzed on noble metal particle surfaces.

<b>Anodic reactions on NMP</b>	Reaction label (Fig. 12)	25°C Rate const: $K_i$ ( $s^{-1}$ )	Activation energy for $k_i$ : $\Delta Hk_i$ (J/mol)	Charge Transfer coefficient: $\alpha_i$	25°C Stand. Pot: $E_i^0$ ( $V_{SCE}$ )	T dependence of $E^0$ : $\Delta E_i^0$ ( $V_{SCE}/K$ )
$H_2O_2 \rightarrow O_2 + 2H^+ + 2e^-$	<b>C*</b>	Experiment <sup>I</sup>	Experiment <sup>I</sup>	Experimental (Tafel analyses) <sup>I</sup>	Literature	Literature
$H_2 \rightarrow 2H^+ + 2e^-$	<b>L*</b>	~0.5 <sup>II</sup>	Experiment <sup>I</sup>	Experimental (Tafel analyses) <sup>I</sup>	Literature	Literature
<b>Cathodic reactions on NMP</b>						
$H_2O_2 + 2e^- \rightarrow 2OH^-$	<b>D*</b>	~0.5 <sup>II</sup>	Experiment <sup>I</sup>	Experimental (Tafel analyses) <sup>I</sup>	Literature	Literature
$O_2 + 2H_2O + 4e^- \rightarrow 4OH^-$	<b>E*</b>	Experiment <sup>I</sup>	Experiment <sup>I</sup>	Experimental (Tafel analyses) <sup>I</sup>	Literature	Literature

**I.** Electrochemical experiments initiated in FY-2012 are focused on providing unknown parameter values for the ANL-MPM as well as confirming literature values that are currently being used (Jerden et al., 2012).

**II.** Calculated from the work of Nilsson and Jonsson, 2008.

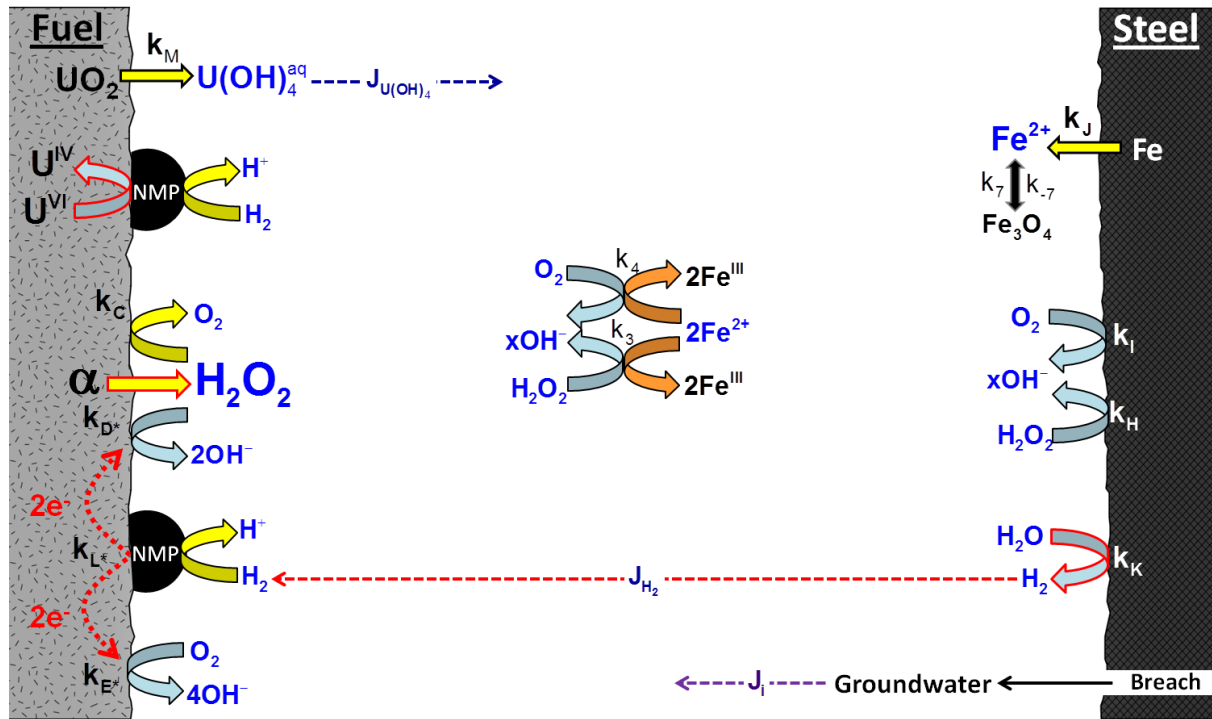


Figure 3.4-16. Simplified reaction scheme (not showing all component fluxes) used in the ANL-MPM modified to include catalytic roles of NMP.

The top schematic in Fig. 3.4-17 highlights the role of the NMP in electrochemically “protecting” the  $\text{UO}_2$  fuel from oxidative dissolution. On the right side, electrons released during the oxidation of  $\text{H}_2$  on the NMP surface can be used to reduce  $\text{U(VI)}$  at the surface back to  $\text{U(IV)}$  and counter the corrosive effect of  $\text{H}_2\text{O}_2$  reduction in Reaction D. On the left side, the NMP catalyzes the decomposition of  $\text{H}_2\text{O}_2$  (Reaction D\*) to lessen the effect of Reaction D. The lower diagram of Fig. 3.4-17 describes the experimental approach that is being taken to quantify key surface redox phenomena (Table 3.4-6, for discussion see Jerden et al., 2012). The NMP and  $\text{UO}_2$  are physically separated but coupled chemically by the common solution and electrically by the potentiostats, but the currents for each reaction can be distinguished. Note that Reaction D\* will occur in the experiments but not be detected electrochemically. The effect of Reaction D\* will be detected by any decrease in the dissolution of  $\text{UO}_2$ , for example, when the potential on the NMP electrode is increased to slow Reaction L\* or when no  $\text{H}_2$  is added to the solution.

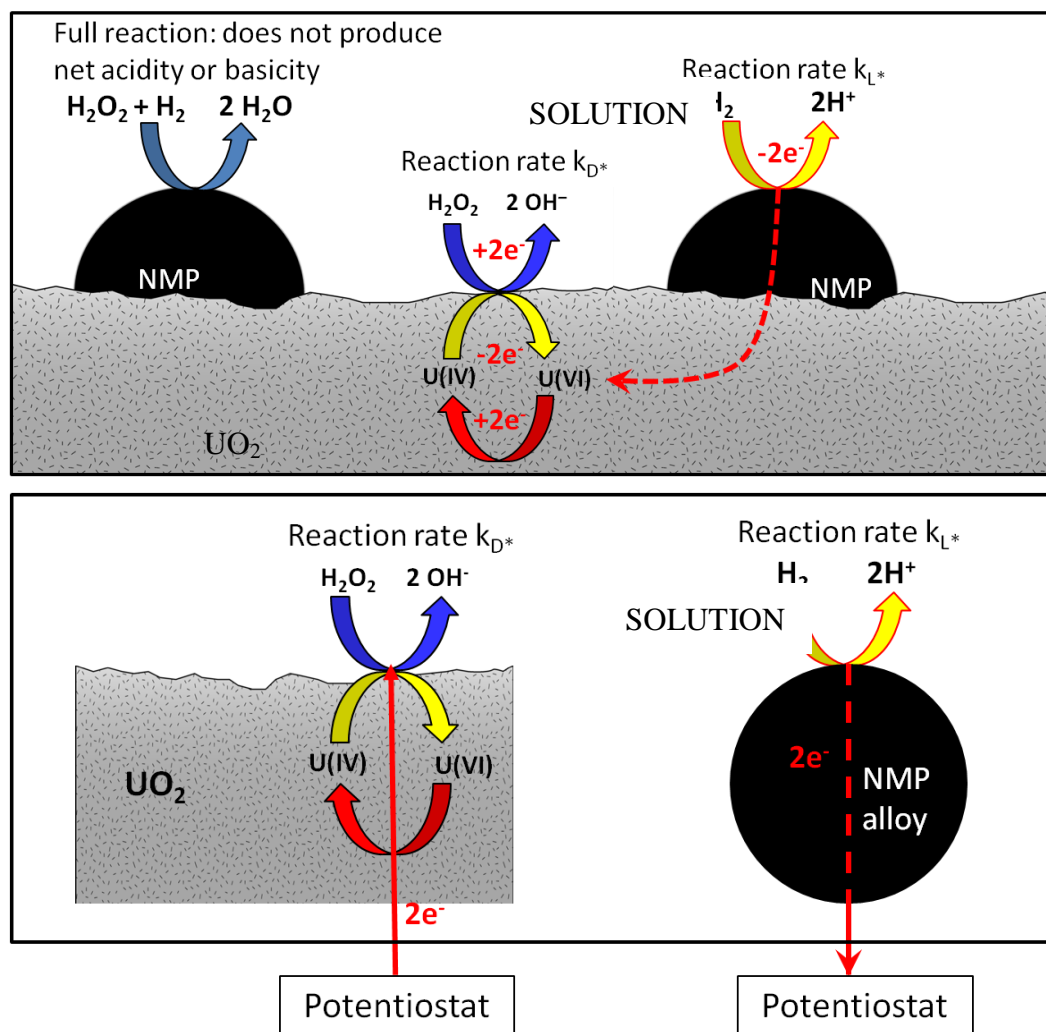


Figure 3.4-17. Schematic representation highlighting the process of interest for the ANL study (top) and the basic experimental approach that will be used (bottom).

The ongoing electrochemical experiments (Jerden et al., 2012) involve measuring reaction current densities, corrosion potentials, and released elemental masses from the  $UO_2$  and NMP alloy electrodes under a relevant range of controlled conditions. The experimental results will be used to implement and validate the NMP module for the ANL-MPM for fuel degradation.

### 3.4.6 Summary and Interface with Generic Performance Assessment Models

The ANL-MPM will provide a fractional matrix degradation rate of used fuel for a specific set of environmental/in-package conditions. These specific environmental conditions will define what ANL-MPM parameter set is used for the used fuel dissolution rate calculation. A library of appropriate parameter sets is the focus of on-going and future experimental work for this project.

The used fuel dissolution rate is calculated on a per surface area basis using the ANL-MPM, where the evolution of the reactive surface area with time is determined by a separate model (e.g., see example discussed in Section 3.4.4 above). The combination of the used fuel dissolution rate from the ANL-MPM and the surface area model is used to determine the overall fractional matrix degradation rate. Source terms for radionuclides are calculated as the product of the fractional degradation rate and radionuclide inventory. Fractional release rates are calculated as the product of the degradation rate and specific surface area.

The used fuel matrix degradation rate and/or the radionuclide source term model results can be treated as direct inputs into the Generic Performance Assessment Model. The resulting radionuclide release rates will have a strong scientific basis as they are ultimately based on the fundamental electrochemical and thermodynamic principles underlying the ANL-MPM.

### 3.4.7 References for Section 3.4

- Amme, M., 2002, Contrary Effects of the Water Radiolysis Product  $H_2O_2$  Upon the Dissolution of Nuclear Fuel in Ground Water and Deionized Water, *Radiochimica Acta*, 90, p. 399-406.
- Amme, M., Renker, B., Schmid, B., Feth, M.P., Bertagnolli, H., Döbelin, W., 2002, Raman Microspectrometric Identification of Corrosion Products Formed on  $UO_2$  Nuclear Fuel During Leaching Experiments, *Journal of Nuclear Materials*, 306, p. 202-212.
- ASTM (2010) *Annual Book of ASTM Standards, Vol. 12.01*, West Conshohocken, Pennsylvania: ASTM-International.
- Barner, J.O., 1985, *Characterization of LWR Spent Fuel MCC-Approved Testing Material-ATM-101*. PNL-5109, Rev. 1. Richland, Washington: Pacific Northwest Laboratory.
- Bethke, C. M., 2009, *The Geochemist's Workbench® Release 8.0 (four volumes)*, Hydrogeology Program, University of Illinois, Urbana, Illinois
- Bethke, C.M., 2008, *Geochemical and Biogeochemical Reaction Modeling*, Cambridge University Press, New York, 543 p.
- Bergel, A., Feron, D., Mollica, A., 2005, Catalysis of Oxygen Reduction in PEM Fuel Cell by Seawater Biofilm, *Electrochemistry Communications*, 7, p. 900-904.
- Broczkowski, M.E., Keech, P.G., Noel, J.J., Shoesmith, D.W., 2010, Corrosion of Uranium Dioxide Containing Simulated Fission Products in Dilute Hydrogen Peroxide and Dissolved Hydrogen, *Journal of The Electrochemical Society*, 157, p. C275-C281.
- Broczkowski, M.E., Noel, J.J., Shoesmith, D.W., 2007a, The influence of dissolved hydrogen on the surface composition of doped uranium dioxide under aqueous corrosion conditions, *Journal of Electroanalytical Chemistry*, 602, p. 8-16.
- Broczkowski, M.E., Noel, J.J., Shoesmith, D.W., 2007b, The influence of temperature on the anodic oxidation/dissolution of uranium dioxide, *Electrochimica Acta*, 52, p. 7386-7395.
- Brokris, J. O'M, Reddy, A.K.N., 1977, *Modern Electrochemistry*, John Wiley and Sons, New York.
- BSC, 2004, CSNF Waste Form Degradation: Summary Abstraction, Bechtel SAIC Co. report ANL-EBS-MD-000015 REV02.
- Carbol, P., Fors, P., Gouder, T., Spahiu, K., 2009a, Hydrogen suppresses  $UO_2$  corrosion, *Geochimica et Cosmochimica Acta*, 73, p. 4366-4375.
- Carbol, P., Fors, P., Van Winckel, S., Spahiu, K., 2009b, Corrosion of Irradiated MOX Fuel in Presence of Dissolved  $H_2$ , *Journal of Nuclear Materials*, 392, p. 45-54.
- Casas, I., Giménez, J., Martí, V., Torrero, M.E., de Pablo, J., 1994, Kinetic Studies of Unirradiated  $UO_2$  Dissolution Under Oxidizing Conditions in Batch and Flow Experiments, *Radiochimica Acta*, 66/77, p. 23-27.
- Choudhary, V.R., Samanta, C., Choudhary, T.V., 2006, Factors Influencing Decomposition of  $H_2O_2$  over Supported Pd Catalyst in Aqueous Medium, *Journal of Molecular Catalysis A: Chemical*, 260, p. 115-120.

- Choudhary, V.R., Samanta, C., 2006, Role of Chloride or Bromide Anions and Protons for Promoting the Selective Oxidation of  $H_2$  by  $O_2$  to  $H_2O_2$  Over Supported Pd Catalysts in an Aqueous Medium, *Journal of Catalysis*, 238, p. 28-38.
- Clarens, F., De Pablo, J., Casas, I., Giménez, J., Rovira, M., Merino, J., Cera, E., Bruno, J., Quiñones, J., Clarens, F., Martínez-Esparza, A., 2005, The oxidative dissolution of unirradiated  $UO_2$  by hydrogen peroxide as a function of pH, *Journal of Nuclear Materials*, 345, p. 225-231,
- Christensen, H., Sunder, S., 2000, Current State of Knowledge of Water Radiolysis Effects on Spent Nuclear Fuel Corrosion, *Nuclear Technology*, 131, (1), p. 102-123.
- Cui, D., Eriksen, T., Eklund, U-B, 2001, On Metal Aggregates in Spent Fuel, Synthesis and Leaching of Mo-Ru-Pd-Rh Alloy, *Mat. Res. Soc. Proc.*, 663, 427 doi:10.1557/PROC-663-427.
- Cui, D., Low, J., Sjostedt, C.J., Spahiu, K., 2004, On Mo-Ru-Tc-Pd-Rh-Te Alloy Particles Extracted from Spent Fuel and Their Leaching Behavior Under Ar and  $H_2$  Atmospheres, *Radiochimica Acta*, 92, p. 551-555.
- Cui, D., Low, J., Rondinella, V.V., Spahiu, K., 2010, Hydrogen catalytic effects of nanostructured alloy particles in spent fuel on radionuclide immobilization, *Applied Catalysis B: Environmental*, 94, p. 173-178.
- Cui, D., Low, J., Spahiu, K., 2011, Environmental Behaviors of Spent Nuclear Fuel and Canister Materials, *Energy & Environmental Science*, DOI: 10.1039/c0ee00582g
- Cui, D., Rondinella, V.V., Fortner, J.A., Kropf, A.J., Eriksson, L., Wronkiewicz, D.J., Spahiu, K., 2012, Characterization of alloy particles extracted from spent nuclear fuel, *Journal of Nuclear Materials*, 420, p. 328-333.
- Cunnane, J.C., Fortner, J.A, Finch, R., 2003, The behavior of light water reactor fuel after the cladding is breached under unsaturated test conditions, *MRS Symposium Proceedings*, 757, p. 385-392.
- Dehaut, P., (2001), Physical and Chemical State of the Nuclear Spent Fuel after Irradiation, Subsection 5.2 of Intrinsic Evolution of Spent Nuclear Fuel in a Closed System (2<sup>nd</sup> Subprogram) in *Synthesis on the Long Term Behavior of the Spent Nuclear Fuel*. Poinssot, C., ed. CEA-R-5958(E). Volume II. Paris, France: Commissariat à l'Énergie Atomique.
- DOE, 2010, *Next Generation Nuclear Plant*, A Report to Congress prepared by DOE, Office of Nuclear Energy, April 2010.
- Ekroth, E, Roth, O., Jonsson, M., 2006, The relative impact of radiolysis products in radiation induced oxidative dissolution of  $UO_2$ , *Journal of Nuclear Materials*, 355, p. 38-46.
- Eriksen, Jonsson, T.M., Merino, J., 2008, Modeling of time resolved and long contact time dissolution studies of spent nuclear fuel in 10 mM carbonate solution – A comparison between two different models and experimental data, *Journal of Nuclear Materials*, 375, p. 331-339.
- Ferry, C., Poinssot, C., Cappelaere, C., Desgranges, L., Jegou, C., Miserque, F., Piron, J.P., Roudil, D., Gras, J-M, 2006, Specific Outcomes of the Research on the Spent Fuel Long-



- Term Evolution in Interim Dry Storage and Deep Geological Disposal, *Journal of Nuclear Materials*, 352, p. 246-253.
- Ferry, C., Piron, J.P., Ambard, A., 2010, Effect of Helium on the Microstructure of Spent Fuel in a Repository: An Operational Approach, *Journal of Nuclear Materials*, 407, p. 100-109.
- Fors, P., Carbol, P., Van Winckel, S. Spahiu, K., 2009, Corrosion of high burn-up structured UO<sub>2</sub> fuel in presence of dissolved H<sub>2</sub>, *Journal of Nuclear Materials*, 394, p. 1-8.
- Fortner, J.A., Kropf, A.J., Finch, R.J., Cunnane, J.C., 2004, Technetium and Molybdenum in Oxide Spent Nuclear Fuel: Impact on Release Estimates, *Material Research Society Symposium Proceedings*, 824, p. 107-112.
- Freeze, G., Mariner, P., Houseworth, J., Cunnane, J., Caporuscio, F., 2010, Used Fuel Disposition Campaign Features, Events, and Processes (FEPs): FY10 Progress Report, August 2010.
- Gauthier-Lafaye, F., Blanc, P.L., 2006, Natural fission reactors in the Franceville basin, Gabon: A review of the conditions and results of a 'critical event' in a geologic system, *Geochimica et Cosmochimica Acta*, 60, p 4831-4852.
- Goldik, J.S., Nesbitt, H.W., Noël, J.J., Shoesmith, D.W., 2004, Surface electrochemistry of UO<sub>2</sub> in dilute alkaline hydrogen peroxide solutions, *Electrochimica Acta*, 49, p. 1699–1709.
- Goldik, J. S., Noël, J.J., Shoesmith, D.W., 2006, The Effects of Simulated Fission Products in the Reduction of Hydrogen Peroxide on Simulated Nuclear Fuel Electrodes, *Journal of The Electrochemical Society*, 153, p. E151-E159.
- Gouder, T., Seibert, A., Havela, L., Rebizant, J., 2007, Search for Higher Oxides of Pu: A Photoemission Study, *Surface Science*, 601, L77.
- Grambow, B., Mennecart, T., Fattahi, M., Blondiaux, B., 2004, Electrochemical Aspects of Radiolytically Enhanced UO<sub>2</sub> Dissolution, *Radiochimica Acta*, 92, p. 603-609.
- Grenthe, I., Fuger, J., Konings, R.J.M., Lemire, R.J., Muller, A.B., Nguyen-Trung, C., Wanner, H., 1992, *Chemical Thermodynamics Volume 1, Chemical Thermodynamics of Uranium* NEA OECD, North-Holland, Amsterdam.
- Guillaumont, R., Fanghanel, T., Fuger, J., Grenthe, I., Neck, V., Palmer, D.A., Rand, M.H., Mompean, F.J., Domenech-Orti, C., Ben-Said, K., Illemass, M., 2003, *Chemical Thermodynamics Volume 5, Update on the Chemical Thermodynamics of Uranium, Neptunium, Plutonium, Americium and Technetium: Chemical Thermodynamics of Uranium* NEA OECD, Elsevier Science, The Netherlands, Amsterdam.
- Guenther, R.J., Blahnik, D.E., Campbell, T.K., Jenquin, U.P., Mendel, J.E., Thornhill, C.K., 1988, *Characterization of Spent Fuel Approved Testing Material—ATM-106*. PNL-5109-106. Richland, Washington: Pacific Northwest Laboratory.
- Haschke, J.M., Allen, T.H., Morales, L.A., 2000, Reaction of Plutonium Dioxide with Water: Formation and Properties of PuO<sub>2+x</sub>, *Science*, 287, p. 285
- He, H., Keech, P., Broczkowski, M.E., Noel, J.J., Shoesmith, D.W., 2007, Characterization of the Influence of Fission Product Doping on the Anodic Reactivity of Uranium Dioxide, *Canadian Journal of Chemistry*, 85, p. 702-713.

- He, H., Zhu, R.K., Qin, Z., Keech, P., Ding, Z., Shoesmith, D.W., 2009a, Determination of Local Corrosion Kinetics on Hyper-Stoichiometric  $\text{UO}_{2+x}$  by Scanning Electrochemical Microscopy, *Journal of The Electrochemical Society*, 156, p. C87-C94.
- He, H., Ding, Z., Shoesmith, D.W., 2009, The determination of electrochemical reactivity and sustainability on individual hyper-stoichiometric  $\text{UO}_{2+x}$  grains by Raman microspectroscopy and scanning electrochemical microscopy, *Electrochemistry Communications*, 11, p. 1724–1727.
- G. Heisbourg, Hubert, S., Dacheux, N., Purans, J., 2004, Kinetic and thermodynamic studies of the dissolution of thoria-urania solid solutions *Journal of Nuclear Materials*, 335, 5 -13.
- Hettiarachchi, S., 2005, BWR SCC Mitigation Experiences with Hydrogen Water Chemistry, *Proceedings of the 12th International Conference on Environmental Degradation of Materials in Nuclear Power System – Water Reactors* –Edited by T.R. Allen, P.J. King, and L. Nelson TMS (The Minerals, Metals & Materials Society), p. 685-701.
- Hossain, M. M., Ekeroth, E., Jonsson, M., 2006, Effects of  $\text{HCO}_3^-$  on the kinetics of  $\text{UO}_2$  oxidation by  $\text{H}_2\text{O}_2$ , *Journal of Nuclear Materials*, 358, p. 202-208.
- Jerden, J., Fortner, J.A., Cruse, T., Cunnane, J., 2011, *Repository Science/Waste Form Degradation & Radionuclide Mobilization*, Prepared for U.S. Department of Energy Used Fuel Disposition Campaign, Argonne National Laboratory Milestone Report M41UF030701 for the work package: FTAN11UF0307, July, 2011.
- Jerden, J., Fortner, J.A., Cruse, T., Frey, K., Ebert, W., 2012, *Experimental Plan for ANL Electrochemical Corrosion Studies*, Prepared for U.S. Department of Energy Used Fuel Disposition Campaign, Argonne National Laboratory Milestone Report FCRD-USED-2012-000, January 6, 2012
- Jégou, C., Muzeau, B., Broudic, V., Roudil, D., Deschanel, X., 2007, Spent Fuel  $\text{UO}_2$  Matrix Alteration in Aqueous Media Under Oxidizing Conditions, *Radiochimica. Acta*, 95, p. 513-522.
- Jové Colón, C. F., F. A. Caporuscio, S. S. Levy, H. Xu, J.A. Blink, W. G. Halsey, T. Buscheck, M. Sutton, M. A. Serrano de Caro, T. J. Wolery, Hui-Hai Liu, J. Birkholzer, C. I. Steefel, J. Rutqvist, Chin-Fu Tsang, E. Sonnenthal, 2010, Disposal System Evaluation and Tool Development – Engineered Barrier System (EBS) Evaluation, 204 pp.
- Johnson, L., Ferry, C., Poinssot, C., Lovera, P., 2005, Spent fuel radionuclide source term model for assessing spent fuel performance in geological disposal. Part I: Assessment of the Instant Release Fraction, *Journal of Nuclear Materials*, 346, p. 66-77.
- Jonsson, M., Nielsen, F., Roth, O., Ekeroth, E., Nilsson, S., Hossain, M.M, 2007, Radiation Induced Spent Nuclear Fuel Dissolution under Deep Repository Conditions, *Environmental Science and Technology*, 41, p. 7087-7093.
- Kaye, M.H., Lewis, B.J., Thompson, W.T., 2007, Thermodynamic treatment of noble metal fission products in nuclear fuel, *Journal of Nuclear Materials*, 366, p. 8–27.

- King, F., Kolar, M., 1999, Mathematical Implementation of the Mixed-Potential Model of Fuel Dissolution Model Version MPM-V1.0, Ontario Hydro, Nuclear Waste Management Division Report No. 06819-REP-01200-10005 R00.
- King, F., Kolar, M., 2002, Validation of the Mixed-Potential Model for Used Fuel Dissolution Against Experimental Data, Ontario Hydro, Nuclear Waste Management Division Report No. 06819-REP-01200-10077-R00.
- King, F., Kolar, M., 2003, The Mixed-Potential Model for UO<sub>2</sub> Dissolution MPM Versions V1.3 and V1.4, Ontario Hydro, Nuclear Waste Management Division Report No. 06819-REP-01200-10104 R00.
- Keech, P.G., Noël, J.J., Shoesmith, D.W., 2008, The electrochemical reduction of hydrogen peroxide on uranium dioxide under intermediate pH to acidic conditions, *Electrochimica Acta*, 53, p. 5675–5683.
- Kelm, M., Metz, V., Bohnert, E., Janata, E., Bube, C., 2011, Interaction of Hydrogen with Radiolysis Products in NaCl Solution – Comparing Pulse Radiolysis Experiments with Simulations, *Radiation Physics and Chemistry*, 80, p. 426-434.
- Kleykamp, H., 1985, The chemical state of the fission products in oxide fuels, *Journal of Nuclear Materials*, 131, p. 221-246.
- Kleykamp, H., Paschoal, J.O., Pejisa, R., Thummler, F., 1985, Composition and Structure of Fission-Product Precipitates in Irradiated Oxide Fuels - Correlation with Phase Studies in the Mo-Ru-Rh-Pd and BaO-UO<sub>2</sub>-ZrO<sub>2</sub>-MoO<sub>2</sub> Systems, *Journal of Nuclear Materials*, 130, p. 426-33.
- Kleykamp, H., 1989, Constitution and Thermodynamics of the Mo-Ru, Mo-Pd, Ru-Pd, and Mo-Ru-Pd Systems, *Journal of Nuclear Materials*, 167, p. 49-63.
- Kropf, A.J., Fortner, J. A., Finch, R.J., Cunnane, J.C., Karanfil, C., 2004, A Bent Silicon Crystal in the Laue Geometry to Resolve Actinide X-Ray Fluorescence for X-Ray Absorption Spectroscopy, *Physica Scripta*, T115, p. 998.
- Kubatko, K. H., Helean, K. B., Navrotsky, A., Burns, P.C., 2003, Stability of Peroxide-Containing Uranyl Minerals, *Science*, 302, p. 1191-1193.
- Lemire, R.J., Garisto, F., 1989, The solubility of U, Np, Pu, Th and Tc in a geological disposal vault for used nuclear fuel. Atomic Energy of Canada Limited Report, AECL- 10009.
- R. J. Lemire, Fuger, J., Nitsche, H., Potter, P., Rand, M.H., Rydberg, J., Spahiu, K., Sullivan, J.C., Ullman, W.J., Vitorge, P., Wanner, H., 2001, *Chemical Thermodynamics Volume 4, Chemical Thermodynamics of Neptunium and Plutonium*, NEA OECD, Elsevier Science, The Netherlands, Amsterdam, 872 pages.
- Li, J., Staykov, A., Ishihara, T., Yoshizawa, K., 2011, Theoretical Study of the Decomposition and Hydrogenation of H<sub>2</sub>O<sub>2</sub> on Pd and Au Pd Surfaces: Understanding toward High Selectivity of H<sub>2</sub>O<sub>2</sub> Synthesis, *Journal of Physical Chemistry C*, 115, p. 7392-7398.
- Lousada, C., Jonsson, M., 2010, Kinetics, Mechanism, and Activation Energy of H<sub>2</sub>O<sub>2</sub> Decomposition on the Surface of ZrO<sub>2</sub>, *Journal of Physical Chemistry C*, 114, p. 11202-11208.

- Merino, J., Cera, E., Bruno, J., Quiñones, J., Casas, I., Clarens, F., Giménez, J., de Pablo, J., Rovira, M., Martínez-Esparza, A., 2005, Radiolytic modeling of spent fuel oxidative dissolution mechanism, Calibration against UO<sub>2</sub> dynamic leaching experiments, *Journal of Nuclear Materials*, 346, p. 40-47.
- Metz V., Loida, A., Bohnert, E., Schild, D., Dardenne, K., 2008, Effects of Hydrogen and Bromide on the Corrosion of Spent Nuclear Fuel and  $\gamma$ -Irradiated UO<sub>2</sub>(s) in NaCl Brine, *Radiochimica Acta*, 96, p. 637-648.
- Nagra, 2005, Spent Fuel Evolution under Disposal Conditions – Synthesis of Results from the EU Spent Fuel Stability (SFS) Project, Technical Report 04-09.
- OECD/NEA/IGSC, 2011, R&D for Geological Repositories – Status and Prospects in NEA Countries (draft report), March 2011.
- Neck, V., Altmaier, M., Fanghänel, Th., 2007, Thermodynamic data for hydrous and anhydrous PuO<sub>2+x</sub>(s), *Journal of Alloys and Compounds*, 444-445, p. 464-469.
- Nielsen, F., Ekeröth, E., Erikwen, T. Ee., Jonsson, M., 2008, Simulation of radiation induced dissolution of spent nuclear fuel using the steady-state approach. A comparison to experimental data, *Journal of Nuclear Materials*, 374, p. 286-289.
- Nielsen, F. Jonsson, M., 2006, Geometrical  $\alpha$  and  $\beta$ -dose distributions and production rates of radiolysis products in water in contact with spent nuclear fuel, *Journal of Nuclear Materials*, 359, p. 1-7.
- Nielsen, F., Jonsson, M., 2008, Simulations of H<sub>2</sub>O<sub>2</sub> concentration profiles in the water surrounding spent nuclear fuel taking mixed radiation fields and bulk reactions into account, *Journal of Nuclear Materials*, 374, p. 281-285.
- Nilsson, S., Jonsson, M., 2011, H<sub>2</sub>O<sub>2</sub> and radiation induced dissolution of UO<sub>2</sub> and SIMFUEL pellets, *Journal of Nuclear Materials*, 410, p. 89-93.
- Pelletier, M., 2001, State of the Art on the Potential Migration of Species, Section 5.4 of *Synthesis on the Long Term Behavior of the Spent Nuclear Fuel*. Poinssot, C., ed. CEA-R-5958(E). Volume I. [Paris], France: Commissariat à l'Énergie Atomique.
- Poinssot C., Ferry, C., eds., 2004, *Spent Fuel Stability under Repository Conditions – Final Report of the European Project*, European Commission contract No. FIKW-CT-2001-00192 SFS.
- Poinssot, C., Ferry, C., Lovera, P., Jegou, C., Gras, J-M, 2005, Spent fuel radionuclide source term model for assessing spent fuel performance in geological disposal, Part II: Matrix alteration model and global performance, *Journal of Nuclear Materials*, 346, p. 66-77.
- Puranen, A., Trummer, M., Jonsson, M., 2009, Can redox sensitive radionuclides be immobilized on the surface of spent nuclear fuel? – A model study on the reduction of Se(IV)<sub>aq</sub> on Pd-doped UO<sub>2</sub> under H<sub>2</sub> atmosphere, *Journal of Nuclear Materials*, 392, p. 505-509.
- Römer, J., Plaschke, M., Beuchle, G., Kim, J.I., 2003, In Situ Investigation of U(IV)-Oxide Surface Dissolution and Remineralization by Electrochemical AFM, *Journal of Nuclear Materials*, 322, p. 80-86.

- Roth, O., Nilsson, S., Jonsson, M., 2006, Radiation enhanced reactivity of  $\text{UO}_2$ , *Journal of Nuclear Materials*, 354, p. 131-136.
- Roth, O., Jonsson, M., 2008, Oxidation of  $\text{UO}_2(\text{s})$  in aqueous solution, *Central European Journal of Chemistry*, 6, p. 1-14.
- Roth, O., Jonsson, M., 2009, On the impact of reactive solutes on radiation induced oxidative dissolution of  $\text{UO}_2$ , *Journal of Nuclear Materials*, 385, p. 595-600.
- Rothe, J., Walther, C., Denecke, M.A., Fanghänel, Th., 2004, XAFS and LIBD Investigation of the Formation and Structure of Colloidal Pu(IV) Hydrolysis Products, *Inorganic Chemistry*, 43, p. 4708–4718.
- Samanta, C., 2008, Direct Synthesis of Hydrogen Peroxide from Hydrogen and Oxygen: An Overview of Recent Developments in the Process, *Applied Catalysis A: General*, 350, p. 133-140.
- Shoesmith, D.W., Sunder, S., Bailey, M.G., Wallace, G.J., 1989, The Corrosion of Nuclear Fuel ( $\text{UO}_2$ ) in Oxygenated Solutions, *Corrosion Science*, 29, p. 1115-1128.
- Shoesmith, D.W., Sunder, S., Tait, J.C., 1998, Validation of an Electrochemical Model for the Oxidative Dissolution of Used CANDU Fuel, *Journal of Nuclear Materials*, 257, p. 89-98.
- Shoesmith, D.W., 2000, Fuel Corrosion Processes Under Waste Disposal Conditions, *Journal of Nuclear Materials*, 282, p. 1-31.
- Shoesmith, D.W., Kolar, M., King, F., 2003, A Mixed-Potential Model to Predict Fuel (Uranium Dioxide) Corrosion Within a Failed Nuclear Waste Container, *Corrosion*, 59, p. 802-816.
- Shoesmith, D. W., 2007, *Used Fuel and Uranium Dioxide Dissolution Studies – A Review*. NWMO TR-2007-03, July 2007 Nuclear Waste Management Organization, 22 St. Clair Avenue East, 6<sup>th</sup> Floor, Toronto, Ontario M4T 2S3, Canada.
- Shoesmith, D. W., 2008, *The Role of Dissolved Hydrogen on the Corrosion/Dissolution of Spent Nuclear Fuel*, NWMO TR-2008-19, November 2008 Nuclear Waste Management Organization, 22 St. Clair Avenue East, 6<sup>th</sup> Floor, Toronto, Ontario M4T 2S3, Canada.
- Soderholm, L., Almond, P., Skanthakumar, S., Wilson, R., Burns, P.C., 2008, The Structure of the Plutonium Oxide Nanocluster  $[\text{Pu}_{38}\text{O}_{56}\text{Cl}_{54}(\text{H}_2\text{O})_8]^{14-}$ , *Angewandte Chemie International Edition*, 47, p. 298–302.
- Sunder, S., Miller, N.H., Shoesmith, D.W., 2004, Corrosion of uranium dioxide in hydrogen peroxide solutions, *Corrosion Science*, 46, p. 1095–1111.
- Spahiu, K., Eklund, U.-B., Cui, D., Lundström, M., 2002, The influence of near-field redox conditions on Spent Fuel leaching, *Materials Research Society Symposium Proceedings*, 713, p. 633-638.
- Stumpf S., Petersmann, T., Seibert, A., Gouder, T., Huber, F., Brenderbach, B., Denecke, M.A., 2010, Comparative Study of the Structural and Electrochemical Properties of Noble Metal Inclusions in a  $\text{UO}_2$  Matrix, *IOP Conference Series: Materials Science and Engineering* 9 012014 (<http://iopscience.iop.org/1757-899X/9/1/012014>)

- Suzuki, T., Abdelouas, A., Grambow, B., Mennecart, T., Blondiaux, G., 2006, Oxidation and Dissolution Rates of  $\text{UO}_2(\text{s})$  in Carbonate-Rich Solutions Under External Alpha Irradiation and Initially Reducing Conditions, *Radiochimica Acta*, 94, p. 567-573.
- Torrero, M.E., Baraj, E., de Pablo, J., Gimenez, J., Casas, I., 1997, Kinetics of Corrosion and Dissolution of Uranium Dioxide as a Function of pH, *International Journal of Chemical Kinetics*, 29, p. 261-267.
- Trummer, M., Roth, O., Jonsson, M., 2009,  $\text{H}_2$  inhibition of radiation induced dissolution of spent nuclear fuel, *Journal of Nuclear Materials*, 383, p. 226-230.
- Trummer, M., Dahlgren, B., Jonsson, M., 2010a, The effect of  $\text{Y}_2\text{O}_3$  on the dynamics of oxidative dissolution of  $\text{UO}_2$ , *Journal of Nuclear Material*, 407, p. 195-199.
- M. Trummer, Jonsson, M., 2010b, Resolving the  $\text{H}_2$  effect on radiation induced dissolution of  $\text{UO}_2$ -based spent nuclear fuel, *Journal of Nuclear Material*, 396, p. 163-169.
- Tsai, H., 2003, NRC Review of ANL High-Burnup Cladding Performance Program, July 16, 2003.
- Nutt et al., 2011, Used Fuel Disposition Campaign Disposal Research and Development Roadmap. FCRD-USED-2011-000065 REV0, March 2011.
- Une, K., Kashibe, S., 1996, Corrosion behavior of irradiated oxide fuel pellets in high temperature water, *Journal of Nuclear Materials*, 232, p. 240-247.
- Utsunomiya S., Ewing R. C., 2006, The fate of the epsilon phase (Mo-Ru-Pd-Tc-Rh) in the  $\text{UO}_2$  of the Oklo natural fission reactors, *Radiochimica Acta*, 94, p. 749-753.
- Van der Lee, J., Lomenech, C., 2004, Towards a common thermodynamic database for speciation models, *Radiochimica Acta*, 92, p. 811-818.
- Wagner C., Traud W., 1938, *Elektrochem.* 44, 391.
- Wolery, T.J., Daveler S. A., 1992, EQ6, A computer program for reaction path modeling of aqueous geochemical systems: Theoretical manual, user's guide, and related documentation (Version 7.0). Lawrence Livermore National Laboratory Report UCRL-MA- 110662 PT IV
- Wronkiewicz, D.J., Watkins, C.S., Baughman, A.C., Miller, F.S., Wolf, S.F., 2002, Corrosion Testing of a Simulated Five-Metal Epsilon Particle in Spent Nuclear Fuel, *Materials Research Society Symposium Proceedings*, 713, p. 625-632.

## 3.5 First Principles Modeling of $\text{UO}_2$ and Uranyl Peroxides

### 3.5.1 First Principles Evaluation of Surface Properties and Chemistry of Uranium Dioxide

We report density functional calculations of the surface properties and chemistry of  $\text{UO}_2(111)$  performed within the generalized gradient approximation corrected with an effective Hubbard parameter (GGA+ $U$  within Dudarev's formalism) to account for the strong on-site Coulomb repulsion between U 5f electrons. The variation of the properties of periodic slab models, with collinear ferromagnetic and antiferromagnetic arrangements of the uranium moments, was investigated while ramping up the effective Hubbard parameter from  $U_{\text{eff}} = 0$  eV, corresponding to standard density functional theory, up to  $U_{\text{eff}} = 4$  eV, the value that correctly reproduces the antiferromagnetic ground state of bulk  $\text{UO}_2$ . The chemical interactions of molecular water, dissociated water, dissociated oxygen and co-adsorbed molecular water and monatomic oxygen with the  $\text{UO}_2(111)$  surface were also studied as functions of the  $U_{\text{eff}}$  parameter. Calculations reveal that some of the key electronic and chemical properties controlling the surface reactivity can be tuned to a large extent by adjusting this strong electron correlation parameter.

#### 3.5.1.1 Background

Understanding the fundamental interfacial processes and the underlying interactions occurring between materials surfaces and their local environment is of paramount importance to control materials performance and limit materials degradation over time. Metal-oxides are particularly prone to redox corrosion and dissolution, which is pervasive and of critical significance for technological applications (Blesa et al., 1994) and environmental systems (Stumm, et al., 1992). Despite the decades-long research effort to elucidate the elementary factors controlling this ubiquitous process, understanding metal-oxide dissolution at the molecular scale remains an open challenge.

Recent advances in metal-oxide dissolution have focused on actinide-oxide systems, owing in part to the central role occupied by uranium dioxide ( $\text{UO}_2$ ) in the nuclear power industry. Upon exposure to water or other oxidizing agents,  $\text{UO}_2$  fuel corrosion occurs, resulting ultimately in the oxidation of some of the  $\text{U}^{4+}$  cations composing the fuel into  $\text{U}^{6+}$ , concomitant with major changes in crystallinity compared to fluorite-structured  $\text{UO}_2$  (McNamara et al., 2003) (Hughes Kubatko et al., 2003). The implications of these physico-chemical changes are critical for the safe storage or disposal of used nuclear fuels, regardless of the repository environment (Ewing et al., 2010) (Cui et al., 2011).

The redox behavior of  $\text{UO}_2$  is particularly complex, due to the ability of U 5f and 6d orbitals to hybridize resulting in multiple oxidation states – uranium exists in oxidation states +3, +4, +5, and +6 in the solid state and in solution – and a broad range of oxygen nonstoichiometry (Roberts, 1963). In  $\text{UO}_2$ , each  $\text{U}^{4+}$  cation possesses two unpaired 5f valence electrons, which can participate in bonding with monatomic and molecular adsorbates or interstitial oxygen and therefore render  $\text{UO}_2$  susceptible to corrosion. This contrasts, for example, with  $\text{ThO}_2$ , an isostructural analogue of  $\text{UO}_2$  with unfilled 5f shells (Th:  $[\text{Rn}]6d^27s^2$ ), which possesses only one oxidation state (+4) and is more resistant to corrosion/dissolution.  $\text{ThO}_2$  is an insulator with a wide band gap of 6 eV (Veal & Lam, 1974), significantly larger than the  $5f^2 \rightarrow 5f^16sd$  transition energy of 2–3 eV in  $\text{UO}_2$  (Baer and Schoenes, 1980) (Schoenes, 1987). This provides further

evidence of the important role played by 5f electrons in the electronic and corrosion properties of uranium dioxide.

While valence electrons are itinerant in metallic  $\alpha$  uranium, U 5f electrons are strongly localized in bulk  $\text{UO}_2$ , as shown in many previous experimental and theoretical studies (Baer and Schoenes, 1980) (Schoenes, 1987) (Arko et al., 1986). For that reason, standard density functional theory (DFT), which greatly underestimates strong electron correlation due to its self-interaction error, fails to reproduce the correct Mott-Hubbard insulating character of bulk  $\text{UO}_2$  and predicts instead a metallic ground state. To palliate this shortcoming, a variety of extensions to standard DFT have been proposed such as the self-interaction corrected (SIC) DFT (Zunger et al., 1980) (Perdew and Zunger, 1981), the DFT+ $U$  (Anisimov et al., 1991) (Anisimov et al., 1997) (Dudarev et al., 1998) and dynamic mean-field theory (DMFT) (Anisimov et al., 1997) (Lichtenstein and Katsnelson, 1998) (Kotliar et al., 2006) methods which add a Hubbard correction to the Hamiltonian, or screened hybrid DFT without the need for material-dependent empirical parameters in the Hamiltonian (Prodan et al., 2007). Although these computational approaches have been widely applied with great success to bulk actinide-oxide systems, relatively few have been used to model actinide-oxide surfaces. In particular, the possible role played by strong electron correlations in the surface properties and chemistry of uranium dioxide remains largely unexplored.

In this study, we report density functional calculations of the surface properties and chemistry of  $\text{UO}_2(111)$  performed within the generalized-gradient approximation corrected with an effective Hubbard parameter (GGA+ $U$  within Dudarev's formalism) to account for the strong on-site Coloumb repulsion between U 5f electrons. Specifically, the variation of the properties of periodic slab models, with collinear ferromagnetic and antiferromagnetic arrangements of the uranium moments, was investigated while ramping up the effective Hubbard parameter from  $U_{\text{eff}} = 0$  eV, corresponding to standard density functional theory, up to  $U_{\text{eff}} = 4$  eV, the value that correctly reproduces the antiferromagnetic ground state of bulk  $\text{UO}_2$ . The chemical interactions of molecular water, dissociated water, dissociated oxygen and co-adsorbed molecular water and monatomic oxygen with the  $\text{UO}_2(111)$  surface were also studied as functions of the  $U_{\text{eff}}$  parameter.

Details of our computational approach are given in the next section, followed by a complete analysis and discussion of our results. A summary of our findings and conclusions is presented in the last section of the manuscript.

### **3.5.1.2 Computational Methods**

First-principles total energy calculations were performed using spin-polarized density functional theory, as implemented in the Vienna Ab initio Simulation Package (VASP) (Kresse and Furthmüller, 1996). The exchange-correlation energy was calculated within the generalized gradient approximation (GGA+ $U$ ) (Perdew, et al., 1992), with the parametrization of Perdew and Wang (PW91) (Perdew and Wang, 1992), corrected with an effective Hubbard parameter to account for the strong on-site Coloumb repulsion between localized uranium 5f electrons. The PW91 functional was found in previous studies to correctly describe the geometric parameters and properties of various uranium oxides and uranium containing structures observed experimentally (Skomurski et al., 2006; Weck et al., 2007; Skomurski et al., 2008; Weck et al., 2010; Weck et al., 2011; Thompson and Wolverton, 2011; Weck et al., 2012).



The rotationally-invariant formalism developed by Dudarev et al. (1998) was used, which consists in adding a penalty functional to the standard GGA total-energy functional,  $E_{\text{GGA}}$ , that forces the on-site occupancy matrix in the direction of idempotency, i.e.

$$E_{\text{GGA}+U} = E_{\text{GGA}} + \frac{(\bar{U}-\bar{J})}{2} \sum_{\sigma} [\text{Tr}(\rho^{\sigma}) - \text{Tr}(\rho^{\sigma} \rho^{\sigma})], \quad 3.5-1$$

where  $\bar{U}$  and  $\bar{J}$  are the spherically-averaged matrix elements of the screened electron-electron Coulomb and exchange interactions, respectively, and  $\rho^{\sigma}$  is the density matrix of 5f electrons with a given projection of spin  $\sigma$ . In Dudarev's approach only  $U_{\text{eff}} = \bar{U} - \bar{J}$  is meaningful. Therefore, only  $\bar{U}$  was allowed to vary in the calculations, while  $\bar{J}$  was set to 0.51 eV, i.e. the value suggested by Kotani and Yamazaki (1992) based on their analysis of core-level X-ray photoemission spectra (XPS) of  $\text{UO}_2$  using the Anderson-impurity model.

The interaction between valence electrons and ionic cores was described by the projector augmented wave (PAW) method (Blöchl, 1994; Kresse and Joubert, 1999). The U(6s,6p,6d,5f,7s) and O(2s,2p) electrons were treated explicitly as valence electrons in the Kohn-Sham (KS) equations and the remaining core electrons together with the nuclei were represented by PAW pseudopotentials. The KS equation was solved using the blocked Davidson (Davidson, 1983) iterative matrix diagonalization scheme. The plane-wave cutoff energy for the electronic wavefunctions was set to 500 eV, ensuring the total energy of the system to be converged to within 1 meV/atom.

All structures were optimized with periodic boundary conditions applied. Ionic relaxation was carried out using the quasi-Newton method and the Hellmann-Feynman forces acting on atoms were calculated with a convergence tolerance set to 0.01 eV/Å. Structural optimizations and properties calculations were carried out using the Monkhorst-Pack special  $k$ -point scheme (Monkhorst and Pack, 1976) with  $5 \times 5 \times 5$  and  $5 \times 5 \times 1$  meshes for integrations in the Brillouin zone (BZ) of bulk and slab systems, respectively. The tetrahedron method with Blöchl corrections (Blöchl et al, 1994) was used for BZ integrations.

Periodic supercells containing 12 atoms ( $Z = 4$ ) for bulk  $\text{UO}_2$  and the clean  $\text{UO}_2(111)$  surface were used in the calculations. Models with both collinear ferromagnetic (FM) and antiferromagnetic (AFM, type-I) arrangements of the uranium moments were studied. The starting geometries considered for the bulk models consisted of the ideal fluorite structure with an ordered oxygen (OO) sublattice (space group  $Fm\bar{3}m$ , with O atoms occupying ideal 8c positions) for both the FM and AFM phases and the AFM structure recently reported by Thompson and Wolverton (Thompson and Wolverton, 2011), which features an energy-lowering, distorted oxygen (DO) sublattice with a distortion along the [111] direction (cf. Fig. 3.5-1).

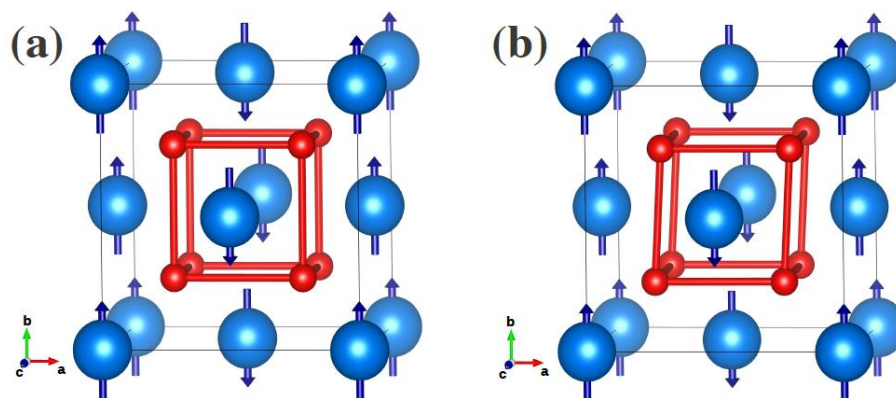


Figure 3.5-1. Crystal structure models of bulk  $\text{UO}_2$  ( $Z = 4$ ) with collinear antiferromagnetic (AFM, type-I) arrangement of the uranium moments with: (a) an ordered oxygen (OO) sublattice (ideal  $8c$  fluorite positions; space group  $Fm\bar{3}m$ ) and (b) an energy-lowering, distorted oxygen (DO) sublattice with a distortion along the  $[111]$  direction. Color legend: U, blue; O, red.

Ionic and cell relaxations of the bulk were performed simultaneously, without symmetry constraints, for each  $U_{\text{eff}}$  value. The  $\text{UO}_2$  surface slab models were constructed by cleaving the optimized bulk structure, for each  $U_{\text{eff}}$  value, along the lowest-energy, natural cleavage plane with  $(111)$  termination (Cox, 1994).  $(2 \times 1)$   $\text{UO}_2(111)$  slab surface models similar to the ones used by Skomurski et al. (Skomurski et al., 2006; Skomurski et al., 2008) were employed in this study (cf. Fig. 3.5-2). Following the classification developed by Tasker for ionic surfaces (Tasker, 1979a; Tasker, 1979b), these surface slab models with layers of anions and cations stacked along  $\langle 111 \rangle$ , charge-neutral  $\text{B}^{1-}\text{A}^{2+}\text{B}^{1-}$  units, and quadrupolar termination, can be labelled as type-II surfaces. Although a large vacuum region of  $15 \text{ \AA}$  (along the  $z$ -axis normal to the surface) was introduced between periodic slabs, the creation of dipoles upon adsorption of atoms on only one side of the slab can lead to spurious interactions between the dipoles of successive slabs. In order to circumvent this problem, a double-sided adsorption approach was used, with an inversion center applied to preserve the slab geometry upon oxidation. Previous studies using double-sided adsorption models have shown that the interaction energy between residual dipoles across similar vacuum gap is of the order of  $1 \text{ meV}$  and is therefore negligible (Skomurski et al., 2008).

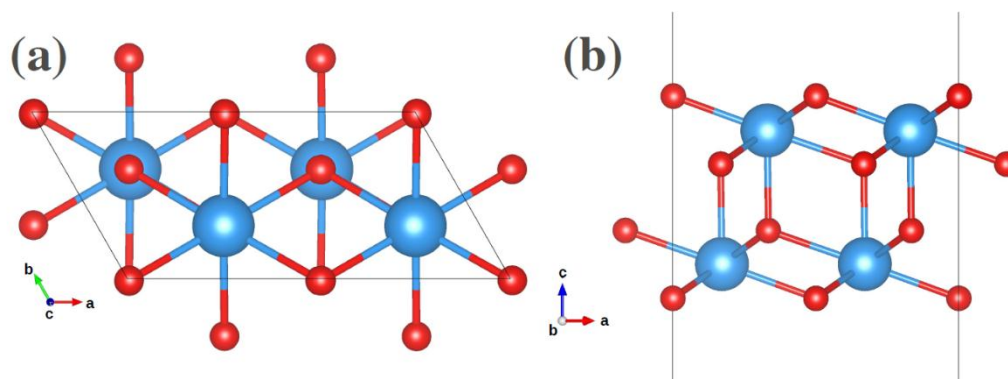


Figure 3.5-2. Ball-and-stick model of the clean (2×1)  $\text{UO}_2(111)$  surface ( $Z = 4$ ) used in the present DFT calculations. (a) Top view and (b) side view. Color legend: U, blue; O, red. Color legend: U, blue; O, red.

### 3.5.1.3 Results and Discussion

Based on the calculations discussed above, the lattice parameters and total energy of the various bulk  $\text{UO}_2$  structures were evaluated. Fig. 3.5-3 shows the variation of the computed lattice parameters and total energy as functions of the effective Hubbard parameter,  $U_{\text{eff}}$ , for bulk  $\text{UO}_2$  with an ideal fluorite structure (i.e. with an ordered oxygen (OO) sublattice) for both the FM and AFM phases and for the AFM structure featuring an energy-lowering, distorted oxygen (DO) sublattice with a distortion along the [111] direction. The FM solution of is energetically more favorable for standard DFT ( $U = 0$  eV), while the AFM solution with oxygen distortion is preferable for  $U_{\text{eff}} = 4$  eV (i.e. the value suggested from the analysis of core-level X-ray photoemission spectra of  $\text{UO}_2$ ). For the FM phase  $a = b = c$  with lattice parameters varying from 5.42 ( $U_{\text{eff}} = 0$  eV) to 5.52 Å ( $U_{\text{eff}} = 4$  eV); for the AFM phase with OO sublattice,  $a = b \neq c$  with large differences between  $a = b$  and  $c$  for at large values of  $U_{\text{eff}}$ : Imposing an OO sublattice seems to affect more significantly the  $c/a$  ratio by inducing a lattice distortion. For the AFM phase with DO sublattice,  $a \neq b \neq c$  with lattice parameters varying from ca. 5.40 ( $U_{\text{eff}} = 0$  eV) to 5.54 Å ( $U_{\text{eff}} = 4$  eV), however the variation of the 3 lattice parameters are in closer agreement with each other compared to the phase with OO sublattice. The experimental lattice constant of bulk  $\text{UO}_2$  is estimated to be 5.470 Å (Villars and Calvert, 1991), therefore the computed lattice parameters are slightly overestimated in the range  $U_{\text{eff}} = 2.0$ -4.0 eV.

In addition to the bulk properties of the  $\text{UO}_2$  structure, the relaxed  $\text{UO}_2(111)$  surface properties were also evaluated. Fig. 3.5-4 depicts the computed variation of the surface energy and work function of the relaxed  $\text{UO}_2(111)$  surface for FM and AFM (DO) solutions as functions of the effective Hubbard parameter  $+U_{\text{eff}}$ , using the same surface model discussed in Skomurski et al. (2008). No significant impact of the  $+U_{\text{eff}}$  correction on the surface energy of the AFM structure is predicted [Fig. 3.5-4(a)], while the use of  $+U > 3$  eV leads to unphysical results for the FM solution. The predicted surface energy of the AFM surface, ca. 0.78  $\text{J/m}^2$ , is in close agreement with the experimental estimate of  $\gamma = 0.85 \text{ J/m}^2$  with up to  $\pm 70\%$  uncertainty (Hall et al., 1987). As shown in Fig. 3.5-4(b), the computed work function exhibits a nearly-linear variation as a function the  $+U_{\text{eff}}$  correction, with only small differences between the FM and AFM solutions. This increase in work function with  $U_{\text{eff}}$  is associated with the increase in energy band gap taking

place as 5f electrons become more localized. The experimental work function estimate,  $\phi = 3.5 \pm 0.5$  eV (Page and Woolley, 1974) is correctly reproduced by the DFT+ $U$  calculations using a  $U_{\text{eff}}$  value in the range 0.0-1.5 eV to account for experimental uncertainty; a value of  $\phi = 3.5$  eV corresponds to  $U_{\text{eff}} = 1$  eV.

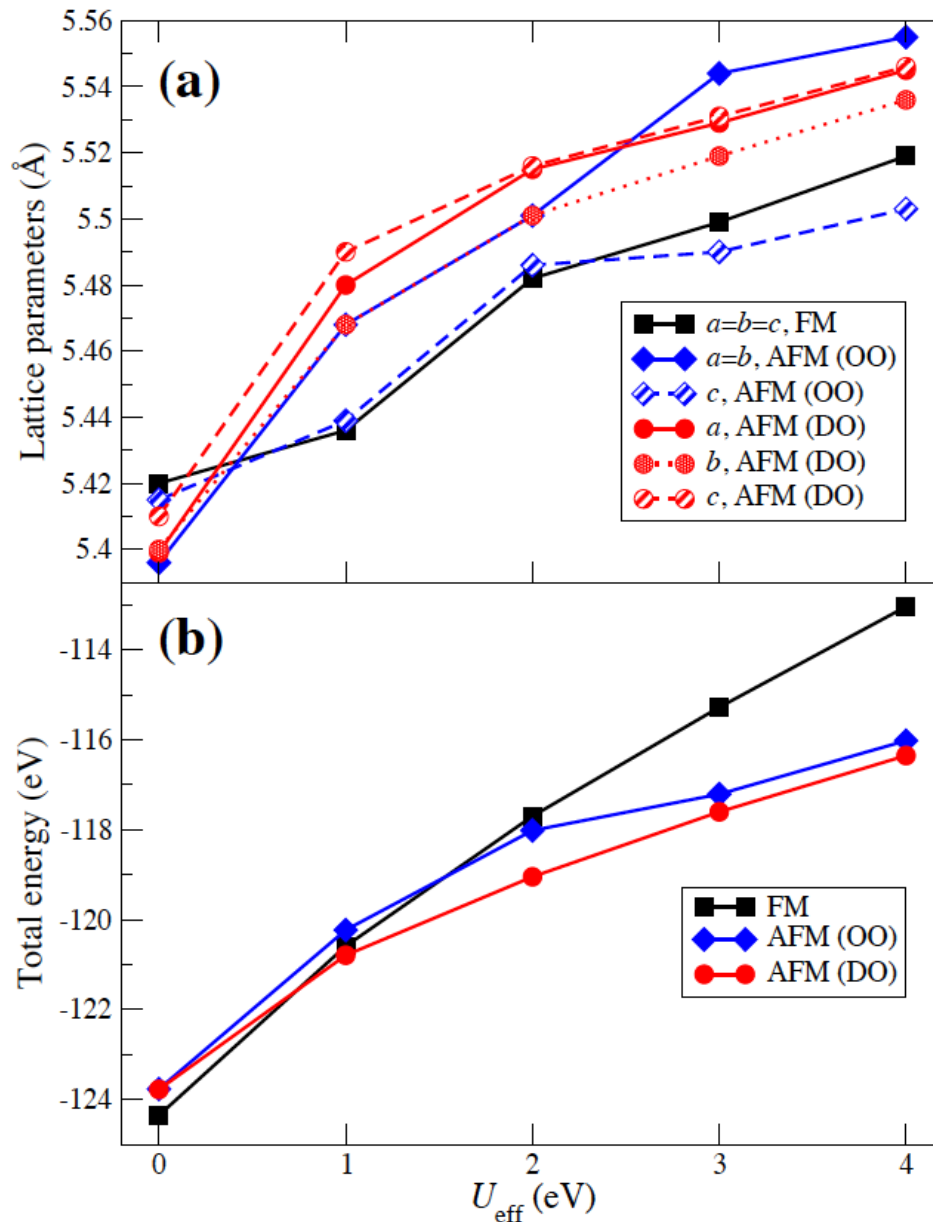


Figure 3.5-3. Evolution of (a) the lattice parameters and (b) the total energy of bulk  $\text{UO}_2$ , with ferromagnetic (FM) and antiferromagnetic (AFM) arrangements of the uranium moments, as functions of the effective Hubbard parameter,  $U_{\text{eff}}$ . For the AFM state, results for the ordered oxygen (OO) sublattice and the distorted oxygen (DO) sublattice are shown.

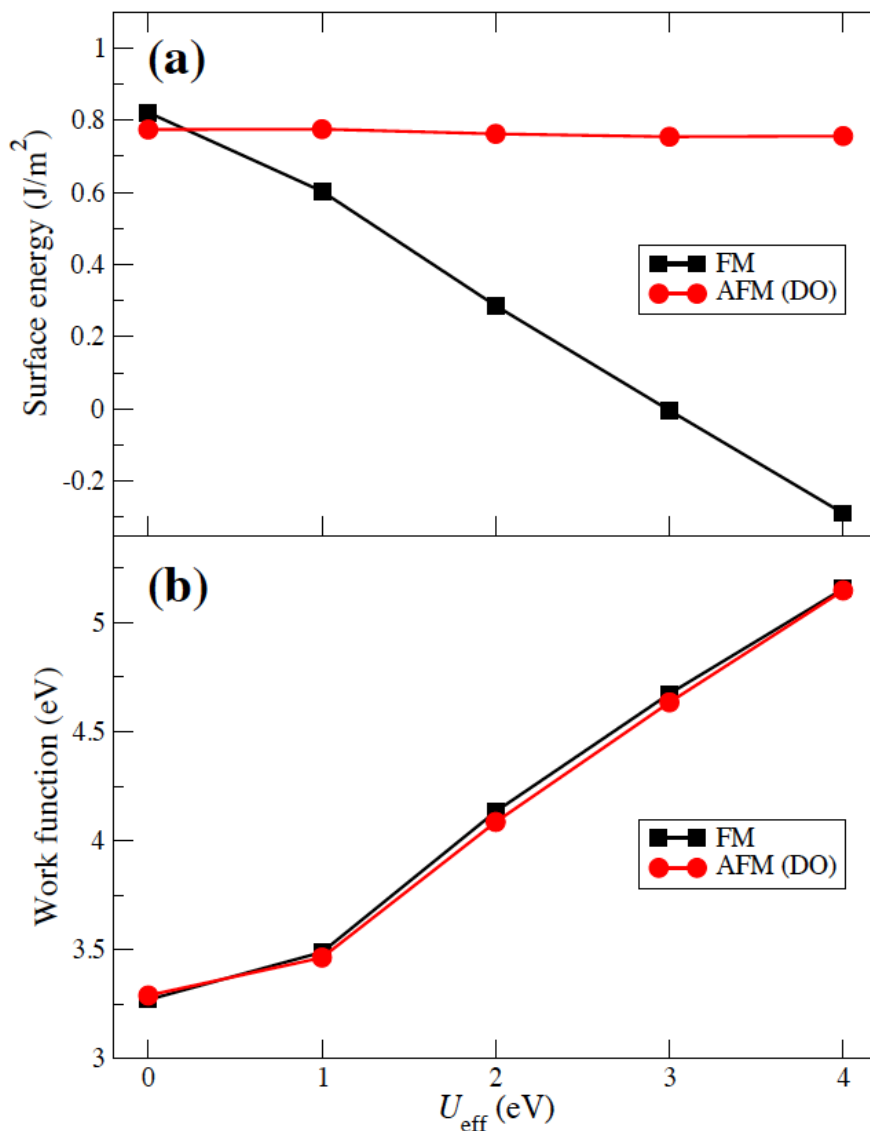


Figure 3.5-4. Variation of (a) the surface energy and (b) the work function of the relaxed  $\text{UO}_2(111)$  surface with ferromagnetic (FM) and antiferromagnetic (AFM) arrangements of the uranium moments as functions of the effective Hubbard parameter,  $U_{\text{eff}}$ .

Representative views of the relaxed  $\text{UO}_2(111)$  surface slab models with half-monolayer coverage ( $\theta = 0.5$  ML) of molecular water, dissociated water, atomic oxygen and a full monolayer coverage ( $\theta = 1$  ML) of water and oxygen are shown in Fig. 3.5-5 for a  $U_{\text{eff}} = 1$  eV correction, which best matches the experimental surface work function and surface energy. The adsorption energy,  $E_{\text{ads}}$ , was calculated using the formula:

$$E_{\text{ads}} = \frac{1}{2} (E_{\text{slab+adsb}} - E_{\text{slab}} - 2E_{\text{adsb}}), \quad 3.5-2$$

where the factor  $\frac{1}{2}$  accounts for the double-sided adsorption used in our slab models,  $E_{\text{slab+adsb}}$  is the total energy of the relaxed slab with atoms/molecules adsorbed,  $E_{\text{slab}}$  is the total energy of the clean slab and  $E_{\text{adsb}}$  is the total energy of an isolated atom/molecule.

For the AFM (111) slab with DO sub-lattice, the adsorption energy of a water molecule is predicted to be: 0.77 eV for  $U=0$  eV, 0.80 eV for  $U=1$  eV, 0.83 eV for  $U=2$  eV, 0.80 eV for  $U=3$  eV and 0.85 eV for  $U=4$  eV. For the FM slab,  $E_{\text{ads}} = 0.78$  eV at the limits of  $U=0$  eV and  $U=4$  eV. For the adsorption of a dissociated water molecule (OH+H) on the AFM (111) slab, the adsorption energy is predicted to be:  $E_{\text{ads}} = 0.41$  eV for  $U=0$  eV,  $E_{\text{ads}} = 0.57$  eV for  $U=1$  eV,  $E_{\text{ads}} = 0.59$  eV for  $U=2$  eV,  $E_{\text{ads}} = 0.59$  eV for  $U=3$  eV and  $E_{\text{ads}} = 0.60$  eV for  $U=4$  eV. For the FM slab:  $E_{\text{ads}} = 0.44$  and  $0.53$  eV in the limits of  $U=0$  eV and  $U=4$  eV, respectively. We conclude that the strong correlation interaction has some impact on the adsorption energy of water and dissociated water in the AFM case; for adsorption on FM slabs, no effect of the  $+U$  correction is predicted for the adsorption of water while some significant effect is predicted for the adsorption of dissociated water. These evaluations will continue with analyses of surface reactions among species such as  $\text{O}_2$  and  $\text{H}_2\text{O}_2$  in the next fiscal year.

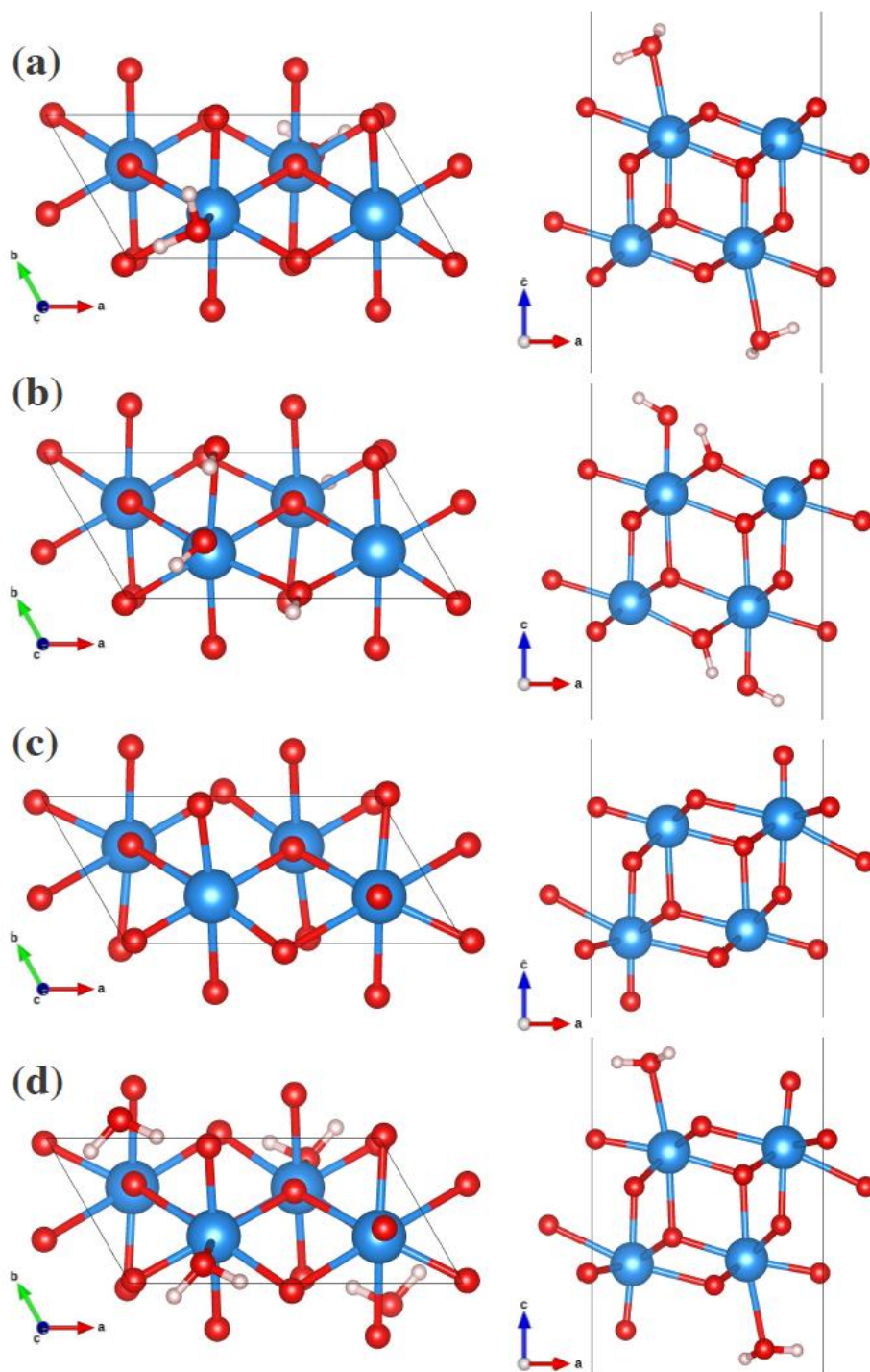


Figure 3.5-5. Ball-and-stick Top view (left) and side view (right) of the UO<sub>2</sub>(111) model surface with half-monolayer coverage ( $\theta = 0.5$  ML) of (a) molecular water, (b) dissociated water, (c) atomic oxygen and (d) a full monolayer coverage ( $\theta = 1$  ML) of water and oxygen. Color legend: U, blue; O, red.

### 3.5.2 Structures of uranyl peroxide hydrates: a first-principles study of studtite and metastudtite

The structures of the only known minerals containing peroxide, namely studtite  $[(\text{UO}_2)\text{O}_2(\text{H}_2\text{O})_4]$  and metastudtite  $[(\text{UO}_2)\text{O}_2(\text{H}_2\text{O})_2]$ , have been investigated using density functional theory. The structure of metastudtite crystallizing in the orthorhombic space group *Pnma* ( $Z = 4$ ) is reported for the first time at the atomic level and the computed lattice parameters,  $a = 8.45$ ,  $b = 8.72$ ,  $c = 6.75$  Å, demonstrate that the unit cell of metastudtite is larger than previously reported dimensions ( $Z = 2$ ) derived from experimental X-ray powder diffraction data.

#### 3.5.2.1 Background

Studtite,  $(\text{UO}_2)\text{O}_2(\text{H}_2\text{O})_4$ , and metastudtite,  $(\text{UO}_2)\text{O}_2(\text{H}_2\text{O})_2$ , are among the important corrosion phases that may form on spent nuclear fuel (SNF) exposed to water (McNamara et al., 2003; Hanson, et al., 2005; McNamara et al., 2005). These hydrates of uranyl peroxide, which incorporate  $(\text{O}_2)^{2-}$  generated by  $\alpha$ -radiolysis of water (Draganic and Draganic, 1971; Sattonnay, et al., 2001; Amme, 2002), may play a crucial role in the degradation of nuclear fuel in the context of nuclear reactor accidents or geological repositories (Hughes Kubatko et al., 2003; Armstrong et al., 2012; Burns et al., 2012). Studtite and metastudtite are also the only two known minerals containing peroxide, and studtite is the only one with a fully elucidated structure (Burns, 2005). In addition to playing a role for corrosion of SNF, studtite may retain released radionuclides through incorporation into its structure (Buck et al., 2004; Shuller et al., 2010).

The structure of synthetic uranyl peroxide dihydrate,  $(\text{UO}_2)\text{O}_2(\text{H}_2\text{O})_2$ , was first characterized by Zachariassen (Zachariassen, 1944) in 1944 as orthorhombic with unit-cell dimensions  $a = 6.50 \pm 0.03$ ,  $b = 4.21 \pm 0.02$ ,  $c = 8.74 \pm 0.05$  Å and uranium positions at (000) and  $(\frac{1}{2}\frac{1}{2}\frac{1}{2})$ . The XRD pattern of  $(\text{UO}_2)\text{O}_2(\text{H}_2\text{O})_2$  was published by Ukazi (1959). In 1961, Sato (1961) found that two crystalline modifications of uranium peroxide hydrate exist and that their formation depends on temperature:  $(\text{UO}_2)\text{O}_2(\text{H}_2\text{O})_4$  precipitates below 50°C following addition of  $\text{H}_2\text{O}_2$  to an aqueous solution containing uranyl ions, whereas  $(\text{UO}_2)\text{O}_2(\text{H}_2\text{O})_2$  precipitates above 70°C; a mixture of the two precipitates at 60°C. Sato also demonstrated that  $(\text{UO}_2)\text{O}_2(\text{H}_2\text{O})_4$  is converted to  $(\text{UO}_2)\text{O}_2(\text{H}_2\text{O})_2$  by drying in air at 100°C or in vacuum for 24 hours at room temperature. The thermal decomposition of both  $(\text{UO}_2)\text{O}_2(\text{H}_2\text{O})_4$  and  $(\text{UO}_2)\text{O}_2(\text{H}_2\text{O})_2$  was also studied by Cordfunke et al. 1963; Cordfunke and Aling, 1963), while Debets (1963) reinvestigated their XRD patterns and reported unit-cell dimensions for  $(\text{UO}_2)\text{O}_2(\text{H}_2\text{O})_2$ :  $a = 6.50 \pm 0.02$ ,  $b = 4.211 \pm 0.005$ ,  $c = 8.78 \pm 0.01$  Å ( $V = 240 \pm 1$  Å<sup>3</sup>;  $Z = 2$ ) with an orthorhombic body-centered structure (space group *Immm*); and for  $(\text{UO}_2)\text{O}_2(\text{H}_2\text{O})_4$ :  $a = 11.85$ ,  $b = 6.785$ ,  $c = 4.245$  Å and  $\beta = 93^\circ 37'$  with a face-centered monoclinic structure.

The mineral studtite was originally described by Vaes (1947) as a hydrated carbonate of uranium from a qualitative chemical analysis; however, subsequent chemical and powder XRD investigations by Walenta (1974) demonstrated that studtite is identical to synthetic  $(\text{UO}_2)\text{O}_2(\text{H}_2\text{O})_4$ , with monoclinic symmetry (space group *C2*, *Cm* or *C2/m*) and unit-cell dimensions  $a = 11.85$ ,  $b = 6.80$ ,  $c = 4.25$  Å and  $\beta = 93^\circ 51'$ . Subsequent analyses of studtite from the type locality (Shinkolobwe) confirmed Walenta's unit-cell determination (Cejka et al., 1996):  $a = 11.85$  Å,  $b = 6.78$  Å,  $c = 4.24$  Å,  $\beta = 93.62^\circ$ . The structure of studtite was reported by Burns and Hughes (2003), who showed it to be monoclinic, space group *C2/c*, with unit-cell dimensions  $a = 14.068(6)$ ,  $b = 6.721(3)$ ,  $c = 8.428(4)$  Å and  $\beta = 123.356(6)^\circ$  ( $V = 665.6(3)$  Å<sup>3</sup>;  $Z = 4$ ), being approximately twice the size of the previously accepted unit-cell volume with  $Z = 2$ .



Burns and co-workers also reported the thermodynamic stability of the peroxide-containing uranyl minerals the same year (Hughes Kubatko et al., 2003).

Walenta had demonstrated that, when heated to 60°C, natural studtite transforms irreversibly to the dihydrate,  $(\text{UO}_2)\text{O}_2(\text{H}_2\text{O})_2$ , with unit cell parameters  $a = 6.51 \pm 0.01$ ,  $b = 8.78 \pm 0.02$ ,  $c = 4.21 \pm 0.01$  Å [ $V = 240.6 \pm 1$  Å<sup>3</sup>;  $Z = 2$ ; the  $b$  and  $c$  parameters as chosen by Debets (1963) were exchanged to comply with the  $c < a < b$  recommendation of the International Mineralogical Association (IMA)], and Walenta suggested that the dihydrate may occur as a mineral. Naturally occurring  $(\text{UO}_2)\text{O}_2(\text{H}_2\text{O})_2$  was subsequently reported by Deliens and Piret (1983), who proposed the name metastudtite, and showed it to be equivalent to the synthetic dihydrate ( $a = 6.51(1)$ ,  $b = 8.78(2)$ ,  $c = 4.21(1)$  Å;  $V = 240.6(1.5)$  Å<sup>3</sup>,  $Z = 2$ ).

However, to the best of our knowledge, no refined structure of metastudtite has been published to date. Interestingly, Burns and Hughes (2003) suggested that, in light of their structure determination for studtite, it is likely that the  $c = 4.21$  Å cell parameter previously reported for metastudtite (Walenta, 1974; Deliens and Piret, 1983) is probably erroneous, since the repeat length of the chains of polyhedra in studtite is  $c = 8.428(4)$  Å and both studtite and metastudtite are expected to contain similar chains of coordination polyhedra. In the absence of well-established crystallographic data for metastudtite, Ostanin and Zeller (2007) proposed, on the basis of first-principles calculations, an energetically favorable orthorhombic cell with space group  $D_{2h}^{16}$  ( $Pnma$ ) and lattice parameters  $a = 8.677$ ,  $b = 6.803$ ,  $c = 8.506$  Å ( $Z = 4$ ) and claimed good agreement with experimental XRD data of Deliens and Piret (1983). However, no crystallographic data for the atomic positions of this candidate structure of metastudtite were reported by Ostanin and Zeller and the computed equilibrium volume was  $V = 502.06$  Å<sup>3</sup> and stated to be 4.3% larger than the experimental estimate.

In this work, the structural properties of studtite and metastudtite have been systematically investigated using density functional theory. The structure of metastudtite crystallizing in the orthorhombic  $Pnma$  space group ( $Z = 4$ ) is reported for the first time at the atomic level and the computed lattice parameters suggest that the unit cell of metastudtite is larger than previously reported dimensions ( $Z = 2$ ) derived from experimental X-ray diffraction data. Particular emphasis is placed here on the determination of an accurate crystal structure of metastudtite needed for further thermodynamic properties calculations.

Details of our computational approach are given in the next section, followed by a complete analysis and discussion of our results, with a summary of our findings and conclusions is presented in the last section.

### 3.5.2.2 Computational Methods

First-principles total energy calculations were performed using the spin-polarized density functional theory (DFT), as implemented in the Vienna *ab initio* simulation package (VASP) (Kresse & Furthmüller, Efficient iterative schemes for *ab initio* total-energy calculations using a plane-wave basis set, 1996). The exchange-correlation energy was calculated using the generalized gradient approximation (GGA), with the parametrization of Perdew and Wang (PW91) (Perdew et al., 1992; Perdew and Wang, 1992). The PW91 functional was found in previous studies to correctly describe the geometric parameters and properties of various uranium oxides and uranium-containing structures observed experimentally (Weck et al., 2007; Weck et al., 2010; Weck et al., 2011).

Although theoretical approaches that go beyond standard DFT are needed to account for the strong on-site Coloumb repulsion between U 5f electrons in bulk UO<sub>2</sub>, previous studies on studtite and uranyl-organic coordination polymers show that standard DFT is appropriate to describe those systems (Ostanin and Zeller, 2007) (Weck et al., 2011).

The interaction between valence electrons and ionic cores was described by the projector augmented wave (PAW) method (Blöchl, 1994; Kresse and Joubert, 1999). The U(6s,6p,6d,5f,7s) and O(2s,2p) electrons were treated explicitly as valence electrons in the Kohn-Sham (KS) equations and the remaining core electrons together with the nuclei were represented by PAW pseudopotentials. The KS equation was solved using the blocked Davidson (Davidson, 1983) iterative matrix diagonalization scheme followed by the residual vector minimization method. The plane-wave cutoff energy for the electronic wavefunctions was set to a value of 500 eV, ensuring the total energy of the system to be converged to within 1 meV/atom. Electronic relaxation was performed with the conjugate gradient method accelerated using the Methfessel-Paxton Fermi-level smearing (Methfessel and Paxton, 1989) with a Gaussian width of 0.1 eV.

Ionic relaxation was carried out using the quasi-Newton method and the Hellmann-Feynman forces acting on atoms were calculated with a convergence tolerance set to 0.01 eV/Å. A periodic unit cell approach was used in the calculations. Structural relaxation was performed without symmetry constraints. The Brillouin zone was sampled using the Monkhorst-Pack *k*-point scheme (Monkhorst and Pack, 1976) with *k*-point meshes of 2×5×3 and 5×3×3 for studtite and metastudtite, respectively. In structural relaxation calculations, the monoclinic structure with space group *C2/c* (*Z* = 4) reported by Burns and Hughes (2003) was used as the starting geometry for studtite and a candidate structure crystallizing in the space group *Pnma* (*Z* = 4), with twice the length of the experimental *c* dimension, was built for metastudtite based on the information reported by Ostanin and Zeller (2007) and the suggestion of Burns and Hughes (2003).

### 3.5.2.3 Results and discussion

#### Crystal structure of studtite

Consistent with XRD data (Burns and Hugues, 2003), the computed equilibrium structure is monoclinic and crystallizes in the space group *C2/c* (*Z* = 4; cf. Fig. 3.5-6). The calculated cell dimensions  $a = 13.93$ ,  $b = 6.84$ ,  $c = 8.55$  Å and  $\beta = 122.7^\circ$  ( $V = 685.6$  Å<sup>3</sup>;  $b/a = 0.49$ ,  $c/a = 0.61$ ) are in close agreement with the XRD parameters of Burns and Hughes, i.e.,  $a = 14.068(6)$ ,  $b = 6.721(3)$ ,  $c = 8.428(4)$  Å and  $\beta = 123.356(6)^\circ$  ( $V = 665.6$  Å<sup>3</sup>;  $b/a = 0.48$ ,  $c/a = 0.60$ ). The computed equilibrium volume is 3.0% larger than the experimental estimate, due to the fact that GGA calculations tend to overestimate the bond distances (Grinberg et al., 2001) and that standard DFT cannot account accurately for long-range intermolecular forces between adjacent chains (Kohn et al., 1998). However, this computed equilibrium volume is in better agreement with experiment than previous GGA calculations (Ostanin and Zeller, 2007) predicting a volume of  $V = 690.1$  Å<sup>3</sup>, i.e. 3.7% larger than experiment.

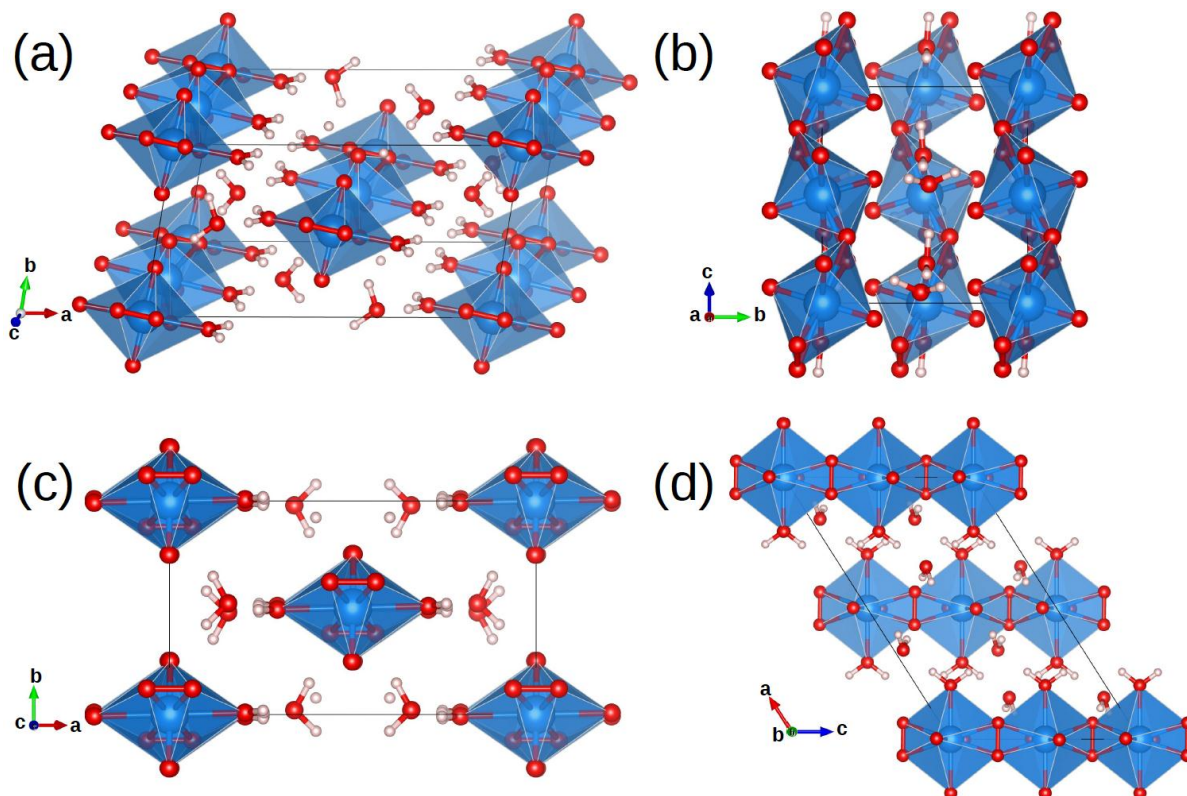


Figure 3.5-6. Crystal unit cell of studtite  $(\text{UO}_2)\text{O}_2(\text{H}_2\text{O})_4$  (space group  $C2/c$ ,  $Z = 4$ ) relaxed with DFT at the GGA/PW91 level of theory. (a) View of the packing of chains showing the uranium coordination polyhedra. Views along the directions: (b) [100], (c) [001] and (d) [010]. Color legend: U, blue; O, red; H, white.

A detailed discussion of the atomistic structure of studtite was given by Burns and Hughes (2003). As shown in Fig. 3.5-6, the studtite structure consists of extended chains propagating along the  $c$  axis. The ubiquitous uranyl unit is positioned with uranium on a  $4a$  Wyckoff site ( $\bar{1}$  symmetry) and coordinated by six equatorial oxygen atoms (on  $8f$  Wyckoff sites) donated by symmetry-related pairs of water and peroxy groups. The local environment of the U metal center is hexagonal bipyramidal with two short axial  $\text{U}=\text{O}$  bonds, calculated (measured) to be both at a distance of  $1.83 \text{ \AA}$  ( $1.769 \text{ \AA}$ ), and a linear  $\text{O}=\text{U}=\text{O}$  angle, and with equatorial oxygen atoms at distances of  $2.38 \text{ \AA}$  ( $2.365 \text{ \AA}$ ) for peroxy oxygen atoms and  $2.41 \text{ \AA}$  ( $2.395 \text{ \AA}$ ) for water oxygen atoms. The peroxy atoms are  $\mu^2$ -bridging between symmetry-related uranium metal centers. The calculated (measured) dihedral angle between equatorial planes of successive uranyl ions along the chains is  $0.2^\circ$  ( $5.99^\circ$ ); as discussed in previous studies of one-dimensional uranium organic polymers (Weck et al., 2011), this large deviation, compared to other structural parameters, suggests that interchain forces, which are not accurately described with standard DFT, may play a role in the relative orientation of adjacent uranium coordination polyhedral. Additional information on the computed and measured interatomic distances and angles in studtite are reported in the next section, along with the discussion of the metastudtite structure.

### Crystal structure of metastudtite

Structural relaxation calculations predict that metastudtite crystallizes in the orthorhombic space group  $Pnma$  ( $Z = 4$ ) with lattice parameters  $a = 6.75$ ,  $b = 8.72$ ,  $c = 8.45$  Å ( $V = 497.4$  Å<sup>3</sup>;  $b/a = 1.29$ ,  $c/a = 1.25$ ). Assuming that the length of the experimental  $c$  dimension should be doubled (Burns and Hughes, 2003), those cell dimensions are in good agreement with the corrected XRD parameters given by Deliens and Piret (1983), i.e.  $a = 6.51(1)$ ,  $b = 8.78(2)$ ,  $c = 8.42(2)$  Å ( $V = 481.3$  Å<sup>3</sup>;  $b/a = 1.35$ ,  $c/a = 1.29$ ). Let us note that the computed equilibrium volume is 3.3% larger than the experimental volume, i.e. close to the volume overestimation in the calculation of the studtite structure. The present calculations represent a slight improvement over the previous calculations of Ostanin and Zeller, who predicted lattice parameters  $a = 6.803$ ,  $b = 8.677$ ,  $c = 8.506$  Å ( $V = 502.1$  Å<sup>3</sup>;  $b/a = 1.27$ ,  $c/a = 1.25$ ), corresponding to an overestimation of the experimental volume by 4.3%. In order to comply with the IMA recommendation  $c < a < b$ , a transformation conserving the  $Pnma$  symmetry was applied so that the final computed cell dimensions of metastudtite are given as  $a = 8.45$ ,  $b = 8.72$ ,  $c = 6.75$  Å. A ball-and-stick representation of the resulting optimized crystal unit cell of metastudtite is shown in Fig. 3.5-7.

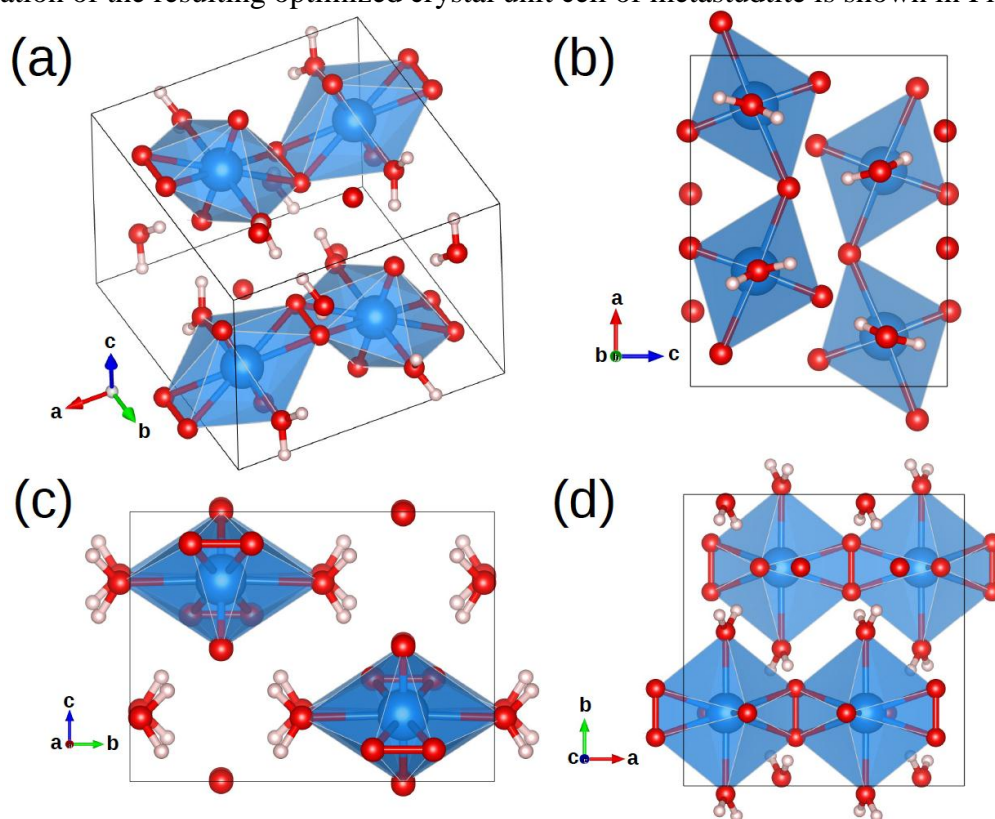


Figure 3.5-7. Crystal unit cell of metastudtite  $(\text{UO}_2)\text{O}_2(\text{H}_2\text{O})_2$  (space group  $Pnma$ ,  $Z = 4$ ) relaxed with DFT at the GGA/PW91 level of theory. (a) View of the packing of chains showing the uranium coordination polyhedra. Views along the directions: (b) [010], (c) [100] and (d) [001]. Color legend: U, blue; O, red; H, white.

Using the orthorhombic structure optimized with DFT, the diffraction pattern of metastudtite was simulated using the Mercury (Macrae, et al., 2008) software and compared with the XRD pattern collected by Debets (1963) for synthetic  $(\text{UO}_2)\text{O}_2(\text{H}_2\text{O})_2$ . Let us note that previous experimental

studies showed only minute differences between the XRD powder patterns for synthetic  $(\text{UO}_2)\text{O}_2(\text{H}_2\text{O})_2$ , natural metastudtite and heated natural studtite (Deliens and Piret, 1983). Although simulated and observed diffraction peaks were found to be in overall good agreement, some peak positions appeared slightly shifted due to the larger volume (+3.3%) of the unit cell relaxed with DFT/GGA compared with the experimentally determined volume. As shown in Fig. 3.5-8, excellent agreement between simulated and observed diffraction patterns was ultimately achieved by a simple rescaling of the computed structure to fit experimental unit-cell dimensions, followed by ionic relaxation. The resulting atomic positions and fractional coordinates for the  $(\text{UO}_2)\text{O}(\text{H}_2\text{O})$  motif (cf. Fig. 3.5-9) are reported in Table 3.5-1, and the corresponding interatomic distances and bond angles are given in Table 3.5-2.

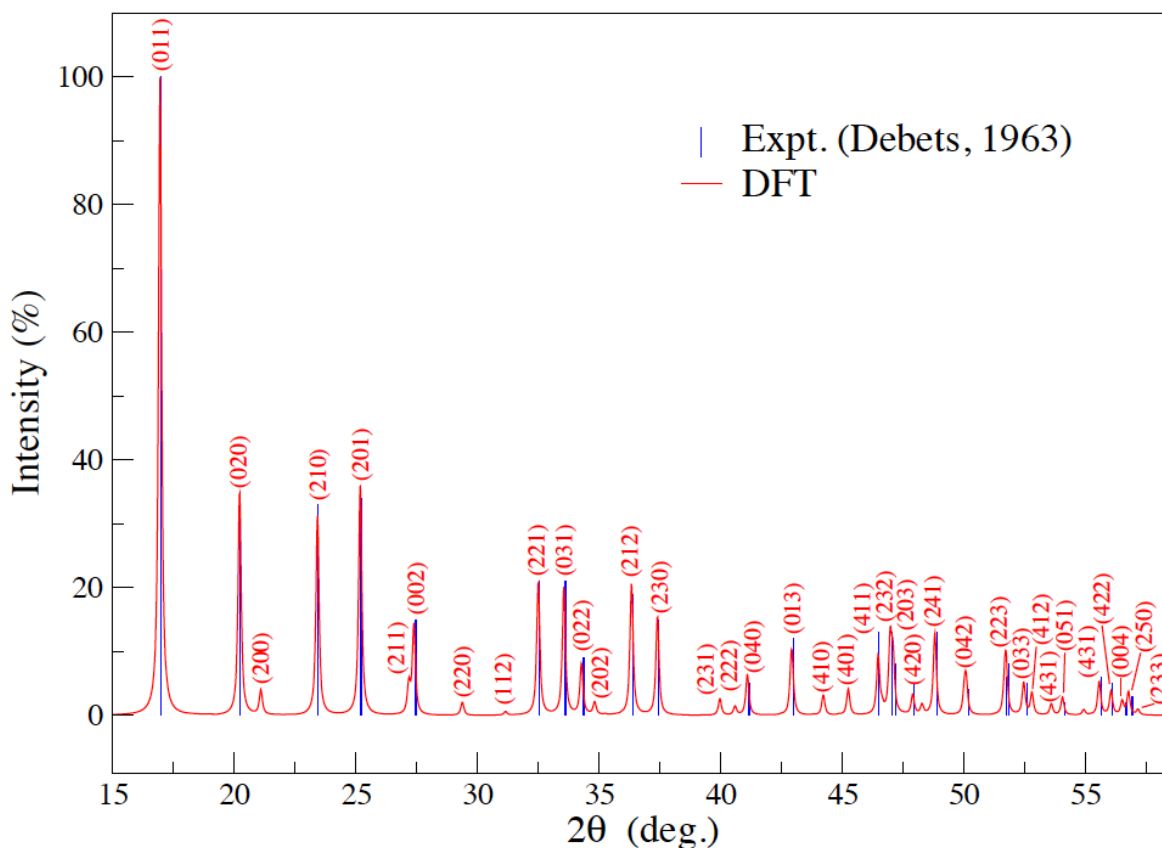


Figure 3.5-8. X-ray diffraction pattern of metastudtite. The experimental powder diffraction pattern for  $\text{Cu K}\alpha_1$  radiation (Debets, 1963) is represented by blue lines. The diffraction pattern simulated from the orthorhombic structure (space group  $Pnma$ ,  $Z = 4$ ) reported in the present study is shown in red. A full-width at half-maximum (FWHM) parameter of  $0.2\ 2\theta$  was used in the simulation.

Similar to the studtite structure, metastudtite consists of polymeric chains propagating along the  $a$  axis (cf. Fig. 3.5-7). The uranyl unit is positioned with uranium on a  $4c$  Wyckoff site ( $m$  symmetry) and coordinated by six equatorial oxygen atoms on  $8d$  Wyckoff sites donated by water and peroxy groups. The local hexagonal bipyramidal environment of the U metal center consists of two short axial  $\text{U}=\text{O}$  bonds calculated to be 1.80 and 1.85 Å long, with a nearly linear

O=U=O angle ( $178.8^\circ$ ), and with equatorial oxygen atoms at distances of 2.39 Å for peroxo oxygen atoms and 2.42 Å for water oxygen atoms (cf. Fig. 3.5-9). The  $\mu^2$ -bridging peroxo atoms have a bond distance O3–O3' of 1.46 Å, identical to the bond distance in studtite. As shown in Table 3.5-2, the predicted bond distances and angles for metastudtite are close to the ones of studtite.

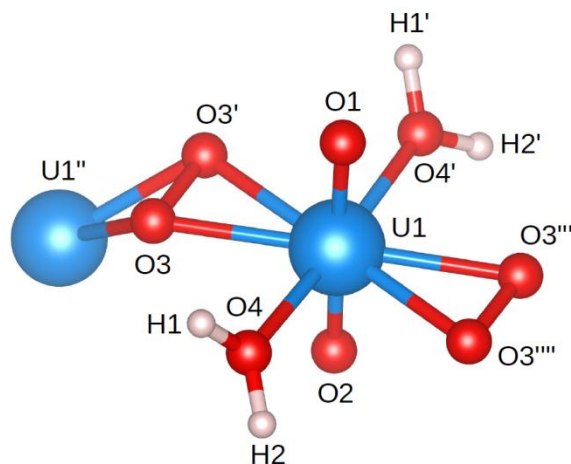


Figure 3.5-9. Ball-and-stick representation of the  $(\text{UO}_2)\text{O}(\text{H}_2\text{O})$  complex composing metastudtite. Color legend: U, blue; O, red; H, white. Symmetry codes: ' =  $x, 5/2 - y, z$ ; '' =  $-1/2 + x, 5/2 - y, 3/2 - z$ ; ''' =  $1/2 + x, 5/2 - y, 3/2 - z$ ; '''' =  $1/2 + x, y, 3/2 - z$ .

Hydrogen bonds linking the  $-yl$  O1 and peroxo O3 oxygen atoms of on chain to the H2 and H1 atoms, respectively, of a neighboring chain are present in metastudtite. The  $\text{O1}\cdots\text{H2}-\text{O4}$  and  $\text{O3}\cdots\text{H1}-\text{O4}$  contact distances are 1.75 and 1.67 Å, respectively. These distances are comparable to the calculated (measured) hydrogen bonds in studtite ranging from 1.62 to 1.79 Å (1.722 to 1.959 Å). The calculated dihedral angle between equatorial planes of successive uranyl ions along the chains is  $0.0^\circ$ , close to the  $0.2^\circ$  value computed for the relaxed structure of studtite.

#### 3.5.2.4 Conclusions

The structures of the only known minerals containing peroxide, i.e. studtite  $[(\text{UO}_2)\text{O}_2(\text{H}_2\text{O})_4]$  and metastudtite  $[(\text{UO}_2)\text{O}_2(\text{H}_2\text{O})_2]$ , have been investigated using density functional theory. The detailed structure of metastudtite crystallizing in the orthorhombic space group  $Pnma$  ( $Z = 4$ ) is explicitly reported for the first time at the atomic level. Excellent agreement was obtained between the observed XRD powder pattern of metastudtite and the structure predicted in this study, thus demonstrating that the unit cell of metastudtite is actually larger than the previously reported cell dimensions ( $Z = 2$ ) derived from experimental X-ray diffraction data.

Further first-principles calculations will investigate the thermal stability of studtite and metastudtite, which are of crucial importance to understand the evolution and possible phase transformations occurring in minerals containing peroxide.

Table 3.5-1. Atomic positions and fractional coordinates of the (UO<sub>2</sub>)O(H<sub>2</sub>O) complex composing metastudtite (space group *Pnma*, *Z* = 4; *a* = 8.42, *b* = 8.78, *c* = 6.51 Å).

UO <sub>2</sub> OH <sub>2</sub> O	Wyckoff position	x	y	z
U1	4c	0.150	0.250	0.750
O1	4c	0.227	0.250	0.016
O2	4c	0.080	0.250	0.488
O3	8d	0.599	0.833	0.382
O4	8d	0.150	0.974	0.761
H1	8d	0.127	0.584	0.889
H2	8d	0.190	0.600	0.659

Table 3.5-2. Selected interatomic distances (Å), angles (°) in the structures of metastudtite and studtite <sup>a</sup>

Parameters	Metastudtite DFT <sup>b</sup>	Studtite DFT <sup>b</sup>	Studtite Expt. <sup>c</sup>
U1–O1	1.85	1.83	1.769
U1–O2	1.80	1.83	1.769
U1–O3	2.39	2.38	2.365
U1–O4	2.42	2.41	2.395
U1–U1''	4.21	4.21	4.214
O3–O3'	1.46	1.46	1.464
O4–H1	1.00	1.00	0.978
O4–H2	1.00	1.00	0.975
O1''–H2	1.75	–	–
O3''–H1	1.67	–	–
H1''–OH <sub>2</sub>	–	1.62	1.722
H2''–OH <sub>2</sub>	–	1.66	1.959
O3''–H <sub>2</sub> O	–	1.71	1.757
O2''–H <sub>2</sub> O	–	1.79	1.956
O1–U1–O2	178.8	180.0	180.00
O1–U1–O3	88.2	88.8	89.73
O1–U1–O4	88.4	86.5	86.53
O2–U1–O3	92.9	92.3	90.27
O2–U1–O4	91.7	87.7	93.47
O3–U1–O3'	35.5	35.5	36.17
O3–U1–O3'''	179.9	180.0	180.00
O3–U1–O3''''	144.5	144.4	143.83
O3–U1–O4	71.6	71.4	71.32
U1–O3–U1''	123.7	124.0	126.60
O4–U1–O3'	107.0	106.9	107.25
O4–U1–O4'	176.5	180.0	180.00
O1–U1–U1''–O1''	0.0	0.2	5.99

<sup>a</sup> Symmetry codes: ' = *x*, 5/2 - *y*, *z*; '' = -1/2 + *x*, 5/2 - *y*, 3/2 - *z*; ''' = 1/2 + *x*, 5/2 - *y*, 3/2 - *z*; '''' = 1/2 + *x*, *y*, 3/2 - *z*.

<sup>b</sup> Experimental cell dimensions were used in the calculations.

<sup>c</sup> Burns and Hughes, 2003.

### 3.5.3 References

- Amme, M., 2002, Contrary effects of the water radiolysis product  $H_2O_2$  upon the dissolution of nuclear fuel in natural ground water and deionized water, *Radiochimica Acta*, 90(7), p. 399-406.
- Anisimov, V., Aryasetiawan, F., Lichtenstein, A., 1997, First-principles calculations of the electronic structure and spectra of strongly correlated systems: The LDA+U method, *Journal of Physics: Condensed Matter*, 9(4), p. 767-808.
- Anisimov, V., Poteryaev, A., Korotin, M., Anokhin, A., Kotliar, G., 1997, First-principles calculations of the electronic structure and spectra of strongly correlated systems: dynamical mean-field theory, *Journal of Physics: Condensed Matter*, 9(35), p. 7359-7367.
- Anisimov, V., Zaanen, J., Andersen, O., 1991, Band Theory and Mott Insulators - Hubbard-U Instead of Stoner-I. *Physical Review B*, 44(3), p. 943-954.
- Arko, A., Koelling, D., Boring, A., Ellis, W., Cox, L., 1986, The Band Structure of  $UO_2$  - An Angle-Resolved and Resonant Photoemission Study, *Journal of the Less-Common Metals*, 122, p. 95-99.
- Armstrong, C., Nyman, M., Shvareva, T., Sigmon, G., Burns, P., Navrotsky, A., 2012, Uranyl peroxide enhanced nuclear fuel corrosion in seawater, *Proceedings of the National Academy of Sciences of the USA*, 109(6), p. 1874-1877.
- Baer, Y., Schoenes, J., 1980, Electronic Structure and Coulomb Correlation-Energy in  $UO_2$  Single-Crystal, *Solid State Communications*, 33(8), p. 885-888.
- Blesa, M., Morando, P., Regazzoni, A., 1994, *Chemical Dissolution of Metal Oxides*. Boca Raton, FL: CRC.
- Blöchl, P., 1994, Projector Augmented-Wave Method, *Physical Review B*, 50(24), p. 17953-17979.
- Blöchl, P., Jepsen, O., Andersen, O., 1994, Improved Tetrahedron Method for Brillouin-Zone Integrations, *Physical Review B*, 49(23), p. 16223-16233.
- Buck, E., Hanson, B., Friese, J., Douglas, M., McNamara, B., 2004, Evidence for neptunium incorporation into uranium (VI) phases. In J. Hanchar, S. Stroes Gascoyne, & L. Browning (Ed.), *28th Symposium on the Scientific Basis for Nuclear Waste Management held at the 2004 MRS Spring Meeting*. 824, p. 133-138. San Francisco, CA: Materials Research Society Symposium Proceedings.
- Burns, P., 2005,  $U^{6+}$  minerals and inorganic compounds: Insights into an expanded structural hierarchy of crystal structures, *Canadian Mineralogist*, 43, p. 1839-1894.
- Burns, P., Hughes, K.-A., 2003, Studtite,  $[(UO_2)(O_2)(H_2O)_2](H_2O)_2$ : The first structure of a peroxide mineral, *American Mineralogist*, 88(7), p. 1165-1168.
- Burns, P., Ewing, R., Navrotsky, A., 2012, Nuclear Fuel in a Reactor Accident, *Science*, 335(6073), p. 1184-1188.



- Cejka, J., Sejkora, J., Deliens, M., 1996, New data on studtite,  $\text{UO}_{4.4}\text{H}_2\text{O}$ , from Shinkolobwe, Shaba, Zaire. *Neues Jahrbuch für Mineralogie - Monatshefte*, 3, p. 125-134.
- Cordfunke, E., & Aling, P., 1963, Thermal Decomposition of Hydrated Uranium Peroxides, *Recueil des Travaux Chimiques des Pays-Bas - Journal of the Royal Netherlands Chemical Society*, 82(3), p. 257-263.
- Cordfunke, E., van der Giessen, A., 1963, Pseudomorphic Decomposition of Uranium Peroxide into  $\text{UO}_3$ , *Journal of Inorganic and Nuclear Chemistry*, 25(5), p. 553-554.
- Cox, P. (1994). *The Surface Science of Metal Oxides*. Cambridge, UK: Cambridge University Press.
- Cui, D., Low, J., Spahiu, K., 2011, Environmental behaviors of spent nuclear fuel and canister materials, *Energy & Environmental Science*, 4, p. 2537-2545.
- Davidson, E. R., 1983, In G. Diercksen, & S. Wilson (Eds.), *Methods in Computational Molecular Physics* (Vol. 113, p. 95). New York, NY: NATO Advanced Study Institute, Series C, Plenum.
- Debets, P., 1963, X-Ray Diffraction Data on Hydrated Uranium Peroxide. *Journal of Inorganic Nuclear Chemistry*, 25(6), p. 727-730.
- Deliens, M., Piret, P., 1983, Metastudtite,  $\text{UO}_{4.2}\text{H}_2\text{O}$ , a New Mineral from Shinkolobwe, Shaba, Zaire. *American Mineralogist*, 68(3-4), p. 456-458.
- Draganic, I., Draganic, Z., 1971, *The Radiation Chemistry of Water*. New York, NY: Academic Press.
- Dudarev, S., Botton, G., Savrasov, S., Humphreys, C., Sutton, A., 1998, Electron-energy-loss spectra and the structural stability of nickel oxide: An LSDA+U study. *Physical Review B*, 57(3), p. 1505-1509.
- Ewing, R., Runde, W., Albrecht-Schmitt, T., 2010, Environmental impact of the nuclear fuel cycle: Fate of actinides, *MRS Bulletin*, 35, p. 859-866.
- Grinberg, I., Ramer, N., Rappe, A., 2001, Quantitative criteria for transferable pseudopotentials in density functional theory. *Physical Review B*, 63(20), p. 201102-1 - 201102-4.
- Hall, R., Mortimer, M., Mortimer, D., 1987, Surface-Energy Measurements on  $\text{UO}_2$  - A Critical Review. *Journal of Nuclear Materials*, 148(3), p. 237-256.
- Hanson, B., McNamara, B., Buck, E., Friese, J., Jenson, E., Krupka, K., Arey, B., 2005, Corrosion of commercial spent nuclear fuel. 1. Formation of studtite and metastudtite. *Radiochim. Acta*, 93(3), p. 159-168.
- Hughes Kubatko, K.-A., Helean, K., Navrotsky, A., Burns, P., 2003, Stability of peroxide-containing uranyl minerals, *Science*, 302, p. 1191-1193.
- Kohn, W., Meir, Y., Makarov, D. E., 1998, van der Waals Energies in Density Functional Theory, *Physical Review Letters*, 80(19), p. 4153-4156.
- Kotani, A., Yamazaki, T., 1992, Systematic Analysis of Core Photoemission Spectra for Actinide Di-oxides and Rare-Earth Sesqui-Oxides, *Progress of Theoretical Physics Supplement*, 108, p. 117-131.

- Kotliar, G., Savrasov, S., Haule, K., Oudovenko, V., Parcollet, O., Marianetti, C. A., 2006, Electronic structure calculations with dynamical mean-field theory, *Reviews of Modern Physics*, 78(3), p. 865-951.
- Kresse, G., Furthmüller, J., 1996, Efficient iterative schemes for ab initio total-energy calculations using a plane-wave basis set, *Physical Review B*, 54(16), p. 11169-11186.
- Kresse, G., Joubert, D., 1999, From ultrasoft pseudopotentials to the projector augmented-wave method. *Physical Review B*, 59(3), p. 1758-1775.
- Lichtenstein, A., Katsnelson, M., 1998, Ab initio calculations of quasiparticle band structure in correlated systems: LDA++ approach. *Physical Review B*, 57(12), p. 6884-6895.
- Macrae, C., Bruno, I., Chisholm, J., Edgington, P., McCabe, P., Pidcock, E., Rodriguez-Monge, L., Taylor, R., van de Streek, J., Wood, P.A., 2008, Mercury CSD 2.0 - new features for the visualization and investigation of crystal structures, *Journal of Applied Crystallography*, 41, p. 466-470.
- McNamara, B., Buck, E., Hanson, B., 2003, Observation of studtite and metastudtite on spent fuel. In R. Finch, & D. Bullen (Ed.), *26th Symposium on the Scientific Basis for Nuclear Waste Management held at the 2002 MRS Fall Meeting*. 757, pp. 401-406. Boston, MA : Mater. Res. Soc. Symp. Proc.
- McNamara, B., Hanson, B., Buck, E., Soderquist, C., 2005, Corrosion of commercial spent nuclear fuel. 2. Radiochemical analyses of metastudtite and leachates, *Radiochimica Acta*, 93(3), p. 169-175.
- Methfessel, M., Paxton, A., 1989, High-Precision Sampling for Brillouin-Zone Integration in Metals, *Physical Review B*, 40(6), p. 3616-3621.
- Monkhorst, H., Pack, J., 1976, Special Points for Brillouin-Zone Integrations, *Physical Review B*, 13(12), p. 5188-5192.
- Ostanin, S., Zeller, P., 2007, Ab initio study of uranyl peroxides: Electronic factors behind the phase stability, *Physical Review B*, 75(7), p. 073101.
- Page, F., Woolley, D., 1974, Ionization Associated with Solid Particles in Flames. 2. Electron Number Density, *Combustion and Flame*, 23(1), p. 121-127.
- Perdew, J., Wang, Y., 1992, Accurate and Simple Analytic Representation of the Electron-Gas Correlation-Energy, *Physical Review B*, 45(23), p. 13244-13249.
- Perdew, J., Zunger, A., 1981, Self-Interaction Correction to Density Functional Approximation for Many-Electron Systems, *Physical Review B*, 23(10), p. 5048-5079.
- Perdew, J., Chevary, J., Vosko, S., Jackson, K., Pederson, M., Singh, D., Fiolhais, C., 1992, Atoms, Molecules, Solids, and Surfaces - Applications of the Generalized Gradient Approximation for Exchange and Correlation, *Physical Review B*, 46(11), p. 6671-6687.
- Prodan, I., Scuseria, G., Martin, R., 2007, Covalency in the actinide dioxides: Systematic study of the electronic properties using screened hybrid density functional theory, *Physical Review B*, 76(3), p. 033101.

- Roberts, L., 1963, In R. Ward (Ed.), *Nonstoichiometric Compounds, Advances in Chemistry* (Vol. 39, p. 66). Washington, D.C.: American Chemical Society.
- Sato, T., 1961, Thermal Decomposition of Uranium Peroxide Hydrate. *Naturwissenschaften*, 48(22), p. 668-693.
- Sattonnay, G., Ardois, C., Corbel, C., Lucchini, J.-F., Barthe, M.-F., Garrido, F., Gosset, D., 2001, Alpha-radiolysis effects on  $\text{UO}_2$  alteration in water, *Journal of Nuclear Materials*, 288(1), p. 11-19.
- Schoenes, J., 1987, Recent Spectroscopic Studies of  $\text{UO}_2$ , *Journal of the Chemical Society, Faraday Transactions II*, 83, p. 1205-1213.
- Shuller, L., Ewing, R., Becker, U., 2010, Quantum-mechanical evaluation of Np-incorporation into studtite, *American Mineralogist*, 95(8-9), p. 1151-1160.
- Skomurski, F., Ewing, R., Rohl, A., Gale, J., Becker, U., 2006, Quantum mechanical vs. empirical potential modeling of uranium dioxide ( $\text{UO}_2$ ) surfaces: (111), (110), and (100), *American Mineralogist*, 91(11-12), p. 1761-1772.
- Skomurski, F., Shuller, L., Ewing, R., Becker, U., 2008, Corrosion of  $\text{UO}_2$  and  $\text{ThO}_2$ : A quantum-mechanical investigation, *Journal of Nuclear Materials*, 375(3), p. 290-310.
- Stumm, W., Sigg, L., Sulzberger, B., 1992, *Chemistry of the Solid-Water Interface: Processes at the Mineral-Water and Particle-Water Interface in Natural Systems*. New York, NY: Wiley & Sons.
- Tasker, P., 1979a, Stability of Ionic Crystal Surfaces, *Journal of Physics C - Solid State Physics*, 12(22), p. 4977-4984.
- Tasker, P., 1979b, Surface Properties of Uranium-Dioxide, *Surface Science*, 87(2), p. 315-324.
- Thompson, A., Wolverton, C., 2011, First-principles study of noble gas impurities and defects in  $\text{UO}_2$ , *Physical Review B*, 84(13), p. 134111.
- Ukazi, R., 1959, On the reactivity of Uranouranic oxide. I. On the Thermal Decomposition of uranyl nitrate (UNH), ammonium diuranate (ADU) and uranium peroxide (UPO), *Journal of the Atomic Energy Society of Japan*, 1, p. 405-411.
- Vaes, J., 1947, Six nouveaux minéraux d'urane provenant de Shinkolobwe. (Katanga), *Annales de la Societe Geologique de Belgique*, 70, p. B212-B229.
- Veal, B., Lam, D., 1974, X-Ray Photoelectron Studies of Thorium, Uranium, and Their Dioxides, *Physical Review B*, 10(12), p. 4902-4908.
- Villars, P., Calvert, L., 1991, *Pearson's Handbook of Crystallographic Data for Intermetallic Phases* (Vol. 2nd ed.). Metals Park, OH: ASM International.
- Walenta, K., 1974, Studtite and its Composition, *American Mineralogist*, 59(1-2), p. 166-171.
- Weck, P., Gong, C.-M., Kim, E., Thuery, P., Czerwinski, K., 2011, One-dimensional uranium-organic coordination polymers: crystal and electronic structures of uranyl-diacetohydroxamate, *Dalton Transactions*, 40(22), p. 6007-6011.

- Weck, P., Kim, E., Balakrishnan, N., Poineau, F., Yeaman, C., Czerwinski, K., 2007, First-principles study of single-crystal uranium mono- and dinitride, *Chemical Physics Letters*, 443(1-3), p. 82-86.
- Weck, P., Kim, E., Jové-Colón, C., Sassani, D., 2012, Structures of uranyl peroxide hydrates: a first-principles study of studtite and metastudtite, *Dalton Transactions*, 41(32), p. 9748-9752.
- Weck, P., Kim, E., Masci, B., Thuery, P., Czerwinski, K., 2010, Density Functional Analysis of the Trigonal Uranyl Equatorial Coordination in Hexahomotrioxacalix[3]arene-based Macrocyclic Complexes, *Inorganic Chemistry*, 49(4), p. 1465-1470.
- Zachariasen, W., 1944, *X-ray Diffraction Results for Uranium and Plutonium Compounds*. Report USAEC, Manhattan District Report CK-1367.
- Zunger, A., Perdew, J., Oliver, G., 1980, A Self-Interaction Corrected Approach to Many-Electron Systems - Beyond the Local Spin-Density Approximation, *Solid State Communications*, 34(12), p. 933-936.

## 4. Summary and Conclusions

The analysis of generic disposal concepts requires the accurate understanding of processes leading to radionuclide releases from the EBS, specifically at the barrier interface between fuel assemblies and containment structures. Multilayered EBS concepts and related materials evaluated by the UFD seek to provide the necessary level of confidence to ensure safe and robust long-term waste isolation. However, it is sensible to anticipate that waste containment failure would affect some canisters therefore exposing fuel to interactions with subsurface fluids eventually leading to radionuclide release. The contributions presented in this report are the result of a concerted effort among three different national laboratories: Argonne National Laboratory (ANL), Sandia National Laboratories (SNL), and Pacific Northwest National Laboratory (PNNL). The main accomplishments of these activities are summarized as follows:

- Computational implementation and validation of the Canadian mixed potential model for  $\text{UO}_2$  fuel corrosion. This model is based on the fundamental electrochemical and thermodynamic properties described by interactions at the fuel – fluid interface. This model captures key processes to fuel degradation such as hydrogen oxidation at the used fuel interface and the catalysis of oxidation/reduction reactions by noble metal particles on the fuel surface (epsilon phases).
- Computational development and implementation of a radiolysis model using a comprehensive set of radiolysis reactions to better account for potential solution compositions to be encountered in repository environments. Such a feature of the current model is not considered by the European radiolysis model and allows for heterogeneous  $\text{CO}_2$  speciation thus accounting for the presence of  $\text{HCO}_3^-$ . Comparisons of modeling results are in good agreement with those reported in other studies.
- A computational first principles study of the structures of the uranyl peroxide hydrates studtite and metastudtite. These two phases are important products of  $\text{UO}_2$  corrosion when exposed to water. The structures obtained from total energy calculations using density functional theory (DFT) are in very good agreement with those characterized by experimental X-ray diffraction methods. Such result is crucial in testing this computational tool to predict the phase stability of  $\text{UO}_2$  corrosion products and quantify their thermodynamic properties. The results of this work have been accepted for publication in the peer-reviewed journal Dalton Transactions.
- Development of distributions for the IRF from the nuclear fuel. The existing data on IRF is largely empirical and strongly dependent on the state of the fuel and cladding, burnup rates, irradiation history (e.g., linear thermal), and extent of interaction with solutions and gases. Therefore, the IRF of radionuclides is described by initial models using distributions to be sampled by PA models. This is implemented in two sets of distributions: (a) triangular distributions representing minimum, maximum, and mean (apex) values for LWR used fuel with burnup at or below 50 MWd/KgU, and (b) a process model has yet to be developed with functional parametrics.
- Development of an idealized strategy for model integration with generic disposal concepts. Significant efforts have produced process and sub-process models at the EBS scales. However, it is an ongoing task to delineate how these process models will couple

to others within the EBS process models and, subsequently, how such coupled models would be incorporated into the GPAM for generic evaluations of the safety case.

In FY2012, the used fuel degradation and RM activities have focused on process model implementation (for both radiolysis and degradation rate of used fuel matrix grains), constraining values of the instant release fractions of radionuclides from breached used fuel, preparation for incorporation of models into the GPAM (including instant release fraction constraints), development of first principle models of  $\text{UO}_2$  alteration, executing experimental programs for (a) generating synthetic fuels for studying radiolytic processes at future fuel conditions and (b) analyzing used fuel degradation process and the role of the epsilon phases using electrochemical cells. Within this fiscal year, these activities generated (or are generating):

- this level 2 milestone report
- the following level 3 and level 4 milestones
  - ANL testing plan—milestone: M4FT-12AN0806011 - Experimental Plan for ANL Electrochemical Corrosion Studies, January 6, 2012.
  - PNNL testing plan—milestone: M4FT-12PN0806052 - Waste Form Degradation and Radionuclide Mobilization Testing Plan, December 2, 2012.
  - ANL modeling report—milestone: M3FT-12AN0806013 - Waste Form Degradation Model Status Report: Electrochemical Model for Used Fuel Matrix Degradation Rate, August 9, 2012.
  - PNNL modeling report—milestone: M3FT-12PN080651- Radiolysis Process Modeling Results for Scenarios, July 2012.
  - ANL status report of experiments—milestone: M3FT-12AN0806015 - Report results of electrochemical experiments, September 21, 2012.
  - PNNL status report of experiments—milestone: M4FT-12PN0806053 - Experimental Results for SimFuels, August 24, 2012.
- the following journal publications (submitted or in preparation) covering
  - PNNL radiolysis model publication
  - First principle models of  $\text{UO}_2$  bulk and surface properties
  - First principle models of Studtite and metastudtite structures
- model implementations for
  - PNNL Radiolysis Model process model
  - ANL Mixed Potential Model for used fuel matrix degradation rates process model
  - constraints on Fast Release Fraction radionuclides for use in GPAM
  - first principle models and analyses of
    - $\text{UO}_2$  bulk and surface chemistry
    - structures of peroxide corrosion products of  $\text{UO}_2$

In addition, these activities initiated/furthered international collaboration efforts within

- the European Commission (EC) Collaborative Project (CP) on the *Fast / Instant Release of Safety Relevant Radionuclides (FIRST – nuclides) from Spent Nuclear Fuel*

- D. Sassani representing SNL (and the DOE NE FCT UFD) as an Associate Group
- *3 year project focused on high-burn-up fuels*
- *10 organizations; 45 participants*
- *KIT-INE and AMPHOS21 - Coordinating organizations*
  - Karlsruhe Institute of Technology - Institute for Nuclear Waste Disposal (KIT-INE) in Karlsruhe, Germany
  - AMPHOS21 Consulting, Barcelona, Spain
- Associated Groups get information access without specific required contributions - signed non-disclosure agreement – information sharing collaboration
  - Participated in the *FIRST – nuclides* kickoff meeting in February, 2012
    - Presented *Brief Overview of the US DOE Used Fuel Disposition Campaign and activities in the Used Fuel Degradation and Radionuclide Mobilization*
- In conjunction with the kickoff meeting
  - Toured facilities and presented detailed seminar on the US DOE Used Fuel Disposition Campaign and activities in the Used Fuel Degradation and Radionuclide Mobilization area under the EBS WP
    - AMPHOS21 in Barcelona, Spain
    - Karlsruhe Institute of Technology - Institute for Nuclear Waste Disposal (KIT-INE) in Karlsruhe, Germany
- the ROK – US Joint Fuel Cycle Study, Fuel Cycle Alternatives Working Group
  - D. Sassani, technical lead for Task 3 - *Spent Fuel Degradation and Durability over Geologic Time*
    - Participated in Working Group Meetings June 5-7 to define information sharing and priorities between our two groups
- Future Direction
  - EBS Modeling
  - Used Fuel Degradation Rate Model Implementation Improvements
    - Coupling to Cladding models
    - Functional dependencies on used fuel properties
    - Disposal environment conditions

In the future, the focus of activities in this Used Fuel Degradation and Radionuclide Mobilization activity will shift to implementation and integration of models for additional waste forms, as well as to addressing the additional FEPs comprehensively. One area that will begin to be addressed in the next fiscal year is that of integration and coupling of models for cladding degradation with the models for degradation of used fuel.

As discussed above, we are participating in the European Commission (EC) Collaborative Project (CP) on the Fast / Instant Release of Safety Relevant Radionuclides (*FIRST – nuclides*) from Spent Nuclear Fuel as an Associate Group. As data are collected within the EC *FIRST – nuclides* CP and made available for use, additional understanding of the interdependence of the

primary parameters controlling IRF in higher burnup fuels will be incorporated into constraints for GPAM source-terms. Future development of model dependencies could be tied to the better constrained FGR information, or could be correlated simultaneously with multiple major variables if the data were abundant enough to support such. Future work in this area will evaluate coupling of cladding models to the used fuel degradation and could develop various correlations to be used depending on particular cladding failure scenarios (e.g., pinhole versus crushed) and physical damage to used fuel.

The future expansion of radiolysis model will account for key chemical constituents (and the generation of their radiolytic species) in additional chemical environments of disposal systems (for example Cl, and Br in salt systems). In addition, future process modeling work will evaluate direct coupling of the PNNL Radiolysis Model with the ANL Mixed Potential Model to evaluate the explicit sensitivity on  $\text{UO}_2$  stability in various disposal environments. The approach described here will be applied to the prediction of the fuel behavior of the combined models to assess how the corrosion processes may affect the sensitivities to radiolysis model parameters. More direct integration with storage environment evaluations will occur via adaptation of the model to relevant storage environments. Under fuel storage conditions, doses will be dominated by gamma fields rather than alpha fields, the temperature will be considerably higher than for a disposal environment, the physical environments and gas compositions will be different. However, given the appropriate rate constants for the relevant processes, this model could be easily applied to fuel storage environments.

The future focus of matrix degradation modeling is to tailor the ANL Mixed Potential Model (ANL-MPM) (which was developed as part of the Canadian repository program) for application to potential US disposal system environments, including salt environments, and to extend the model to account for key dissolution rate determining processes not included in the original Canadian model. Key processes that are being incorporated into the ANL-MPM are the role of hydrogen oxidation at the used fuel interface and the catalysis of oxidation/reduction reactions (hydrogen oxidation, hydrogen peroxide, oxygen reduction) by noble metal particles on the fuel surface (epsilon phases). Additional work to construct a library of appropriate parameter sets that cover the range of disposal environment conditions is the focus of on-going and future experimental work for this project.

Given that first principle calculations show that the strong correlation interaction has some impact on the adsorption energy of water and dissociated water in the AFM case, these evaluations will continue with analyses of surface reactions among species such as  $\text{O}_2$  and  $\text{H}_2\text{O}_2$  in the next fiscal year, potentially progressing to full alteration analyses. Further first-principles calculations will investigate the thermal stability of studtite and metastudtite, which are of crucial importance to understand the evolution and possible phase transformations occurring in minerals containing peroxide. In addition, the thermochemical properties of other alteration phases of  $\text{UO}_2$  will be constrained (e.g., schoepite and metaschoepite) to begin constructing a data set for these from first principle calculations. Similar first principle approaches are also planned to be applied to analyze the noble metal particles (epsilon phase) surface reactions.

A coarse connection to chemical environment (defined in the GPAM and needed as input to the used fuel degradation and RM models) exists in the current GDSM models. At present this is sufficient as the used fuel degradation and RM models below are developed for granitic reducing environments and explicit coupling to chemistry variation is expected to be developed next fiscal



year with a primary target of extending the applicability into brine environments appropriate to salt systems. This is also the case for thermal and pressure dependencies that will begin to be explicitly incorporated into the used fuel degradation and RM models in FY2013. It is expected that as these enhanced models are incorporated into the GPAM, providing expanded environment coverage will become more efficient.